Development of compact schemes for the biharmonic form of Navier-Stokes equations on compact nonuniform grids without transformation

by

Pankaj Kumar

DEPARTMENT OF MECHANICAL ENGINEERING
INDIAN INSTITUTE OF TECHNOLOGY GUWAHATI
GUWAHATI-781039, INDIA

JANUARY, 2021

Development of compact schemes for the biharmonic form of Navier-Stokes equations on compact nonuniform grids without transformation

A thesis submitted

in partial fulfillment of the requirements

for the degree of

DOCTOR OF PHILOSOPHY

by

Pankaj Kumar

(Roll Number: 136103005)

DEPARTMENT OF MECHANICAL ENGINEERING

INDIAN INSTITUTE OF TECHNOLOGY GUWAHATI

GUWAHATI-781039, INDIA

December, 2020

Declaration

I hereby declare that the work contained in the thesis entitled **"Development of compact schemes for the biharmonic form of Navier-Stokes equations on compact nonuniform grids without transformation"** has been done by me, under the guidance of **Dr. Jiten C. Kalita**, Professor, Department of Matheamtics, Indian Institute of Technology Guwahati, for the award of the degree of Doctor of Philosophy and this work has not been submitted elsewhere for a degree.

Guwahati
January 2021.

Pankaj Kumar
Roll No: 136103005
Department of Mechanical Engineering
Indian Institute of Technology Guwahati
Guwahati-781039, India

Certificate

I hereby declare that the work contained in the thesis entitled **"Development of compact schemes for the biharmonic form of Navier-Stokes equations on compact nonuniform grids without transformation"** has been done by **Mr. Pankaj Kumar**, a student of the Department of Mechanical Engineering, Indian Institute of Technology Guwahati, for the award of the degree of Doctor of Philosophy has been carried out under my supervision and this work has not been submitted elsewhere for a degree.

Guwahati
January 2021

Prof. Jiten C. Kalita
Department of Mathematics
Indian Institute of Technology Guwahati
Guwahati-781039, India

Dedicated

To

My Family

Acknowledgements

PhD is a long journey and it would not have been possible to reach the destination without the support and guidance from many people. I would like to take this opportunity to express my deepest gratitude for their generous support.

Firstly, I would like to express my sincere gratitude to my supervisor Prof. Jiten C. Kalita for the continuous support of my research journey through his patience, motivation, and immense knowledge. His guidance helped me through out my time as a research scholar. I could not have imagined having a better supervisor and mentor for my Ph.D. I want to thank my previous supervisor, Late Professor Dr. Subhash C. Mishra, who was a great help at the beginning of my thesis and introduced me to scientific research of high quality.

Besides my advisor, I would like to thank the rest of my doctoral committee members: Prof. Vinayak Kulkarni, Prof. Anoop K. Dass, and Dr. Pankaj K. Mishra, for their insightful comments and encouragement, which motivated me to widen my research from various perspectives.

My sincere thanks also goes to Dr. Yogesh G. Bhumkar, Mr. Naveen Ganta, and Mr. Bikash Mahato, who provided me an opportunity to join their team for a short while in IIT Bhubaneswar, and who gave access to the laboratory and research facilities. Without they precious support it would not be possible to conduct this research.

I am also grateful to all the staff members of the Department of Mathematics and Mechanical Engineering for their assistance in various ways during my research period.

I would like to thank my friends and colleagues Sailen, Devanand, Raghav, Kamaljyoti, Subhra and many others for all their encouragement and support during this period. My special appreciation goes to my close friends Sailen with whom I have shared some of the best moments of my life.

Last but not the least, I am extremely grateful to my father (Mr. Sohan Prasad Sharma), who as a teacher of Mathematics & Physics himself started me on this journey of research, my mother (Smt. Veena Devi) for her unending love & nurture, my elder sisters (Premlata , Hemlata), my elder brother (Manoj), my nephew (Praanshu) and all other family members for their sacrifices, supports and unconditional love to make me

what I am trying to be.

Finally, I would like to acknowledge everybody who is important to the successful completion of the thesis as well as express my apology that I could not mention each of them individually.

And above all, I thank God for everything.

January, 2021 **Pankaj Kumar**

Abstract

This work is concerned with developing compact finite difference schemes for simulating incompressible viscous flows governed by the Navier-Stokes (N-S) equations on nonuniform grids without transformations. The main work is concerned with developing two efficient schemes, one for the steady-state form of the N-S equations and the other one, is for its transient counterpart. They are developed for the the pure streamfunction formulation of the N-S equations, and second order accurate in both time and space. Apart from simulating several complex fluid flow situations for validating our schemes, emphasis is given more on simulating flow past bluff bodies, which finds wide ranging applications in laboratories and industries. In the process, numerical rate of convergence of the schemes and grid independence of the computed solutions are also established. Comprehensive analysis is carried out for the flow past stationary, rotating and oscillating circular cylinders in uniform flows for moderate Reynolds numbers (Re) and starting flow for the stationary case for high Res. For the stationary case, high quality simulations are accomplished for a wide range of Res ranging from $10^0 \leq Re \leq 10^4$ in the laminar regime, including the periodic flow characterized by von Kármán vortex street. The α, β, sub-α and sub-β phenomena, which are the trademark of the secondary and tertiary vortex dynamics associated with such flows, are studied in detail. However, the highlight of the thesis is the simulation of flow past sharp edges in uniform and accelerated flows, where we have considered the flat plate and a suspended wedge as our test cases. For the flat plate, several modes of vortex shedding patterns are established through a comprehensive FFT analysis. For the wedge, onset of turbulence is verified by the presence of coherent and three-fold structures in the flow. Moreover, the proposed schemes have also been utilized to accurately simulate heat transfer problems, including conjugate heat transfer problems in suddenly expanding channels. In all the cases, our numerical results are seen to be extremely close to the available numerical and experimental results.

भारतीय प्रौद्योगिकी संस्थान गुवाहाटी
Indian Institute of Technology Guwahati

LIST OF FIGURES

LIST OF TABLES

CONTENTS

भारतीय प्रौद्योगिकी संस्थान गुवाहाटी
Indian Institute of Technology Guwahati

CHAPTER 1

INTRODUCTION

1.1 Background

We live in a world surrounded by fluid flows everywhere, and we have been a part of some fluid flow phenomena in our day to day life, either voluntarily or involuntarily since time immemorial. Many physical systems are there to describe these phenomena: a river flowing through a terrain; air passing over a bird's wing; blood moving through arteries; an aircraft propelling through the atmosphere with supersonic speed, and many more. As such, it has attracted the attention of Engineers and Scientists alike and they have taken a very keen interest in such problems. One way to understand these phenomena is to express it mathematically, which led to the advent of the famous Navier-Stokes (N-S) equations. These equations have been in the forefront of the study of Fluid Mechanics for decades, and the most common model to predict fluid flows. In particular, they have been used to model incompressible viscous flows quite accurately.

The N-S equations constitute a set of highly nonlinear coupled partial differential equations (PDEs) and are extremely difficult to solve analytically. Only in extremely few cases, analytical solution are available, that too, after making so many assumptions [132]. Therefore, in most of the cases involving physical problems, one must go for numerical methods to solve these equations. The approach of using numerical methods and algorithms to solve and analyze problems involving fluid flows is known as Computational Fluid Dynamics (CFD) [3, 24, 118]. With remarkable advancement in computer architec-

ture, it is now possible to get into fluid flow problems which seemed impossible for the CFD community a few decades ago. In CFD, one of the most popular approaches is the use of finite difference methods (FDM), owing to their ease of application. Here, the basic approach is to discretize the problem domain by setting up a structured grid and then approximating the derivatives appearing in the governing N-S equations by difference quotients at each grid point. Such approximation yields a system of algebraic equations that can be solved by some matrix solution algorithm.

The most common finite difference representation of the derivatives is based on the Taylor series expansion of the variables at the grid points. The leading term in the truncation error (TE) of this expansion determines the order of the scheme's accuracy. For example, if this TE is asymptotically proportional to h^m, where h is the distance between two successive points, the difference scheme is said to be accurate of order m denoted by shortly $O(h^m)$. The central difference schemes, which are of order $O(h^2)$, are a popular choice for constructing discrete approximations to linear Partial differential equations (PDEs) for quite some time because of its ease and straight-forwardness in application. Such methods are known to yield quite good results on reasonable meshes if the solution is well behaved. But for specific problems, such as high Reynolds numbers, the solution may exhibit physically infeasible behaviour if the mesh is not sufficiently refined. However, mesh refinement invariably brings in additional points into the system resulting in increased system size. Consequently, more memory and CPU time are required to solve such problems. Moreover, traditional high-order accurate approximation of the derivatives at the grid points leads to an elongated stencil, thus increasing the coefficient matrix's bandwidth. Both mesh refinement and increased matrix bandwidth ultimately result in increased arithmetic operations. Thus neither a lower-order accurate method on a fine mesh nor a higher-order accurate one on a non-compact stencil could be computationally cost-effective. Therefore, there is a need to develop schemes that are both higher-order accurate and compact at the same time.

The evolution and increasing interest of compact schemes [1, 10, 13, 44, 46, 48, 49, 69, 70, 73, 75, 78, 79, 146–148, 150, 164] have revamped the curiosity of the CFD community in the finite difference (FD) approach. A compact finite difference scheme utilizes grid points located only directly adjacent to the node on which the approximation to the derivatives

are sought. These schemes are highly precise even when the grid size is small. Opposed to the wide-molecule methods [19, 52, 53, 151], the compact schemes have the ability to gather flow information solely from the nearest neighbours. The distinct advantage of compact discretization is that it lands on a system of equations resulting in a coefficient matrix with a much smaller bandwidth than non-compact schemes.

Traditionally, the primitive variable and stream function-vorticity (ψ-ω) formulations of the N-S equations have been the most popular approaches for computing viscous incompressible fluid flows. The details of the fundamental formulations of incompressible N-S equations can be found out in a review document by Gupta [45]. For two dimensional (2D) flows, the ψ-ω formulation is more famous for being computationally efficient and requires handling of only two unknowns instead of three for primitive variables. Furthermore, it ensures the exact satisfaction of the mass conservation equation. Nevertheless, in the case of three-dimensional flows, the primitive variable formulation is preferred. The three-dimensional counterpart of ψ-ω formulation also exists in the literature [24], but one needs to deal with six unknowns in six equations. For decades, the CFD community has been extensively using both the primitive variable and ψ-ω formulations to compute incompressible viscous flows governed by the N-S equations. Both these formulations have their relative advantages and disadvantages. In the primitive variable formulation, direct solution of the associated equations poses a great challenge due to the presence of the pressure term in the governing equations. On the other hand, a typical difficulty with the ψ-ω formulation stems out from the need of specifying the vorticity values at the no-slip boundaries. Owing to the above facts, the stream function-velocity (ψ-v) [46, 73] and pure stream function formulations [11–13, 96] (the biharmonic form of the N-S equations) have emerged as one of the most appealing alternative approaches for solving the N-S equations.

The ψ-v and pure stream function formulations have their origin in the Biharmonic equation of the form $\nabla^4\psi = f(x, y)$ [45], which represents Stoke's flow and also the linearized form of the N-S equations. The early part of the development of finite difference schemes for the Biharmonic equation involved splitting the original equation into two Poisson equations. However, such approaches, which became very popular immediately after their inception, had inherent issues with discretization near the boundary points.

The problem was circumvented by the work of Altas *et al.* in 1998 [1], where the dependent variable ψ and its derivatives ψ_x and ψ_y were evaluated simultaneously. This approach was able to overcome issues of the artificial boundary conditions associated with the first of the Poisson equations involved in the splitting method. The conditions for the dependent variable and its derivatives along the normal direction was exactly satisfied at the boundaries.

Fortunately for 2D incompressible viscous flows, the definition of the velocities in terms of the streamfunction exactly facilitates the use of the approach in [46] to discretize the N-S equation in pure streamfunction form. Subsequently, it led to the development of several finite difference approaches [13, 46, 96] for the pure streamfunction formulation of the N-S equations. These approaches eliminate the need to compute pressure and vorticity as a part of the computational process and are, therefore, computationally much more efficient than the primitive variable and ψ -ω formulations; they have a three-fold advantage over the other two approaches:

1. Avoid difficulties associated with primitive variables, mainly pressure.

2. Avoid use of artificial vorticity boundary conditions associated with ψ-ω formulation.

3. The iterations in solving the resulting matrix equation involve only a single variable.

The CFD community has seen the use of the biharmonic pure stream function formulation for the time-dependent N-S system in rectangular planar domains [42] for almost three decades. However, the compact schemes have made its stride into the biharmonic form of N-S equations only in the beginning of the twenty first century [11–13, 46, 73, 96]. The development of compact schemes for pure stream function formulation of the incompressible viscous N-S equations dates back to the work of Kupferman [96] in 2001. He used a central difference scheme and demonstrated the method's accuracy and robustness by computing high Reynolds number (Re) flows in a lid-driven cavity. In 2005, Ben-Artzi *et al.* developed a compact second order formulation for the biharmonic pure stream-function form to compute flows in the single and double lid-driven cavity problems [13]. Besides, they had also shown the uniqueness and decaying character of the solution of pure stream function formulation derived in a rectangular Cartesian coordinate system.

Further, in 2006, they proved the scheme's convergence and consistency for the full non-linear system [11]. The authors continued with their study of biharmonic formulation of N-S equations in Cartesian coordinates and were able to increase the accuracy of their schemes in 2010 [12]. Almost simultaneously, in 2005, Gupta and Kalita [46] proposed a second order accurate stream function-velocity (ψ-v) formulation that uses the biharmonic form of the steady-state N-S equations, which was followed by a fourth order counterpart in 2006 [47]. They used this formulation to compute steady state flows for different Re values in a lid-driven cavity. They have also successfully tackled a rectangular cavity with an aspect ratio of 2 as well as the backward facing step flow. They extended their work to transient flows in 2010 [73]. Here, along with the lid-driven cavity problem, they used this formulation to simulate flows for backward-facing step and vortex shedding behind a square prism.

Nevertheless, all these schemes developed so far mentioned above, used only uniform grids for discretizing the governing equations and, as such, could not accomplish the benefits associated with nonuniform grids, especially in the regions of large gradient of the flow variables in the physical domain to resolve small scales. Clustering the grids in high gradient regions and spreading them out in small gradient regions are essential for the achievement of computational efficiency and economy. Apart from accurately resolving smaller scales, it could bring considerable savings in computational time. In finite-volume or finite-element set up, nonuniform grids for flow computation are frequently used, where the physical and computational domain is the same. However, in a finite-difference set up, most of the computations performed on nonuniform grids are accomplished by transforming the governing equations from the physical domain onto the computational domain embedded with a uniform grid. Here, the governing equations are firstly solved on the computational space before mapping them back onto the physical space. In the same vein, almost all the finite difference schemes developed for the solution of the biharmonic form of the N-S equations on nonuniform grids [113,135,137,138] resorted to this practice, which has certain disadvantages as listed in chapter 2.

1.2 Motivation

A thorough study of the works discussed so far reveals certain issues concerning compact schemes and their applicability on nonuniform grids, in particular, the pure streamfunction form of the N-S equations. Thus the window to explore the possibility of developing compact schemes for the pure streamfunction form of the N-S equations on nonuniform grid without transformation is still wide open; more so for problems involving irregular geometries. The benefits of compact schemes on a nonuniform Cartesian grids for problems involving such geometries described in the curvilinear coordinate system do not come for free. It requires a transformation of the differential equation. The very few attempts, scantily found in the existing literature which used nonuniform grids without transformation, only dealt with rectangular geometries. One such endeavour is by Yu and Tian [169] who used the ψ-v form of the N-S equations. However, their scheme was based on a five point compact stencil, and they neglected many essential terms in developing the scheme, leading to additional errors. As a result, it could not handle extreme clustering essential for capturing smaller scales in very high gradient zones of the flow region.

To the best of our knowledge, no compact scheme on a nonuniform Cartesian grid without transformation has been developed till date for the pure streamfunction form of the N-S equations for geometries beyond rectangular. As such the earlier schemes failed to achieve the full potential of pure stream function formulation in resolving complex fluid flows e.g., the flow past an impulsively started circular cylinder. To resolve such complex flow phenomena accurately, we need compact schemes developed for the body-fitted coordinate system. This is the motivation behind the present research.

1.3 Objectives

The objectives of the work are as follows:

1. To develop robust efficient schemes for a transformation-free ψ-v formulation of the Navier-Stokes equations on 2D compact nonuniform Cartesian grids.

2. To validate the algorithms resulting from the above mentioned schemes by applying them to problems on internal and external flows on complex geometries, including

ones having interaction between the fluid and solid surface.

3. To gain new physical insights into the fluid flow problems under consideration.

1.4 The work

The FD schemes developed in this thesis work are basically a combination of all the advantages of compact schemes and the Biharmonic formulation. The base of the associated schemes works on the Taylor series expansion of a continuous function at a particular point for two different step lengths and approximation of the derivatives appearing in the Biharmonic equation on a non-uniform stencil. Conferred schemes not only frees one from constraints such as transformation but also paves the way for utilizing the non-uniformity of the grids in any direction wherever needed.

In the first part, we have developed a second-order accurate compact finite difference scheme for the biharmonic form of the steady-state Navier-Stokes (N-S) equations on non-uniform Cartesian grids without transformation. Contrary to the schemes developed on rectangular Cartesian grids for N-S equations that could handle only rectangular boundaries, the proposed scheme can easily accommodate bluff bodies with curved boundaries. The scheme is applied to one problem with an analytical solution, three purely fluid flow problems and two heat transfer problems, all with varied complexities. Four of them, viz., the lid-driven cavity, backward facing step problem, natural convection around a heated solid body in a square cavity and conjugate heat transfer in a suddenly expanding channel, depict internal flows. On the other hand, the remaining ones, viz., the flow past a circular cylinder and flat plates (including one mounted on a wall with an angle of inclination) immersed in uniform flow represent external flows. The scheme's efficiency is demonstrated not only by its ability to capture smaller scales up to the post quaternary level of vortices for the flow in the lid-driven cavity but also its robustness in handling non-rectangular boundaries of immersed bodies. While the scheme has dealt with the boundary of an immersed body not necessarily aligned to the gridlines for one of the problems, it has tackled a curved boundary on the Cartesian grid without roping in any immersed interface in the process. Its efficiency is further asserted by the proximity of the computed solutions to available experimental results.

In the second part, we extend the aforesaid formulation ideas and propose a second-order spatially compact, implicit, stable ψ-v formulation for the unsteady incompressible N-S equations. Contrary to the existing ψ-v finite-difference formulations which use grid transformation, the proposed scheme is developed for non-uniform Cartesian grids without transformation designed explicitly for 2D laminar flow past bluff bodies. It has been implemented on problems of internal flows inside curved regions as well as those involving fluid-embedded body interaction. However, the robustness of the scheme is highlighted by the accurate resolution of a host of complex flows past bluff bodies with different physical set-ups and boundary conditions. It was seen to handle problems across a wide range of structures of varied shapes, viz., a flat plate, a circular cylinder and an inclined square cylinder. The robustness of the scheme was exemplified by not only its ability to elegantly capture all the details of the shedded vortex structures under different circumstances, but also the vortex structures beyond tertiary level in the high Reynolds number regime. As in the case of the scheme developed for the steady case, it could also handle both Dirichlet and Neumann boundary conditions with equal ease. Our results are found to be extremely close to the available numerical and experimental results in all the cases.

In the third part, the above scheme is employed to undertake a comprehensive simulation of the flow past an impulsively started circular cylinder with special emphasis on vortex dynamics in the secondary and tertiary levels. High-quality simulations are accomplished for a wide range of Reynolds numbers (Re) ranging from $5 \leq Re \leq 10000$ in the laminar regime, including the periodic flow characterized by von Kármán vortex street. The α, β, sub-α and sub-β phenomena, which are the trademark of the secondary and tertiary vortex dynamics associated with such flows, are studied in detail. Our results are compared with experimental and existing numerical results, and close comparison is obtained in all the cases exemplifying their accuracy. In the process, for the first time, we also provide a tabular documentation of the early stages of the flow for $Re \geq 700$. In addition to the stationary cylinder, flows past an oscillatory and a rotating cylinders are also studied to testify the versatility of the scheme developed for the transient N-S equations.

Lastly, the scheme is applied to study the flows past sharp edges in uniform and accelerated flows, where a flat plate and a wedge hinged on a wall were considered as the

bluff bodies. With our scheme, we were able to resolve and analyze various modes of vortex shedding very accurately for the flat plate. In the case of the wedge, our simulation has replicated the flow visualization from Pullin and Perry's famous experiment of 1980 [121]. In all the cases, our results are found to be extremely close to the experimental results. In Pullin and Perry's experiment, the flow was stopped after a very short duration of time, while we continued our simulation for a much longer duration till the onset of turbulence, which has been established using the Q-criterion. We have also shown and described the threefold stages and two cores of the spiral shear layer. The validation of the accuracy of our simulations comes from their immense proximity to the experimental visualizations, specifically in the case of the spiral vortex for the accelerated flow past the wedge.

1.5 Organization of the work

The current dissertation includes six chapters. Chapter 2 describes the development of a compact finite difference scheme for the steady N-S equations in biharmonic pure streamfunction form on a non-uniform Cartesian grid. In Chapter 3, we develop a compact, implicit second-order temporally and spatially accurate FD scheme for unsteady N-S equations for incompressible viscous flows. Chapter 4 discusses the application of the scheme developed in Chapter 3 to the flow past an impulsively started circular cylinder for Reynolds numbers ranging from 5 to 9500 and flow problems with moving boundaries. Chapter 5 deals with the flow fast sharp edges in uniform and accelerated flow leading to extremely complicated flow patterns. Finally, Chapter 6 summarizes and comments on the whole work and discusses the scope for future work.

CHAPTER 2

A TRANSFORMATION-FREE ψ-V FORMULATION OF THE STEADY STATE NAVIER-STOKES EQUATIONS ON COMPACT NONUNIFORM GRIDS

2.1 Introduction

The viscous fluid flows abide the Navier-Stokes (N-S) and continuity equations. The governing equations for unsteady 2D incompressible flow for the above fluid in primitive variable (velocity-pressure) form can be written as,

$$u_t + uu_x + vu_y = -\frac{1}{\rho}p_x + \nu\left(u_{xx} + u_{yy}\right), \tag{2.1}$$

$$v_t + uv_x + vv_y = -\frac{1}{\rho}p_y + \nu\left(v_{xx} + v_{yy}\right), \tag{2.2}$$

$$u_x + v_y = 0 \tag{2.3}$$

where t is the time, u, v, p, ρ and ν are the x-, y-velocities, pressure, density and kinematic viscosity of the fluid respectively. We carry out non-dimensionalization of fluid variables by the transformations $x^* = x/L$, $y^* = y/L$, $u^* = u/U$, $v^* = v/U$, $t^* = tU/L$ and $p^* = p/\rho U^2$, where U is some characteristic velocity and L, a characteristic length. With these, equations (2.1)-(2.3) reduce to (by removing * sign):

$$u_t + uu_x + vu_y = -p_x + \frac{1}{Re}\left(u_{xx} + u_{yy}\right), \tag{2.4}$$

$$v_t + uv_x + vv_y = -p_y + \frac{1}{Re}\left(v_{xx} + v_{yy}\right), \tag{2.5}$$

$$u_x + v_y = 0 \tag{2.6}$$

where Re is the Reynolds number given by $Re = \dfrac{UL}{\nu}$.

Equations (2.4) and (2.5) have three unknowns, which on using the continuity equation (2.6) and defining streamfunction ψ (from the incompressibility condition) and vorticity ω as

$$u(x,y) = \psi_y, \qquad v(x,y) = -\psi_x, \quad \omega = v_x - u_y, \tag{2.7}$$

reduce to the streamfunction-vorticity (ψ-ω) formulation

$$\omega_t + u\omega_x + v\omega_y = \frac{1}{Re}\left(\omega_{xx} + \omega_{yy}\right), \tag{2.8}$$

$$\psi_{xx} + \psi_{yy} = -\omega\left(x,y\right), \tag{2.9}$$

thus eliminating the variable p from (2.4) and (2.5). Substitution of (2.9) in (2.8) yields the following equation

$$\frac{\partial^4\psi}{\partial x^4} + 2\frac{\partial^4\psi}{\partial x^2\partial y^2} + \frac{\partial^4\psi}{\partial y^4} - Re\left[v\nabla^2 u - u\nabla^2 v\right] = Re\left[\frac{\partial}{\partial t}(\nabla^2\psi)\right] \tag{2.10}$$

For steady-state, the above reduces to:

$$\frac{\partial^4\psi}{\partial x^4} + 2\frac{\partial^4\psi}{\partial x^2\partial y^2} + \frac{\partial^4\psi}{\partial y^4} = Re\left[v\nabla^2 u - u\nabla^2 v\right]. \tag{2.11}$$

The above equation was termed as the ψ-v formulation of the Navier-Stokes equation by Gupta and Kalita [46]. In the above, with the values of u and v from (2.7), it reduces to the pure streamfunction formulation of the 2D steady N-S equations [1]

$$\frac{\partial^4\psi}{\partial x^4} + 2\frac{\partial^4\psi}{\partial x^2\partial y^2} + \frac{\partial^4\psi}{\partial y^4} = Re\left[\frac{\partial\psi}{\partial y}\left(\frac{\partial^3\psi}{\partial x^3} + \frac{\partial^3\psi}{\partial x\partial y^2}\right) - \frac{\partial\psi}{\partial x}\left(\frac{\partial^3\psi}{\partial x^2\partial y} + \frac{\partial^3\psi}{\partial y^3}\right)\right]. \tag{2.12}$$

[1]Part of this study has been published in [93].

This formulation enables us to avoid difficulties associated with computation of vorticities values especially on solid boundaries, encountered when solving the ψ-ω formulation and solving pressure-Poisson equation of the conventional v-p formulation of N-S equations.

There has been several attempts to develop compact schemes for the pure streamfunction-velocity formulation for the 2D N-S equations [12, 46, 47, 73]. Nevertheless, these schemes were developed for uniform grids and as such could not accomplish the benefits associated with non-uniform grids, especially, in the regions of large gradient of flow variables in physical domain to resolve small scales. Clustering the grids in regions of high gradient and spreading it out in small gradient regions is one of the better ways of efficient computation. Apart from accurately resolving smaller scales, it could bring huge savings in computational time. In finite volume or finite element set up, nonuniform grids for flow computation are used very frequently, where the physical and computational domain is the same. However, in finite difference set up, most of the computations performed on nonuniform grids is accomplished by transforming the governing equations from the physical domain onto the computational domain embedded with uniform grid. The equations are first solved on the computational space before mapping this solution back onto the physical space. Keeping with this, almost all the finite difference schemes developed for the solution of the biharmonic form of the N-S equations on nonuniform grids [113, 135, 137, 138] resorted to this practice. But, there are certain disadvantages of using this approach:

1. Substantial increase in the number of terms to be discretized in transformed governing equations leads to rise in computational time [3, 65, 71, 156].

2. Often transformed equation results in the appearance of cross-derivative terms which increases the computational complexity [54, 113, 114, 136].

3. Besides, if the transformation is not explicitly known, it needs to go through variety of numerical approximations for obtaining the solution resulting in addition errors [136, 156].

4. Overall, the solution process turns into a complicated, expensive and sometimes an error-prone one [65, 113, 114].

Because of the reasons cited above, it is imperative that one develops numerical schemes for the ψ-v form of the N-S equations on nonuniform grids without transformation. However, a very few attempts could be found in the existing literature in this direction. One such endeavour is by Yu and Tian [169]; but this scheme was developed on five point compact stencil and many significant terms were neglected in the process of developing the scheme leading to addition errors. As such, it could not handle extreme clustering essential for capturing smaller scales in very high gradient zones of the flow region.

In the present work, we propose a finite difference scheme for numerically solving the ψ-v formulation of the N-S equations on a compact nine point stencil on non-uniform grids without using any transformation. It is based on Taylor series expansions of a continuous function at a particular point for two different step lengths and approximation of the derivatives appearing in the biharmonic equation (2.12) on non-uniform stencil. The present scheme not only frees one from constraints such as transformation but also paves the way for utilizing non-uniformity of the grids in any direction wherever needed. In order to validate our scheme for efficiency and its applicability, we apply it to one problem having analytical solution and four fluid flow problems, and two heat transfer problems having different complexities. Amongst the fluid flow problems, two of them depict internal flows, the last two are flows past an immersed body representing external flows. The scheme is shown to handle both Dirichlet and Neumann boundary conditions with equal ease. The robustness of the scheme is demonstrated by its ability to handle extreme clustering, thus enabling the capture of smaller scales up to post quaternary level of vortices for the lid-driven cavity flow. Its efficiency is further asserted by the proximity of the computed solutions with available experimental results.

The chapter is organized into six sections. In section 2, we describe the development of the numerical scheme for the nine point steady streamfunction-velocity formulation on nonuniform grid. In section 3, we describe the solution procedure of algebraic systems associated with proposed scheme. We present detailed results of our computation for purely fluid flow and then to heat transfer problems respectively in sections 4 and 5 respectively, and finally we summarize our achievements in section 6 containing the conclusions.

2.2 The numerical scheme

Consider a rectangular domain $[a_1, a_2] \times [b_1, b_2]$ in the xy-plane. We divide the interval $[a_1, a_2]$ into m sub-intervals, not necessarily of equal lengths, by the points $a_1 = x_0, x_1, x_2, x_3, \ldots, x_{m-1}, x_m = a_2$ and similarly $[b_1, b_2]$ into n subintervals by the points $b_1 = y_0, y_1, y_2, y_3, \ldots, y_{n-1}, y_n = b_2$.

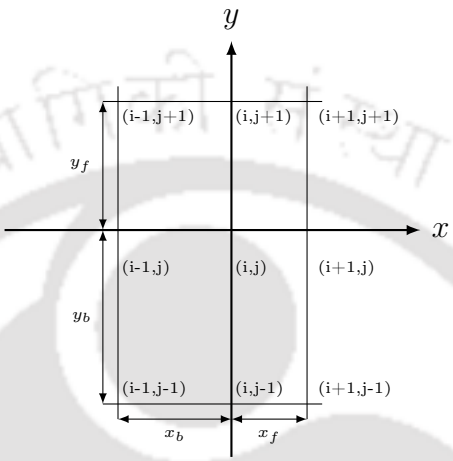

Figure 2.1: The compact stencil on nonuniform Grid

In the x-direction, we define the forward and backward step-lengths x_f, x_b at the $(i, j)^{\text{th}}$ point (see figure 2.1) of the problem domain as,

$$x_f = (x_{i+1,j} - x_{i,j})$$
$$x_b = (x_{i,j} - x_{i-1,j}).$$

Likewise, in the y-direction,

$$y_f = (y_{i,j+1} - y_{i,j})$$
$$y_b = (y_{i,j} - y_{i,j-1}).$$

With the above, the Taylor series expansions of $\psi_{i+1,j}$ and $\psi_{i-1,j}$ at the $(i, j)^{\text{th}}$ point become

$$\psi_{i+1,j} = \psi_{i,j} + x_f \frac{\partial \psi}{\partial x} + \frac{x_f^2}{2}\frac{\partial^2 \psi}{\partial x^2} + \frac{x_f^3}{6}\frac{\partial^3 \psi}{\partial x^3} + \frac{x_f^4}{24}\frac{\partial^4 \psi}{\partial x^4} + O(x_f^5), \tag{2.13}$$

$$\psi_{i-1,j} = \psi_{i,j} - x_b \frac{\partial \psi}{\partial x} + \frac{x_b^2}{2}\frac{\partial^2 \psi}{\partial x^2} - \frac{x_b^3}{6}\frac{\partial^3 \psi}{\partial x^3} + \frac{x_b^4}{24}\frac{\partial^4 \psi}{\partial x^4} + O(x_b^5). \tag{2.14}$$

From equations (2.13) and (2.14), we have

$$\frac{\partial\psi}{\partial x} = \frac{\psi_{i+1,j}-\psi_{i-1,j}}{x_f+x_b} - \frac{1}{2}(x_f-x_b)\frac{\partial^2\psi}{\partial x^2} - \frac{1}{6}(x_f^2+x_b^2-x_fx_b)\frac{\partial^3\psi}{\partial x^3} + O((x_f-x_b)(x_f^2+x_b^2)) \quad (2.15)$$

and

$$\left.\frac{\partial^2\psi}{\partial x^2}\right|_{i,j} = \frac{2}{(x_f+x_b)}\left[\frac{\psi_{i+1,j}}{x_f} - \left(\frac{1}{x_f}+\frac{1}{x_b}\right)\psi_{i,j} + \frac{\psi_{i-1,j}}{x_b}\right] - \frac{(x_f-x_b)}{3}\frac{\partial^3\psi}{\partial x^3} - \frac{1}{12}\left(x_f^2+x_b^2-x_fx_b\right)\frac{\partial^4\psi}{\partial x^4} + O((x_f-x_b)(x_f^2+x_b^2)). \quad (2.16)$$

Defining the first and second order central difference operators in the x-direction as

$$\delta_x\psi = \frac{\psi_{i+1,j}-\psi_{i-1,j}}{x_f+x_b} \text{ and } \delta_x^2\psi = \frac{2}{(x_f+x_b)}\left[\frac{\psi_{i+1,j}}{x_f} - \left(\frac{1}{x_f}+\frac{1}{x_b}\right)\psi_{i,j} + \frac{\psi_{i-1,j}}{x_b}\right],$$

equation (2.16) reduces to

$$\left.\frac{\partial^2\psi}{\partial x^2}\right|_{i,j} = \delta_x^2\psi - \frac{(x_f-x_b)}{3}\frac{\partial^3\psi}{\partial x^3} - \frac{1}{12}\left(x_f^2+x_b^2-x_fx_b\right)\frac{\partial^4\psi}{\partial x^4} + O((x_f-x_b)(x_f^2+x_b^2)). \quad (2.17)$$

With (2.17), the first derivative in equation (2.15) may be approximated as

$$\left.\frac{\partial\psi}{\partial x}\right|_{i,j} = \delta_x\psi - \frac{1}{2}(x_f-x_b)\delta_x^2\psi - \frac{x_fx_b}{6}\frac{\partial^3\psi}{\partial x^3} + O((x_f-x_b)(x_f^2+x_b^2)). \quad (2.18)$$

Likewise in the y-direction:

$$\delta_y\psi = \frac{\psi_{i,j+1}-\psi_{i,j-1}}{y_f+y_b} \text{ and } \delta_y^2\psi = \frac{2}{(y_f+y_b)}\left[\frac{\psi_{i,j+1}}{y_f} - \left(\frac{1}{y_f}+\frac{1}{y_b}\right)\psi_{i,j} + \frac{\psi_{i,j-1}}{y_b}\right].$$

The mixed derivative term can be discretized as ([70])

$$\frac{\partial^4\psi}{\partial x^2\partial y^2} = \delta_x^2\delta_y^2\psi + O(x_f^2, x_b^2, x_fx_b) \quad (2.19)$$

where,

$$\delta_x^2\delta_y^2\psi = \frac{1}{hk}\left[\frac{\psi_{i+1,j+1}}{x_fy_f} + \frac{\psi_{i-1,j+1}}{x_by_f} - \left(\frac{1}{x_fy_f}+\frac{1}{x_by_f}\right)\psi_{i,j+1} - \left(\frac{1}{x_fy_f}+\frac{1}{x_fy_b}\right)\psi_{i+1,j} + \left(\frac{1}{x_fy_f}+\frac{1}{x_fy_b}+\frac{1}{x_by_f}+\frac{1}{x_by_b}\right)\psi_{i,j} - \left(\frac{1}{x_fy_b}+\frac{1}{x_by_b}\right)\psi_{i,j-1} - \left(\frac{1}{x_by_f}+\frac{1}{x_by_b}\right)\psi_{i-1,j} + \frac{\psi_{i+1,j-1}}{x_fy_b} + \frac{\psi_{i-1,j-1}}{x_by_b}\right]$$

with $h = 0.5(x_f + x_b)$ and $k = 0.5(y_f + y_b)$.

From equations (2.13) and (2.14), and using expressions similar to (2.18) for $\dfrac{\partial v}{\partial x}$, we have

$$\frac{1}{x_f^3}\psi_{i+1,j} + \frac{1}{x_b^3}\psi_{i-1,j} = \left(\frac{1}{x_f^3} + \frac{1}{x_b^3}\right)\psi_{i,j} + \left(\frac{1}{x_f^2} - \frac{1}{x_b^2}\right)\frac{\partial \psi}{\partial x} + \frac{1}{2}\left(\frac{1}{x_f} + \frac{1}{x_b}\right)\frac{\partial^2 \psi}{\partial x^2} + \frac{x_f + x_b}{24}\frac{\partial^4 \psi}{\partial x^4} + O(x_f^2 - x_b^2)$$

$$\begin{aligned}\frac{1}{x_f^3}\psi_{i+1,j} + \frac{1}{x_b^3}\psi_{i-1,j} - \left(\frac{1}{x_f^3} + \frac{1}{x_b^3}\right)\psi_{i,j} &= \left(\frac{x_f^2 - x_b^2}{x_f^2 x_b^2}\right)v + \frac{h}{x_f x_b}\left[-\frac{\partial v}{\partial x}\right] + \frac{h}{12}\frac{\partial^4 \psi}{\partial x^4} + O(x_f^2, x_b^2) \\ &= \left(\frac{x_f^2 - x_b^2}{x_f^2 x_b^2}\right)v \\ &\quad - \frac{h}{x_f x_b}\left[\delta_x v - \frac{1}{2}(x_f - x_b)\delta_x^2 v - \frac{x_f x_b}{6}\frac{\partial^3 v}{\partial x^3}\right] \\ &\quad + \frac{h}{12}\frac{\partial^4 \psi}{\partial x^4} + O(x_f^2, x_b^2) \\ &= \left(\frac{x_f^2 - x_b^2}{x_f^2 x_b^2}\right)v - \frac{h}{x_f x_b}\delta_x v \\ &\quad + \frac{h}{2}\frac{(x_f - x_b)}{x_f x_b}\delta_x^2 v - \frac{h}{12}\frac{\partial^4 \psi}{\partial x^4} + O(x_f^2 - x_b^2).\end{aligned} \tag{2.20}$$

From the above, the fourth order partial derivative of ψ can be approximated as

$$\begin{aligned}\frac{\partial^4 \psi}{\partial x^4} = \frac{12}{h}&\left[-\frac{1}{x_f^3}\psi_{i+1,j} - \frac{1}{x_b^3}\psi_{i-1,j} + \left(\frac{1}{x_f^3} + \frac{1}{x_b^3}\right)\psi_{i,j}\right] \\ &+ \frac{6(x_f - x_b)}{x_f x_b}\delta_x^2 v - \frac{12}{x_f x_b}\delta_x v + \frac{24(x_f - x_b)}{x_f^2 x_b^2}v + O(x_f - x_b)\end{aligned} \tag{2.21}$$

and likewise,

$$\begin{aligned}\frac{\partial^4 \psi}{\partial y^4} = \frac{12}{k}&\left[-\frac{1}{y_f^3}\psi_{i,j+1} - \frac{1}{y_b^3}\psi_{i,j-1} + \left(\frac{1}{y_f^3} + \frac{1}{y_b^3}\right)\psi_{i,j}\right] \\ &- \frac{6(y_f - y_b)}{y_f y_b}\delta_y^2 u + \frac{12}{y_f y_b}\delta_y u - \frac{24(y_f - y_b)}{y_f^2 y_b^2}u + O(y_f - y_b)\end{aligned} \tag{2.22}$$

Defining the fourth order operators in the x- and y-directions as

$$\delta_x^4\psi = \frac{12}{h}\left[-\frac{1}{x_f^3}\psi_{i+1,j} - \frac{1}{x_b^3}\psi_{i-1,j} + \left(\frac{1}{x_f^3}+\frac{1}{x_b^3}\right)\psi_{i,j}\right] \tag{2.23}$$

and

$$\delta_y^4\psi = \frac{12}{k}\left[-\frac{1}{y_f^3}\psi_{i,j+1} - \frac{1}{y_b^3}\psi_{i,j-1} + \left(\frac{1}{y_f^3}+\frac{1}{y_b^3}\right)\psi_{i,j}\right], \tag{2.24}$$

equations (2.21) and (2.22) can be written as,

$$\frac{\partial^4\psi}{\partial x^4} = \delta_x^4\psi + \frac{6(x_f-x_b)}{x_f x_b}\delta_x^2 v - \frac{12}{x_f x_b}\delta_x v + \frac{24(x_f-x_b)}{x_f^2 x_b^2}v + O(x_f - x_b), \tag{2.25}$$

and

$$\frac{\partial^4\psi}{\partial y^4} = \delta_y^4\psi - \frac{6(y_f-y_b)}{y_f y_b}\delta_y^2 u + \frac{12}{y_f y_b}\delta_y u - \frac{24(y_f-y_b)}{y_f^2 y_b^2}u + O(y_f - y_b). \tag{2.26}$$

Here,

$$\begin{aligned}\frac{\partial^3\psi}{\partial x^3} &= -\frac{\partial^2 v}{\partial x^2}\\ &= -\delta_x^2 v + \frac{(x_f-x_b)}{3}\frac{\partial^3 v}{\partial x^3} + O\left(x_f^2 + x_b^2 - x_f x_b\right)\\ &= -\delta_x^2 v - \frac{(x_f-x_b)}{3}\frac{\partial^4\psi}{\partial x^4} + O\left(x_f^2 + x_b^2 - x_f x_b\right).\end{aligned} \tag{2.27}$$

Likewise in y-direction,

$$\begin{aligned}\frac{\partial^3\psi}{\partial y^3} &= \frac{\partial^2 u}{\partial y^2}\\ &= \delta_y^2 u - \frac{(y_f-y_b)}{3}\frac{\partial^3 v}{\partial y^3} + O\left(y_f^2 + y_b^2 - y_f y_b\right)\\ &= \delta_y^2 u - \frac{(y_f-y_b)}{3}\frac{\partial^4\psi}{\partial y^4} + O\left(y_f^2 + y_b^2 - y_f y_b\right).\end{aligned} \tag{2.28}$$

$$\begin{aligned}\frac{\partial^3\psi}{\partial x^2\partial y} &= \frac{\partial^2 u}{\partial x^2}\\ &= \delta_x^2 u - \frac{(x_f-x_b)}{3}\frac{\partial^3 u}{\partial x^3} + O\left(x_f^2 + x_b^2 - x_f x_b\right)\\ &= \delta_x^2 u - \frac{(x_f-x_b)}{3}\frac{\partial^4\psi}{\partial x^4} + O\left(x_f^2 + x_b^2 - x_f x_b\right).\end{aligned} \tag{2.29}$$

$$\begin{aligned}\frac{\partial^3\psi}{\partial x\partial y^2} &= -\frac{\partial^2 v}{\partial y^2}\\ &= -\delta_y^2 v + \frac{(y_f - y_b)}{3}\frac{\partial^3 v}{\partial y^3} + O\left(y_f^2 + y_b^2 - y_f y_b\right)\\ &= -\delta_y^2 v - \frac{(y_f - y_b)}{3}\frac{\partial^4 \psi}{\partial y^4} + O\left(y_f^2 + y_b^2 - y_f y_b\right).\end{aligned} \tag{2.30}$$

Substituting equations (2.19), (2.25), (2.26), (2.27), (2.28), (2.29) and (2.30) into equation (2.11) and rearranging, we have

$$\begin{aligned}p\delta_x^4\psi + 2\delta_y^2\delta_x^2 + q\delta_y^4\psi =& Re\left[v\left(\delta_x^2 u + \delta_y^2 u\right) - u\left(\delta_x^2 v + \delta_y^2 v\right)\right] - \frac{6p(x_f - x_b)}{x_f x_b}\delta_x^2 v + \frac{12p}{x_f x_b}\delta_x v\\ &- \frac{24p(x_f - x_b)}{x_f^2 x_b^2}v + \frac{6q(y_f - y_b)}{y_f y_b}\delta_y^2 u - \frac{12q}{y_f y_b}\delta_y u + \frac{24q(y_f - y_b)}{y_f^2 y_b^2}u\\ &+ O(x_f - x_b, y_f - y_b)\end{aligned} \tag{2.31}$$

where $p = 1 + \frac{Re}{3}(x_f - x_b)(u + v)$ and $q = 1 + \frac{Re}{3}(y_f - y_b)(u + v)$.

Making use of the approximations for the operators δ_x, δ_y, δ_x^2, δ_y^2, δ_x^4, δ_y^4, and $\delta_x^2\delta_y^2$ as provided above, (2.31) can be discretized compactly on the nonuniform nine-point stencil (figure 2.1) as

$$\begin{aligned}&A\psi_{i+1,j+1} + B\psi_{i,j+1} + C\psi_{i-1,j+1} + D\psi_{i+1,j} + E\psi_{i,j}\\ &+ F\psi_{i-1,j} + G\psi_{i+1,j-1} + H\psi_{i,j-1} + I\psi_{i-1,j-1} = f_{i,j}\end{aligned} \tag{2.32}$$

where

$$A = \frac{2}{hkx_f y_f}$$

$$B = -\frac{12q}{ky_f^3} - \frac{2}{hk}\left(\frac{1}{x_f y_f} + \frac{1}{x_b y_f}\right)$$

$$C = \frac{2}{hkx_b y_f}$$

$$D = -\frac{12p}{hx_f^3} - \frac{2}{hk}\left(\frac{1}{x_f y_f} + \frac{1}{x_f y_b}\right)$$

$$E = \frac{12p}{h}\left(\frac{1}{x_f^3} + \frac{1}{x_b^3}\right) + \frac{12q}{k}\left(\frac{1}{y_f^3} + \frac{1}{y_b^3}\right) + \frac{2}{hk}\left(\frac{1}{x_f y_f} + \frac{1}{x_f y_b} + \frac{1}{x_b y_f} + \frac{1}{x_b y_b}\right)$$

$$F = -\frac{12p}{hx_b^3} - \frac{2}{hk}\left(\frac{1}{x_b y_f} + \frac{1}{x_b y_b}\right)$$
$$G = \frac{2}{hkx_f y_b}$$
$$H = -\frac{12q}{ky_b^3} - \frac{2}{hk}\left(\frac{1}{x_f y_b} + \frac{1}{x_b y_b}\right)$$
$$I = \frac{2}{hkx_b y_b}$$

and

$$\begin{aligned} f_{i,j} =& \frac{6p}{h}\left(\frac{v_{i+1,j} - v_{i-1,j}}{x_f x_b}\right) - \frac{1}{h}\left(\frac{6p(x_f - x_b)}{x_f x_b} + Re.u_{i,j}\right)\left[\frac{v_{i+1,j}}{x_f} + \frac{v_{i-1,j}}{x_b} - \left(\frac{1}{x_f} + \frac{1}{x_b}\right)v_{i,j}\right] \\ & - \frac{Re.u_{i,j}}{k}\left[\frac{v_{i,j+1}}{y_f} + \frac{v_{i,j-1}}{y_b} - \left(\frac{1}{y_f} + \frac{1}{y_b}\right)v_{i,j}\right] - \frac{24p(x_f - x_b)}{x_f^2 x_b^2}v_{i,j} \\ & - \frac{6q}{k}\left(\frac{u_{i,j+1} - u_{i,j-1}}{y_f y_b}\right) + \frac{1}{k}\left(\frac{6q(y_f - y_b)}{y_f y_b} + Re.v_{i,j}\right)\left[\frac{u_{i,j+1}}{y_f} + \frac{u_{i,j-1}}{y_b} - \left(\frac{1}{y_f} + \frac{1}{y_b}\right)u_{i,j}\right] \\ & \frac{Re.v_{i,j}}{h}\left[\frac{u_{i+1,j}}{x_f} + \frac{u_{i-1,j}}{x_b} - \left(\frac{1}{x_f} + \frac{1}{x_b}\right)u_{i,j}\right] + \frac{24q(y_f - y_b)}{y_f^2 y_b^2}u_{i,j} \end{aligned}$$

Equation (2.32) utilizes the values of ψ at the eight neighbours of $(i,j)^{\text{th}}$ point including the corners in the compact stencil and the values of u and v at the nearest neighbours. The order of accuracy of this formulation is two or less. On a uniform grid, it reduces to the second order formulation of Gupta and Kalita [46]. However, in most of the cases where a stretching function is used to generate clustered grids, the distribution of the nodes is such that $x_f \to x_b$ and $y_f \to y_b$, rendering a convergence rate very close to two (see section 2.4.1).

The velocities u and v can be approximated in the following way

$$\begin{aligned} u_{i,j} =& \frac{\partial \psi}{\partial y} \\ =& \delta_y \psi_{i,j} - \frac{1}{2}(y_f - y_b)\delta_y^2 \psi_{i,j} - \frac{y_f y_b}{6}\frac{\partial^3 \psi}{\partial y^3} + O((y_f - y_b)(y_f^2 + y_b^2)). \\ =& \delta_y \psi_{i,j} - \frac{1}{2}(y_f - y_b)\delta_y^2 \psi_{i,j} - \frac{y_f y_b}{6}\frac{\partial^2 u}{\partial y^2} + O((y_f - y_b)(y_f^2 + y_b^2)). \end{aligned}$$

Making use of the formulas for the first and second order central difference operators

given above and rearranging, this reduces to

$$\frac{y_b}{6k}u_{i,j+1} - \left(1 - \frac{y_f + y_b}{6k}\right)u_{i,j} + \frac{y_f}{6k}u_{i,j-1} = \frac{(\psi_{i,j+1} - \psi_{i.j-1})}{2k} - \frac{(y_f - y_b)}{2k}\left[\frac{\psi_{i,j+1}}{y_f} + \frac{\psi_{i,j-1}}{y_b} - (\frac{1}{y_f} + \frac{1}{y_b})\psi_{i,j}\right], \tag{2.33}$$

likewise v can be obtained from the following equation

$$\frac{x_b}{6h}v_{i+1,j} - \left(1 - \frac{x_f + x_b}{6h}\right)v_{i,j} + \frac{x_f}{6h}v_{i-1,j} = \frac{(\psi_{i-1,j} - \psi_{i+1,j})}{2h} + \frac{(x_f - x_b)}{2h}\left[\frac{\psi_{i+1,j}}{x_f} + \frac{\psi_{i-1,j}}{x_b} - (\frac{1}{x_f} + \frac{1}{x_b})\psi_{i,j}\right]. \tag{2.34}$$

The expressions for u and v in the form of equations (2.33) and (2.34) facilitate the use of Tridiagonal solvers for computing them.

REMARK:

1. The discretization of equation (2.12) on a nonuniform compact stencil by Yu and Tian [169] resulted in a five point formula; in the process, they ignored quite a few significant terms in the formulation. For example, while we have used a nine point formula for the mixed derivative $\frac{\partial^4\psi}{\partial x^2\partial y^2}$ in equation (2.19), they have converted them into third order mixed derivatives of the velocities. Likewise, while we have retained the terms involving $\frac{\partial^4\psi}{\partial x^4}$ and $\frac{\partial^4\psi}{\partial y^4}$ on the right hand sides of equations (2.27)-(2.30) and combined them with the fourth order derivatives of the original Biharmonic equation (2.12), they were completely ignored in the formulation of [169].

2. Although the value added by a 2D 9-point-stencil for low-order accurate schemes may seem less significant compared to a high order compact (HOC) one [70, 71, 113, 115], still in the context of the compactness of the stencil, the accomplishment of a lower order scheme such as the present one is quite noteworthy in terms of computational gain. Under normal circumstances, a second order central difference approximation to the fourth order derivative will result in a stencil spanning at least two points on either side. For example, consider the formula

$$\left.\frac{\partial^4\psi}{\partial x^4}\right|_{i,j} = \frac{\psi_{i+2,j} - 4\psi_{i+1,j} + 6\psi_{i,j} - 4\psi_{i-1,j} + \psi_{i-2,j}}{h^2} + O(h^2)$$

on uniform grid of step size h on either direction [118]. Using such formula the Biharmonic equation (2.12) would have resulted in a 25 point stencil leading to huge computational cost.

2.3 Solution of algebric systems

We now discuss the solution of algebric systems resulting from the discretization of the newly proposed finite difference approximation. The system of equations formed by equation (2.32) can be written in matrix form as:

$$A\boldsymbol{\psi} = \mathbf{f}(\mathbf{Re}, \mathbf{u}, \mathbf{v}) \tag{2.35}$$

where for a grid of size $m \times n$, the coefficient matrix A is of order mn and is non symmetric because of non-uniformity of the grid structure.

The computation of the steady-state solutions of fluid flow problems governed by equation (2.12) involves an outer-inner iteration procedure. After initializing u, v and ψ with appropriate boundary conditions, (2.35) is solved for ψ. Once ψ is computed, u and v are computed from equations (2.33) and (2.34) by employing Thomas algorithm [2] for the tridiagonal system of equations. This constitutes one outer iteration. Making use of the updated values of u, v and ψ on the right hand side of (2.35), ψ is computed again. This process is repeated till maximum ψ-error (defined as the difference between ψ values of the current and previous outer iterations) reaches 10^{-13}.

The inner iterations involve solving the matrix equation (2.35) at each outer iteration by iterative solvers. We have used bicongugate gradient stabilized method (BiCGStab) [144] with preconditioning, where Incomplete LU decomposition is used as a preconditioner. Preconditioning was particularly useful for high Reynolds numbers on finest grids with extreme clustring where we have used the Lis library [111]. The inner iterations were stopped when the Euclidean norm of the residual vector $\boldsymbol{r} = \boldsymbol{f} - A\boldsymbol{\psi}$ arising out of equation (2.35) fell below 10^{-13}. We have used a relaxation parameter α for both inner and outer iteration cycles. Larger the value of Reynolds number, smaller is the value of α. All of our computations were carried out on a Intel core i7 based PC with 16GB RAM.

2.4 Numerical experments with fluid flow problems

The proposed scheme has been applied to five pertinent test cases for validation and examining its robustness. They are (i) a problem with a constructed solution, (ii) the lid-driven square cavity problem, (iii) the backward facing step problem, the flow past an impulsively started (iv) circular cylinder and (v) a flat plate for the cases where the plate is vertical to the uniform inflow and also, when it has an angle of inclination. Existence of analytical solution of the first test case enables us to carry out a detailed comparison of the errors. Abundance of numerical solutions for the second test case allows us to test the efficiency of our scheme in the context of other existing ones. On the other hand, experimental results exist for certain values of the parameters in the last test cases, which again allows to compare our numerical results with the expeimental ones to check the robustness of our scheme.

2.4.1 Test case 1: Problem with Analytical Solution

As our first numerical test case, we have chosen a problem having analytical solution in the domain $0 \leq x, y \leq 1$ where (2.12) has an extra source term on the right hand side given by

$$g(x,y) = -\frac{p^4(e^{-px} + e^{-py} - 4e^{-p(x+y)})}{(1-e^{-p})^2} - Re\frac{p^4 e^{-p(x+y)}(e^{-px} - e^{-py})}{(1-e^{-p})^4}$$

and the exact solution is given by

$$\psi = \frac{(1-e^{-px})(1-e^{-py})}{(1-e^{-p})^2},$$

with corresponding u and v as

$$u = \frac{pe^{-py}(1-e^{-px})}{(1-e^{-p})^2}, \qquad v = -\frac{pe^{-px}(1-e^{-py})}{(1-e^{-p})^2}.$$

The solution has a boundary layer in the vicinity of $x = 0$ and $y = 0$; higher the value of p, steeper is the boundary layer. As such these regions are clustered using the following

stretching functions in x- and y-directions

$$x_i = \frac{i}{i_{max}} - \frac{\lambda}{\pi}\sin\left(\frac{\pi i}{i_{max}}\right), \quad y_j = \frac{j}{j_{max}} - \frac{\lambda}{\pi}\sin\left(\frac{\pi j}{j_{max}}\right),$$

where i and j denote the indices along x- and y-directions respectively and λ $(0 \leq \lambda < 1)$ is the clustering parameter with a larger value of λ indicating a greater intensity of clustering. A typical grid of size 21×21 with $\lambda = 0.9$ is shown in figure 2.2. Note that during computations, the source term is accommodated on the right hand side of (2.32). In our computations, we have used two values of p, viz., 10 and 100.

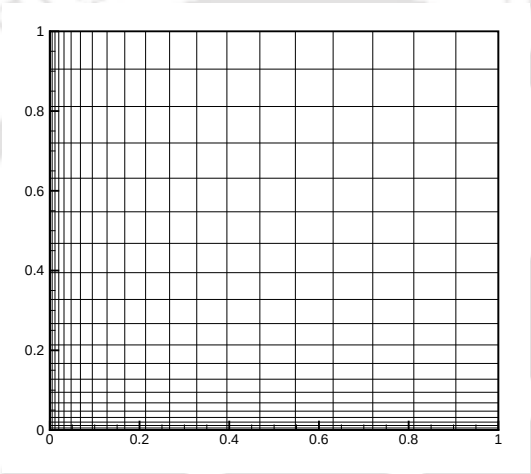

Figure 2.2: *A typical* 21×21 *grid used for test problem 1 with* $\lambda = 0.9$

In figures 2.3(a)-(b), we show the streamlines and corresponding post-processed vorticity contours computed for $Re = 100,\ p = 20$ on a grid of size 21×21 (refer to figure 2.2). It is heartening to note that on grid as coarse as this, the boundary layers were resolved very accurately by our scheme.

In table 2.1, we present the maximum errors for u, v and ψ for two combinations $Re = 100$, $p = 10$ and $p = 100$ and likewise, in table 2.2, for $Re = 10,\ p = 100$ on several grids. The grids were chosen in such a way that we can compare our results with those of [115, 169]. The rates of convergence are calculated using the formula $\dfrac{\ln(E_C/E_F)}{\ln 2}$ where $E_F = \phi - \phi_F$ and $E_C = \phi - \phi_C$ where ϕ, ϕ_F and ϕ_C denote the exact solution, and the computed solutions on finer and coarser grids respectively; here ϕ stands for either u, v or ψ. As expected, one can see the errors decaying at a rate of two. It is worth mentioning that although both the proposed scheme and the scheme of [169] exhibit the same rate

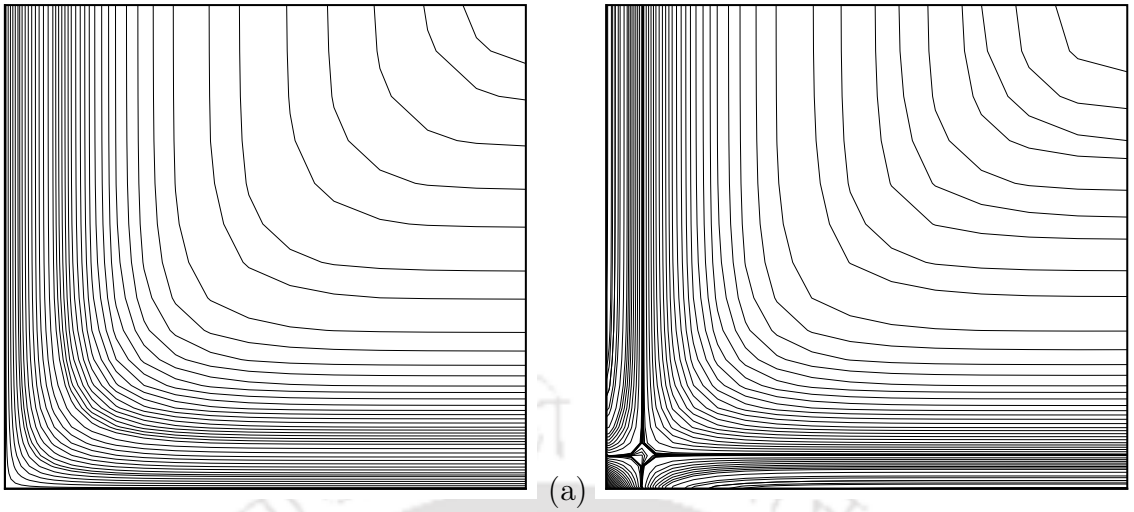

(a) (b)

Figure 2.3: *(a) Streamlines and (b) post-processed vorticity contours for test problem 1 for* $Re = 100$, $p = 10$ *on a* 21×21 *grid.*

Table 2.1: Maximum absolute errors for u, v and ψ for $Re = 100$ for test problem 1.

Grid		21×21	Rate	41×41	Rate	81×81
	u	4.827985×10^{-3}	2.005	1.200580×10^{-3}	1.999	3.003319×10^{-4}
$\lambda = 0.6$	v	5.433067×10^{-3}	1.999	1.359541×10^{-3}	2.000	3.396618×10^{-4}
$p = 10$	ψ	6.296070×10^{-4}	2.018	1.545492×10^{-4}	2.002	3.853601×10^{-5}
	u	1.273135×10^{-2}	1.984	3.232369×10^{-3}	2.001	8.064850×10^{-4}
$\lambda = 0.9$	v	1.424831×10^{-2}	1.993	3.583884×10^{-3}	2.003	8.929494×10^{-4}
$p = 10$	ψ	1.288372×10^{-3}	2.024	3.143919×10^{-4}	2.003	7.833032×10^{-5}
	u	1.709146×10^{0}	2.120	3.800080×10^{-1}	2.112	8.519197×10^{-2}
$\lambda = 0.9$	v	1.069841×10^{0}	2.067	2.553348×10^{-1}	2.187	5.605750×10^{-2}
$p = 100$	ψ	1.055259×10^{-1}	1.966	1.727221×10^{-2}	1.967	4.418279×10^{-3}

of convergence, from the data available in [169], one can see that their errors are more than thrice of ours. Moreover, despite being $O(h^2)$, the errors from the present scheme compare very well with the errors resulting from the $O(h^4)$ scheme of [115].

2.4.2 Test case 2: Lid Driven Cavity

The next problem considered here is the famous lid-driven square cavity problem which is probably the most frequently used benchmark problem in the area of computational fluid dynamics for the assesment of newly developed numerical schemes, particularly for steady-state solution of incompressible fluid flows goverened by the Navier-Stokes equations. The

Table 2.2: Maximum absolute errors for u, v and ψ for $Re = 10$ and $p = 100$ for test problem 1.

Grid		17×17	Rate	33×33	Rate	65×65
	u	2.11915×10^{0}	2.132	4.83446×10^{-1}	2.000	1.20895×10^{-1}
$\lambda = 0.9$	v	1.97343×10^{0}	2.029	4.83344×10^{-1}	2.004	1.20497×10^{-1}
	ψ	3.04723×10^{-1}	1.975	7.77487×10^{-2}	1.989	1.9589×10^{-2}

huge interest generated by this problem stems out from the fact that in the simplest of geometric settings, it displays almost all fluid mechanical phenomena attributed to incompressible viscous flows.

The cavity is defined as the unit square $0 \leq x, y \leq 1$ bounded by solid walls where all the walls are stationary except the top one ($y = 1$) which is moving in its own plane from left to right. As such, boundary conditions are $u = 1$, $v = 0$ on the top wall and on all the other three walls of the cavity the velocities are zero ($u = v = 0$). The stream-function values on all four walls are set as zero ($\psi = 0$). The moving wall is the main driving factor generating fluid motion inside the cavity. A sequence of vortices of decreasing size and intensity is generated at the bottom corners of the cavity. At high Res secondary vortices also appear in the top left of the cavity. The flow characteristics depend upon the value of the Re being considered.

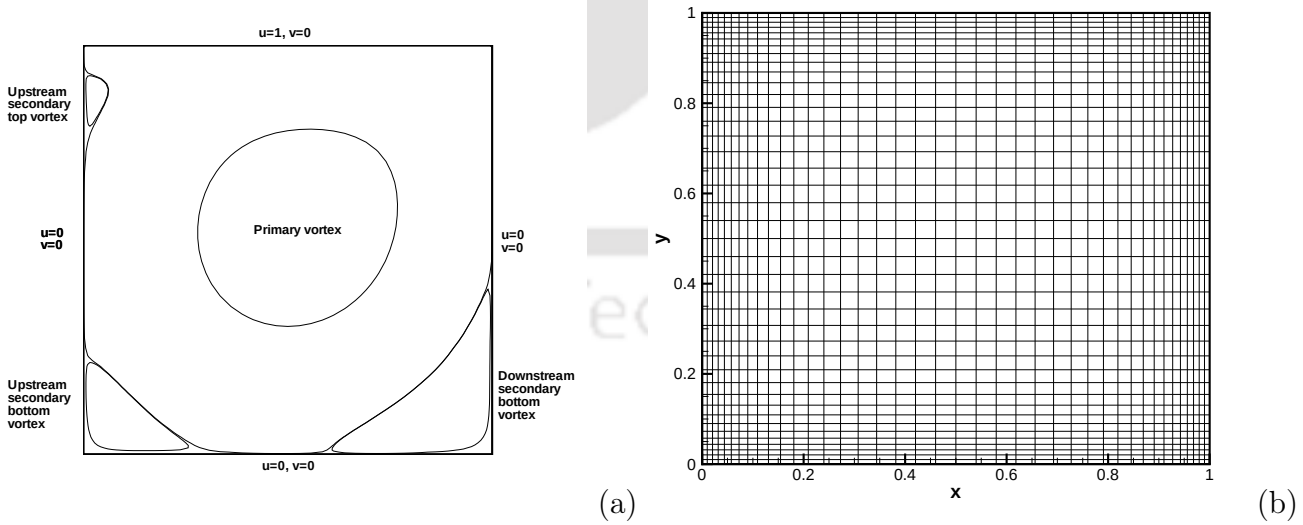

Figure 2.4: *(a) Configuration of the lid-driven square cavity flow problem and (b) a typical* 41×41 *grid with centrosymmetric clustering with* $\lambda = 0.6$.

Computations were performed for Reynolds number in the range of $100 \leq Re \leq 7500$ on grid sizes ranging from 11×11 to 321×321. Because of the presence of large gradients near the walls, it is essential that the regions in the neighbourhood of the solid walls have enough points for resolving the small scales accurately. Therefore, we have used a clustered grid near the walls. In all the cases, the criteria of Kolmogorov length scale $\delta \sim Re^{-0.5}$ and $h^* \sim Re^{-0.75}$ were maintained such that there are enough points in the vicinity of the corners; here δ and h^* are the boundary layer thickness (non-dimensional) and distance between a wall and the point closest to it respectively [33,142]. To generate a centro-symmetric grid with clustering near the walls, we use the stretching function [17,70]

$$x_i = \frac{i}{i_{max}} - \frac{\lambda}{2\pi} \sin\left(\frac{2\pi i}{i_{max}}\right), \; 0 < \lambda \leq 1 \tag{2.36}$$

in both x- and y-directions. The flow configuration and a typical 41×41 grid are shown in figure 2.4. Our finest grid computation on a grid of size 321×321 in conjunction with $\lambda = 0.99$ resulted in a value $h^* = 3.144883 \times 10^{-5}$. Note that extreme clustering such as this allowed us to resolve even the post quaternary vortices for moderately high Re while in [169], the authors could reach only up to tertiary level with a maximum value of $\lambda = 0.5$ for this particular problem.

In figures 2.5 (a)-(b), we compare the horizontal velocities along the vertical centerline and the vertical velocities along the horizontal centerline for $Re = 100$, 400 and 1000 with the bencmark results of Ghia *et al.* [41]. The same for $Re = 3200$, 5000 and 7500 are presented in figure 2.6. One can clearly see from the figures that our results are extremely close to those of [41] on grids much coarser than those used thereat.

In figures 2.7(a)-(f), we present the steady-state streamfunction contours for $100 \leq Re \leq 7500$. These results are extremely close to the well established numerical results of [21, 37, 41, 46, 70, 73, 115]. One can clearly see the center of the primary vortex moving from the top right to the geometric center of the cavity as Reynolds number increases. The typical separations and formation of secondary and tertiary vortices at the bottom corners and the top left region for $Re = 7500$, which starts appearing from approximately $Re = 2000$ onwards, can also be seen from these figures.

It is a well known fact that the bottom corners of the lid-driven square cavity flow are

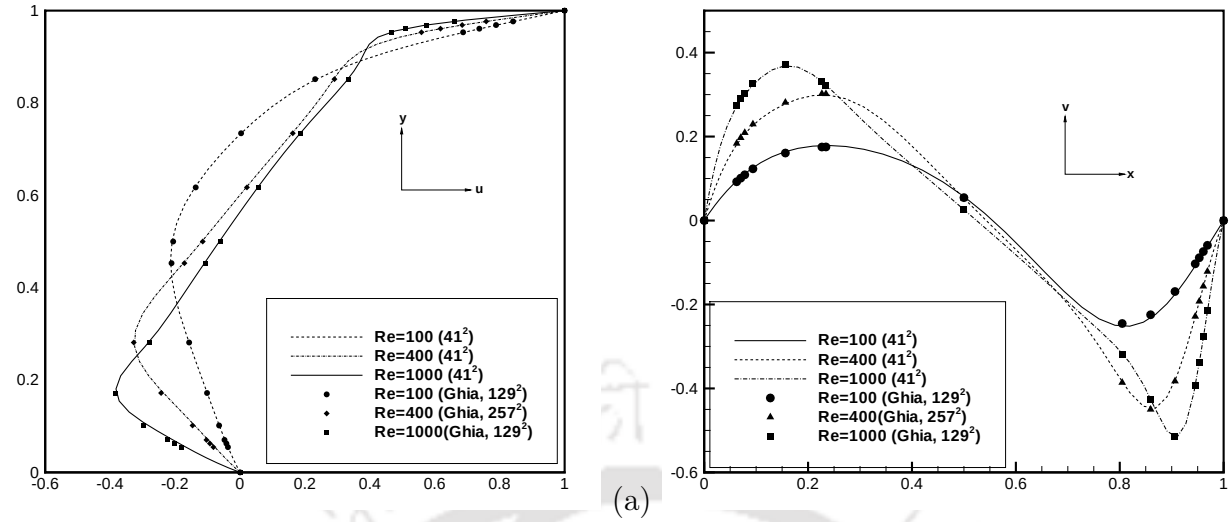

(a) (b)

Figure 2.5: *Comparisons of steady-state (a) horizontal velocity along the vertical centerline and (b) vertical velocity along the horizontal centerline for the lid-driven square cavity flow problem for* $Re = 100$, 400 *and* 1000 *with [41].*

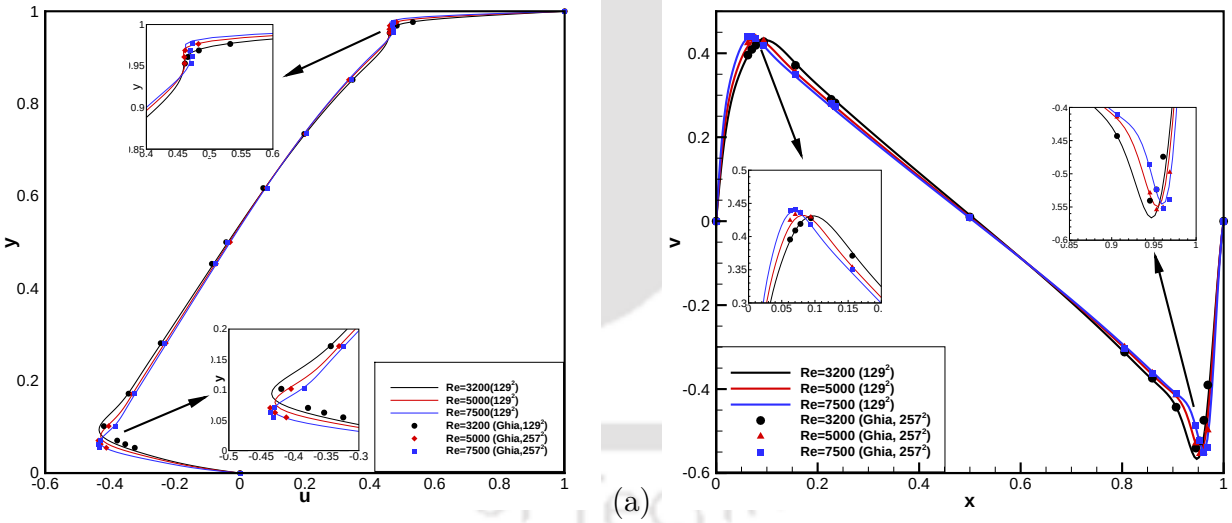

(a) (b)

Figure 2.6: *Comparisons of steady-state (a) horizontal velocity along the vertical centerline and (b) vertical velocity along the horizontal centerline for the lid-driven square cavity flow problem for* $Re = 3200$, 5000 *and* 7500 *with [41].*

synonymous with the existence of a sequence of vortices of decreasing size and intensity [67, 140, 142]. Since figure 2.7 could demonstrate only the secondary and tertiary vortices

in this sequence, in order to get a better view of the latter vortices of the sequence, we present them in figures 2.8-2.11. The secondary, tertiary, quaternary and post-quaternary vortices at the bottom left corners have been denoted by BL_1, BL_2, BL_3 and BL_4, and likewise for the vortices on the right corners. We have used multiple frames to depict the vortices appearing in each corner. In each frame, a pair of successive vortices gradually decreasing in size is plotted with the next pair appearing side by side in the adjacent frame. The smaller vortex in the previous frame is magnified for clarity in the next frame, which is now the bigger of the two vortices and is marked with arrowheads. It is heartening to note that for high Res, even the post-quaternary vortices have been captured with apt details.

In tables 2.3-2.7, we present the primary, secondary, tertiary, quaternary and post-quaternary vortex data for $100 \leq Re \leq 7500$ from the present computation and compare them with established benchmark data whenever available. One can clearly see that our data are close match to the available numerical results. This is probably the first time the quaternary and post-quaternary vortex data are being presented for this flow in the whole range $100 \leq Re \leq 7500$.

In figure 2.12, we present the top right corner streamlines for $Re = 7500$ computed with different grid sizes and clustering parameters. Figure 2.12(a) depicts the streamlines computed on a uniform grid of size 129×129 (corresponding to $\lambda = 0.0$) with the current scheme while figure 2.12(b) depicts the ones computed by the five point formula of [169] with $\lambda = 0.5$. One can clearly see prominent wiggles at the corner for the streamlines computed on the uniform grid which could be removed to some extent by using a value of $\lambda = 0.5$. Simply increasing the value slightly further to 0.6, the wiggles could be completely removed by using our scheme in figure 2.12(c). The robustness of our scheme can be gauged by the fact that while the scheme in [169] could handle a value up to a moderate $\lambda = 0.5$ on a 129×129 grid, our scheme could handle extreme clustering with $\lambda = 0.99$ on a 321×321 grid. Contrary to the minimum step length value 3.908×10^{-3} that could be handled by the scheme in [169], our scheme could utilize a value as low as 3.145×10^{-5} (figure 2.12(d)).

In table 2.8 and figures 2.13(b) and 2.14(a)-(d), we provide the convergence history data for our computation of the lid-driven cavity flow on grid sizes ranging from 11×11

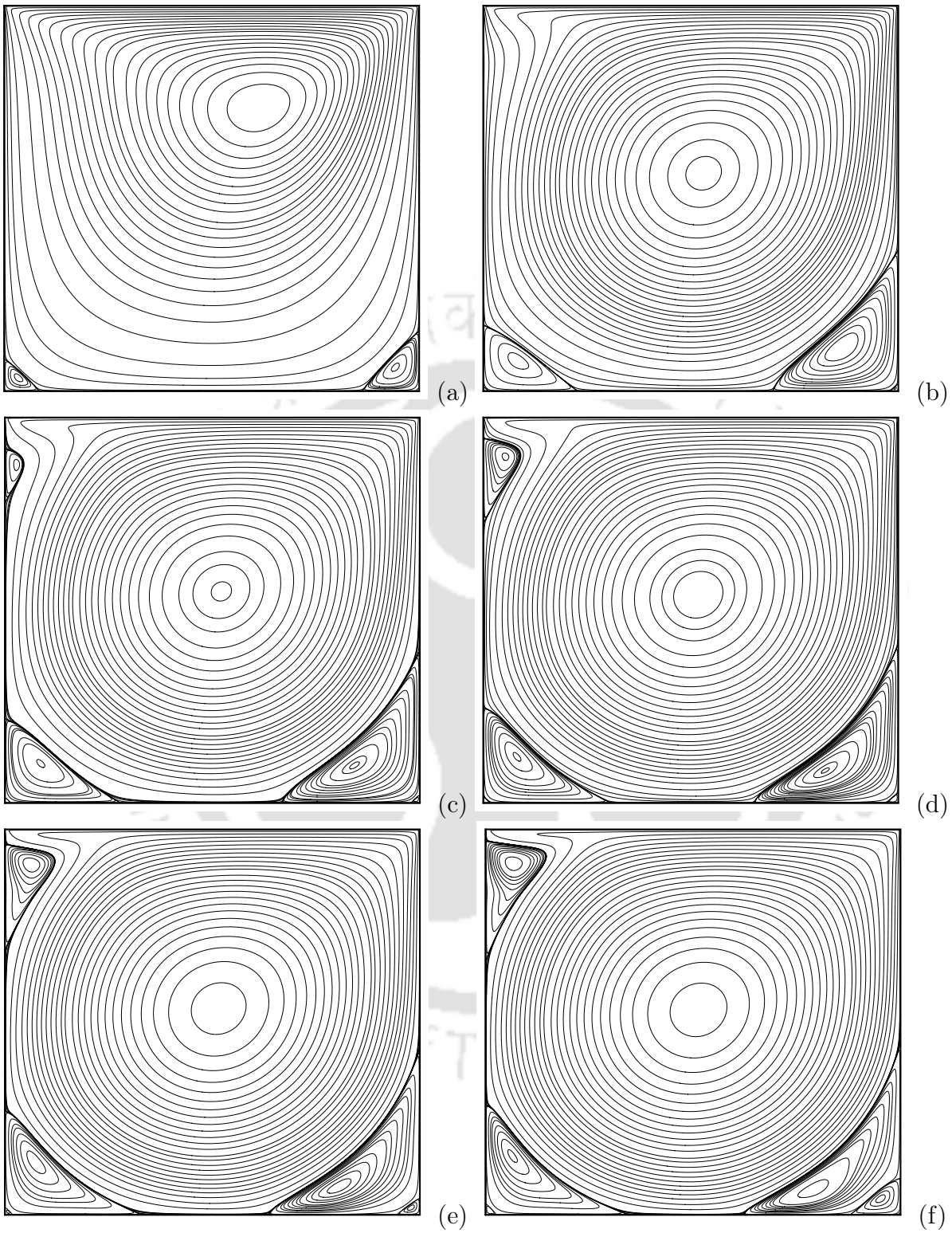

Figure 2.7: *Finest grid* (321×321, $\lambda = 0.99$) *streamfunction Contours for the lid-driven cavity flow for (a)Re=100, (b) Re=1000, (c) Re= 2000, (d) Re= 3200, (e) Re= 5000 and (f) Re= 7500.*

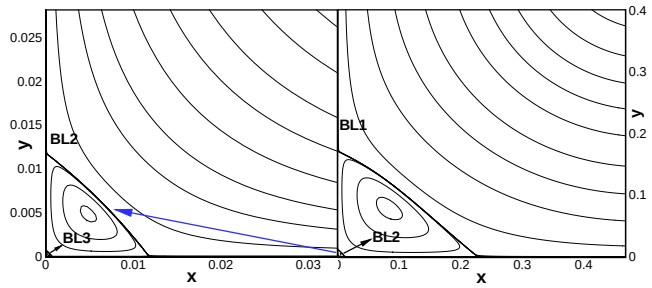

(a)

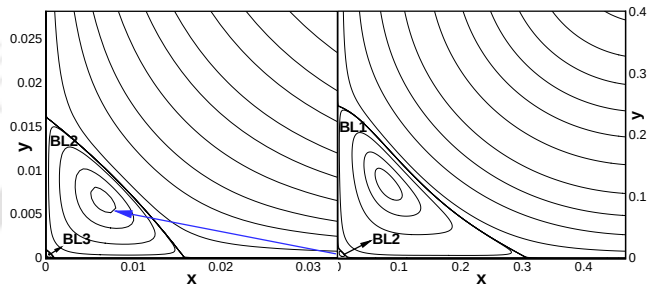

(b)

Figure 2.8: *Bottom left corner vortices on grid size* 321×321*: (a)* $Re = 1000$ *and (b)* $Re = 3200$.

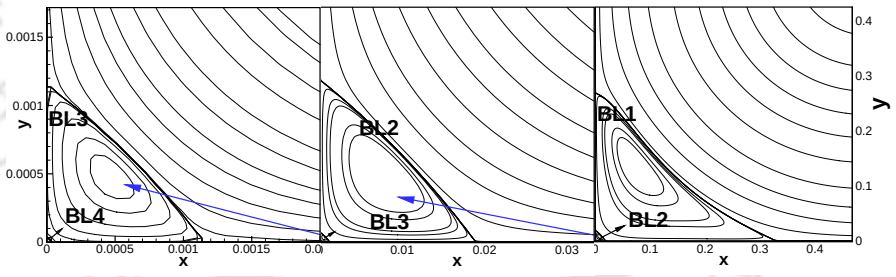

(a)

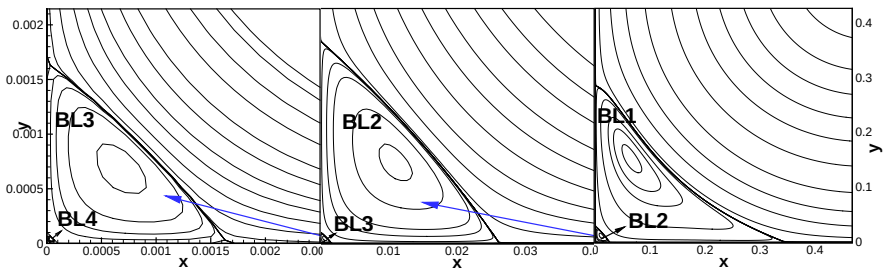

(b)

Figure 2.9: *Bottom left corner vortices on grid size* 321×321*: (a)* $Re = 5000$ *and (b)* $Re = 7500$.

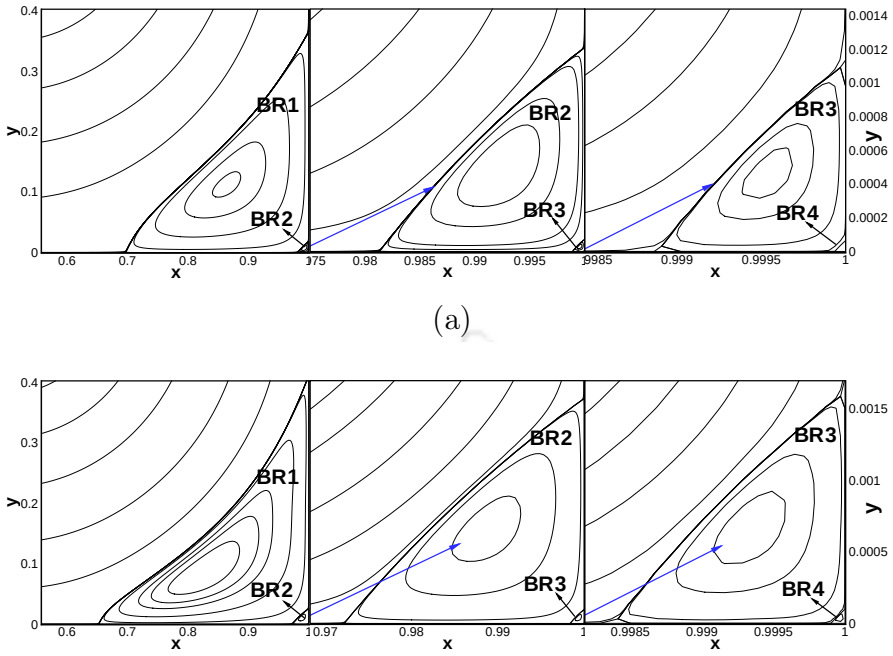

(a)

(b)

Figure 2.10: *Bottom right corner vortices on grid size* 321×321*: (a)* $Re = 1000$ *and (b)* $Re = 3200$.

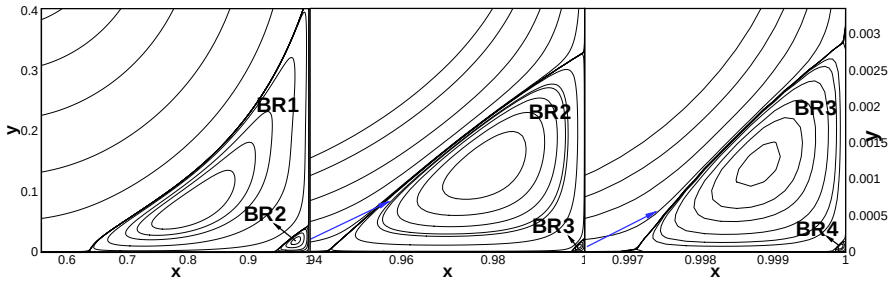

(a)

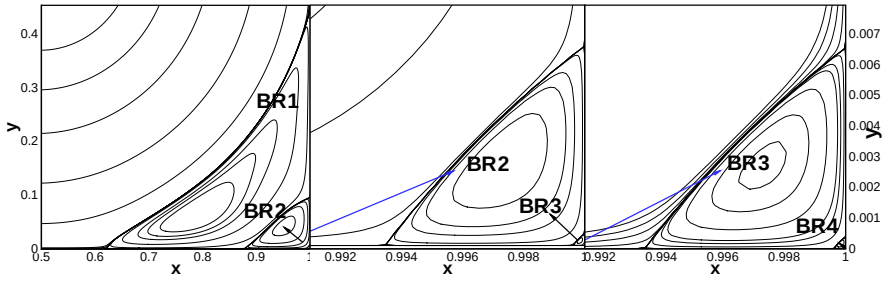

(b)

Figure 2.11: *Bottom right corner vortices on grid size* 321×321*: (a)* $Re = 5000$ *and (b)* $Re = 7500$.

Table 2.3: Strength and location of the centers of primary vortex for the lid-driven square cavity problem.

Re		ψ_{min}	x	y
100	[159]	-0.103	0.6188	0.7375
	[41]	-0.103	0.6172	0.7344
	[57]	-0.103	0.6196	0.7373
	[46]	-0.103	0.6125	0.7375
	Present	-0.103	0.6173	0.7364
400	[159]	-0.114	0.5563	0.6000
	[41]	-0.114	0.5547	0.6055
	[133]	-0.113	0.5571	0.6071
	[57]	-0.112	0.5608	0.6078
	[46]	-0.113	0.5500	0.6125
	Present	-0.114	0.5533	0.6058
1000	[159]	-0.117	0.5438	0.5625
	[41]	-0.118	0.5313	0.5625
	[57]	-0.118	0.5333	0.5647
	[46]	-0.117	0.5250	0.5625
	[37]	-0.118	0.5300	0.5650
	[104]	—	0.5305	0.5653
	Present	-0.118	0.5311	0.5681
2000	[159]	-0.112	0.5250	0.5500
	[57]	-0.120	0.5255	0.5490
	[46]	-0.120	0.5186	0.5496
	Present	-0.118	0.5311	0.5681
3200	[41]	-0.120	0.5165	0.5469
	[46]	-0.122	0.5188	0.5438
	Present	-0.122	0.5186	0.5434
5000	[159]	-0.092	0.5125	0.5313
	[41]	-0.119	0.5117	0.5352
	[57]	-0.121	0.5176	0.5373
	[7]	-0.122	0.5113	0.5283
	[46]	-0.122	0.5125	0.5375
	[37]	-0.121	0.5150	0.5350
	Present	-0.122	0.5124	0.5373
7500	[41]	-0.120	0.5117	0.5322
	[57]	-0.122	0.5176	0.5333
	[7]	-0.122	0.5132	0.5321
	[46]	-0.122	0.5125	0.5313
	[37]	-0.121	0.5133	0.5317
	Present	-0.122	0.5124	0.5311

Table 2.4: Strength and location of the centers of secondary vortex: Bottom of the lid-driven square cavity.

		Bottom Left			Bottom Right		
Re		ψ_{max}	x	y	ψ_{max}	x	y
100	[159]	1.94e-6	0.0375	0.0313	1.14e-5	0.9375	0.0563
	[41]	1.75e-6	0.0313	0.0391	1.25e-5	0.9453	0.0625
	[57]	1.72e-6	0.0392	0.0353	1.22e-5	0.9451	0.0627
	[46]	1.83e-6	0.0375	0.0375	1.45e-5	0.9375	0.0625
	[17]	1.55e-6	0.0329	0.0329	1.145e-5	0.9431	0.0617
	Present	1.80e-6	0.0341	0.0341	1.27e-5	0.9427	0.0615
400	[159]	1.46e-5	0.0500	0.0500	6.45e-4	0.8875	0.1188
	[41]	1.42e-5	0.0508	0.0469	6.42e-4	0.8906	0.1250
	[133]	1.45e-5	0.0500	0.0429	6.44e-4	0.8857	0.1143
	[57]	1.30e-5	0.0549	0.0510	6.19e-4	0.8902	0.1255
	[46]	1.30e-5	0.0500	0.0500	6.48e-4	0.8875	0.1250
	[17]	1.31e-5	0.0502	0.0459	6.41e-4	0.8842	0.1230
	Present	1.43e-5	0.0512	0.0474	6.43e-4	0.8868	0.1230
1000	[159]	2.24e-4	0.0750	0.0813	1.74e-3	0.8625	0.1063
	[41]	2.31e-4	0.0859	0.0781	1.75e-3	0.8594	0.1094
	[57]	2.22e-4	0.0902	0.0784	1.69e-3	0.8667	0.1137
	[46]	2.02e-4	0.0875	0.0750	1.70e-3	0.8625	0.1125
	[37]	2.32e-4	0.0833	0.0783	1.73e-3	0.8633	0.1117
	[17]	2.33e-4	0.0833	0.0775	1.73e-3	0.8657	0.1128
	[104]	—	0.0832	0.0771	—	0.8658	0.1136
	Present	2.32e-4	0.0833	0.0775	1.73e-3	0.8657	0.1123
2000	[159]	6.90e-4	0.0875	0.1063	2.60e-3	0.8375	0.0938
	[57]	7.26e-4	0.0902	0.1.59	2.44e-3	0.8471	0.0980
	[46]	8.58e-4	0.0875	0.1000	2.41e-3	0.8375	0.1000
	Present	7.17e-4	0.0863	0.102	2.45e-3	0.8416	0.0956
3200	[41]	9.78e-4	0.0859	0.1094	3.14e-3	0.8125	0.0859
	[46]	1.03e-3	0.0813	0.1188	2.86e-3	0.8125	0.0875
	[17]	1.05e-3	0.0804	0.1194	2.84e-3	0.8243	0.0833
	Present	1.11e-3	0.0804	0.1194	2.82e-3	0.8243	0.0833
5000	[159]	1.67e-3	0.0625	0.1563	5.49e-3	0.8500	0.0813
	[41]	1.36e-3	0.0703	0.1367	3.08e-3	0.8086	0.0742
	[57]	1.35e-3	0.0784	0.1313	3.03e-3	0.8078	0.0745
	[46]	1.32e-3	0.0750	0.1313	2.96e-3	0.8000	0.0750
	[37]	1.36e-3	0.0733	0.1367	3.06e-3	0.8050	0.0733
	Present	1.37e-3	0.0720	0.1381	3.06e-3	0.8062	0.0748
7500	[41]	1.47e-3	0.0645	0.1504	3.28e-3	0.7813	0.0625
	[57]	1.51e-3	0.0706	0.1529	3.20e-3	0.7922	0.0667
	[46]	1.60e-3	0.0688	0.1500	3.05e-3	0.7813	0.0625
	[37]	1.52e-3	0.0650	0.1517	3.216e-3	0.7900	0.0650
	Present	1.53e-3	0.0642	0.154	3.21e-3	0.7872	0.0642

Table 2.5: Strength and location of the centers of tertiary vortex: Bottom of the lid-driven square cavity.

		Bottom Left			Bottom Right		
Re		ψ_{min}	x	y	ψ_{min}	x	y
100	[17]	-4.08e-11	1.95e-3	1.95e-3	-2.93e-10	0.9965	3.46e-3
	Present	-4.91e-11	2.08e-3	2.08e-3	-3.49e-10	0.9963	3.68e-3
400	[17]	-3.58e-10	2.79e-3	2.79e-3	-1.81e-8	0.9926	7.39e-3
	Present	-3.94e-10	2.94e-3	2.94e-3	-1.77e-8	0.9928	7.68e-3
1000	[17]	-6.13e-9	4.70e-3	4.70e-3	-4.877e-8	0.9926	7.39e-3
	[104]	—	4.40e-3	4.24e-3	—	0.9932	7.27e-3
	Present	-6.34e-9	4.70e-3	4.70e-3	-5.034e-8	0.9922	7.70e-3
2000	Present	-2.059e-8	5.68e-3	5.68e-3	-9.16e-8	0.9913	8.70e-3
3200	[41]	-6.33e-8	0.0078	0.0078	-2.526e-7	0.9844	0.0078
	[46]	-3.74e-8	0.0063	0.0063	-2.376e-7	0.9875	0.0125
	[17]	-3.81e-8	0.0068	0.0068	-2.126e-7	0.9882	0.0109
	Present	-3.64e-8	0.0062	0.0062	-1.95e-7	0.9890	0.0109
5000	[41]	-7.09e-8	0.0117	0.0078	-1.43e-6	0.9805	0.0195
	[20]	-2.33e-7	0.0117	0.0098	-2.47e-6	0.9668	0.0293
	[7]	-6.67e-8	0.0079	0.0079	-1.43e-6	0.9786	0.0188
	[46]	-5.15e-8	0.0063	0.0063	-1.70e-6	0.9750	0.0188
	Present	-6.59e-8	0.0080	0.0080	-1.38e-6	0.9787	0.0188
7500	[41]	-1.83e-7	0.0117	0.0117	-3.28e-5	0.9492	0.0430
	[7]	-2.04e-7	0.0112	0.0118	-3.28e-5	0.9517	0.0422
	[46]	-1.64e-7	0.0063	0.0125	-1.89e-5	0.9500	0.0375
	Present	-2.00e-7	0.0110	0.0118	-3.15e-5	0.9520	0.0419

Table 2.6: Strength and location of the centers of quaternary vortex: Bottom of the lid-driven square cavity.

		Bottom Left			Bottom Right		
Re		ψ_{max}	x	y	ψ_{max}	x	y
100	[17]	9.62e-16	1.20e-4	1.20e-4	7.37e-15	0.9998	2.00e-4
	Present	1.26e-15	2.37e-4	2.37e-4	9.22e-15	0.9998	2.30e-4
400	[17]	1.00e-14	1.80e-4	1.80e-4	5.05e-13	0.9995	4.20e-4
	Present	1.08e-14	1.81e-4	1.81e-4	4.86e-13	0.9996	4.26e-4
1000	[17]	1.58e-13	2.80e-4	2.80e-4	1.33e-12	0.9995	4.20e-4
	[104]	—	2.50e-3	2.50e-3	—	0.9996	4.20e-4
	Present	1.74e-13	2.87e-4	2.87e-4	1.35e-12	0.9995	4.60e-4
2000	Present	5.68e-13	3.52e-4	3.52e-4	2.50e-12	0.9995	5.11e-4
3200	[17]	9.38e-13	3.80e-4	3.90e-4	4.70e-12	0.9994	6.10e-4
	Present	9.81e-13	3.89e-4	3.89e-4	5.24e-12	0.9993	6.63e-4
5000	Present	1.77e-12	4.68e-4	4.68e-4	3.70e-11	0.9988	1.22e-3
7500	Present	5.35e-12	6.65e-4	6.63e-4	8.48e-10	0.9972	2.78e-3

Table 2.7: Strength and location of the centers of post-quaternary vortex: Bottom of the lid-driven square cavity.

		Bottom Left			Bottom Right		
Re		ψ_{min}	x	y	ψ_{min}	x	y
400	Present	—	—	—	-7.99e-18	9.9997e-1	3.10e-5
1000	[104]	—	—	—	—	9.9997e-1	2.70e-5
	Present	—	—	—	-3.39e-17	9.9997e-1	3.10e-5
2000	Present	—	—	—	-7.14e-17	9.9997e-1	3.10e-5
3200	[104]	—	—	—	-1.74e-16	9.9996e-1	3.00e-5
	Present	—	—	—	-1.13e-16	9.9997e-1	3.10e-5
5000	Present	-1.77e-12	3.10e-5	3.10e-5	-9.59e-16	9.9993e-1	6.40e-5
7500	Present	-1.06e-16	3.15e-5	3.15e-5	-2.25e-14	9.9983e-1	1.59e-4

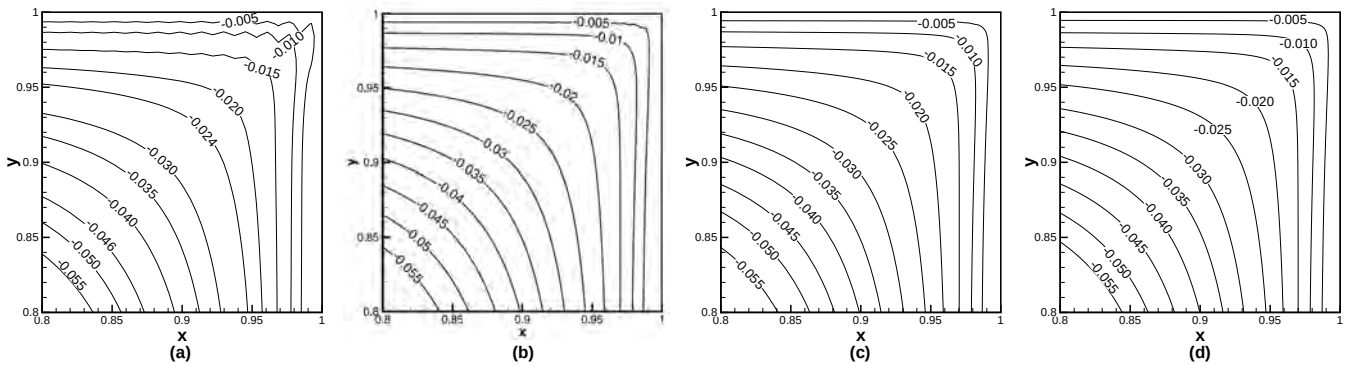

Figure 2.12: *The comparison of the streamline in the top-right corner for* $Re = 7500$ *with: (a) uniform mesh* 129×129 *and (b) nonuniform mesh with* $\lambda = 0.5$ *on* 129×129 *grid [169] (c) nonuniform mesh with* $\lambda = 0.6$ *on* 129×129 *grid (d) nonuniform mesh with* $\lambda = 0.99$ *on* 321×321 *grid.*

to 321×321 for $0.5 \leq \lambda \leq 0.99$. It is heartening to see that even on a grid size as coarse as 11×11, our scheme is able to capture the corner vortces for $Re = 100$ (see figure 2.13(a) which corresponds to the first row of data in table 2.8). Note that in all the computations, for $Re = 100$, the code was run from scratch with zero initial data at the interior, while for other Reynolds numbers, the converged data from the previous Reynolds number was set as the initial data. Table 2.8 provides a comprehensive data for a wide range of combination of the grid size, Reynolds number Re and the clustering parameter λ during the inner and outer iteration process. While for the inner iterations, we have used a pre-conditioned BiCGStab algorithm, the outer iterations were either under or over-relaxed in order to attain convergence. For $\lambda \leq 0.9$, the tolerance limit for the inner iterations was set at 10^{-9} and for $\lambda > 0.9$, it was set at 10^{-13}. After a few outer iterations, the number of inner iterations was seen to settle into constant value; this value is listed in the 6^{th} column of table 2.8. In the same table, the third column represents the optimized value of the under-relaxation/ over-relaxation parameter. As expected, increase in Reynolds number and grid size prompts an increase in the CPU time (presented here in seconds), inner and outer iteration numbers.

In figure 2.13(b), we show the effect of the steady-state criterion on the convergence of the iterations. It is clear from the figure that a tolerance limit of 10^{-8} is good enough for attaining steady-state against the steady-state criterion of 10^{-13} imposed here as the $\max|\psi|$ settles into a constant value much before that. As such, table 2.8 and figures 2.14(a)-(d) correspond to a stopping criterion of 10^{-8} for the max ψ-error for reaching steady-state.

In figure 2.14(a), we show the effect of clustering on the convergence for $Re = 100$ on a relatively coarser grid of size 81×81; one can clearly see that with the increase in the intensity of clustering, there is a decrease in the outer iteration number. Figure 2.14(b) shows the effect of the Reynolds number on convergence on the same grid with moderate clustering ($\lambda = 0.7$) and 2.14(d) with extreme clustering ($\lambda = 0.99$) on the finest grid (321×321) considered in the current computation; note that $Re = 100$ consumes more outer iterations (hence CPU time) than $Re = 400$ because zero initial data was used for $Re = 100$ whereas $Re = 400$ utilized the converged $Re = 100$ data for initialization. Figure 2.14(c) shows the effect of the grid size on convergence for $Re = 100$ with $\lambda = 0.7$.

Re	Grid	SOR/SUR	λ	CPU (Sec)	Inn Itr	Otr ITR
100	11×11	1.7	0.7	0.011	5	120
100	21×21	1.8	0.7	0.205	7	495
100	41×41	1.98	0.7	3.172	12	1695
100	81×81	1.98	0.5	86.690	31	6466
100	81×81	1.98	0.6	74.474	24	6286
100	81×81	1.98	0.7	64.456	24	5991
100	81×81	1.98	0.8	53.661	21	5554
100	81×81	1.98	0.9	43.079	17	4940
100	81×81	1.98	0.95	47.177	23	4554
100	81×81	1.98	0.99	38.772	19	4203
100	129×129	1.98	0.99	327.018	30	9769
100	161×161	1.98	0.7	2399.680	53	20437
100	321×321	1.98	0.7	61713.290	122	67424
100	321×321	1.98	0.99	31835.820	91	47991
400	81×81	1.98	0.7	46.438	24	4147
400	321×321	1.50	0.99	32396.370	91	39177
1000	81×81	0.65	0.7	102.557	24	9159
1000	321×321	0.80	0.99	43851.671	89	53433
2000	81×81	0.18	0.7	343.371	24	31857
2000	321×321	0.80	0.99	41561.140	89	50912
3200	81×81	0.06	0.7	1014.444	25	91231
3200	321×321	0.40	0.99	79744.960	90	93544
5000	81×81	0.01	0.7	6183.956	25	552526
5000	321×321	0.20	0.99	138882.140	90	186974
7500	321×321	0.08	0.99	309748.300	89	462455

Table 2.8: Convergence history data for the lid-driven cavity flow.

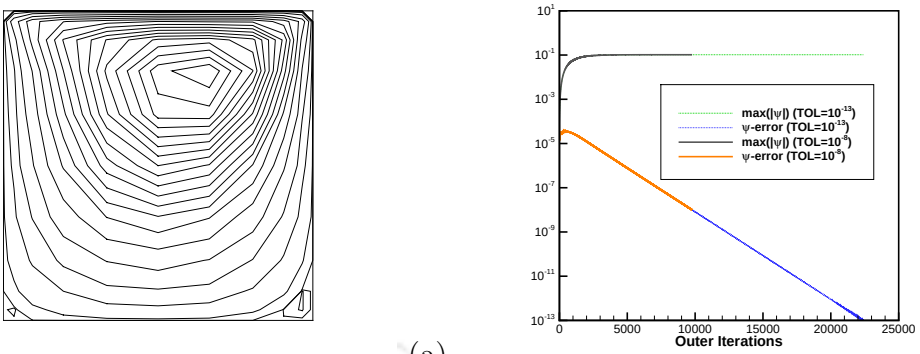

(a) (b)

Figure 2.13: *Test problem 2: (a) Steady-state streamlines for* $Re = 100$ *on a grid of size* 11×11 *with* $\lambda = 0.7$ *and (b) Effect of steady state criterion on the convergence history for* $Re = 100$ *on a* 129×129 *grid with* $\lambda = 0.99$.

In all the cases, the convergence was seen to be very smooth.

2.4.3 Test case 3: Backward Facing Step

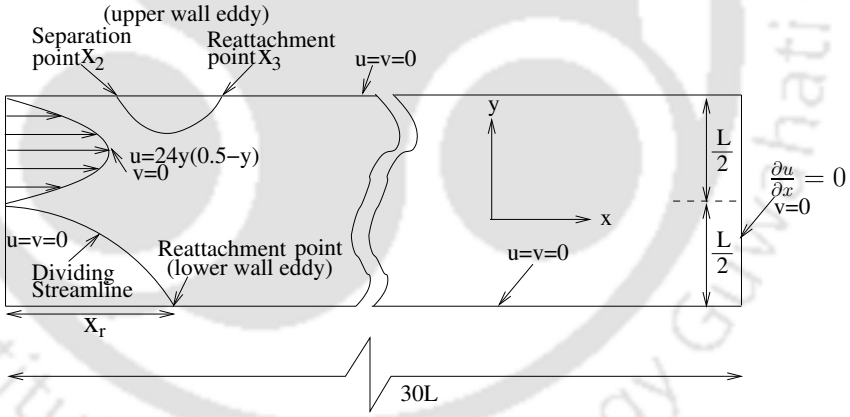

Figure 2.15: Problem statement of flow over a backward facing step

Next, we consider the flow over the backward facing step in a channel. Here, reattcahment length is a function of Reynolds number. The problem setup is presented in figure 2.15. In this case, Reynolds number is defined as $Re = \dfrac{u_{av}L}{\nu}$, where u_{av} is average inlet velocity, L is the channel height and ν is the kinematic viscosity of the fluid. In all our computations L was set as 1.0.

At the inlet, a parabolic velocity is introduced as $u = 12y(1-2y),\ v = 0$ [40]. The downstream length of channel is taken as 30 times of channel height in order to allow the

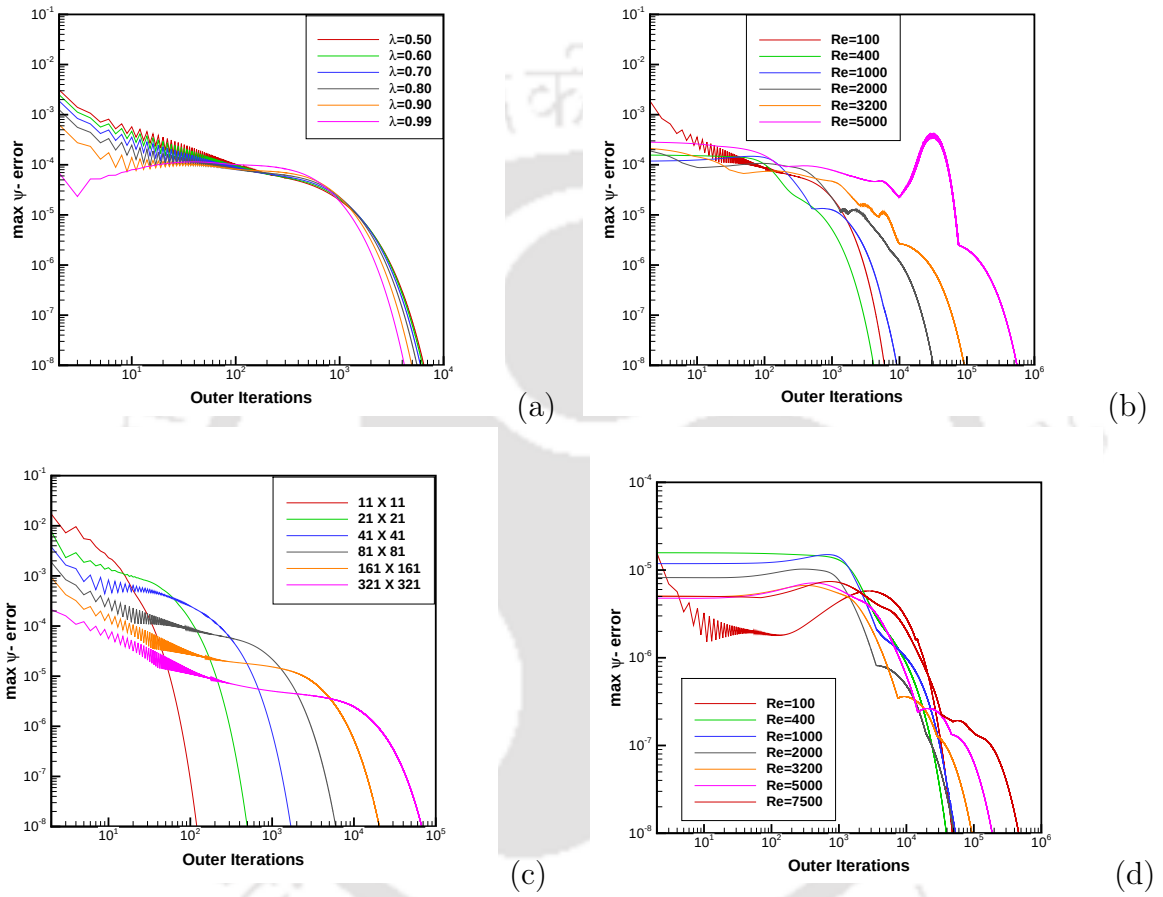

Figure 2.14: *(a) Effect of the clustering parameter λ on the convergence history on a coarser grid with moderate clustering, (b) Effect of the Reynolds number Re on the convergence history, (c) Effect of the grid size on the convergence history and (d) Effect of the clustering parameter λ on the convergence history on the finest grid with extreme clustering.*

flow to become fully developed. Thus, at the outlet, boundary conditions are $\frac{\partial u}{\partial x} = 0$ and $v = 0$. At the stationary walls, $u = 0,\ v = 0$; while $\psi = 0.5$ at the upper wall, at the lower wall and the step $\psi = 0$. At the inlet, ψ can be calculated using the the values of u and v and at the outlet, Neumann boundary condition $\frac{\partial \psi}{\partial x} = 0$ is used. Numerical simulations are carried out for Reynolds numbers ranging from 1 to 800 on grids of sizes ranging from 101×41 to 301×201. We used a centrosymmetric stretching in the y-direction using the stretching function used in test case 2 with $\lambda = 0.7,\ 0.99$. In the x-direction, for the portion $0 \leq x \leq 12$, a one-sided clustering was employed using the stretching function used in test case 1 with $\lambda = 0.99$ and 0.9995 over $\frac{4(i_{\max} - 1)}{5} + 1$ points; for the remaining portion $12 \leq x \leq 30$, we used a uniform grid spacing using $\frac{i_{\max} - 1}{5}$ points where $i_{\max}$ is the total number of points used in the x-direction. A close-up view of the grid at the corner of the step is shown in figure 2.16.

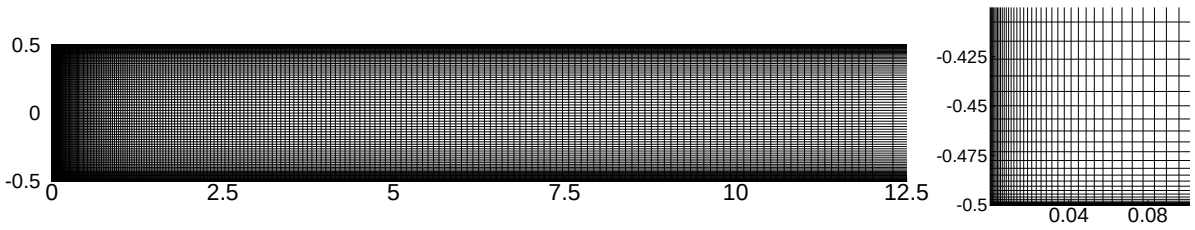

Figure 2.16: A portion of the 301×201 grid used for the flow over a backward facing step with a close up view of the step with extreme clustering.

In figures 2.17(a)-(h), we present the steady-state stremlines for this flow for Reynolds numbers in the range $1 \leq Re \leq 800$. One can see the development of a corner vortex at the step for Stokes flow at $Re = 1$ which grows in size with increasing Reynolds numbers completely occupying the face of the step from $Re = 10$ onwards. As such, Biswas *et al.* [16] consider "recirculation region" to be more a more apt term to describe these eddies from $Re = 10$ onwards and our observations are consistent with theirs. From $Re = 500$ onwards, another eddy is seen developing on the upper wall slowly growing in size and moving towards the downstream direction.

According to theory of Moffatt [16, 67, 140, 141], at the corner of the step there should exist a series of vortices of decreasing intensity and size for $Re \to 0$. However, we observe such sequence of vortices for the computed flow throughout the entire range of Reynolds

numbers considered here. The second vortex in this series has also been depicted in the right panels of the same figures 2.17(a)-(h). One can see these vortices also growing in size with increasing Reynolds numbers with a much slower growth rate for high Res. In figure 2.18, we show the latter vortices in the sequence for the smallest and the largest Reynolds numbers considered in this study, viz., $Re = 1$ (figure 2.18(a)) and $Re = 800$ (figure 2.18(b)). With extreme clustering, by employing a value of clustering parameter $\lambda = 0.9995$ in the x-direction and 0.99 in the y-direction on a 301×201 grid, we were also able to capture the fourth vortex in the sequence from $Re = 10$ onwards; the one for $Re = 800$ is shown in figure 2.18(b).

In table 2.9 we present data for the first vortex in the the lower wall for $100 \leq Re \leq 800$ and in table 2.10, the data for the upper wall eddy for $500 \leq Re \leq 800$. In both the tables, we compare our data with established numerical results and close matches are obtained in all the cases. In figure 2.19, we compare the reattachment length of the primary recirculation region at the step in the Reynolds number range $1 \leq Re \leq 800$ with the experimental results of [5] and the numerical results of Kim and Moin [83], and Biswas *et al.* [16]. Note that while the works of [5, 16] used an expansion ratio 1.9428 for the step, we have used a value 2 for the same in our computation. Here also, our results are extremely close to the numerical ones and closer to the experimental results than the other two. The deviation of the numerical results from the experimental ones for $Re > 600$ is attributed to the development of three-dimensionality in the flow for that range.

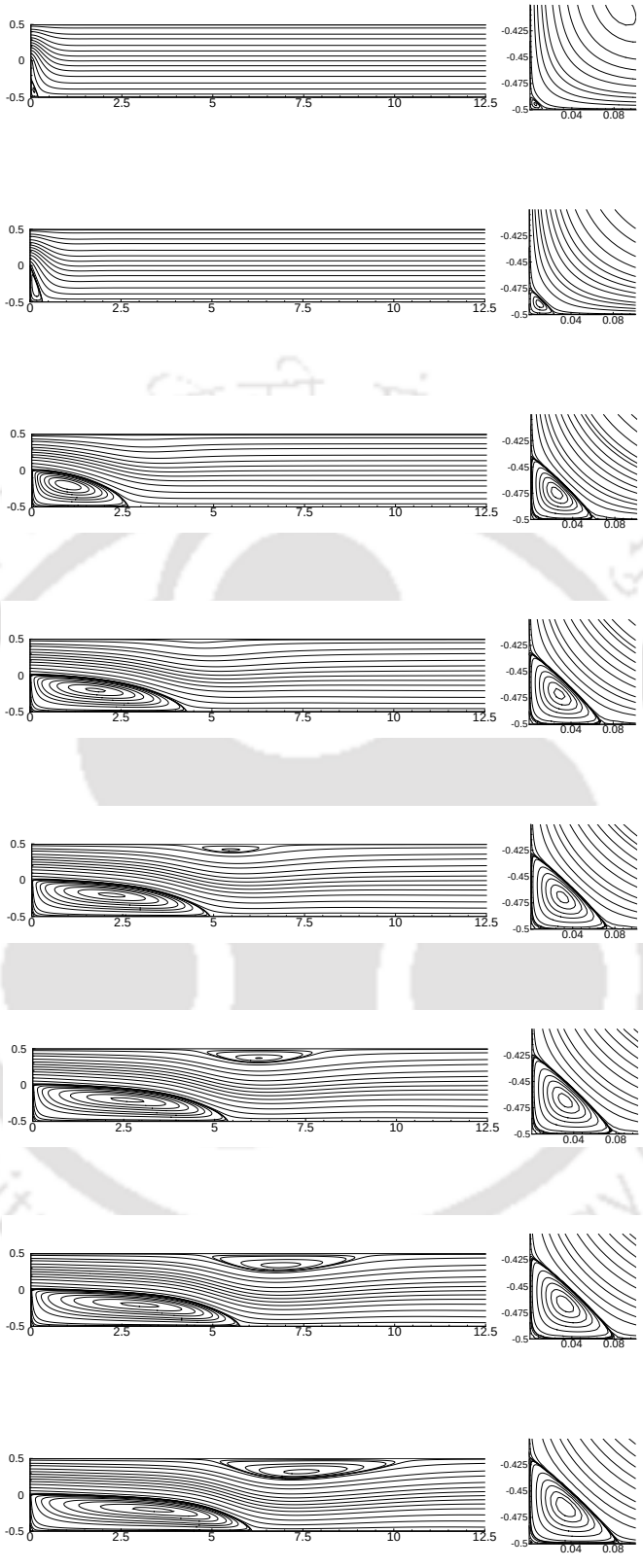

Figure 2.17: *Backward facing step flow for (a) $Re = 1$, (b) $Re = 10$, (c) $Re = 200$, (d) $Re = 400$, (e) $Re = 500$, (f) $Re = 600$, (g) $Re = 700$ and (h) $Re = 800$. The secondary vortices at the step are shown in close-up on the right.*

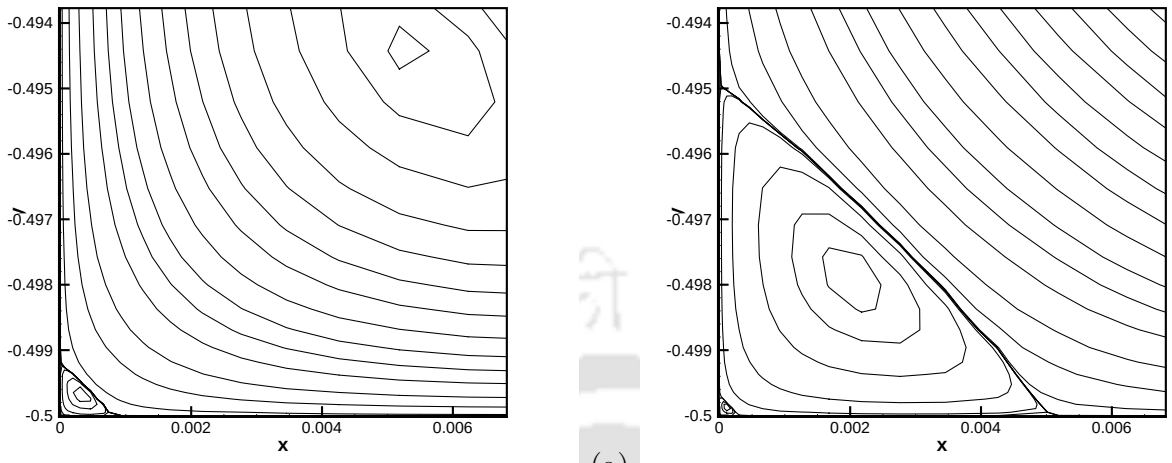

Figure 2.18: *The corner vortices at the step: (a) second and third vortices for $Re = 1$ and (b) the third and the fouth vortices for $Re = 800$.*

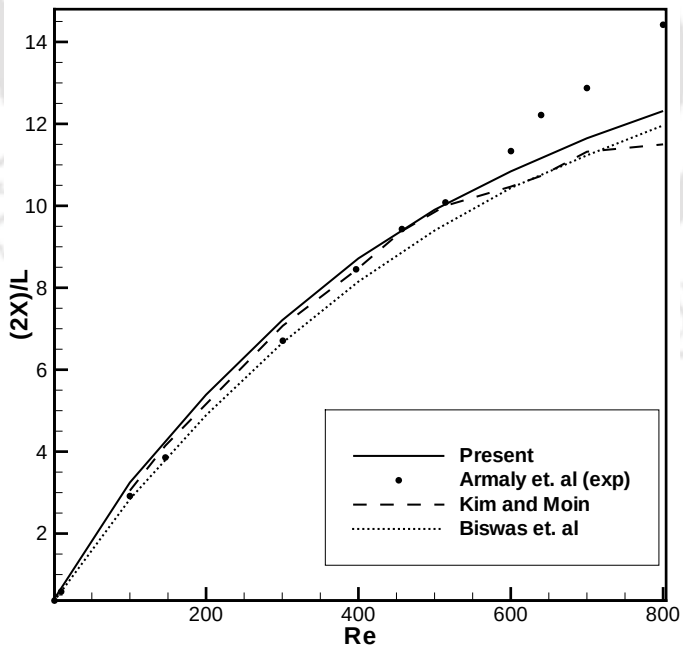

Figure 2.19: *The reattcahment length as a function of Reynolds number*

Table 2.9: Properties of the lower wall eddy from $Re = 100$ to $Re = 800$

Re	Eddy Center (x, y)	ψ	Recirculation length
100	(0.5835,-0.1963)	-0.02992	1.623099
200	(0.9756,-0.1963) (0.938,-0.188) [47]	-0.0330 -0.03276 [47]	2.69469 2.633 [47]
300	(1.385,-0.1963) (1.132,-0.188) [47]	-0.0337 -0.03341 [47]	3.60356 3.510 [47] 3.390 [8]
400	(1.750,-0.1963) (1.705,-0.188) [47]	-0.0339 -0.03364 [47]	4.35846 4.239 [47] 4.32 [149]
500	(2.1688,-0.1963)	-0.0340	4.95186 5.16 [8]
600	(2.6947,-0.2112) (2.438,-0.188) [47] (3.350,-0.200) [40]	-0.0341 -0.03375 [47]	5.42004 5.319 [47] 5.495 [8] 5.50 [149]
700	(3.101,-0.2112)	-0.0341 -0.0342 [40]	5.8251 6.5 [43]
800	(3.4742,-0.211) (3.500,-0.219) [47]	-0.0341 -0.03381 [47]	6.15698 6.000 [47] 6.22 [149] 6.10 [40] 5.75 [83] 5.75 [145]

Table 2.10: Properties of the upper wall eddy from $Re = 500$ to $Re = 800$

Re	Eddy Center (x, y)	ψ	Separation point x_2	Reattachment point x_3
500	(5.499,0.421) (5.438,0.406) [47]	0.5006 0.5005 [47]	4.14 4.309 [47]	6.844 6.555 [47]
600	(6.241,0.371) (6.170,0.375) [47]	0.5023 0.5023 [47]	4.358 4.505 [47] 4.13 [8]	8.109 7.908 [47] 7.83 [8]
700	(6.844,0.340) (6.867,0.342) [47]	0.5044 0.5043 [47]	4.577 4.717 [47]	9.341 9.127 [47]
800	(7.467,0.318) (7.400,0.300) [40] (7.385,0.313) [47]	0.5064 0.5064 [40] 0.5066 [47]	4.800 4.85 [40] 4.897 [47] 4.28 [8] 4.70 [145] 5.13 [149]	10.512 10.48 [40] 10.279 [47] 9.28 [8] 9.40 [145] 10.22 [149]

2.4.4 Test case 4: Flow past a circular cylinder

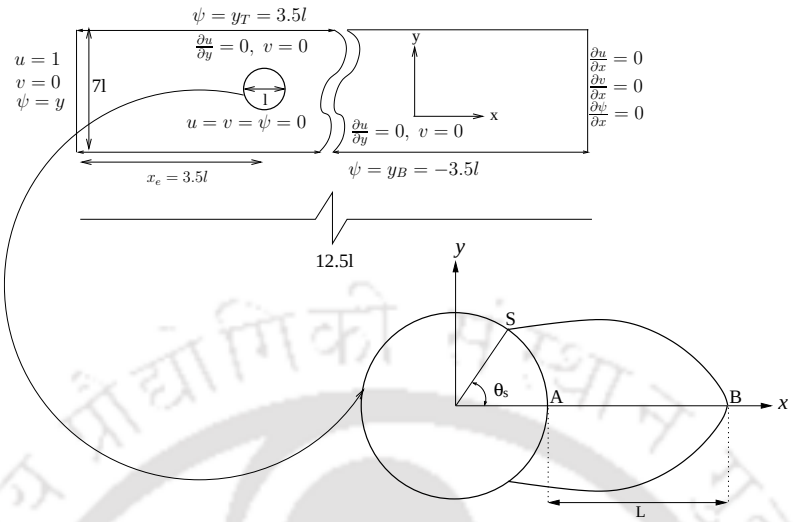

Figure 2.20: Problem statement of flow past an impulsively started circular cylinder.

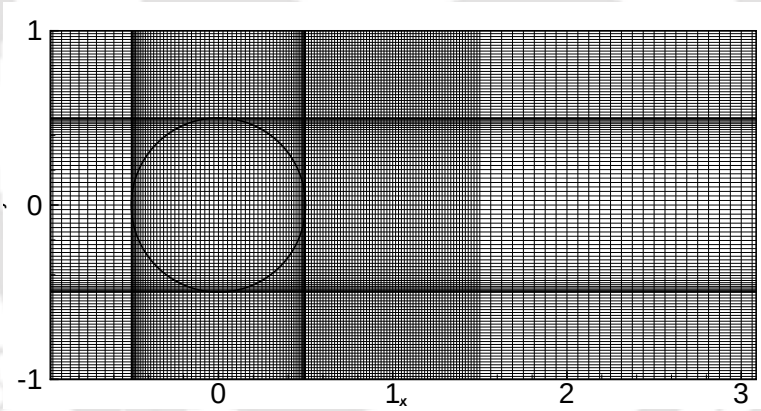

Figure 2.21: The close-up view of the grid used for flow past an impulsively started circular cylinder.

Next, we consider the steady-state flow past an impulsively started circular cylinder in a free stream. The problem setup is presented in figure 2.20. Here, Reynolds number is defined as $Re = \dfrac{u_{av} D}{\nu}$, where u_{av} is average inlet velocity, D is the cylinder diameter and ν is the kinematic viscosity of the fluid. In all our computations D was set as 1.0. Note that for the Reynolds numbers under consideration, the flow is always symmetric about the x-axis as shown in figure 2.20.

The computational domain is considered as $-3.5l \leq x \leq 9l$, $-3.5l \leq y \leq 3.5l$, where $l = D = 1$. The cylinder was placed at $(x, y) = (0, 0)$ as its center. On the surface of

the cylinder $u = v = \psi = 0$; the same conditions were imposed inside the cylinder as well during computation. At the inlet, uniform flow is considered as $u = 1$, $v = 0$ while at the outlet, Neumann boundary conditions are prescribed as $\frac{\partial u}{\partial x} = 0$, $\frac{\partial v}{\partial x} = 0$ and $\frac{\partial \psi}{\partial x} = 0$. At the top and bottom $\frac{\partial u}{\partial y} = 0$, $v = 0$ with $\psi = 3.5$ and $\psi = -3.5$ at the upper and lower boundaries respectively.

The Neumann boundary condition at the outlet is approximated as follows. At the boundary where $x = b_0$, a Taylor series expansion for ϕ at the point $x = b_0 - H_i$ about $x = b_0$ is given by

$$\phi_{b_0-i,j} = \phi(b_0 - H_i) = \phi(b_0) - H_i \left.\frac{\partial \phi}{\partial x}\right|_{b_0,j} + \frac{H_i^2}{2} \left.\frac{\partial^2 \phi}{\partial x^2}\right|_{b_0,j} - \frac{H_i^3}{6} \left.\frac{\partial^3 \phi}{\partial x^3}\right|_{b_0,j} + O(H_i^4), i = 1, 2, 3$$

Here H_1, H_2 and H_3 are the distances of the first, second and third grid points away from the boundary. Performing some simple mathematical operations on the three equations above, a third order accurate approximation of the Neumann boundary condition is obtained as

$$\left.\frac{\partial \phi}{\partial x}\right|_{b_0,j} = -\frac{A\phi(b_0 - H_1) + B\phi(b_0 - H_2) + C\phi(b_0 - H_3) - (A + B + C)\phi(b_0)}{AH_1 + BH_2 + CH_3}$$

resulting in

$$A\phi_{b_0-1,j} + B\phi_{b_0-2,j} + C\phi_{b_0-3,j} - (A + B + C)\phi_{b_0,j} = 0, \tag{2.37}$$

where $A = H_2^2 H_3^2 (H_2 - H_3)$, $B = H_3^2 H_1^2 (H_3 - H_1)$ and $C = H_1^2 H_2^2 (H_1 - H_2)$. Here ϕ stands for either u, v or ψ.

We then proceed to carry out numerical simulations for Reynolds numbers 10, 20 and 40 on grid size 301×181 where we generate the grid in such a way that the geometry of cylider passes through the grid points (see the close up of the grid around the cylinder in figure 2.21). This has been accomplished following the algorithm described in [80]. An elaborate description of the generation of the grid can be found in chapter 4.

We further compute the wake length L, which is the distance between rear end point

Table 2.11: Comaprison of wake lengths, separation angles and drag coefficients for different Reynolds numbers.

	Re	[27] (exp)	[32]	[38]	[50]	[112]	[66]	Present
	10	—	0.530	—	0.474	—	—	0.533
L	20	1.86	1.880	1.820	1.842	1.920	1.825	1.830
	40	4.38	4.690	4.480	4.490	4.510	4.420	4.250
	10	—	2.846	—	3.170	—	—	2.629
C_D	20	—	2.045	2.001	2.152	2.111	2.052	2.172
	40	—	1.522	1.498	1.499	1.574	1.534	1.590
	10	—	29.6	—	26.89	—	—	30
θ_s	20	44.4	43.7	42.9	42.96	42.79	43.50	45
	40	53.4	53.8	51.5	52.54	52.94	53.54	54

A of cylinder and the end of the separation at the point B, continuously increasing with increased Reynolds number; the separation angle θ_s, which the angle between the x-axis and the line joining the center of the cylinder and the separation point S on the cylinder (figure 2.20). These are tabulated in table 2.11 along with the drag coefficient C_D which is computed by utilizing the momentum balance along the horizontal direction. We then compared our results with established numerical as well as the famous experimental results of Coutanceau and Bouard [27]. One can clearly see from the table that our numerical results are very close to them.

In figures 2.22(a)-(d), we present the portion of the steady-state stremlines for Reynolds numbers 10, 20 and 40 along with the expereimental visualizations of Coutanceau and Bouard [27, 28] for $Re = 40.3$; here one can clearly see the closeness of our numerical simulation with the experimental visualization. One can see the development of a wake field at the rear of cylinder at $Re = 10$ in figure 2.22(a) which grows in size with increasing Reynolds numbers (figures 2.22(b)-(d)).

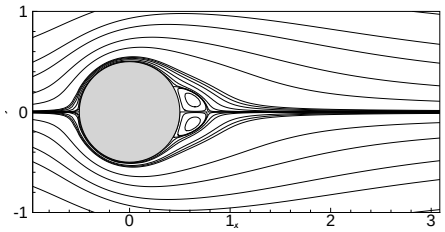

(a)

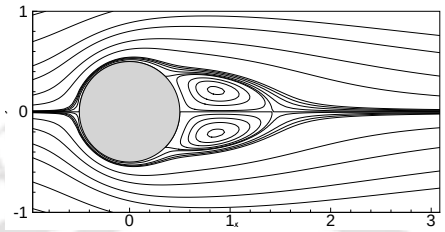

(b)

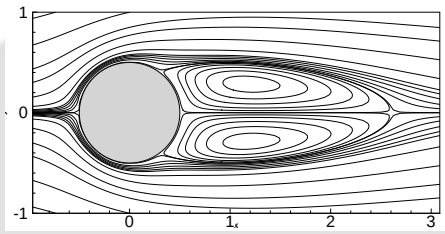

(c)

(d)

Figure 2.22: Streamlines for flow past an impulsively started cylinder (a) $Re = 10$, (b) $Re = 20$, (c) $Re = 40$ and (d) $Re = 40.3$ (experimental [27, 28]).

2.4.5 Test case 5: Flow past a Flat Plate

Next test problem is the flow past an immersed flat plate depicting external flow. The flow is difficult to compute because of the edge singularity. Two cases are considered here: the first one corresponds to the one where the plate is held normal to a uniform flow in an infinite domain and the second one where the plate is mounted on a wall with an angle of inclination. The problem configuration corresponding to both the cases are shown in

figure (2.23) along with the computational domain and the boundary conditions used. In both the cases, the Reynolds number is defined as $Re = \frac{u_{av}l}{\nu}$, where u_{av} is average inlet velocity, l is the plate height and ν is the kinematic viscosity of the fluid. In all our computations l was set as 1.0.

The dimensions of the computational domain was set as $0 \leq x \leq \chi l$ and $-2.5 \leq y \leq 2.5$ in the first case and $0 \leq y \leq 5$ in the second. The length of this domain is chosen in such a way that the flow becomes fully developed. The fluid is assumed to be flowing from left to right. In both the cases we have computed the flow for such Reynolds numbers for which experimental results are available.

Case 1: flat plate immersed in free stream

Here (see figure 2.23(a)) the boundary conditions are considered as $u = 1$, $v = 0$ at the inlet. By integrating u and v we can calculate stream function at inlet as $\psi = y$. As ψ is constant along the streamline therefore at the top and bottom wall $\psi_{top} = 2.5$ and $\psi_{bottom} = -2.5$; also $\frac{\partial u}{\partial y} = 0$, $v = 0$ thereat. On the surface of the plate, $u = v = \psi = 0$. At the outlet, where $\chi = 30$, the zero-flux boundary condition $\frac{\partial \psi}{\partial x} = \frac{\partial u}{\partial x} = \frac{\partial v}{\partial x} = 0$ is used and equation (2.4.4) has been employed to discretize them.

We have carried out computations on grid of size 301×101, where in order to generate a centro-symmetric grid with clustering near the plate in both x-and y-directions, we use the stretching function [105]:

$$x_i = \alpha \left\{ 1 + \frac{sinh(\lambda(i - B))}{sinh(\lambda B)} \right\}; 0 < \lambda \leq 1 \tag{2.38}$$

where $B = \frac{1}{2r} \ln \left[\frac{1 + \alpha(e^{\lambda} - 1)}{1 + \alpha(e^{-\lambda} - 1)} \right]$ and λ has the same role as in the other numerical examples and is set as 0.7. We have chosen α to be 0.25 such that plate can be placed at 25% of the total computational domain in the x direction. In the y-direction $\alpha = 0.5$ is used so that plate can be placed at center.

In figure 2.24, we present our computed steady-state streamlines for $Re = 10$ and 20 along with the experimental visualizations of Ingham *et al.* [59]. One can clearly see from the figures that our computed results are very close to their experimental results [59].

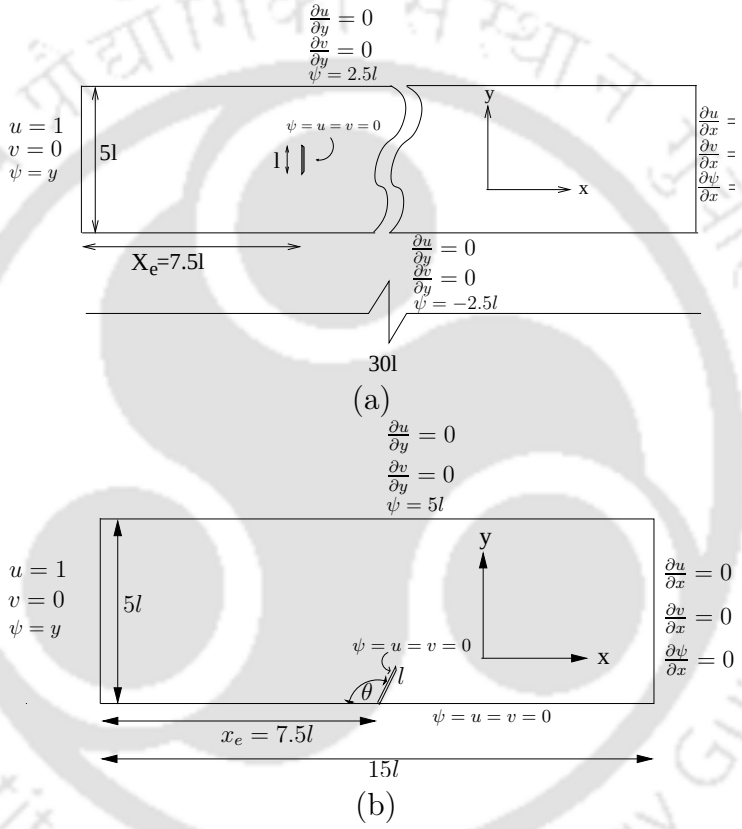

Figure 2.23: Problem statement of flow over a flat plate: (a) plate held normal to the flow and (b) plate mounted on wall with an inclination.

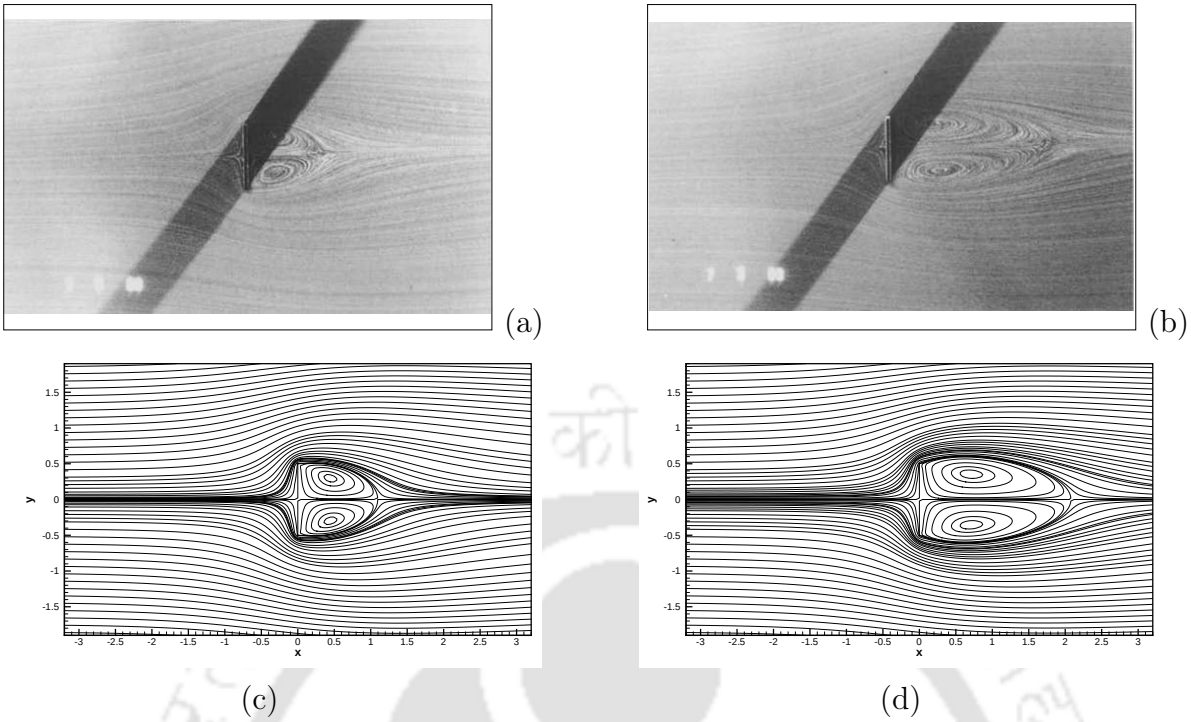

Figure 2.24: *Streamlines for the flow past a flat plate immersed in viscous fluid: (a) Experimental (Re = 10, [59]), (b) Experimental (Re = 20, [59]), (c) Numerical (Re = 10) and (d) Numerical (Re = 20.)*

Case 2: flat plate mounted on a wall with an angle of inclination

For this case, the boundary conditions are considered as $u = 1$, $v = 0$ at the inlet. By integrating u and v we can calculate stream function at inlet as $\psi = y$. As ψ is constant along the streamlines, at the top, considered to be a free surface and the wall at the bottom, it reduces to $\psi_{top} = 0$ and $\psi_{bottom} = 5$ respectively. Other boundary conditions are: $\dfrac{\partial u}{\partial y} = 0$, $v = 0$ at the top and $u = v = 0$ at the bottom wall. On the surface of the plate, $u = v = \psi = 0$. At the outlet where $\chi = 15$, outflow boundary condition $\dfrac{\partial \psi}{\partial x} = \dfrac{\partial u}{\partial x} = \dfrac{\partial v}{\partial x} = 0$ is used as in case 1.

Numerical simulations is carried out for Reynolds number 0.014 on grid size 581×81 in the computational domain $-7.5 \leq x \leq 7.5$, $0 \leq y \leq 5$. The plate was placed at at $(x, y) = (0, 0)$. Four cases are considered here: (a) $\theta = 90°$, (b) $\theta = 105°$, (c) $\theta = 120°$, (b) $\theta = 135°$.

For the cases where $\theta \neq 90°$, we generate the grid in such a way that the geometry of the inclined plate passes through the grid points. This has been accomplished in the

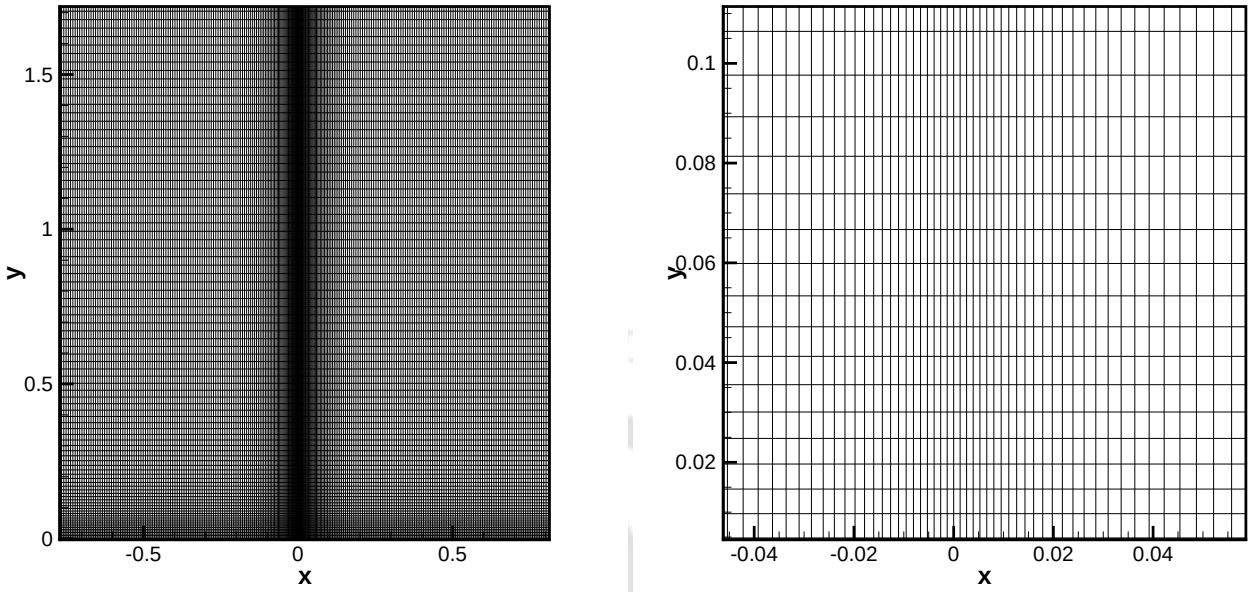

Figure 2.25: *Close-up views of the grid used for the flow past a flat plate mounted on a wall.*

following way: for the portion $-7.5 \leq x \leq -1$ a uniform grid grid spacing is used and then we use a centrosymmetric stretching for $-1 \leq x \leq 1$ using the stretching function used in test case 2 with $\lambda = 0.9$; for the remaining portion, once again a uniform grid grid spacing is used. In the y-direction for the portion $0 \leq y \leq 1$ we have used one directional stretching by employing the same stretching function used in test case 1 with $\lambda = 0.9$. In the subdomain $-1 \leq x \leq 1$, $0 \leq y \leq 1$, once the grid has been generated, the vertical length is further scaled by multiplying it by a factor $\tan(180^\circ - \theta)$; this accommodates the plate geometry to pass through the grid points. The remaining portion in the y-direction has a uniform grid spacing. A close-up view of the grid near the plate is shown in figure 2.25.

In figure 2.26, we present our computed steady-state streamlines along with the experimental visualizations of Taneda for $\theta = 90^\circ$ and 105°. For both the cases, the results were extremely close to the experimental reults of Taneda [36, 155]. The symmetry of the vortices across either side of the wall vanishes when the plate is not inclined at right angle to the wall. We also present the steady-state streamlines for this Re for $\theta = 120^\circ$ and 135° in figures 2.27(a)-(b). As the angle of inclination is raised to 135°, the vortex on the

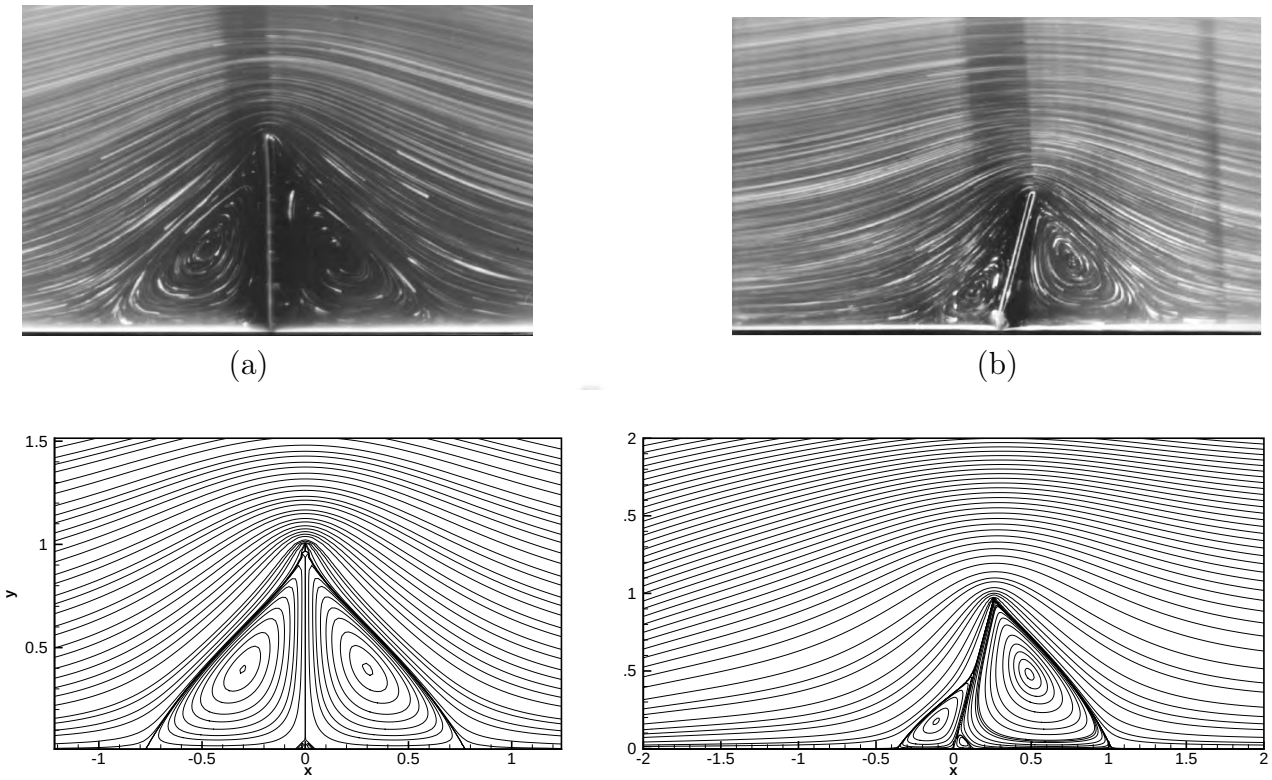

Figure 2.26: *Steady flow past a flat plate mounted on wall for* $Re = 0.014$ *with angle of incidence* θ *(a) Experimental* ($\theta = 90^o$, *Taneda [36, 155]), (b) Experimental* ($\theta = 105^o$, *Taneda [155]), (c) Numerical* ($\theta = 90^o$) *and (d) Numerical* ($\theta = 105^o$).

rear side of the plate disappears. For the same inclination of the plate, we further present the steady-state streamlines for $Re = 10$ in figures 2.27(c)-(d). As expected, the size and strength of the vortices increases with Re. Also, the vortices are formed in the zone past the plate. Overall, with increase in angle of inclination, the size of the vortices was seen to decrease. To the best of our knowledge, this is perhaps the first time that numerical simulation has been carried out for this flow configuration (2.23(b)) on a finite difference set-up over a Cartesian grid. Also, this is an example of flow computation in the finite difference set up where the boundary of an immersed body is not aligned with the grid lines, thus exemplifying the robustness of the proposed scheme.

2.5 Application to Heat Transfer Problems

This section is specifically devoted to the steady state-computation of heat transfer problems through the proposed scheme. We have simulated two cases, viz, natural convection

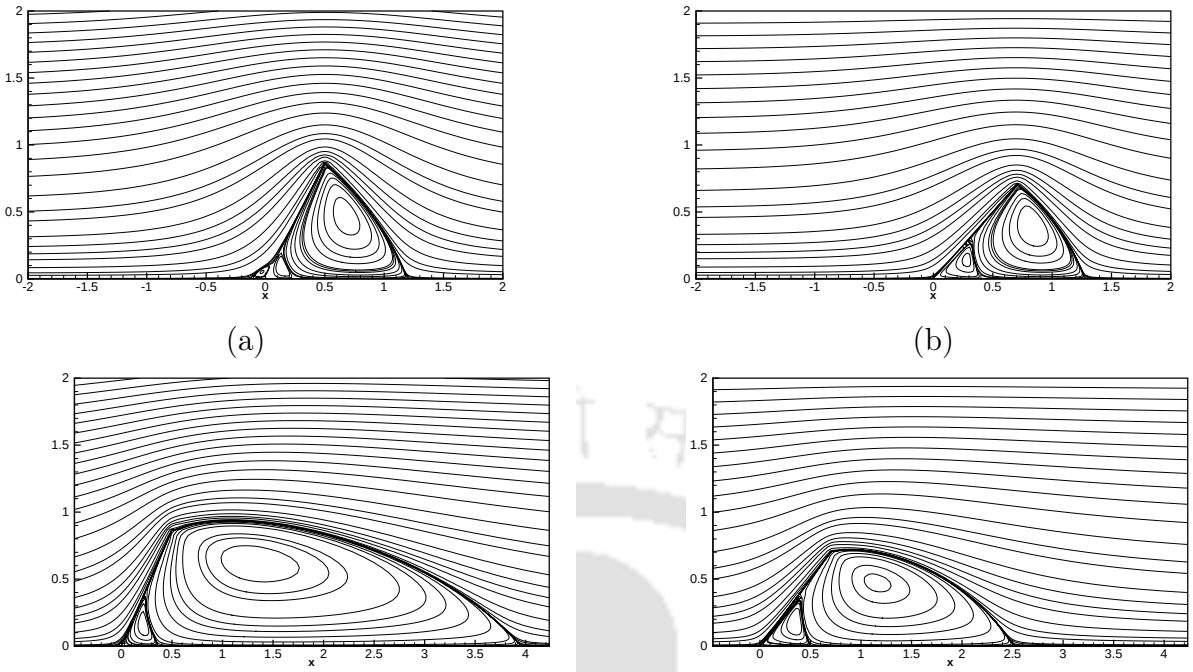

Figure 2.27: *Steady flow past a flat plate mounted on wall with angle of incidence: Top row: $Re = 0.014$ (a) $\theta = 120^o$, (b) $\theta = 135^o$ and Bottom row: $Re = 10$ (c) $\theta = 120^o$ and (d) $\theta = 135^o$.*

around heated solid bodies in a square cavity and conjugate heat transfer in a suddenly expanding channel.

2.5.1 Natural Convection Around a Heated Solid Body in a Square Cavity

Natural convection in an enclosure has a wide range of engineering applications, both in industry and environment. Its presence can be seen in heat exchangers, nuclear reactors, heat sinks, the motion of Earth's mantle, and stratified atmospheric boundary layers etc. However, in engineering applications, the geometries are more complicated than a simple enclosure filled with a convective fluid. Therefore, studies on the geometric configuration with bodies inside the enclosure have gathered much attention among scientists lately[2]. After invoking the Boussinesq approximation, the governing equations for such problems are given by:

[2]This part has been published in [34]

Governing Equation

$$\frac{\partial^4\psi}{\partial x^4}+2\frac{\partial^4\psi}{\partial x^2\partial y^2}+\frac{\partial^4\psi}{\partial y^4}=\frac{1}{Pr}\left[\frac{\partial\psi}{\partial y}\left(\frac{\partial^3\psi}{\partial x^3}+\frac{\partial^3\psi}{\partial x\partial y^2}\right)-\frac{\partial\psi}{\partial x}\left(\frac{\partial^3\psi}{\partial x^2\partial y}+\frac{\partial^3\psi}{\partial y^3}\right)\right]+Ra\frac{\partial T}{\partial x} \tag{2.39}$$

$$u\frac{\partial T}{\partial x}+v\frac{\partial T}{\partial y}=\nabla^2 T \tag{2.40}$$

where Ra is the Rayleigh number, Pr is the Prandtl number and the variable T stands for the non-dimensional temperature. Rayleigh number, Ra and Prandtl number are defined as

$$Ra=\frac{g\beta\Delta TL^3}{\nu\alpha} \quad \text{and} \quad Pr=\frac{\nu}{\alpha}$$

Where g, β, L, ν and α are gravitational acceleration, thermal expansion coefficient, characteristic length, kinematic viscosity and thermal diffusivity. Here L is considered as 1.

For Heat transfer problems Nusselt number is an important parameter that identifies heat transfer rate all over the cavity. The local Nusselt number in the horizontal direction at any point in the cavity is defined as

$$Q(x,y)=uT-\frac{\partial T}{\partial x}$$

Nusselt number along the x-axis, through any line parallel to the $y-$ axis, is calculated as

$$Nu_x=\int_0^1 Q(x,y)\,dy \tag{2.41}$$

Finally, by integrating Nu_x along the x-direction, the average Nusselt number is given by

$$\overline{Nu}=\int_0^1 Nu_x\,dx \tag{2.42}$$

In order to perform integration for equations (2.5.1) and (2.5.1), we employ Simpson's one-third rule on nonuniform grids.

Table 2.12: Comparison of Nusselt numbers

A Regular Cavity		
References	Nu_{hot}	Nu_{max}
De Vahl Devis [31]	16.32	8.82
Le Quere [98]	16.38	8.82
Kalita et al. [68]	16.42	8.76
Yu and Tian [169]	16.36	8.24
present	16.34	8.77
Circlular cylinder at the center		
	Nu_{surf}	Nu_{encl}
Kim et al. [81]	4.46	14.17
Present	4.6	14.83
Diamond cylinder at the center		
	Nu_{cold}	Nu_{surf}
De and Dalal [30] ($a = 0.2$)	13.21	-6.67
Present ($a = 2\sqrt{2}$)	10.26	-6.93

Three cases are being considered here, the first of which corresponds to natural convection in a differentially heated cavity, and the next two to heated bodies in a square cavity. The problem configurations corresponding to all three cases along with the boundary conditions and grids being used are shown in the figure 2.28. Generally, the sides of the enclosures are either insulated ($\frac{\partial T}{\partial n} = 0$, n being the normal direction) or maintained at certain temperatures. At the boundaries, T_h and T_c represent hot and cold temperatures, which has been assumed to be 1 and 0 in the present computation. As all the walls are stationary, $u = v = 0$ and the ψ value is set as zero thereat in all the three cases. The dimensions of the computational domain were set as $-0.5 \leq x, y \leq 0.5$ in all the cases. In figure 2.29, we present streamlines and isotherms for $Ra = 10^6$ and $Pr = 0.71$ computed on a grid of size 321×321. In table 2.12 we compare various Nusselt numbers with some numerical results available in the existing literature; here Nu_{hot}, Nu_{surf}, Nu_{encl}, Nu_{cold} and Nu_{max} stand for Nusselt numbers along the hot wall, the enclosure, the surface of the heated object, the cold wall and the maximum Nusselt number respectively. As one can see from the figures and tables, our results are very close to the other results except for the ones at the cold walls with De and Dalal [30]. This discrepancy may have stemmed out from the fact that they used a heated object of a slightly different dimension.

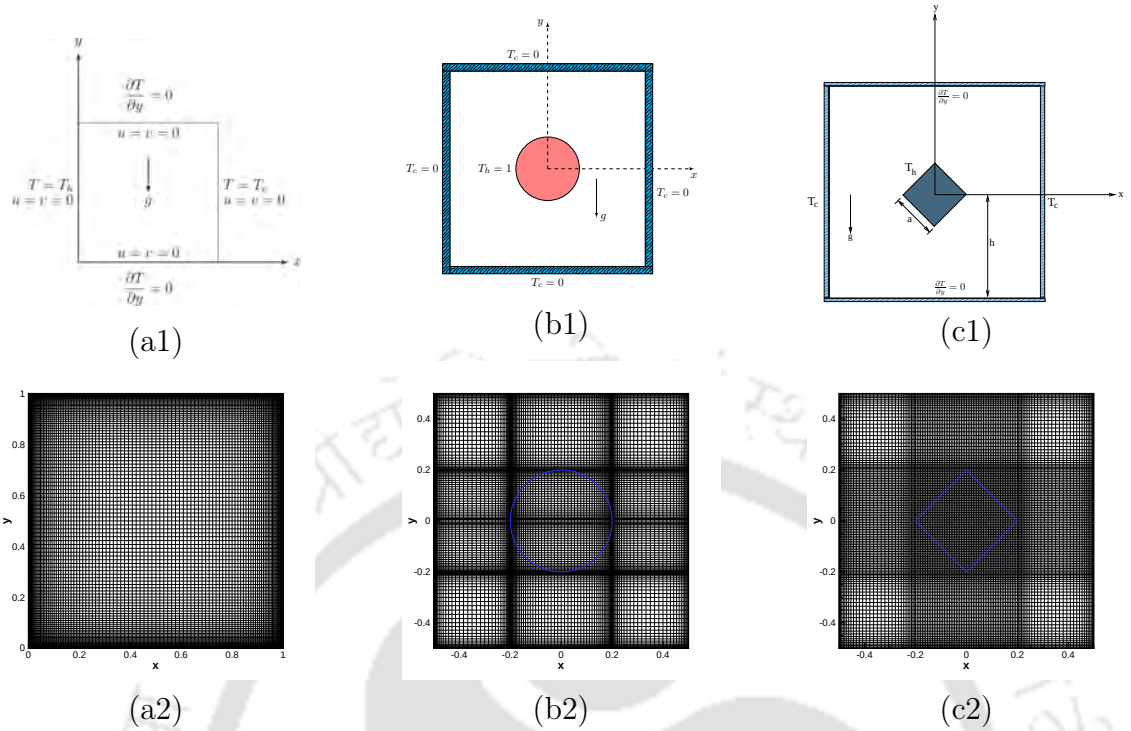

Figure 2.28: Schematic and grid used for natural convection in (a1, a2) a regular cavity, (b1, b2) cavity with a heated circular cylinder at the center, and (c1, c2) cavity with a heated diamond cylinder at the center.

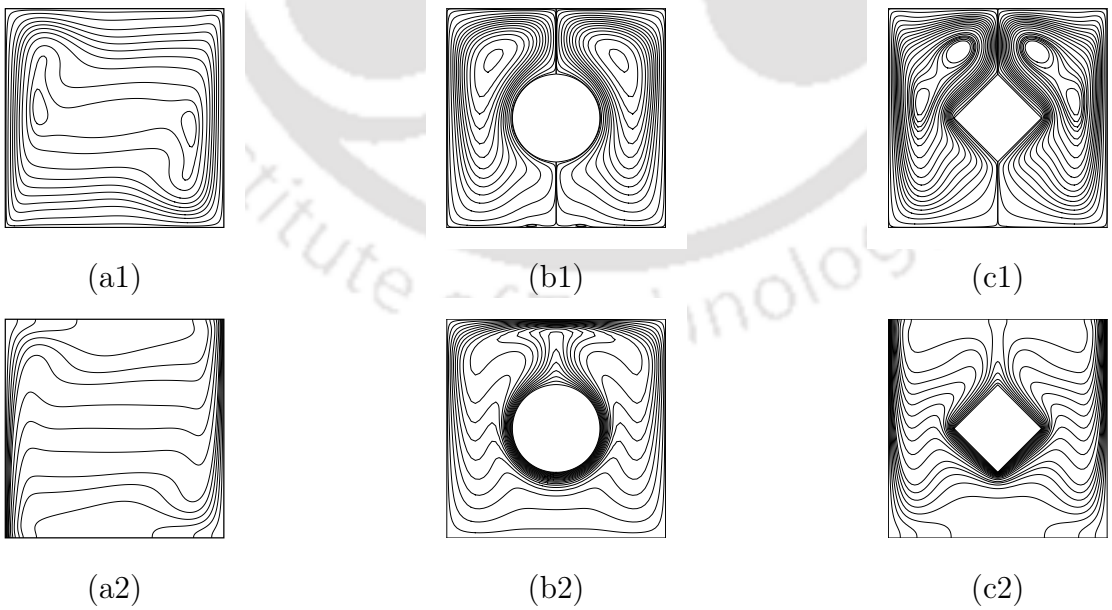

Figure 2.29: Streamfunction and Isotherms in differentially heated cavity in three different cases.

2.5.2 Conjugate Heat Transfer in a Suddenly Expanding Channel

Here, we have simulated conjugate heat transfer[3] and fluid flow in the backward facing step problem discussed earlier (see section 2.4.3), where at the bottom of the channel, a solid block having twice the height of the channel is attached. The flow configuration along with the boundary conditions can be seen in figure 2.30, while the grid used for computation along with close-up view is shown in 2.31. The governing equations consist of the pure streamfunction equation (2.12) and the non-dimensional steady state energy equations in the fluid and solid regions given by

$$u\frac{\partial T_f}{\partial x} + v\frac{\partial T_f}{\partial y} = \frac{1}{Re\,Pr}\Big(\frac{\partial^2 T_f}{\partial x^2} + \frac{\partial^2 T_f}{\partial y^2}\Big), \tag{2.43}$$

and

$$\frac{\partial^2 T_s}{\partial x^2} + \frac{\partial^2 T_s}{\partial y^2} = 0 \tag{2.44}$$

respectively, where the subscripts f and s denote the fluid and solid regions respectively and Pr is the Prandtl number.

Boundary conditions for ψ, u and v are the same as backward facing step in fluid part and in solid part $\psi = u = v = 0$. The temperature at the interface boundary is given by $\left(\frac{\partial T_s}{\partial y}\right) = k\left(\frac{\partial T_f}{\partial y}\right)$ and $T_s = T_f$. Here $k = k_f/k_s$, with k_f and k_s being the thermal conductivities of the fluid and the solid respectively At the bottom wall of solid: $T = 1$; boundary condition on the remaining walls is $\frac{\partial T}{\partial n} = 0$, where n is normal direction.

Numerical simulation is carried out for the combination $Re = 800$, $Pr = 0.71$ and $k = 10$ on a grid of size 301×201. In figure 2.32, we have presented our computed streamlines and isotherm contours, while in figure 2.33, we compare our computed temperature and Nusselt number distributions along the interface with the benchmark results of Ramšak [123]; once again one can see extremely close comparison between the result.

Note that while (2.39) was discretized using a slight readjustment of the proposed scheme for the extra term on the right hand side, equations (2.40)-(2.5.2) were discretized employing the high order compact scheme on nonuniform grids by Kalita *et al.* [70]. The

[3]Part of this study is published in [35]

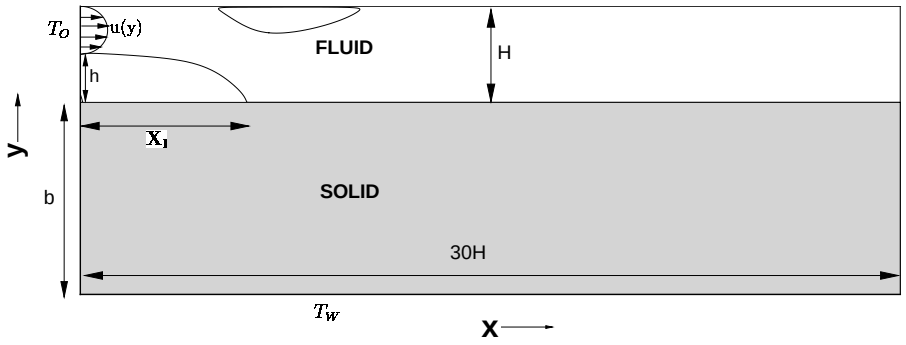

Figure 2.30: Configuration of the conjugate heat transfer in backward facing step.

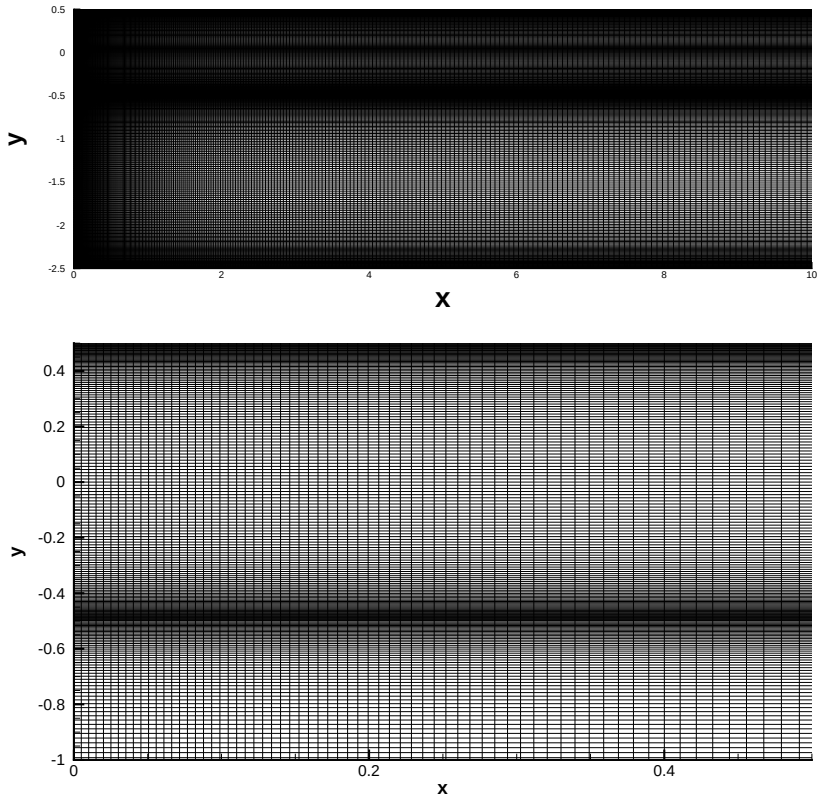

Figure 2.31: Typical grid of size 301×201 used for the conjugate heat transfer in backward facing step and close-up view of the grid.

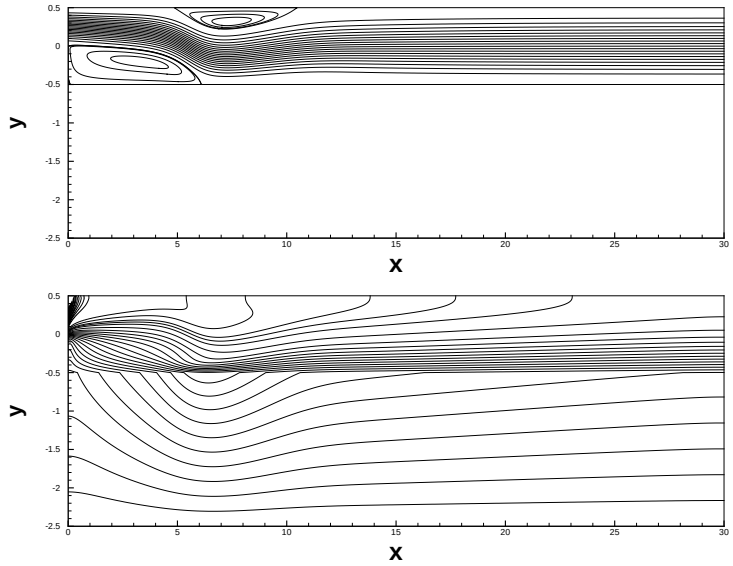

Figure 2.32: Streamlines and Isotherm contour for $Re = 800$,$Pr = 0.71$ and $k = 10$.

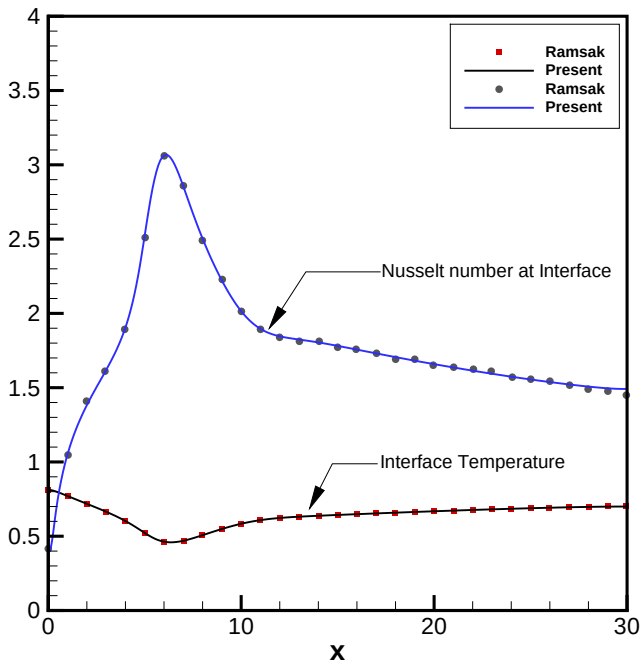

Figure 2.33: Comparison of present data (interface temperature and Nusselt number) with that of Ramšak [123]

inner-outer process described in section 2.3 was repeated till the criteria for steady-state for ψ along with T was met, viz., when additionally, the maximum T-error also reached a value 10^{-13}.

2.6 Conclusions

In this chapter, we have developed a second order compact finite difference scheme for the biharmonic form of the steady-state N–S equations on nonuniform grids without transformation. In contrast to the earlier finite difference schemes on rectangular Cartesian grids for N–S equations, which could handle only simple boundaries on rectangular settings, the proposed scheme was seen to accommodate flow past bluff bodies with curved boundary as well. We have applied our scheme to one problem having analytical solution and numerous fluid flow and heat transfer problems having different complexities. In the process, we also establish the theoretical rate of convergence of our numerical scheme. The scheme was seen to handle both Dirichlet and Neumann boundary conditions with equal ease. The robustness of the scheme was demonstrated by its remarkable ability of handling extreme clustering, thus enabling the capture of smaller scales up to post quaternary level of vortices in the lid-driven cavity flow. These new results are tabulated and graphically presented up to the smallest scale being captured by our computation. While the flow past an inclined flat plate mounted on a wall demonstrated one of the rare examples of flow computation in the finite difference set up where the boundary of an immersed body is not aligned with the grid lines, for the cases involving bodies of circular shapes, a curved boundary was tackled without the need of inserting an immersed interface. For all the cases considered for flow past bluff bodies in the current study, our computed streamlines and flow attributes were extremely close to the experimental results of well established studies. For the accomplishments listed above, we consider the proposed scheme to be an important addition to the already existing numerical schemes for computing incompressible viscous flows by the biharmonic form of the N–S equations. A transient formulation of the proposed scheme with a slight variation of the space discretization will be presented in the next chapter.

CHAPTER 3

AN EFFICIENT ψ-V SCHEME FOR 2D LAMINAR FLOW PAST BLUFF BODIES ON COMPACT NONUNIFORM GRIDS.

3.1 Introduction

The study of flow past bluff bodies is an integral part of many engineering applications, particularly in the naval field. A bluff body may be defined as a body, which, owing to its shape has separated flow over a large part of its surface [26]. Its study encompasses the hydrodynamics of floating and fixed structures which generate a substantial quantity of vortical structures and separation regions. Bluff body flows are often very complex and quite difficult to predict; it is generally associated with high Reynolds numbers. Because of the generation of disturbance through instability mechanisms, turbulence and three-dimensionality could be observed in such flows [103, 107, 130]. Besides, generation and shedding of vortex structures are highly prevalent in such flows. In the current study, we propose a spatially second order compact scheme for the biharmonic form of the Navier-Stokes (N-S) equations

$$\frac{\partial^4\psi}{\partial x^4} + 2\frac{\partial^4\psi}{\partial x^2\partial y^2} + \frac{\partial^4\psi}{\partial y^4} = Re\left[v\nabla^2 u - u\nabla^2 v\right], \tag{3.1}$$

specifically designed to tackle flow past bluff bodies of different shapes. Opposed to the scheme developed in chapter 2, the spatial accuracy of this scheme is independent of the grid spacing. Then we propose a second order accurate discretization of the time derivative present in the transient version of (3.1) is given by

$$\frac{\partial^4\psi}{\partial x^4} + 2\frac{\partial^4\psi}{\partial x^2\partial y^2} + \frac{\partial^4\psi}{\partial y^4} - Re\left[v\nabla^2 u - u\nabla^2 v\right] = Re\left[\frac{\partial}{\partial t}(\nabla^2\psi)\right], \tag{3.2}$$

eventually leading to a compact finite difference scheme which is uniformly second order accurate in both space and time.

The N-S equations are the mainstay of the approaches of studying fluid dynamics: from both theoretical and computational perspectives. In the current study, we are concerned with the laminar incompressible viscous flows pertaining to bluff bodies, where the flow is governed by the N-S equations. The details of the governing equations have already been introduced in chapter 2.

Several numerical schemes exist for solving the steady-state counterpart of (3.2). However, most of the schemes [137] that have been developed so far for numerically solving (3.2) involved transforming the governing equations from physical plane to the computational plane; the transformation mappings were inherently chosen to facilitate the shape of the bluff body [137, 138]. Resorting to such practice are generally associated with certain disadvantages as listed in Chapter 2. Moreover, the grid distribution in the computational domain is restricted by the choice of the transformation mapping. The proposed scheme is probably the first one developed for computing transient flows past bluff bodies on nonuniform Cartesian grids fitted to the surface of the bluff-bodies without the need of using transformation. Note that most of the earlier schemes that have been developed for flow past bluff bodies on the finite difference or finite volume framework has adopted the immersed interface approach [56, 84] that invariably results in some extra computations arising out of interpolation. This is because of the inability of the frequently used finite difference schemes to handle boundaries not aligned to the grid lines of the finite difference mesh. The proposed scheme, which is second order accurate in both space and time, has the ability to handle curved boundaries on Cartesian grids without roping in any immersed interface in the process.

Before applying to problems involving flow past bluff bodies, the proposed scheme is validated by applying it on a problem having analytical solution and an internal fluid

flow problem. Next, it is used to solve problems of past bluff bodies immersed in uniform flow. The bluff bodies considered are: a flat plate placed normal to the incoming flow, an impulsively started circular cylinder and a square cylinder inclined at 45° angle to the direction of the free stream velocity. All the test cases are chosen in such a way that apart from posing challenges of varied computational complexity both in terms of the shape of the bluff bodies as well as the fluid flow structures, experimental and benchmark numerical results are available for comparison purpose. For all the cases considered in our study, our computed solutions are found to be extremely close to the available experimental and numerical results.

The chapter is organized into five sections. In section 2, we document the development of the numerical scheme for the nine point transient streamfunction-velocity formulation on nonuniform grid. In section 3, we describe the solution procedure of algebraic systems associated with proposed scheme. In section 4, we present the detailed results of our computation and finally we summarize our achievements in section 5 containing the conclusions.

3.2 The numerical scheme

In our previous chapter, we had developed a transformation-free compact scheme on nonuniform Cartesian grids for (3.1). The space discretization of this equation was carried out by considering a rectangular domain $[a_1, a_2] \times [b_1, b_2]$ in the xy-plane, where the interval $[a_1, a_2]$ is divided into m sub-intervals, not necessarily of equal lengths, by the points $a_1 = x_0, x_1, x_2, x_3, \ldots, x_{m-1}, x_m = a_2$ and similarly $[b_1, b_2]$ into n subintervals by the points $b_1 = y_0, y_1, y_2, y_3, \ldots, y_{n-1}, y_n = b_2$.

In the x-direction, the forward and backward step-lengths x_f, x_b at the $(i, j)^{\text{th}}$ point are defined as (see the n^{th} time level of figure 3.1) of the problem domain as,

$$x_f = (x_{i+1,j} - x_{i,j})$$
$$x_b = (x_{i,j} - x_{i-1,j}).$$

Likewise, in the y-direction,

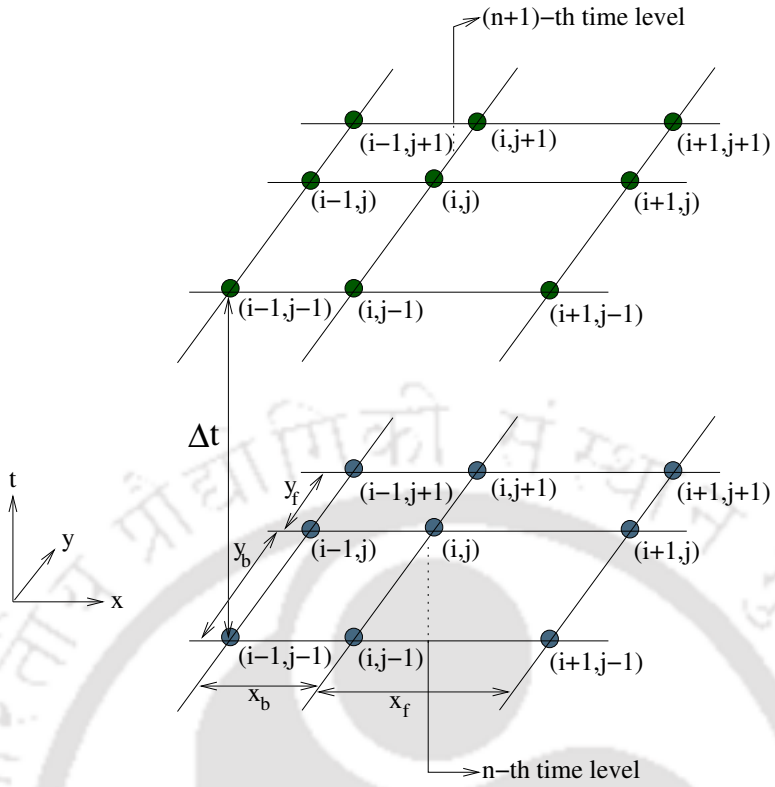

Figure 3.1: The unsteady stencil used in the present computation.

$$y_f = (y_{i,j+1} - y_{i,j})$$
$$y_b = (y_{i,j} - y_{i,j-1}).$$

The truncation error of the previously developed scheme in chapter 2 for the steady-state N-S equations was of order ≤ 2 on nonuniform and exactly two on uniform grids. In the current study, we endeavor to develop a compact scheme for the unsteady N-S equations which is uniformly second order accurate both in uniform and nonuniform spatial grids[1]. In order to achieve this, consider the Taylor series expansions of $\psi_{i+1,j}$ and $\psi_{i-1,j}$ about the $(i,j)^{\text{th}}$ point

$$\psi_{i+1,j} = \psi_{i,j} + x_f \frac{\partial \psi}{\partial x} + \frac{x_f^2}{2}\frac{\partial^2 \psi}{\partial x^2} + \frac{x_f^3}{6}\frac{\partial^3 \psi}{\partial x^3} + \frac{x_f^4}{24}\frac{\partial^4 \psi}{\partial x^4} + O(x_f^5), \tag{3.3}$$

$$\psi_{i-1,j} = \psi_{i,j} - x_b \frac{\partial \psi}{\partial x} + \frac{x_b^2}{2}\frac{\partial^2 \psi}{\partial x^2} - \frac{x_b^3}{6}\frac{\partial^3 \psi}{\partial x^3} + \frac{x_b^4}{24}\frac{\partial^4 \psi}{\partial x^4} + O(x_b^5). \tag{3.4}$$

[1]This part has been published in [94]

From equations (3.3) and (3.4), we have

$$\frac{1}{x_f^5}\psi_{i+1,j}+\frac{1}{x_b^5}\psi_{i-1,j}=\left(\frac{1}{x_f^5}+\frac{1}{x_b^5}\right)\psi_{i,j}+\left(\frac{1}{x_f^4}-\frac{1}{x_b^4}\right)\frac{\partial\psi}{\partial x}+\frac{1}{2}\left(\frac{1}{x_f^3}+\frac{1}{x_b^3}\right)\frac{\partial^2\psi}{\partial x^2}$$
$$+\frac{1}{6}\left(\frac{1}{x_f^2}-\frac{1}{x_b^2}\right)\frac{\partial^3\psi}{\partial x^3}+\left(\frac{x_f+x_b}{24x_fx_b}\right)\frac{\partial^4\psi}{\partial x^4}+O(x_f+x_b)$$

$$\frac{1}{x_f^5}\psi_{i+1,j}+\frac{1}{x_b^5}\psi_{i-1,j}-\left(\frac{1}{x_f^5}+\frac{1}{x_b^5}\right)\psi_{i,j}=\left(\frac{x_f^4-x_b^4}{x_f^4x_b^4}\right)v+\frac{1}{2}\left(\frac{x_f^3+x_b^3}{x_f^3x_b^3}\right)\left[-\frac{\partial v}{\partial x}\right]$$
$$+\frac{1}{6}\left(\frac{x_f^2-x_b^2}{x_f^2x_b^2}\right)\left[\frac{\partial^2 v}{\partial x^2}\right]+\frac{h}{12x_fx_b}\frac{\partial^4\psi}{\partial x^4}+O(x_f+x_b)$$

$$\frac{x_fx_b}{2h}\left[\frac{1}{x_f^5}\psi_{i+1,j}+\frac{1}{x_b^5}\psi_{i-1,j}-\left(\frac{1}{x_f^5}+\frac{1}{x_b^5}\right)\psi_{i,j}\right]$$
$$=\frac{(x_f^2+x_b^2)(x_f-x_b)}{x_f^3x_b^3}v-\frac{x_f^2+x_b^2-x_fx_b}{2x_f^2x_b^2}\left[\delta_x v-\frac{1}{2}(x_f-x_b)\delta_x^2 v-\frac{x_fx_b}{6}\frac{\partial^3 v}{\partial x^3}\right]$$
$$+\frac{x_f-x_b}{6x_fx_b}\left[\delta_x^2 v-\frac{(x_f-x_b)}{3}\frac{\partial^3 v}{\partial x^3}\right]+\frac{1}{24}\frac{\partial^4\psi}{\partial x^4}+O(x_fx_b)$$
$$=\frac{(x_f^2+x_b^2)(x_f-x_b)}{x_f^3x_b^3}v-\frac{x_f^2+x_b^2-x_fx_b}{2x_f^2x_b^2}\delta_x v+\frac{(3x_f^2+3x_b^2-x_fx_b)(x_f-x_b)}{12x_f^2x_b^2}\delta_x^2 v$$
$$-\frac{2x_f^2+2x_b^2-x_fx_b}{72x_fx_b}\frac{\partial^4\psi}{\partial x^4}+O(x_fx_b),$$

which, after some simplifications yields the approximation of the fourth order partial derivative of ψ as

$$\frac{\partial^4\psi}{\partial x^4}=\frac{36x_f^2x_b^2}{h(2x_f^2+2x_b^2-x_fx_b)}\left[-\frac{1}{x_f^5}\psi_{i+1,j}-\frac{1}{x_b^5}\psi_{i-1,j}+\left(\frac{1}{x_f^5}+\frac{1}{x_b^5}\right)\psi_{i,j}\right]$$
$$+\frac{6(3x_f^2+3x_b^2-x_fx_b)(x_f-x_b)}{x_fx_b(2x_f^2+2x_b^2-x_fx_b)}\delta_x^2 v-\frac{36(x_f^2+x_b^2-x_fx_b)}{x_fx_b(2x_f^2+2x_b^2-x_fx_b)}\delta_x v \qquad (3.5)$$
$$+\frac{72(x_f^2+x_b^2)(x_f-x_b)}{x_f^2x_b^2(2x_f^2+2x_b^2-x_fx_b)}v+O\left(\frac{x_f^2x_b^2}{(2x_f^2+2x_b^2-x_fx_b)}\right).$$

Likewise,

$$\begin{aligned}\frac{\partial^4\psi}{\partial y^4} =& \frac{36y_f^2y_b^2}{k(2y_f^2+2y_b^2-y_fy_b)}\left[-\frac{1}{y_f^5}\psi_{i,j+1}-\frac{1}{y_b^5}\psi_{i,j-1}+\left(\frac{1}{y_f^5}+\frac{1}{y_b^5}\right)\psi_{i,j}\right]x \\ &-\frac{6(3y_f^2+3y_b^2-y_fy_b)(y_f-y_b)}{y_fy_b(2y_f^2+2y_b^2-y_fx_b)}\delta_y^2u+\frac{36(y_f^2+y_b^2-y_fy_b)}{y_fy_b(2y_f^2+2y_b^2-y_fy_b)}\delta_yu \\ &-\frac{72(y_f^2+y_b^2)(y_f-y_b)}{y_f^2y_b^2(2y_f^2+2y_b^2-y_fy_b)}u+O\left(\frac{y_f^2y_b^2}{(2y_f^2+2y_b^2-y_fy_b)}\right).\end{aligned} \tag{3.6}$$

Defining the fourth order operators in the x- and y-directions as

$$\delta_x^4\psi=\frac{36x_f^2x_b^2}{h(2x_f^2+2x_b^2-x_fx_b)}\left[-\frac{1}{x_f^5}\psi_{i+1,j}-\frac{1}{x_b^5}\psi_{i-1,j}+\left(\frac{1}{x_f^5}+\frac{1}{x_b^5}\right)\psi_{i,j}\right], \tag{3.7}$$

and

$$\delta_y^4\psi=\frac{36y_f^2y_b^2}{k(2y_f^2+2y_b^2-y_fy_b)}\left[-\frac{1}{y_f^5}\psi_{i,j+1}-\frac{1}{y_b^5}\psi_{i,j-1}+\left(\frac{1}{y_f^5}+\frac{1}{y_b^5}\right)\psi_{i,j}\right], \tag{3.8}$$

equations (3.5) and (3.6) can be recast as,

$$\begin{aligned}\frac{\partial^4\psi}{\partial x^4} =& \delta_x^4\psi+\frac{6(3x_f^2+3x_b^2-x_fx_b)(x_f-x_b)}{x_fx_b(2x_f^2+2x_b^2-x_fx_b)}\delta_x^2v-\frac{36(x_f^2+x_b^2-x_fx_b)}{x_fx_b(2x_f^2+2x_b^2-x_fx_b)}\delta_xv \\ &+\frac{72(x_f^2+x_b^2)(x_f-x_b)}{x_f^2x_b^2(2x_f^2+2x_b^2-x_fx_b)}v+O\left(\frac{x_f^2x_b^2}{(2x_f^2+2x_b^2-x_fx_b)}\right),\end{aligned} \tag{3.9}$$

and

$$\begin{aligned}\frac{\partial^4\psi}{\partial y^4} =& \delta_y^4\psi-\frac{6(3y_f^2+3y_b^2-y_fy_b)(y_f-y_b)}{y_fy_b(2y_f^2+2y_b^2-y_fx_b)}\delta_y^2u+\frac{36(y_f^2+y_b^2-y_fy_b)}{y_fy_b(2y_f^2+2y_b^2-y_fy_b)}\delta_yu \\ &-\frac{72(y_f^2+y_b^2)(y_f-y_b)}{y_f^2y_b^2(2y_f^2+2y_b^2-y_fy_b)}u+O\left(\frac{y_f^2y_b^2}{(2y_f^2+2y_b^2-y_fy_b)}\right).\end{aligned} \tag{3.10}$$

$$\frac{\partial^3\psi}{\partial x^3}=-\delta_x^2v-\frac{(x_f-x_b)}{3}\frac{\partial^4\psi}{\partial x^4}+O\left(x_f^2+x_b^2-x_fx_b\right) \tag{3.11}$$

Likewise in $y-$direction,

$$\frac{\partial^3\psi}{\partial y^3}=\delta_y^2u-\frac{(y_f-y_b)}{3}\frac{\partial^4\psi}{\partial y^4}+O\left(y_f^2+y_b^2-y_fy_b\right), \tag{3.12}$$

The mixed derivative can be approximated as

$$\frac{\partial^4\psi}{\partial x^2\partial y^2}=\delta_x^2\delta_y^2\psi+\left(\frac{x_f-x_b}{3}\right)\delta_x^2\delta_y^2v-\left(\frac{y_f-y_b}{3}\right)\delta_x^2\delta_y^2u+O\left((x_f-x_b)(y_f-y_b)\right) \tag{3.13}$$

The third order mix derivative terms can be derived in a similar way,

$$\frac{\partial^3\psi}{\partial x\partial y^2} = -\delta_y^2 v - \left(\frac{y_f - y_b}{3}\right)\delta_x\delta_y^2 u + O\left((y_f^2 + y_b^2 - y_f y_b)\right) \tag{3.14}$$

and

$$\frac{\partial^3\psi}{\partial x^2\partial y} = \delta_x^2 u + \left(\frac{x_f - x_b}{3}\right)\delta_x^2\delta_y v + O\left((x_f^2 + x_b^2 - x_f x_b)\right). \tag{3.15}$$

Substitution of equations (3.9), (3.10),(3.11), (3.12), (3.13), (3.14) and (3.15) into equation (3.2) and a forward time approximation of the time-derivative yields

$$\begin{aligned}
Re\delta_t^+\left(\nabla^2\psi\right) =\ & p\delta_x^4\psi + 2\delta_x^2\delta_y^2\psi + q\delta_y^4\psi - Re\left\{v\left(\delta_x^2 u + \delta_y^2 u\right) - u\left(\delta_x^2 v + \delta_y^2 v\right)\right\} \\
& + \frac{6p(3x_f^2 + 3x_b^2 - x_f x_b)(x_f - x_b)}{x_f x_b(2x_f^2 + 2x_b^2 - x_f x_b)}\delta_x^2 v - \frac{36p(x_f^2 + x_b^2 - x_f x_b)}{x_f x_b(2x_f^2 + 2x_b^2 - x_f x_b)}\delta_x v \\
& + \frac{72p(x_f^2 + x_b^2)(x_f - x_b)}{x_f^2 x_b^2(2x_f^2 + 2x_b^2 - x_f x_b)}v - \frac{6q(3y_f^2 + 3y_b^2 - y_f y_b)(y_f - y_b)}{y_f y_b(2y_f^2 + 2y_b^2 - y_f y_b)}\delta_y^2 u \\
& + \frac{36q(y_f^2 + y_b^2 - y_f y_b)}{y_f y_b(2y_f^2 + 2y_b^2 - y_f y_b)}\delta_y u - \frac{72q(y_f^2 + y_b^2)(y_f - y_b)}{y_f^2 y_b^2(2y_f^2 + 2y_b^2 - y_f y_b)}u \\
& - Re.v\frac{(x_f - x_b)}{3}\delta_x^2\delta_y v + Re.u\frac{(y_f - y_b)}{3}\delta_x\delta_y^2 u + \frac{2(x_f - x_b)}{3}\delta_x^2\delta_y^2 v - \frac{2(y_f - y_b)}{3}\delta_x^2\delta_y^2 u \\
& + O\left(\frac{x_f^2 x_b^2}{(2x_f^2 + 2x_b^2 - x_f x_b)}, (x_f - x_b)(y_f - y_b), \frac{y_f^2 y_b^2}{(2y_f^2 + 2y_b^2 - y_f y_b)},\right. \\
& \left.(x_f^2 + x_b^2 - x_f x_b), (y_f^2 + y_b^2 - y_f y_b), \Delta t\right)
\end{aligned} \tag{3.16}$$

where $p = 1 + \frac{Re}{3}(x_f - x_b)u$ and $q = 1 + \frac{Re}{3}(y_f - y_b)v$.

A general formulation is obtained by using a weighted time average parameter μ by employing a uniform time step Δt and making use of the approximations for the operators δ_t^+, δ_x, δ_y, δ_x^2, δ_y^2, δ_x^3, δ_y^3, δ_x^4, δ_y^4, $\delta_x\delta_y$, $\delta_x^2\delta_y$, $\delta_x\delta_y^2$ and $\delta_x^2\delta_y^2$ as provided above and are further detailed in appendix A.

With this, (3.16) can be discretized compactly on the nonuniform nine-point stencil as

$$
\begin{aligned}
&\frac{1}{h}\left[\frac{\psi^{n+1}_{i+1,j}}{x_f}+\frac{\psi^{n+1}_{i-1,j}}{x_b}-\left(\frac{1}{x_f}+\frac{1}{x_b}\right)\psi^{n+1}_{i,j}\right]+\frac{1}{k}\left[\frac{\psi^{n+1}_{i,j+1}}{y_f}+\frac{\psi^{n+1}_{i,j-1}}{y_b}-\left(\frac{1}{y_f}+\frac{1}{y_b}\right)\psi^{n+1}_{i,j}\right]\\
&=\frac{\mu\Delta t}{Re}\Big\{\Big(A\psi^{n}_{i+1,j+1}+B\psi^{n}_{i,j+1}+C\psi^{n}_{i-1,j+1}+D\psi^{n}_{i+1,j}+E\psi^{n}_{i,j}+F\psi^{n}_{i-1,j}+G\psi^{n}_{i+1,j-1}\\
&\qquad+H\psi^{n}_{i,j-1}+I\psi^{n}_{i-1,j-1}\Big)-\phi^{n}_{i,j}\Big\}\\
&+\frac{(1-\mu)\Delta t}{Re}\Big\{\Big(A\psi^{n+1}_{i+1,j+1}+B\psi^{n+1}_{i,j+1}+C\psi^{n+1}_{i-1,j+1}+D\psi^{n+1}_{i+1,j}+E\psi^{n+1}_{i,j}+F\psi^{n+1}_{i-1,j}+G\psi^{n+1}_{i+1,j-1}\\
&\qquad+H\psi^{n+1}_{i,j-1}+I\psi^{n+1}_{i-1,j-1}\Big)-\phi^{n+1}_{i,j}\Big\}\\
&+\frac{1}{h}\left[\frac{\psi^{n}_{i+1,j}}{x_f}+\frac{\psi^{n}_{i-1,j}}{x_b}-\left(\frac{1}{x_f}+\frac{1}{x_b}\right)\psi^{n}_{i,j}\right]+\frac{1}{k}\left[\frac{\psi^{n}_{i,j+1}}{y_f}+\frac{\psi^{n}_{i,j-1}}{y_b}-\left(\frac{1}{y_f}+\frac{1}{y_b}\right)\psi^{n}_{i,j}\right]\\
&+\frac{x_f-x_b}{2h}\left[\frac{v^{n}_{i+1,j}}{x_f}+\frac{v^{n}_{i-1,j}}{x_b}-\left(\frac{1}{x_f}+\frac{1}{x_b}\right)v^{n}_{i,j}\right]-\frac{y_f-y_b}{2k}\left[\frac{u^{n}_{i,j+1}}{y_f}+\frac{u^{n}_{i,j-1}}{y_b}-\left(\frac{1}{y_f}+\frac{1}{y_b}\right)u^{n}_{i,j}\right]\\
&+\frac{x_f-x_b}{2h}\left[\frac{v^{n+1}_{i+1,j}}{x_f}+\frac{v^{n+1}_{i-1,j}}{x_b}-\left(\frac{1}{x_f}+\frac{1}{x_b}\right)v^{n+1}_{i,j}\right]-\frac{y_f-y_b}{2k}\left[\frac{u^{n+1}_{i,j+1}}{y_f}+\frac{u^{n+1}_{i,j-1}}{y_b}-\left(\frac{1}{y_f}+\frac{1}{y_b}\right)u^{n+1}_{i,j}\right]
\end{aligned}
\tag{3.17}
$$

The details of all the coefficients above can be found in appendix A.

The spatial order of accuracy of the above formulation is exactly two on both uniform and nonuniform grid and temporal accuracy depends on the value of μ. $\mu = 0$ and 1 render an accuracy of 'one' (Euler forward and backward respectively) and if $\mu = 0.5$, then accuracy is 'two' (Crank-Nicolson scheme). Here, the superscripts n and $n+1$ depict the n^{th} and $(n+1)^{\text{th}}$ time levels respectively. The compact scheme developed above uses nine points both at the n^{th} and $(n+1)^{\text{th}}$ time levels as shown in figure 3.1 and as such may be designated as a $(9, 9)$ scheme.

The velocities are approximated up to third order accuracy by the same approach (see equations (2.33) and (2.34)) as in chapter 2.

Note that the substitution of the values of u and v from above in equation (3.17) instead of the closed form ones is likely to reduce the accuracy of computation. However, it does not effect the theoretical rate of convergence of the proposed scheme as would be seen later on.

3.3 Solution of Algebraic system

We now discuss the solution of algebraic systems resulting from the discretization of the newly developed finite difference approximation. The system of equations resulting from

the Equation (3.17) can be written as

$$A\boldsymbol{\psi} = f(Re, \boldsymbol{\psi}^n, \boldsymbol{u}^n, \boldsymbol{v}^n, \boldsymbol{u}^{n+1}, \boldsymbol{v}^{n+1}) \tag{3.18}$$

where for a grid size of $m \times n$, the coefficient matrix A is of order mn and $\boldsymbol{\psi}^n, \boldsymbol{u}^n, \boldsymbol{v}^n, \boldsymbol{u}^{n+1}, \boldsymbol{v}^{n+1}$, $\boldsymbol{\psi}^n, \boldsymbol{u}^n, \boldsymbol{v}^n, \boldsymbol{u}^{n+1}, \boldsymbol{v}^{n+1}$ are vectors with mn components. Here Coefficient matrix A is non symmetric because of nonuniformity of the grid. The computation of transient state solutions of fluid flow governed by (3.2) requires an inner-outer iteration procedure. After initializing u, v and ψ, and with appropriate boundary conditions, (3.18) is solved for discrete values of ψ. Once ψ is computed, the velocities u, v can be computed from the third order approximations by employing Thomas algorithm [3] for tridiagonal system of equations. This constitute one outer iteration or time step.

Note that equation (3.18) contains the $(n+1)^{th}$ time level values of u and v, which is available only when the stream function values are known at $(n+1)^{th}$ time level. Here we follow local linearization technique for which the algorithm is as follows:

1. Initalize $\boldsymbol{\psi}^{n+1}$, $\boldsymbol{u}^{n+1}$ and $\boldsymbol{v}^{n+1}$ (with $\boldsymbol{\psi}^n, \boldsymbol{u}^n, \boldsymbol{v}^n$).
2. Set $\boldsymbol{\psi}^{n+1}_{old} = \boldsymbol{\psi}^{n+1}$.
3. Compute $\boldsymbol{\psi}^{n+1}$ using equation (3.18).
4. Compute $\boldsymbol{u}^{n+1}$ and $\boldsymbol{v}^{n+1}$ using equation (2.33) and (2.34).
5. If max $|\boldsymbol{\psi}^{n+1} - \boldsymbol{\psi}^{n+1}_{old}|<$ tolerance limit, then stop; else repeat step $2-5$ until convergence.

Another method is to calculate stream function from the first order time accurate scheme given in equation (3.17) and then calculating the $(n+1)^{th}$ time level values of velocities using (2.33) and (2.34). This is a predictor-corrector type approach and slightly more expensive computationally than the other approach.

The inner iterations involve solving matrix equation (3.18) at each time step by iterative solvers. We have used bicongugate gradient stabilized method (BiCGStab) [144] with preconditioning, where Incomplete LU decomposition is used as a preconditioner. Preconditioning was particularly useful for high Reynolds numbers on finest grids with extreme clustring where we have used the Lis library [111]. The inner iterations were

stopped when the Euclidean norm of the residual vector $\boldsymbol{r} = \boldsymbol{f} - A\boldsymbol{\psi}$ arising out of equation (3.18) fell below 10^{-9}. For the cases where steady-state have been reached through time marching, it is assumed to reach when the l_∞ norm of the error between the current and previous outer time iterations fell below 10^{-9}. All of our computations were carried out on a Intel core i7 based PC with 16GB RAM.

3.4 Numerical experiments

In order to validate our code and demonstrate the efficiency of the proposed formulation, we have applied it to several pertinent test cases. Apart from a problem having analytical solution, they range from problems of internal flows inside curved regions to those involving fluid-embedded body interaction representing a host of complex flows past bluff bodies with different physical set-ups and boundary conditions. The problems under consideration in the current study can be broadly divided into the following categories:

3.4.1 Test case 1: Taylor vortex

The first test case considered here is the Taylor vortex problem which has an analytical solution and represents the flow in the annular region between two concentric cyliders, where one of them is rotating at a constant speed and the other one is held stationary. We consider the domain to be $0 \leq x, y \leq 2\pi$ with initial conditions

$$\begin{aligned} u(x,y,0) &= -cos(Nx)sin(Ny), \\ v(x,y,0) &= sin(Nx)cos(Ny), \\ \psi(x,y,0) &= \frac{1}{N}cos(Nx)cos(Ny). \end{aligned} \tag{3.19}$$

The exact solutions of this problem is given by

$$\begin{aligned} u(x,y,t) &= -cos(Nx)sin(Ny)e^{-2N^2t}, \\ v(x,y,t) &= sin(Nx)cos(Ny)e^{-2N^2t}, \\ \psi(x,y,t) &= \frac{1}{N}cos(Nx)cos(Ny)e^{-2N^2t}. \end{aligned} \tag{3.20}$$

where N is a positive integer determining the number of vortices being generated; a total number of N^2 vortices are generated from the above system. As such the grids are generated in such a way that points are clustered in the vicinity of lines of separartion between two vortices. In figure 3.2(a) we present a typical grid of size 81×81. Here, the grid is generated in eight clusters and grid points are compressed in the neighbourhood two successive vortices using the following streching functions in x- and y-directions.

$$\begin{aligned} x_i &= \frac{i}{i_{max}} + \frac{\lambda}{2\pi}\sin\left(\frac{2\pi i}{i_{max}}\right),\ 0 < \lambda \leq 1 \\ y_j &= \frac{j}{j_{max}} + \frac{\lambda}{2\pi}\sin\left(\frac{2\pi j}{j_{max}}\right),\ 0 < \lambda \leq 1 \end{aligned} \tag{3.21}$$

In figure 3.2(b) we present the post processed vorticity contours for $Re = 1000$ and $N = 4$ at $t = 2$ with $\Delta t = 0.01$. The horizontal velocities along the vertical centerline and vertical velocities along the horizontal centerline at $t = 10$ and $Re = 100$ for $N = 1$, 2 and 4 along with the exact solutions are compared in figures 3.3(a) and (b) respectively. In all the cases, our numerical solutions are seen to be extremely close to the analytical ones. In order to establish the grid-independence of our computed solutions, in the next figure 3.4, we plot the same variables, but now only for one combination of the parameters, viz., $N = 2$ and $Re = 10000$ at time $t = 1$ on grid of sizes 33×33, 65×65 and 129×129; it is heartening to note that grid independence is achieved on a grid of size as coarse as 33×33. Variation in the velocities on either sides exhibits identical behavior with nearly equal peaks.

In table 3.1, we present the root mean square errors for u, v and ψ for two combinations $Re = 10000$, $\lambda = 0.8$ and $\lambda = 0.9$. The rates of convergence are calculated using the formula $\dfrac{\ln(E_C/E_F)}{\ln 2}$ where $E_F = \phi - \phi_F$ and $E_C = \phi - \phi_C$ where ϕ, ϕ_F and ϕ_C denote the exact solution, and the computed solutions on finer and coarser grids respectively; here ϕ stands for either u, v or ψ. One can see that the errors decay at a rate which is higher than the theoretical one.

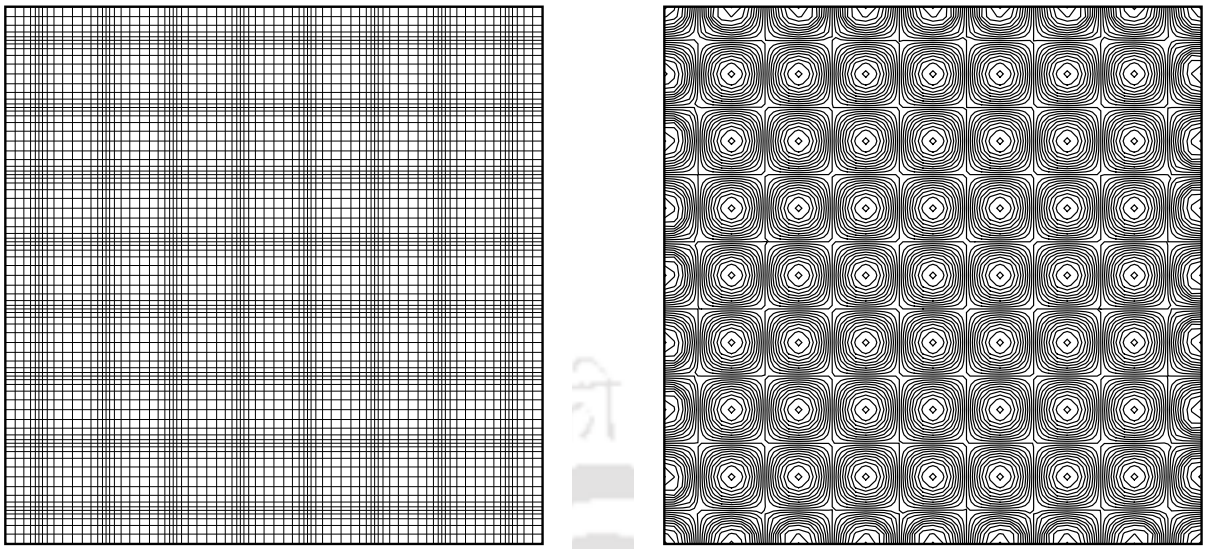

(a) (b)

Figure 3.2: *(a) a typical* 81×81 *grid used for test problem 1 with* $\lambda = 0.7$ *and (b) Vorticity contour of Taylor vortex for* $N = 4$ *at* $t = 2$.

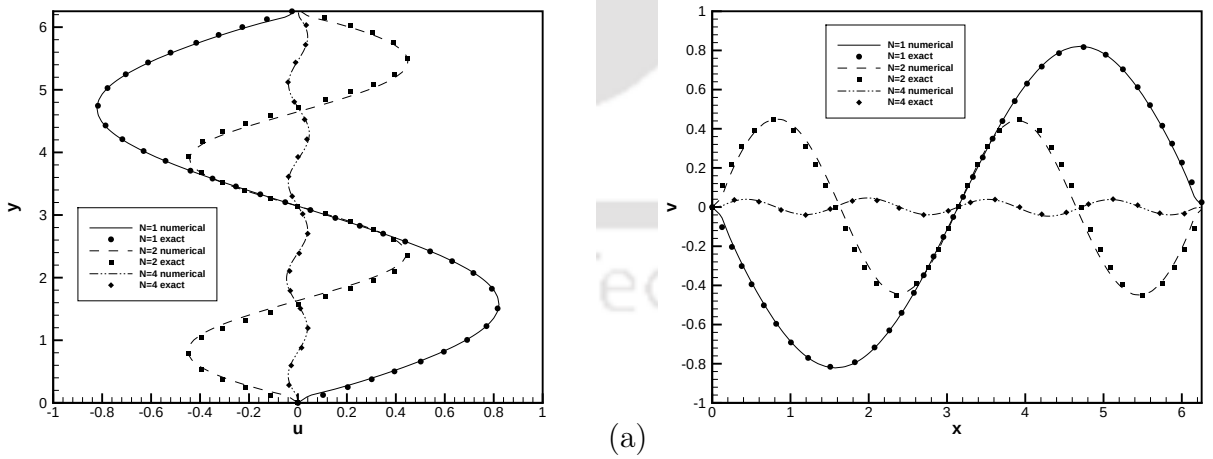

(a) (b)

Figure 3.3: *Comparisons of (a) horizontal velocity along the vertical centerline and (b) vertical velocity along the horizontal centerline for Taylor's vortex problem at* $t = 10$ *for* $N = 1$, 2 *and* 4, *and* $Re = 100$ *with exact solution.*

Table 3.1: Root mean square errors for u, v and ψ for $Re = 10000$ for test problem 1.

Grid		33×33	Rate	65×65	Rate	129×129
$\lambda = 0.8$	u	3.881916e-04	2.6117	5.691090e-05	2.4698	1.096928e-05
	v	3.881916e-04	2.6117	5.691090e-05	2.4698	1.096928e-05
	ψ	1.408023e-04	2.6119	1.806850e-05	2.6033	2.666354e-06
$\lambda = 0.9$	u	1.603723e-04	2.7606	2.104238e-05	2.3762	3.726574e-06
	v	1.603723e-04	2.7606	2.104238e-05	2.3762	3.726574e-06
	ψ	6.603258e-05	2.8244	8.304430e-06	2.6760	1.159619e-06

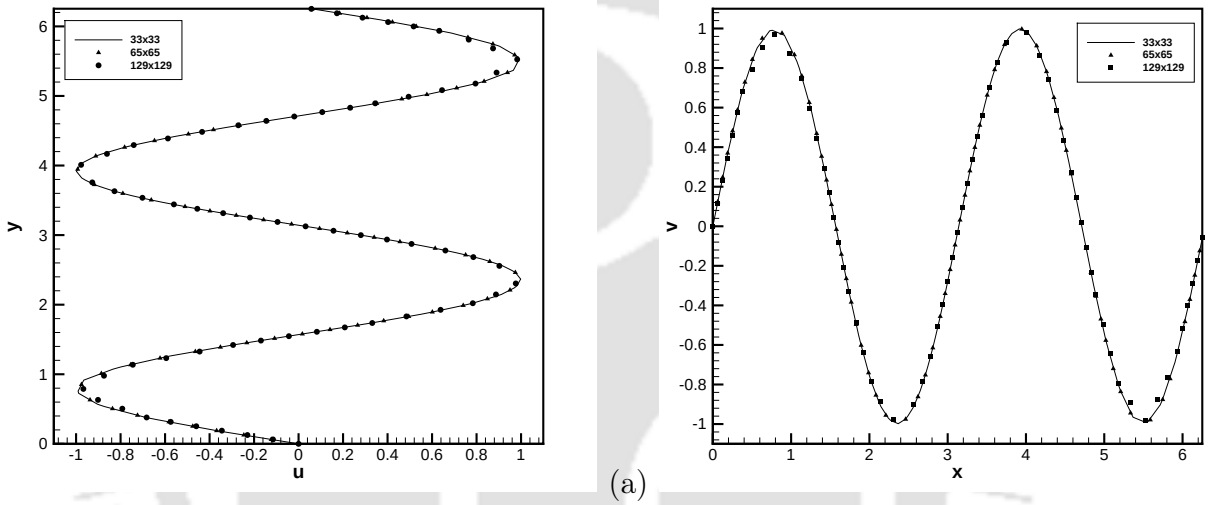

(a) (b)

Figure 3.4: *Grid independence of the computed solutions for the Taylor vortex problem: (a) horizontal velocity along the vertical centerline and (b) vertical velocity along the horizontal centerline for Taylor's vortex problem at $t = 1$ for $N = 2$ and $Re = 10000$ on grid of sizes 33×33, 65×65 and 129×129 for $\lambda = 0.8$.*

3.4.2 Test case 2: Lid-driven quarter-circle cavity

The next test case considered here is the lid-driven quarter-circle cavity problem, which is an example of internal flow. The problem aptly demonstrates the capacity of the current formulation in handling curved boundaries on Cartesian grids. Unlike the lid-driven square cavity problem, where the flow domain is bounded by four walls, here, the domain resembles the fourth quadrant of a circular region, and is bounded on three sides. The problem setup is presented in figure 3.5. The cavity in polar coordinates (r, θ) can be

defined as $0 \leq r \leq R$ and $0 \leq \theta \leq 90$. It is bounded by a vertical wall on the left and a circular arc on the right, both of which are solid walls, and the horizontal top wall which is moving at constant velocity from left to right. As such, no slip boundary condition, $u = v = \psi = 0$ is applied on the circular and vertical walls and, $u = 1$ and $v = \psi = 0$ on the top wall. The moving wall is the driving force which generates fluid motion inside the cavity. A series of vortices with decreasing size and strength is generated at the bottom of the cavity. At high Res, secondary vortices are also formed at the top left of the cavity. Here, Reynolds number is defined as $Re = \frac{u_{top}R}{\nu}$, where u_{top} is velocity of the top wall, R is the radius of the circular region and ν is the kinematic viscosity of the fluid. In all our computations R was set as 1.0.

Numerical simulations are carried out for Reynolds number 100, 1000, 3200 and 5000 on a grid of size 161×161, where we generate the grid in the following way: in the x-direction clustered grid are generated using the following stretching function

$$x = \frac{i}{i_{max}} - \frac{\lambda}{\pi} \sin\left(\frac{\pi}{i_{max}}\right).$$

In the y- direction, the grids are generated in such a way that the geometry of curved boundary of quarter circle passes through the grid points (see the the grid around the curved boundary in figure 3.5). This has been accomplished following the algorithm descibed in [80].

In figures 3.6(a)-(d), we present the computed streamfunction contours for 100, 1000, 3200,and 5000 which are extremely close to the well established numerical result of [161]. One can clearly see the center of the primary vortex moving from the top right to the geometric center of the cavity as Reynolds number increases. For $Re = 100$ and 1000 our computed streamline patterns are similar to the ones computed by Vynnycky and Kimura [161]. However, no tertiary vortex was reported in their study. The typical separations and formation of secondary and tertiary vortices at the bottom corners and the top left region for $Re = 3200$ and $Re = 5000$ can also be observed from these figures.

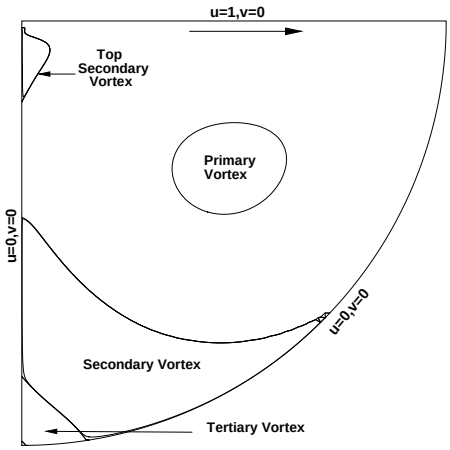

(a)

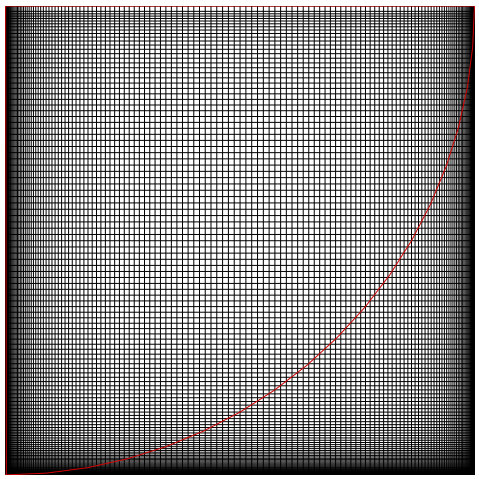

(b)

Figure 3.5: *(a) Configuration of the quarter lid-driven cavity flow problem and (b) a typical* 161×161 *grid with centrosymmetric clustering with* $\lambda = 0.8$.

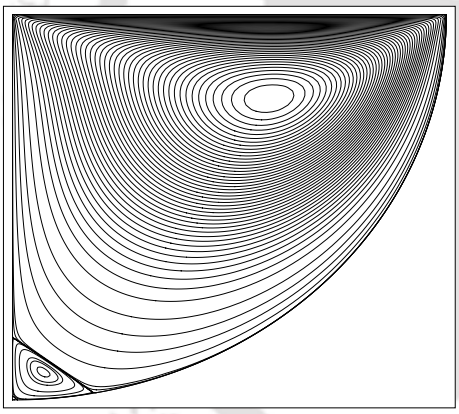

(a)

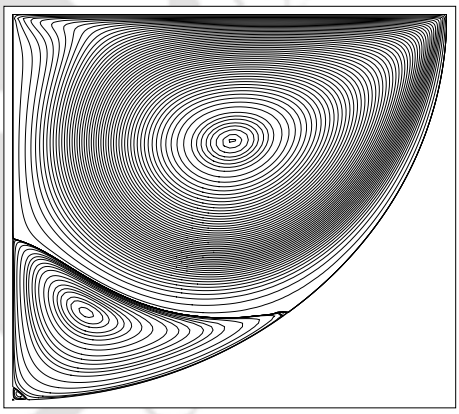

(b)

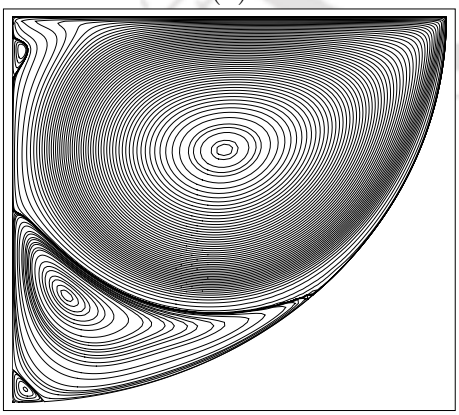

(c)

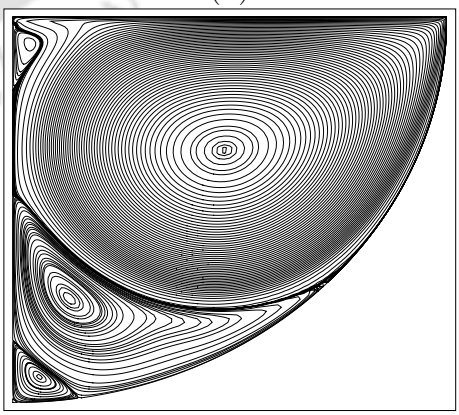

(d)

Figure 3.6: *Finest grid* (161×161) *streamfuntion Contours for the lid-driven quarter-circle cavity flow for (a) Re=100, (b) Re=1000, (c)Re=3200 and (d) Re= 5000.*

Similiar to the flow in lid-driven square cavity, there exists a series of vortices of decreasing size and strength [17] at the sole bottom corner of the cavity. Since vortices up to only tertiary level could be observed in figures 3.6(a)-(d), in order to get a better view of the vortices beyond tertiary level in the series, we present close-up views of them in figures 3.7-3.8. The secondary, tertiary, quaternary and post-quaternary vortices at the bottom corner have been denoted by BL_1, BL_2, BL_3 and BL_4. We have used multiple frames to depict the vortices appearing in each corner. In each frame, a pair of successive vortices gradually decreasing in size is plotted with the next pair appearing side by side in the adjacent frame. The smaller vortex in the previous frame is magnified for clarity in the next frame, which is now the bigger of the two vortices and is marked with arrowheads. It is heartening to note that for high *Re*s, even the post-quaternary vortices have been captured with apt details.

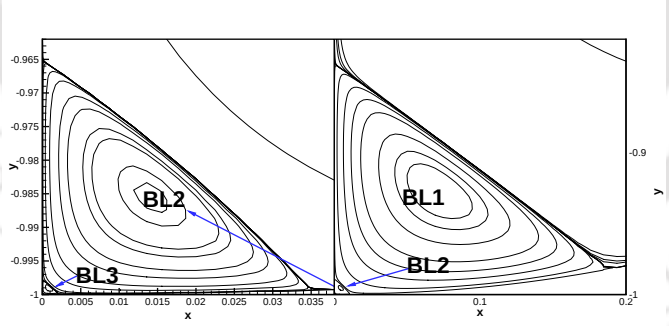

(a)

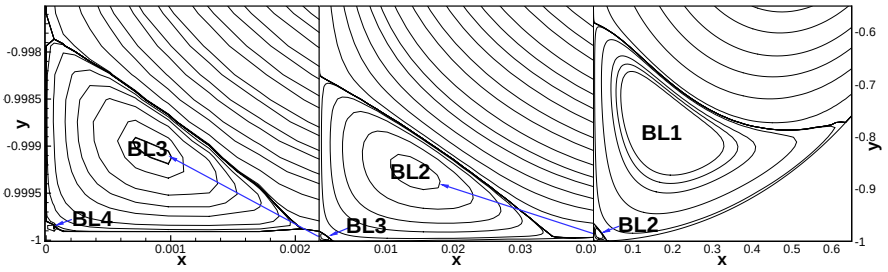

(b)

Figure 3.7: *Bottom corner vortices on grid size* 161×161*: (a) Re* = 100 *and (b) Re* = 1000.

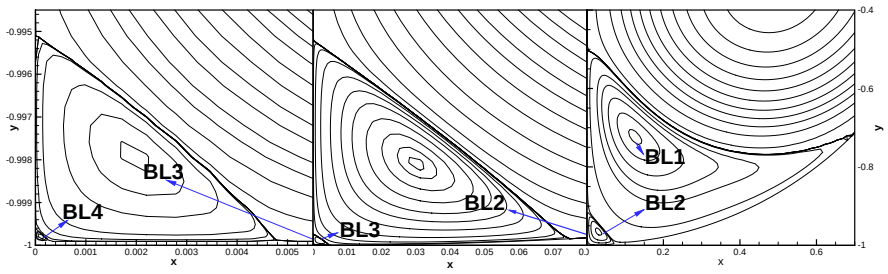

(a)

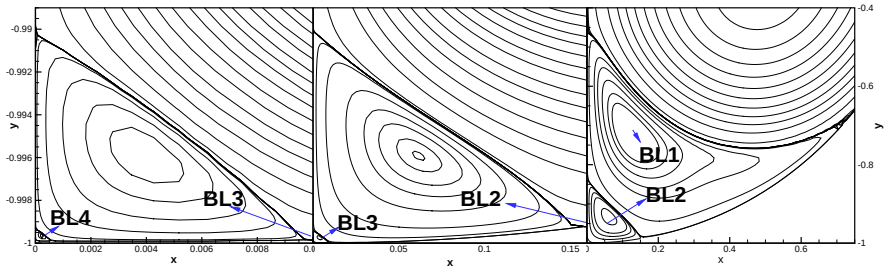

(b)

Figure 3.8: *Bottom corner vortices on grid size* 161×161*: (a)* $Re = 3200$ *and (b)* $Re = 5000$.

3.4.3 Test cases 3: Flow past bluff bodies in uniform flow

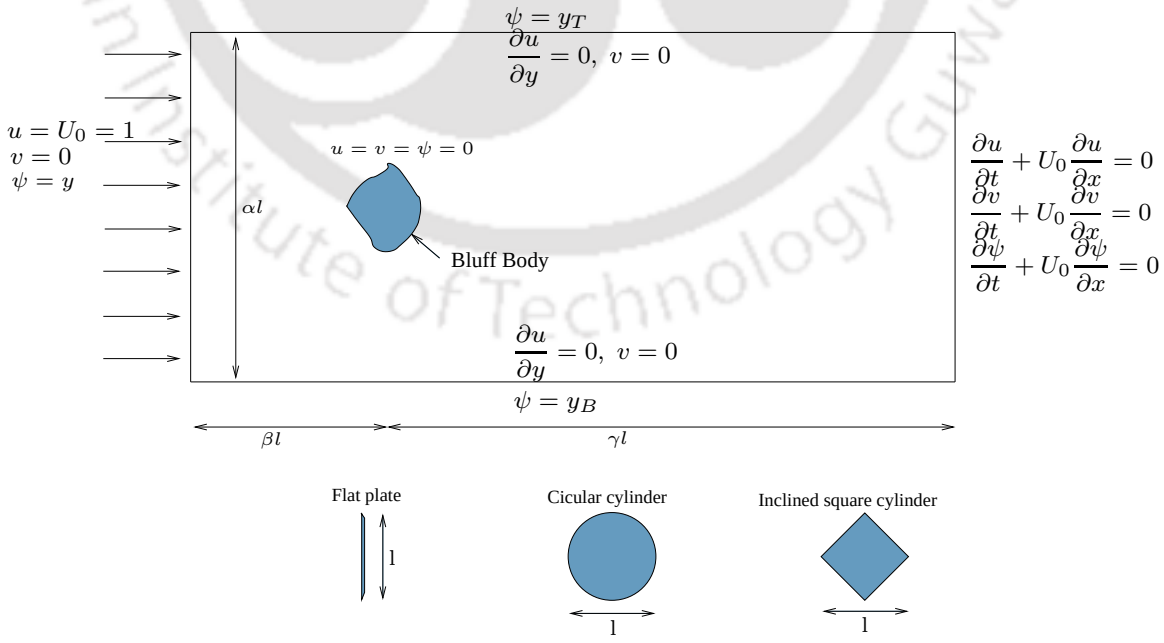

Figure 3.9: Configuration of the flow past bluff bodies in uniform and accelerated flow.

The next test cases considered here are representatives of flow past bluff bodies, where a solid body is assumed to be immersed in a fluid in an infinite domain and the flow is from left to right. The bluff bodies considered are: a flat plate placed normal to the incoming flow, an impulsively started circular cylinder and a square cylinder inclined at 45° angle to the direction of the freestream velocity. The schematic of the test cases including the boundary conditions and the computational domain are shown in figure 3.9. At the upstream, a uniform velocity $u = U_0 = 1$ is prescibed while in the downstream, a convective boundary condition $\frac{\partial \phi}{\partial t} + U_0 \frac{\partial \phi}{\partial x} = 0$ (ϕ representing either u, v or ψ) is imposed. On the surface of the body $u = v = \psi = 0$. At the other two boundaries, $\frac{\partial u}{\partial y} = v = 0$ with $\psi = y_T$ and $\psi = y_B$ at the top and bottom boundaries respectively, where y_T and y_B are the y coordinates thereat.

Flow configuration and the grid used

In the following, we provide a brief description of the computational domain along with the grid used for each of the cases under consideration. The size of the computational domain and the location of the bluff bodies are chosen in such a way that ample space is available on either side of the body in the streamwise and normal directions so that the computed flow is free from any entrance effect and a smooth shedding of the vortices is guaranteed when the flow is unsteady.

Case 1: Flow past a flat plate Flow past a geometry with sharp edges is difficult to compute because of edge singularity. The first case that we consider under the present category is that of the flow past a flat plate in uniform flow where the plate is kept normal to incoming flow from left. For this flow setup (refer to figure 3.9), Reynolds number is defined as $Re = \frac{U_0 l}{\nu}$, where U_0 is the average inlet velocity, l is the plate height and ν is the kinematic viscosity of the fluid. In all our computations l was set as 1.0. We have chosen $\alpha = 10$, $\beta = 7.5$ and $\gamma = 22.5$ in figure 3.9 such that the corresponding dimensions of the computational domain are $-7.5 \leq x \leq 22.5$ and $-5 \leq y \leq 5$; as such $y_T = 5.0$ and $y_B = -5.0$. The plate was placed at at $(x, y) = (0, 0)$.

Numerical simulations are carried out for the range of Reynolds numbers $10 \leq Re \leq 200$ on a grid of size 301×201. In order to generate centro-symmetric stretching near the

plate in both x- and y-directions , we use the following stretching function [105]:

$$x_i = \overline{\alpha}\left\{1 + \frac{sinh(\lambda(i-B))}{sinh(\lambda B)}\right\}; 0 < \lambda \leq 1 \tag{3.22}$$

where $B = \frac{1}{2r}\ln\left[\frac{1+\overline{\alpha}(e^{\lambda}-1)}{1+\overline{\alpha}(e^{-\lambda}-1)}\right]$ and λ is the stretching factor and is set as 0.6. We have kept $\overline{\alpha}$ to be 0.25 so that plate can be placed from the inlet at 25% of the total length in the x direction. In the y-direction $\overline{\alpha} = 0.5$ is used so that the plate can be placed at middle.

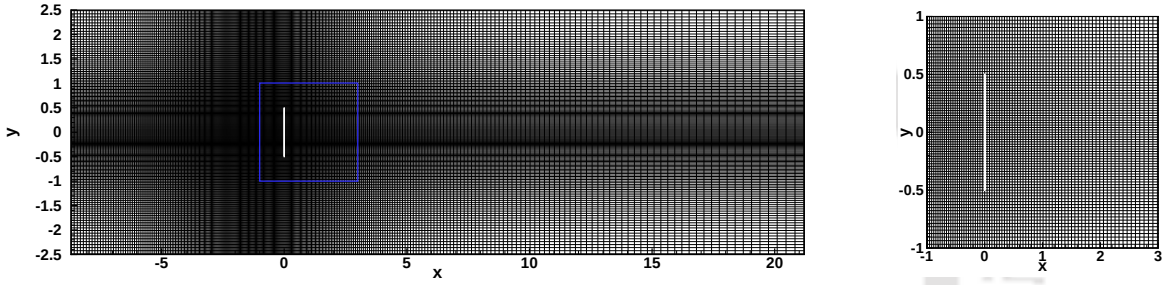

(a) (b)

Figure 3.10: *(a) A typical grid for* 301×201 *with* $\lambda = 0.5$ *used for computation of flow past a flat plate (b) close-up view inside the blue box.*

Case 2: Flow past a circular cylinder Next, we consider flow past an impulsively started circular cylinder in a free stream with uniform velocity. The schematic of the problem is already presented in figure 3.9 where the bluff body is nothing but the circular cylinder depicted in the bottom (middle) of the figure. Here the Reynolds number is defined as $Re = \frac{U_0 D}{\nu}$, where U_0 is uniform inlet velocity, D is the cylinder diameter and ν is the kinematic viscosity of the fluid. In all our computations D was set as 1.0. We have chosen $\alpha = 8$, $\beta = 6.5$ and $\gamma = 22.5$ in figure 3.9 such that the corresponding dimensions of the computational domain are $-8 \leq x \leq 22.5$ and $-6.5 \leq y \leq 6.5$; as such $y_T = 6.5$ and $y_B = -6.5$. The cylinder center is located at $(x, y) = (0, 0)$.

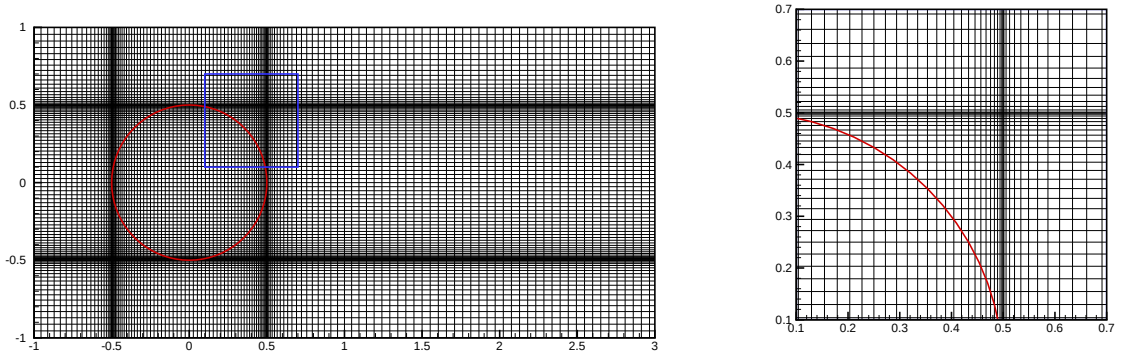

(a) Representative grid

(b) Close-up view inside the blue box

Figure 3.11: Representative grid and close-up view of a part of the grid for the flow past a circular cylinder

Numerical simulations are carried out for Reynolds numbers 10, 20, 40, 100 and 200 on grid size 361×241 where we generate the grid in such a way that the geometry of cylinder passes through the grid points (see the close up of the grid around the cylinder in figure 3.11). The procedure for generating the grid for the stationary cylinder is described in chapter 4 in detail. During this task, it must be assured that continuity of the grid lines in each direction of the overall computational domain is maintained.

Case 3: Flow past an inclined square cylinder The flow configuration for the next case is exactly similar to the previous one except for the fact that instead of a circular cylinder, a square cylinder inclined at 45° angle to the free-stream (figure 3.9, bottom right) is placed with center at $(x, y) = (0, 0)$. Similar to flat plate, this cylinder in the shape of a diamond also has sharp edges and causes complication in simulation because of the edge singularity. However, unlike the flow past a flat plate, it has a surface near to singularity which makes the flow a relatively stable one. Here the characteristic length l in the definition of Reynolds number is the diamond diameter, which is assumed to be unity for all our computation.

Numerical simulations are carried out for Reynolds numbers 10, 20 and 100 on grid size 301×201 where we create the grid in such a way that the boundary of the diamond cylinder passes through the grid points. The procedure for grid-generation is similar to the case of circular cylinder, except that the first block is, the block containing the cylinder,

generated by using uniform grids in either direction. The close-up view of grid is shown in the figure. 3.12.

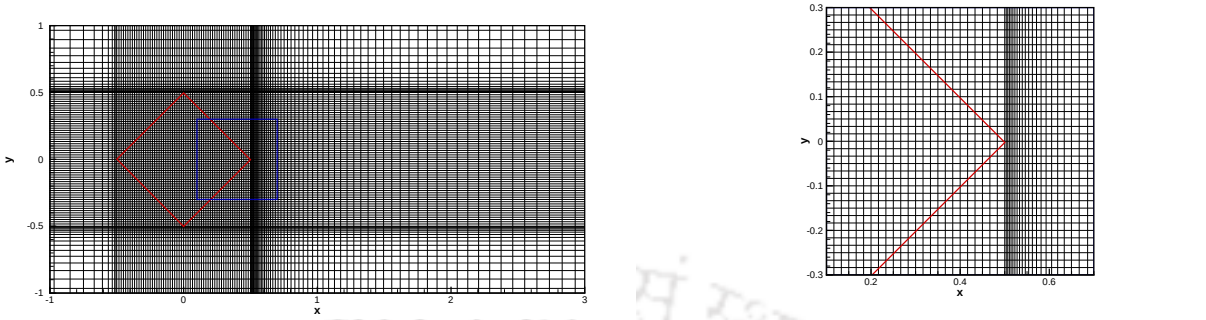

(a) Representative grid

(b) Close-up view inside the blue box

Figure 3.12: Representative grid and close-up view of a part of the grid for the flow past a inclined square cylinder

A comparative description of the flow

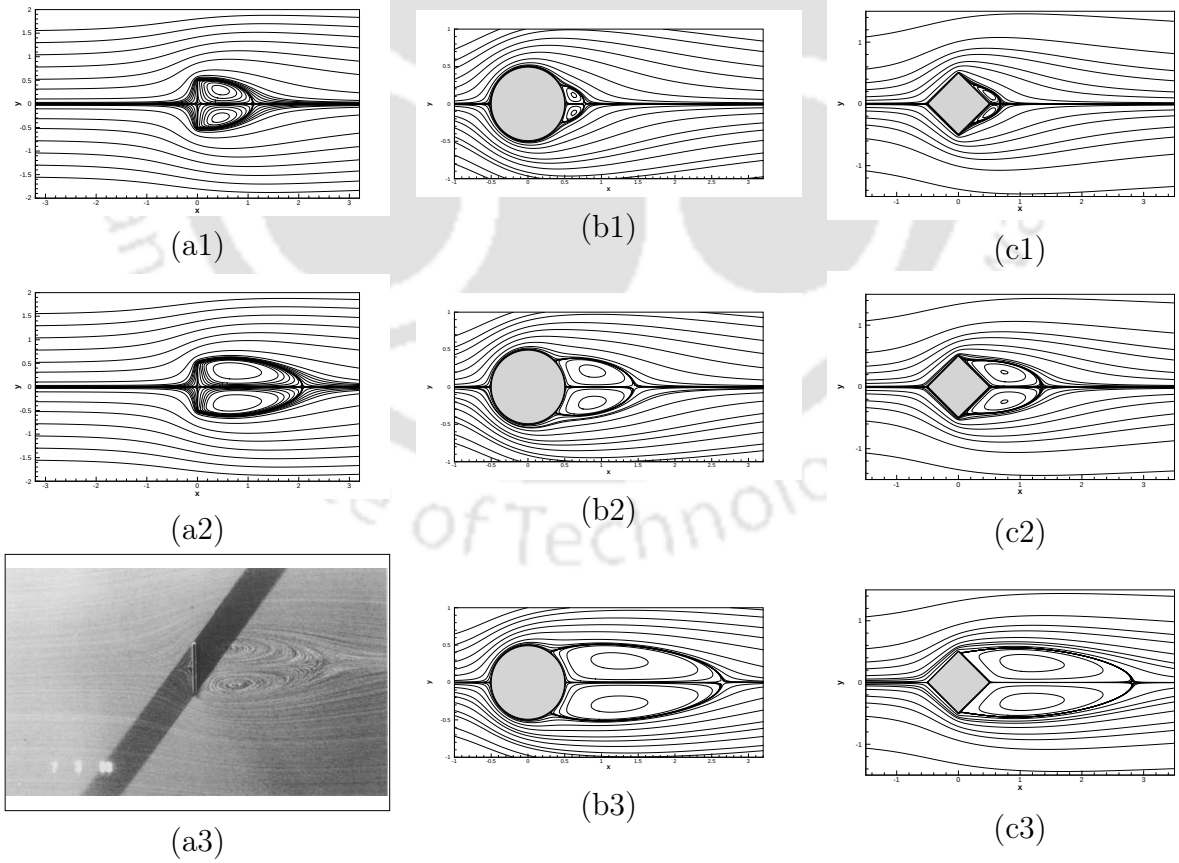

(a1) (b1) (c1)

(a2) (b2) (c2)

(a3) (b3) (c3)

Figure 3.13: Steady-state streamlines behind the bluff bodies: flat plate (left column), circular cylinder (middle column) and diamnond cylinder (right column).

Firstly, we show the flow structures in the steady-state regime in figure 3.13. Note that the critical Reynolds number (which indicates the flow transitioning from a stready to unsteady state) for the flat plate flow is around $Re = 28$ [60] which is much lower than the flows past the circular and diamond cylinders which occur for the Reynolds numbers in their late forties [55, 72, 89].

In figures 3.13(a1)-(a3), we present the steady-state streamline contours of the flow past flat plate for $Re = 10,$ and 20 and the experimental visualization of Ingham [59] for $Re = 20$ respectively. It is apparent from the figures that our computed results are extremely close to the experimental result. In the middle column of the same figure (figures 3.13(b1)-(b3)), we show the steady-state streamlines for $Re = 10$, 20 and 40 for the flow past circular cylinder problem, and the corresponding streamlines for the flow past the diamond cylinder are plotted in figures 3.13(c1)-(c3) in the right column. From the these figures one can see two symmetric wakes behind the bluff bodies increase in size as Reynolds number increases.

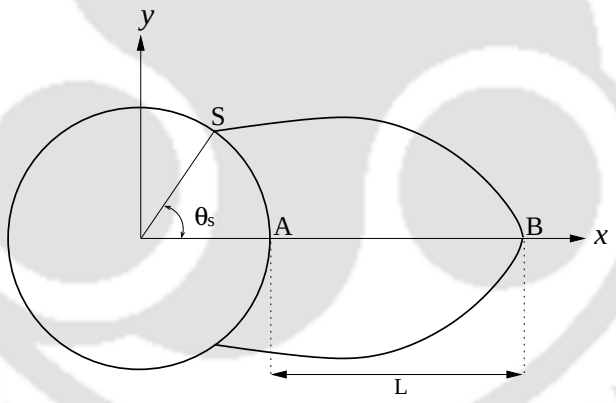

Figure 3.14: Flow parameters corresponding to table 3.2 for the flow past an impulsively started circular cylinder.

For the circular cylinder, we further compute the wake length L, which is the distance between rear end point A of cylinder and the end of the separation at the point B, continuously increasing with increased Reynolds number; the separation angle θ_s, which the angle between the x-axis and the line joining the center of the cylinder and the separation point S on the cylinder (figure 3.14). These are tabulated in table 3.2 along with the drag coefficient C_D which is computed by utilizing the momentum balance along the horizontal direction. We then compared our results with established numerical as well

Table 3.2: Comaprison of wake lengths, separation angles and drag coefficients for different Reynolds numbers for circular cylinder.

	Re	[27] (exp)	[137]	[152]	[101]	[87]	[66]	[93]	Present
	10	—	0.504	—	—	—	—	0.533	0.531
L	20	1.86	1.851	1.860	1.940	1.860	1.825	1.830	1.874
	40	4.38	4.625	4.560	4.660	4.620	4.420	4.250	4.278
	10	—	2.699	—	—	—	—	2.629	2.690
C_D	20	—	1.949	2.16	2.07	2.100	2.052	2.172	2.160
	40	—	1.439	1.61	1.55	1.580	1.534	1.590	1.576
	10	—	29.732	—	—	—	—	30	29.69
θ_s	20	44.4	43.141	43.9	44.1	44.40	43.50	45	42.66
	40	53.4	53.226	53.4	54.1	54.1	53.54	54	53.08

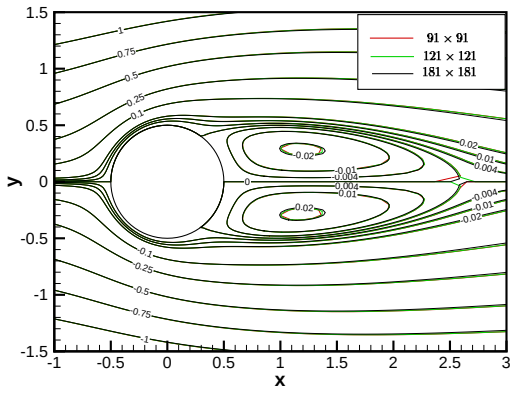

Figure 3.15: Grid independence of the computed solution depicted by streamlines for $Re = 40$ on three different grids of size 91×91, 121×121 and 181×181.

as the experimental results of Coutanceau and Bouard [27]. We have also presented the steady-state streamlines for $Re = 40$ on three different grids of size 91×91, 121×121 and 181×181 in figure 3.15. One can clearly see from the table and figure that our numerical results are not only very close to the experimental ones, they are also grid-independent.

In figure 3.16, we show the evolution of the flow for $Re = 100$ at different instants of time by plotting the streamlines in the left (figures 3.16(a1)-(a7)), middle (figures 3.16(b1)-(b7)) and the right (figures 3.16(c1)-(c7)) panels for the flat plate, circular and diamond cylinders respectively. The first four rows correspond to times $t = 2.0$, 6.0, 8.0 and 11.0 respectively. One can observe from these figures that the wakes behind the bluff

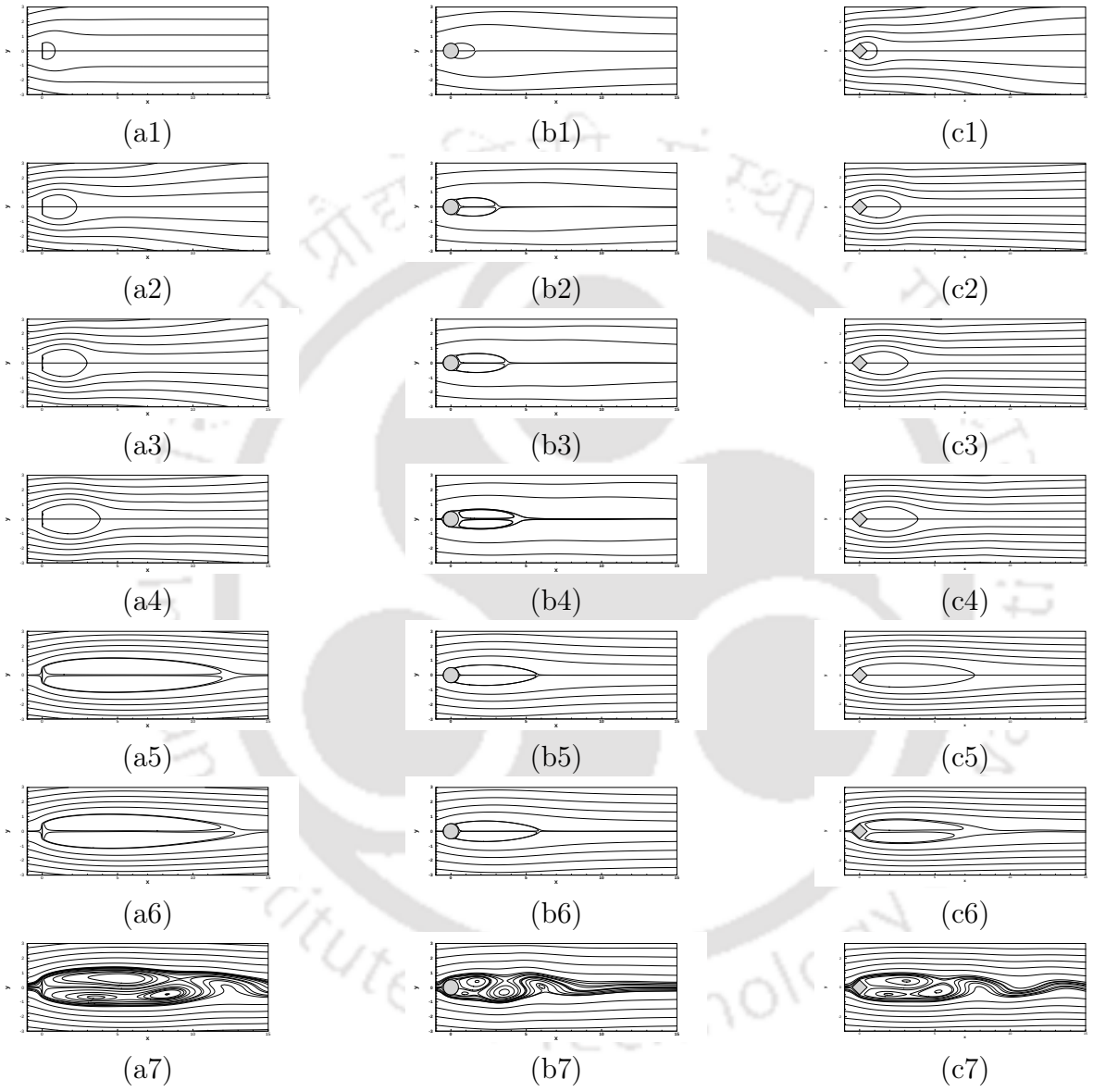

Figure 3.16: Streamlines showing the evolution of flow for flat plate (left column a1-a7), circular cylinder (middle column b1-b7) and diamond cylinder (right column c1-c7).

bodies are symmetric about $y = 0$ and grow in size with passage of time. In the next two rows, we present the wakes just before and after the onset of symmetry-break which occurs approximately at $t = 71.0$, 44.0 and 41.0 respectively for the flat plate, cicular cylinder and diamond cylinder. These figures also depict the maximum wake-length (see table 3.3) attained by the corresponding bluff bodies before the symmetry of the flow is broken. As one can see from the figures and table 3.3, the rate at which the symmetric vortices grow and the instant at which the symmetry is broken are different for differently shaped bluff bodies. The last row corresponds to instants $t = 95.0$, 70.0 and 85.0 where the symmetry is completely broken. The flow eventually settles into a periodic motion, which is accompanied by the formation of the famous von Kármán vortex street, where vortices are alternately shed from the top and bottom edges of the bluff bodies. The phenomenon can be seen more clearly in figure 3.17, where the streamlines, vortcity contours (post-processed) and streaklines behind the bluff bodies are depicted at the instant $t = 400.0$. It is worth mentioning that our scheme has resolved very accurately the famous **2S** mode of vortex shedding [129] for the flat plate, typical of this flow configuration which can be seen from figures 3.17(a2)-(a3).

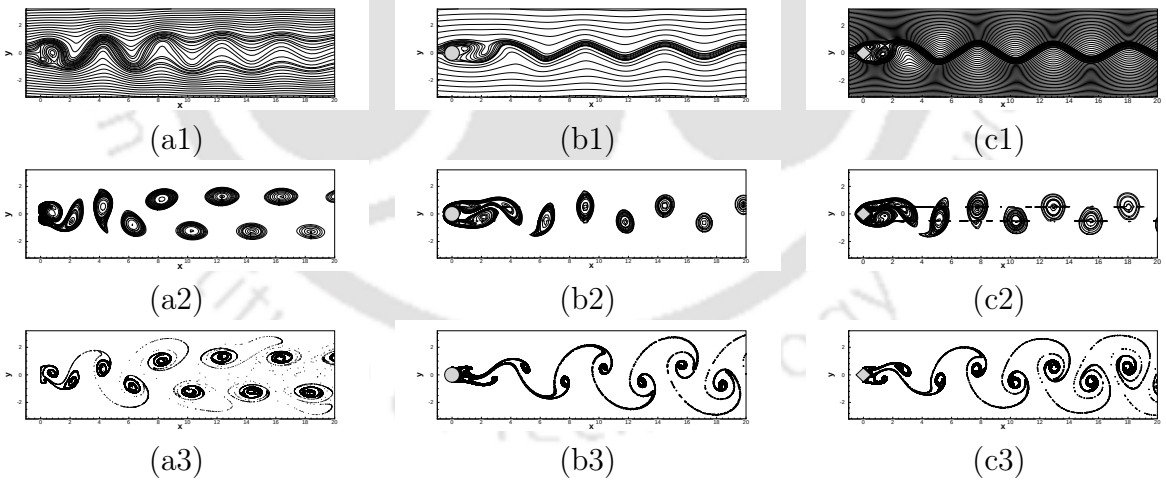

Figure 3.17: Vortex shedding behind flat plate ((a1)-(a3)), circular cylinder ((b1)-(b3)) and diamnond cylinder ((c1)-(c3)) for $Re = 100$: (top) Steamlines, (middle) vorticity contours and (bottom) streaklines.

In the next figure 3.18 we present the history of drag and lift coefficients C_D and C_L for 100, which are computed by utilizing the momentum balance along the horizontal and vertical direction respectively. From the graph of the history of C_D and C_L, one can also

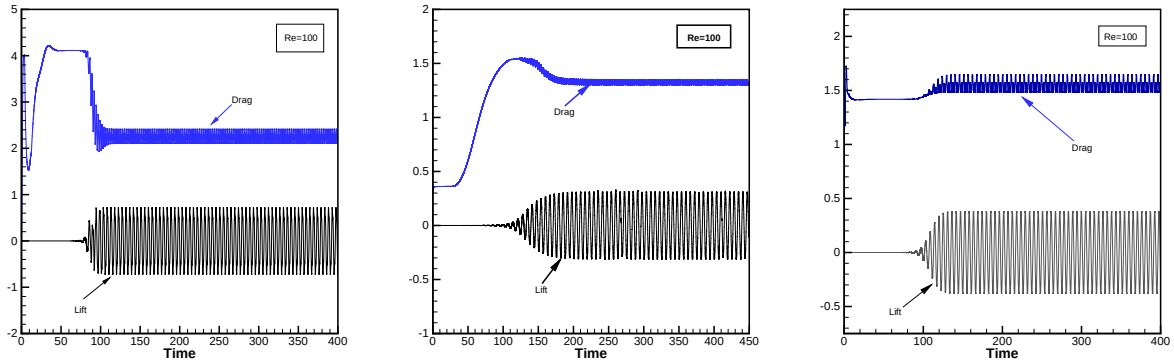

(a) (b) (c)

Figure 3.18: History of drag and lift coefficients for flow past: (a) a flat plate normal to the flow, (b) an impulsively started circular cylinder and (c) an impulsively started diamnond cylinder.

perceive the time at which wakes behind the bluff bodies begin to lose their symmetry. At that instant the graph of C_L, which was horizontal initially, starts to grow wavy in nature and we further observe that higher the value of C_D, greater is the maximum wake-lengths attainable by corresponding bluff bodies. The normalized power spectra of lift coefficient for the same Reynolds numbers are presented in figure. 3.19(a), while in figure. 3.19(b), we present phase plane of u- and v-velocities at $(1.0, 0.0)$ behind the bluff bodies in the time intervals as shown in table 3.3. The existence of a single dominant mode and the close trajectory reconfirms the periodicity of the flow for $Re = 100$ for all the three flow configurations considered. From the frequency f corresponding to the maximum normalized power spectra observed from figure. 3.19(a), we compute the Strouhal number from the formula $St = \dfrac{fl}{U_0}$, the values of which are shown in table 3.3. Larger the Strouhal number, higher the number of vortices being shed behind the bluff bodies as can be seen from the middle and bottom rows of figure 3.17. For the circular cylinder case, we have also compared the Strouhal numbers, drag and lift coefficients for $Re = 100$ with established numerical and experimental results in table 3.4, and once again the results from our computation are extremely close to them.

A note on the utility of the mesh used: The worth of the Cartesian mesh used in the current computation could be realized from figure 3.20; here we have shown a 181×301 grid which was used in the original computational domain in the shape of a circular annulus in [76] in 3.20(a). This grid had 181 points in the radial and 301 points on

Table 3.3: Flow characteristics for differently shaped bluff bodies

	Flat plate	Circular cylinder	Diamond cylinder
Wake length	9.52	5.34	7.82
St	0.220	0.162	0.202
Time interval (fig. 3.19)	$300 \leq t \leq 400$	$400 \leq t \leq 500$	$300 \leq t \leq 400$
Instant of separation	0.015	0.02	0.018
Instant of symmetry break (apprx.)	$t = 71$	$t = 44$	$t = 41$

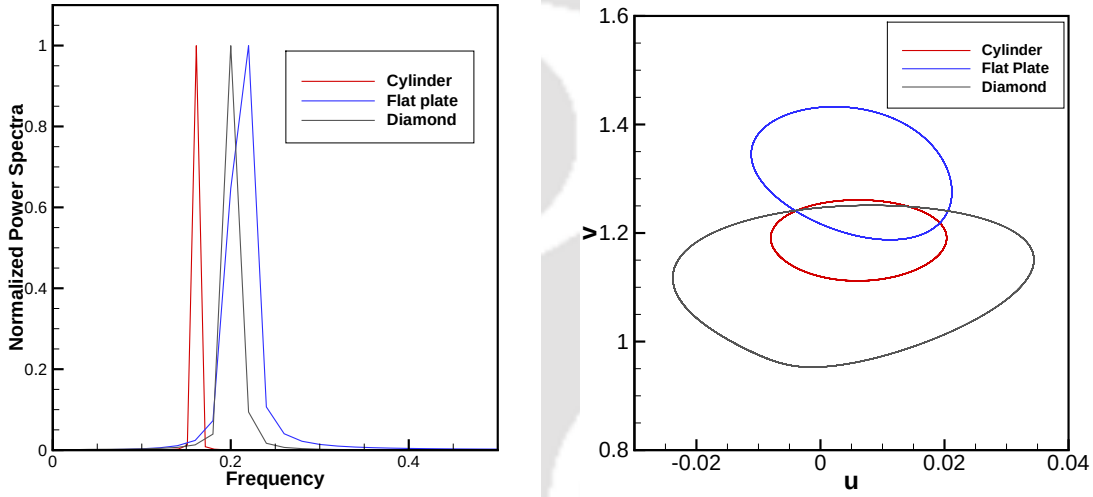

(a) (b)

Figure 3.19: *(a) Power spectrum and (b) phase portraits for flow past bluff bodies for* $Re = 100$.

Table 3.4: *(Strouhal number, drag and lift coefficient comparison for* $Re = 100$.

		St	C_D	C_L
Re=100	D. Calhoun [22]	0.175	1.333 ± 0.014	± 0.298
	Silva *et al.* [143]	0.15	1.39	—
	Russel & Wang. [127]	0.169	1.38 ± 0.007	± 0.300
	Linnick & Fasel. [101]	0.166	1.34 ± 0.009	± 0.333
	Xu & Wang [162]	0.171	1.42 ± 0.013	± 0.340
	Kolahdouz *et al.* [87]	0.168	1.370 ± 0.015	± 0.351
	Tritton (Exp.) [157]	0.167	—	—
	Present	0.162	1.325 ± 0.026	± 0.306

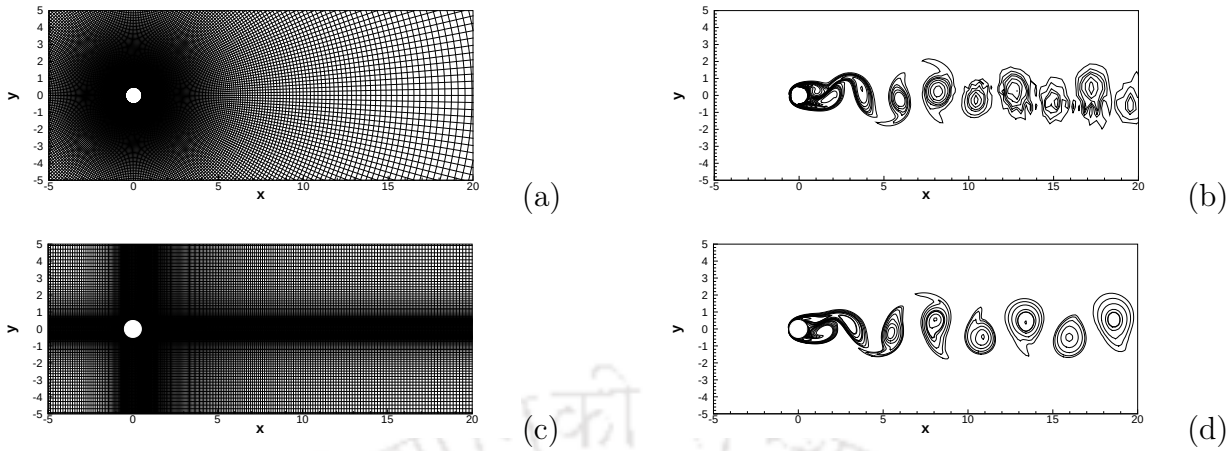

Figure 3.20: Computation for the flow past circular cylinder problem on equivalent polar and Cartesian grids: (a) polar grid used in [76], (b) post-processed vorticity contours for $Re = 200$ on polar grid, (c) Cartesian grid used in the present study, (b) post-processed vorticity contours for $Re = 200$ on Cartesian grid.

the azimuthal direction, meaning the same number points on the surface of the cylinder. The post-processed vorticity contours computed on the transformed plane are presented in figure 3.20(b). Likewise, the grid used in the current computation, which is of size 301×181, equivalent of having 181 points on the surface of the cylinder is presented in figure 3.20(c) and post processed vorticity contours computed on the same grid in figure 3.20(d). One can clearly see that because of the elongation of the step lengths in the radial direction away from the cylinder, the vorticity contours in figure 3.20(b) are distorted. On the other hand, because of the freedom of choice at hand for the Cartesian grid away from the cylinder, much smoother vorticity contours could be observed in figure 3.20(d).

3.4.4 Problems of Moving Boundaries Using the Biharmonic Approach

Our next test problems are examples with moving boundaries. In the first one we consider impulsively started flow past an oscillating cylinder in a cross-flow direction and the next one is the flow past an impulsively started rotating circular cylinder in a viscous medium. The schematics of these problems can be seen in figure 3.21, where on the left, one can see the circular cylinder oscillating transversely and on the right, the cylinder rotating in the counter-clock wise direction. All the other boundary conditions except on the surface

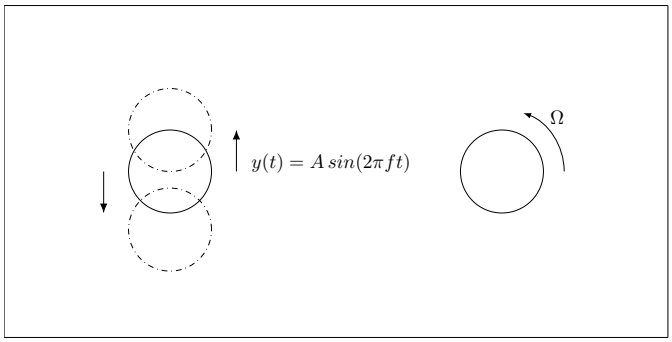

Figure 3.21: Schematic of oscillating (left) and rotating (right) cylinder.

of the cylinder in the computational domain are as in figure 3.9.

Cross Oscillation of cylinder in a fluid at rest

Here, the flow is considered a fluid-structure interaction problem due to oscillating bodies in a stationary or moving fluid or stationary bodies in an oscillating flow. It is of great importance in many science and engineering fields. Well versed documentation of some of the experimental and numerical results can be found in [126, 165, 166]. This example is a perfect for showcasing the robustness of the proposed scheme. The transverse motion of the cylinder is prescribed by a simple harmonic oscillation

$$y(t) = Asin(2\pi ft), \quad x(t) = 0,$$

where A is the amplitude of the oscillation and f is the characteristic frequency of the oscillation. In this problem, length and velocities have been non-dimensionalized with respect to the diameter D and U_{max} respectively, where U_{max} is the maximum velocity of the cylinder motion. As such, the Reynolds number for this flow is defined as $Re = \frac{U_{max}D}{\nu}$.

The dimensions of the computational domain was set as $-8 \leq x \leq 60$ and $-8 \leq y \leq 8$, which corresponds to $\alpha = 16$, $\beta = 8$ and $\gamma = 60$ in figure 3.9. As the cylinder is oscillating in a simple harmonic motion as a function of time, the generation of the grid is accomplished by adopting the following strategy.

The oscillation of the cylinder is achieved by making the top and bottom portions of the grid adapt through moving them upwards or downwards as a function of time while

keeping the middle portion fixed (see figure 3.22). The grid inside this middle portion has a vertcal height 4 with the circular cylinder lying in the middle where $-1 \leq x \leq 1$. This fixed portion moves up or down through the entire height, viz., 16 of the computational domain by compression and elongation of the top and bottom portions, and vice versa; this is attained through the same simple harmonic function for y defined above.

We consider two cases with the following combinations, (i) $A = 0.5$ and $f = 0.93$ and (ii) $A = 1.0$ and $f = 1.33$ having different amplitudes and frequencies for $Re = 392$. These cases are considered to validate our numerical results with the experiments performed by Williamson and Roshko [165], which exhibit different modes of vortex shedding. We show the streamlines at two time stations $t = 350$ and 400 for these two combinations in figure 3.23, which clearly demonstrates the difference in shedding patterns for them. However, this distinction is more evident from the corresponding streaklines in figures 3.24(a)-(b), including the effect of the amplitude as one can clearly see the vortices being shed in figure 3.24(b) covering much more vertical height than in figure 3.24(a). While 3.24(a) exhibits a **2S** pattern approximately up to $x = 30$ behind the cylinder followed by an **S** pattern, a **2P** pattern is seen in 3.24(b) throughout the whole computational domain. Our observation for both these combinations are consistent with Williamson and Roshko [165].

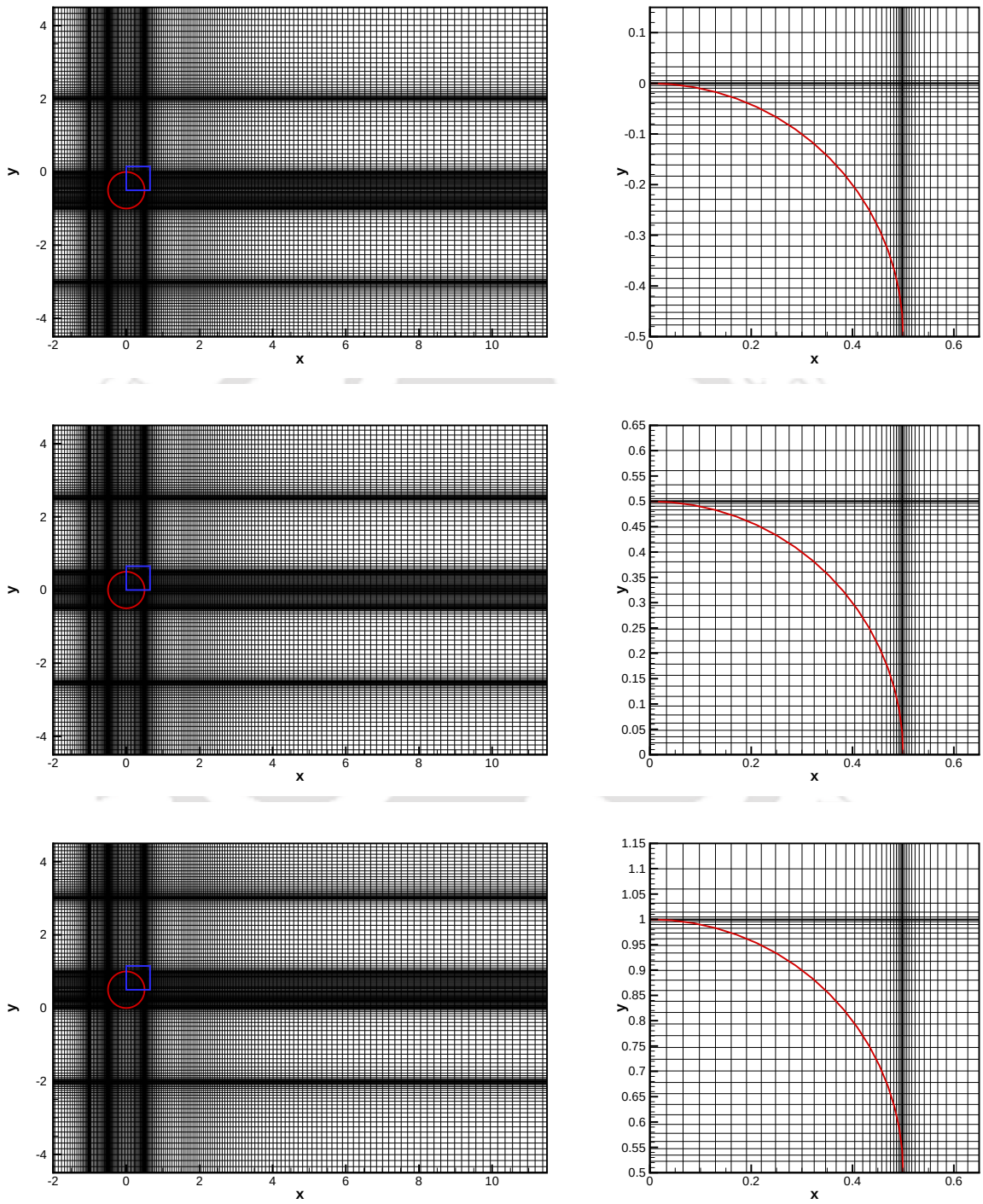

Figure 3.22: Grid used for oscillating cylinder

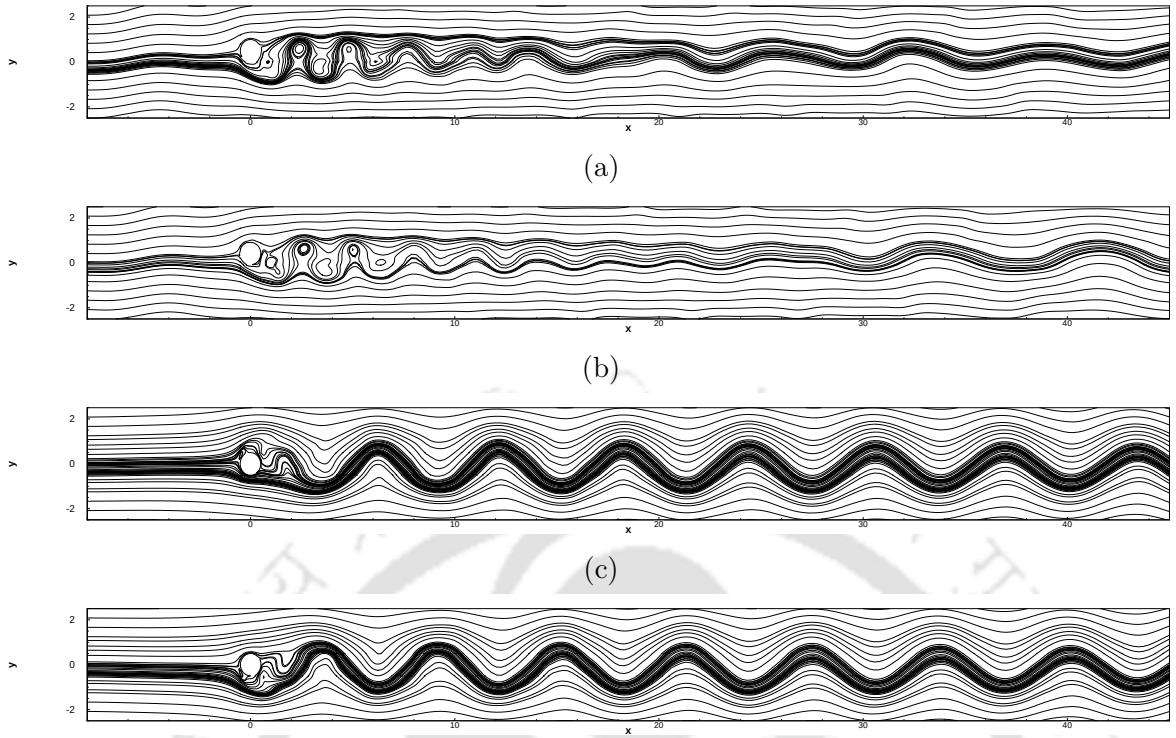

Figure 3.23: Oscillating Cylinder, streamlines for $Re = 392$: for $f = 0.93$ and $A = 0.5$ a) $t = 350$, (b) $t = 480$, and for $f = 1.33$ and $A = 1.0$, (c) $t = 350$, (d) $t = 400$ (Grid size: 541×241) .

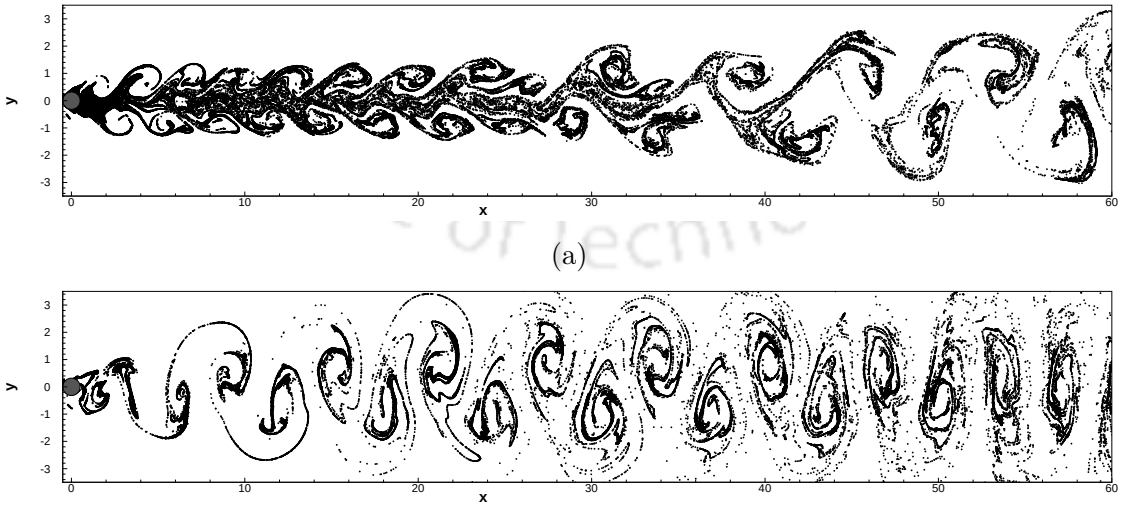

Figure 3.24: Streaklines for $Re = 392$ for (a) $f = 0.93$ and $A = 0.5$, and for (b) $f = 1.33$ and $A = 1.0$.

3.4.5 Flow Past a Rotating Cylinder

Here, the cylinder is rotating with constant angular velocity. This case has an importance of its own as it exhibits the suppression of the separated vortex. Studies have shown that steady flows with no vortex shedding for high enough velocity ratios are possible even for high Re values [6]. On the surface of the cylinder, an angular velocity Ω is imposed; because of the use of a Cartesian grid, it can be easily achieved by defining u and v velocities at any point on the surface as

$$u = -\Omega Y \quad \text{and} \quad v = \Omega X,$$

where X and Y are the coordinates of a point in x- and y- direction.

Numerical simulations are carried out for Reynolds number 1000 and angular velocities, $\Omega = \frac{1}{2}$ and 1.0 on a grid of size 481×241. To the best of our knowledge, this is perhaps the first time that numerical simulation of this kind has been attempted on a finite-difference setup over a Cartesian grid, thus again exemplifying the robustness of the proposed scheme.

In figure 3.25, we have presented the early evolution of the flow at the early stage. From figure 3.25(a), one can see that immediately after the impulsive start at $t = 0.5$, the primary vortex starts to form above x-axis and grow in size. Meanwhile, a secondary vortex starts to develop below x-axis and starts to grow in size (figures 3.25(b)-(d)). One can also see the development of a tertiary vortex on the upper half of the cylinder (figures 3.25(e)-(f)). With passage of time, these vortices acquire strength and reach their maximum size. It is heartening to note that our scheme has been able to capture the flow phenomena very accurately as can be seen from the comparison with the experimental results of Badr *et al.* [6] and our computed results at time $t = 1.5$ (figures 3.25(c)-(d)) and $t = 2.0$ (figures 3.25(e)-(f)). Note that the time scales have been normalized in order to match those of [6], as their non-dimensional time was obtained through a different scaling. The evolution of vortices for $\alpha = 1.0$ almost follow the same pattern as in the case of $\alpha = 0.5$ during the initial period. However, at later times, the vortices starts to open up and move upwards in the downstream direction leading to shedding of vortices as can be seen from the streamfunction and vorticity field at two different time step $t = 13$

and $t = 15$ as shown in figures 3.26(a)-(b).

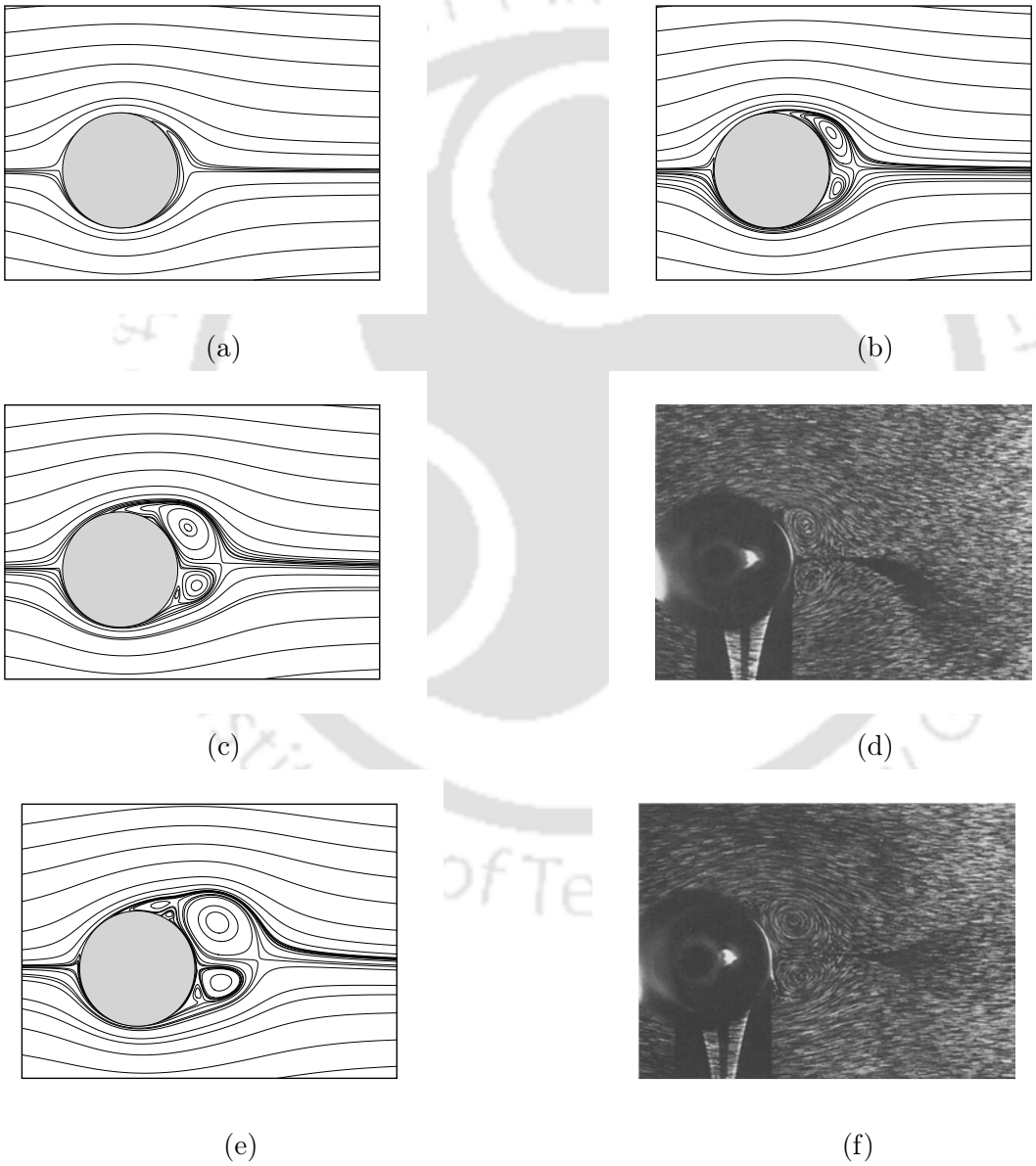

Figure 3.25: Evolution of the streamlines at different times for $Re = 1000$ and $\Omega = 0.5$: (a) $t = 0.5$, (b) $t = 1.0$, (c) $t = 1.5$, (d) $t = 1.5$ (experimental [6]) (e) $t = 2.0$ and (f) $t = 2.0$ (experimental [6]).

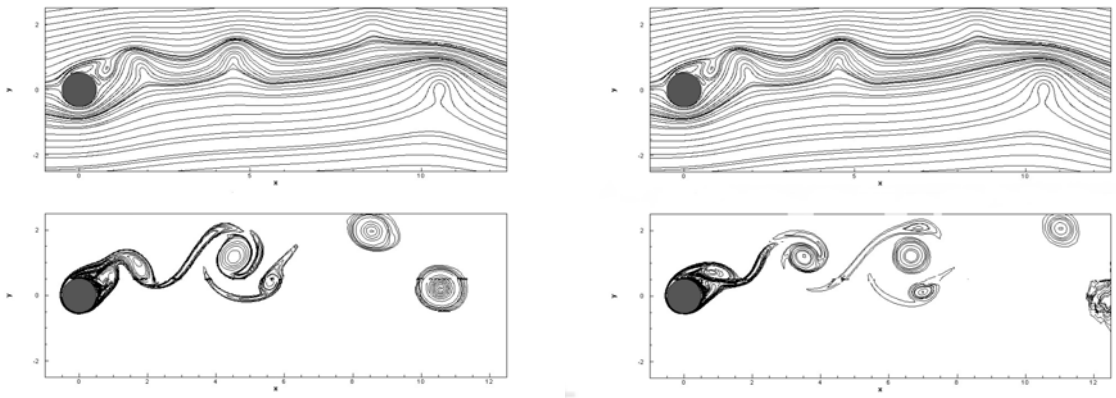

(a) (b)

Figure 3.26: Streamline and Vorticity fields for $Re = 1000$ and $\Omega = 1$ at (a) $t = 13$ and (b) $t = 15$.

3.5 Conclusion

In this chapter, we have developed a second order compact finite difference implicit, stable scheme for the biharmonic form of the transient N-S equations on nonuniform Cartesian grids. Unlike the existing ψ-v formulations on nonuniform grids which are inherently associated with the use of tranformation mappings, the proposed scheme does not use any transformation, paving the way for the physical and computational domain to remain the same. It thus removes the debilitating constraint of the grid distribution in the computational domain being completely dependent upon the choice of the transformation mapping. It is probably the first one developed for computing transient flows past bluff bodies on nonuniform Cartesian grids fitted to the surface of the bluff-bodies without the need of using transformation or roping in the immersed interface approach.

In order to extensively investigate the efficiency of the proposed scheme, it has been applied to seven different problems of varying physical complexities. They include problems of internal flows inside curved regions as well as those involving fluid-embedded body interaction. The first test case considered here is the Taylor vortex problem which has an analytical solution, and our coarse grid numerical solutions were found to be very close to the analytical ones. We have chosen the lid-driven quarter-circle cavity as our second test case, which is an example of internal flow inside a curved region. The effectiveness of the scheme was again demonstrated here by its ability to capture smaller scales up to the

post-quaternary level of vortices. However, the robustness of the scheme is highlighted by the accurate resolution of a host of complex flows past bluff bodies having different configurations and boundary conditions. It was seen to handle problems involving flows across a wide range of structures of varied shape, viz., a flat plate, a circular cylinder and inclined square cylinder. All the details of the shedded vortex structures under different circumstances have been captured very elegantly by the proposed scheme, which was able to handle both Dirichlet and Neumann boundary conditions with equal ease. We have established grid-independence of our computed solutions not only for the problem having an analytical solution, but also for flow past bluff bodies in uniform flows. In addition to the stationary cylinder, flows past an oscillatory and a rotating cylinders are also studied to testify the versatility of the scheme developed for the transient N-S equations. The advantage of the proposed scheme over the ones with grid transformations in terms of the flexibility of placing suitable Cartesian grids away from bluff bodies with curved boundaries have also been demonstrated. In all the cases, our results are found to be extremely close to the available numerical and experimental results, both qualitatively and quantitatively.

Having demonstrated the efficiency and robustness of the proposed scheme by accurately simulating flows for a wide range of problems of varied complexities, we will embark on a journey to probe the problem of flow past an impulsively started circular cylinder more closely. In the next chapter, we provide a comprehesive study of the secondary and tertiary vortex phenomena for this problem for a wide range of Reynolds numbers.

CHAPTER 4

A COMPREHENSIVE STUDY OF SECONDARY AND TERTIARY VORTEX PHENOMENA OF FLOW PAST A CIRCULAR CYLINDER: A CARTESIAN GRID APPROACH

4.1 Introduction

As observed in the previous chapter, bodies kept in fluid flow are characterized as being streamlined or blunt/bluff, depending on its overall shape and structure. An object can be considered as a bluff body if the fluid does not touch the whole boundary of it [26], while immersed in fluid flow. Flow past bluff bodies is a very common phenomena and it happens all around us. Some common examples are the flows past an airplane, a submarine, an automobile, or wind blowing past a high-rise building. Such flows are very complex and involve the interactions of three shear layers in the same problem, namely a boundary layer, a separating free shear layer, and a wake [166]. Moreover, there is a very strong interaction between the viscous and inviscid regions. Because of the vortical instabilities in the wakes, they are often difficult to predict and their understanding poses a great challenge to the scientific community.

Although bluff bodies can be of different shapes and sizes, the circular cylinder is considered to be the representative of all two dimensional bluff bodies. On the study of the wake behind the flow past an impulsively started circular cylinder alone, literally

hundreds of papers have been published, in part due to its engineering significance, and in part due to the tempting simplicity in setting up such an arrangement in an experimental or computational laboratory. In the simplest of geometric settings, it exhibits almost all the characteristics of incompressible viscous flow phenomena. As such it has attracted the attention of engineers, scientists and mathematicians alike, who have been engaged in carrying out theoretical, experimental and numerical studies on this problem over the past few decades [9, 18, 60, 66, 77, 82, 102, 126, 139, 157, 166].

Plethora of numerical studies on this problem attempted through all three well known approaches of discretization [60, 66, 77, 82, 102, 139]: finite element, finite volume and finite difference, can be found in the existing literature. Of late, the Lattice Boltzman method has also become quite popular as a tool for the simulation such flows [50, 51, 99, 112]. However, the finite difference approach, which is otherwise easy to implement, possesses the greatest challenge amongst all the approaches primarily because of the circular geometry, where a body fitted coordinate system is extremely difficult to construct. Consequently, majority of the simulations on this paricular problem on finite difference set up were performed on polar grids [51, 74, 122]. The very few simulations performed on a finite difference set-up on Cartesian grid, mainly utilized the immersed interface approach [22, 87, 101, 127, 143, 152], which requires additional computation owing to interpolation at the points on the circular boundary where the grid lines intersect.

In the current study, in order to discretize the biharmonic form of the Navier-Stokes equations [12, 46, 47, 73, 76, 137, 138] for incompressible viscous flows, we use the scheme developed in Chapter 3. Here, the grid is generated in such a way that the circular geometry passes through the grid points, thus dispensing with the need to use the immersed interface approach. A quick look at the numerical works on this problem reveals that very few studies detail the flow description for the whole range of $10^0 \leq Re \leq 10^4$ by employing a single numerical scheme. Particularly the ones on Cartesian grid through the immersed interface approach also dealt only with the low Reynolds number regime. Keeping that in mind, rather than describing the vortex dynamics in both unseparated (for example, splitter-plate flows) and separated wakes for all the different types of 3D and nominally 2D body shapes, the current attempt is an endeavour to present an overview of the vortex dynamics phenomena in the wake of a circular cylinder over this entire range

in the laminar regime.

Our study is mainly concerned with the vortex phenomena beyond primary level, which are typical of the laminar stage of flows at high Reynolds numbers that are well depicted in the works of [18, 77]. Of particular interest is the study of the tertiary vortex dynamics, which is presented in detail at the early stage of the flow for the moderately high Reynolds number 7500. For other Reynolds numbers, viz., $Re \geq 700$ they are systematically organised in a tabular summary. In the process, we have also studied the priodic flow regime characterised by the von Kármán vortex shedding. All the results are qualitatively and quantitatively validated through comparison with experimental and well established numerical results and they are found to be extremely close. This is due to the fact that the scheme utilizes the advantage of grid clustering in the regions of small scales which invariably requires more grid points to resolve the scale irrespective of the spatial accuracy of the scheme.

This chapter has been arranged in five sections. Section 2 deals with the problem and grid generation, section 3 with the grid independence and code validation, section 4 discusses the results and finally, section 5 summarizes the whole work. [1]

4.2 The problem and grid generation

The problem is that of the unsteady flow past an impulsively started circular cylinder, flow configuration of which has already been discussed in details in chapter 3. Since we had only provided schematics for flow past bluff bodies in general, we again show the schematic of this problem including the boundary conditions and the computational domain in figure 4.1 as a specific case. The computational domain is considered as $-8 \leq x \leq 25$, $-8 \leq y \leq 8$, where $l = D = 1$ so that $H = 16$, $x_L = 8$ and $x_R = 25$. The cylinder was placed at $(x, y) = (0, 0)$ as its center. On the surface of the cylinder $\phi = 0$ (ϕ representing either u, v or ψ); the same conditions were imposed inside the cylinder as well during computation. At the upstream, a uniform velocity $u = U_0 = 1$ is prescribed while in the downstream, a convective boundary condition $\frac{\partial \phi}{\partial t} + U_0 \frac{\partial \phi}{\partial x} = 0$ is imposed. On the surface of the body $u = v = \psi = 0$. At the other two boundaries, $\frac{\partial u}{\partial y} = 0 = v$ with $\psi = y_T$

[1] This work is published in [95]

and $\psi = y_B$ at the top and bottom boundaries respectively, where y_T and y_B are the y coordinates thereat.

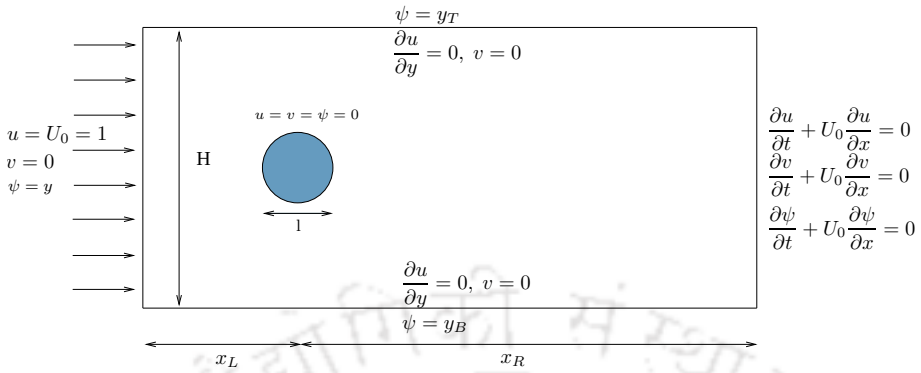

Figure 4.1: Configuration of the flow past a cylinder.

For our simulations, we have used grids of size ranging from 81×81 to 601×481, where the choice is made depending upon the Reynolds number and the flow situation, and the time step Δt is adjusted accordingly. The size of the computational domain and the location of the circular cylinder is chosen in such a way that ample space is available on either side of the cylinder in the stream wise and normal directions so that the computed flow is free from any entrance effect and a smooth shedding of the vortices is guaranteed when the flow is unsteady. Note that when the physical plane is considered in cylindrical polar coordinates, since grid lines are aligned with the cylinder geometry, one is mainly concerned with the grid clustering [51, 74, 122] nearby the surface of the cylinder or length of the outer radius of the annular region under consideration. However, if both the computational and physical plane is considered over a Cartesian grid along with the accommodation of the circle geometry set in the grid passing exactly through grid points, grid generation could be quite tricky. As promised in Chapter 3, we now provide a detailed description of how the grid is generated for computing the flow.

Since the current computation does not use any immersed interface approach, the grid essentially needs to be generated in such a way that the geometry of cylinder passes through the grid points (see the close up of the grid around the cylinder in figure 4.3). Following is the procedure to accomplish this: firstly a square block is created (block 1 in figure 4.2), where we generate the grid for the circular geometry by distributing the points along x-axis ($-0.5 \leq x \leq 0.5$) through the function $\cos\theta, \quad 0 \leq \theta \leq 2\pi$; likewise, along the y-axis ($-0.5 \leq y \leq 0.5$), one can distribute the grid points by using the $\sin\theta$

function. After that, the neighboring blocks (2 to 9), created by using different stretching function according to the computation requirement, are assembled. Note that one can also generate the grid in block 1 by firstly using a cenro-symmetric distribution of points along x-axis and then distribute the points along y-axis by using the formula $y = \pm\sqrt{a^2 - x^2}$, where a is the desired radius of the circle. However, the first approach mentioned above generates the points along the surface of the cylinder at uniform interval.

During this task, it must be assured that continuity of the grid lines in each direction of the overall computational domain is maintained as the computation is extremely sensitive to the grid being used. The grid has to be chosen in such a way that there is smooth transition of step lengths as one moves from one point to the next one. This has been illustrated in figure 4.3, where we show the close-up view of the grid around the circular geometry. Here one can see the circular geometry passing through the grid points in block 1 along with the transition of the grids around the junction of the blocks 1, 2, 7 and 8 (red box) and the clustering that has been mentioned in the figure 4.3 (green box) pertains to only the junction of block 1, 3, 7 and 9, more specifically of block 1 .

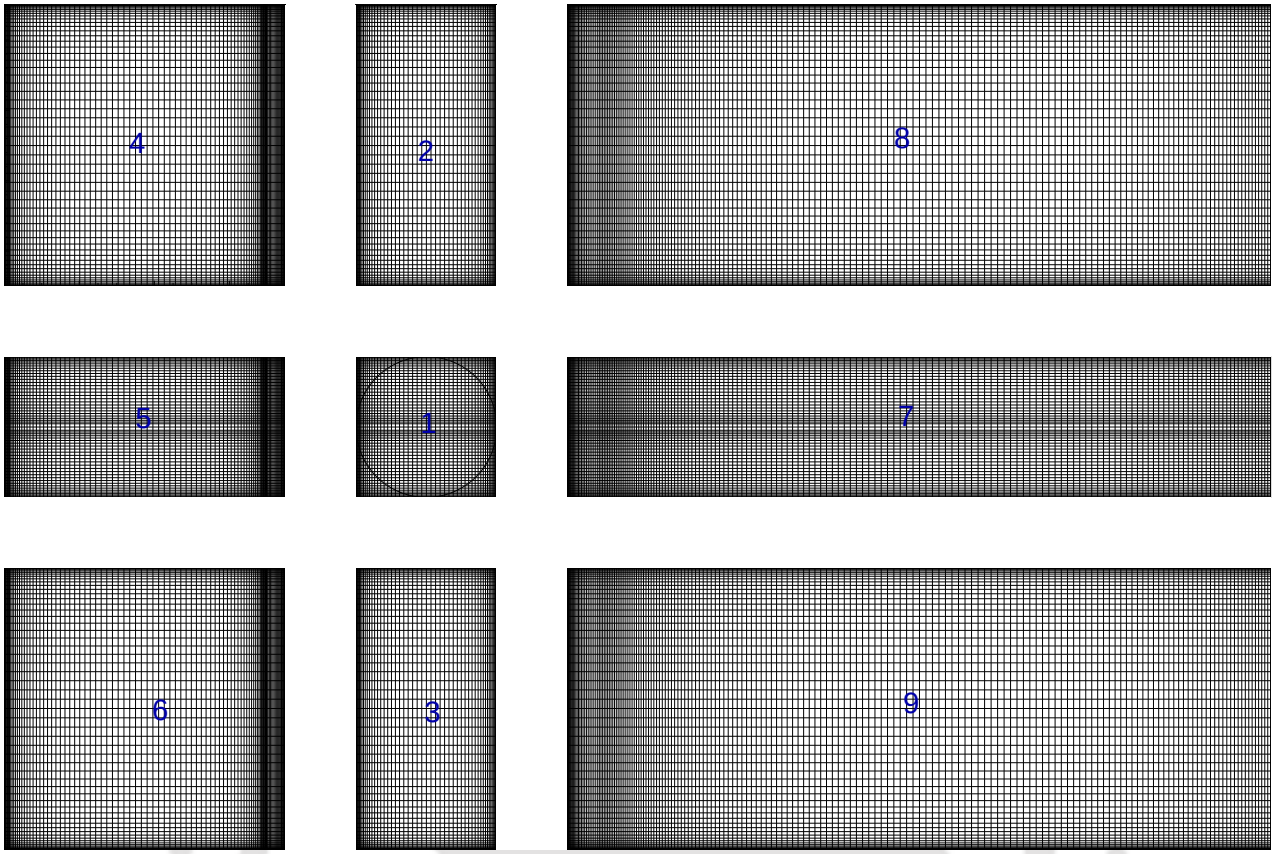

Figure 4.2: Assembly of grids on the different parts of the computational domain for the flow past an impulsively started circular cylinder.

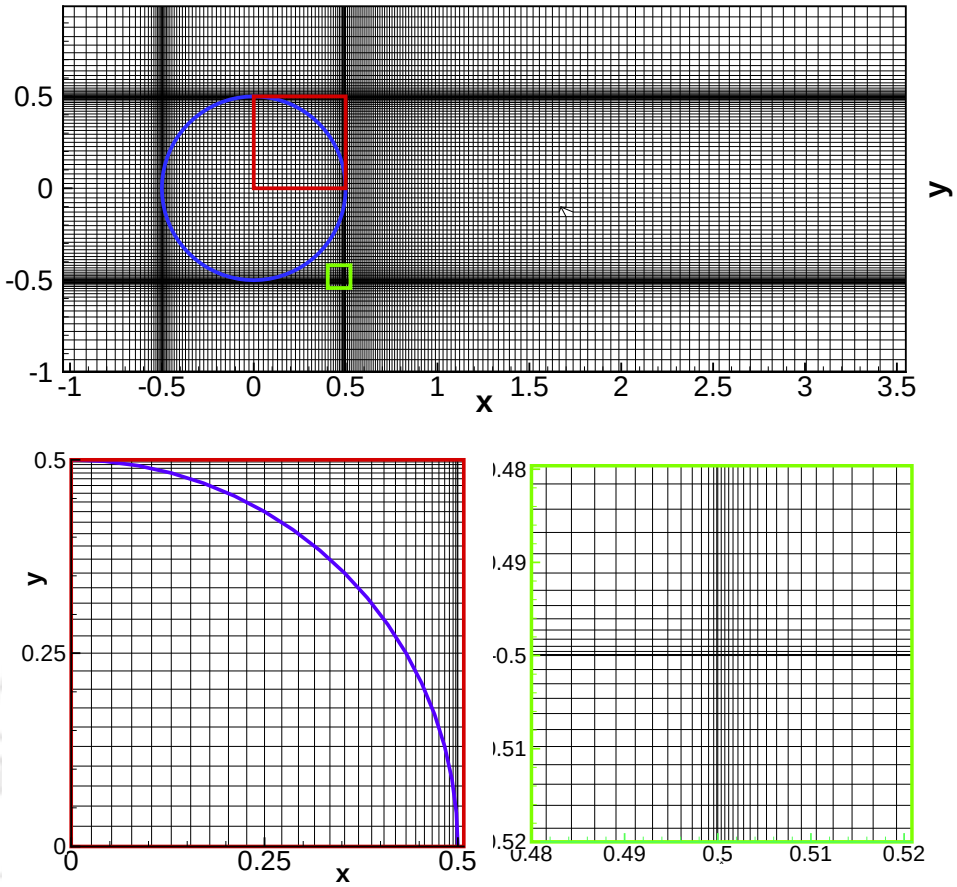

Figure 4.3: Representative grid and close-up views of parts of the grid

4.3 Grid independence and code validation

In order to validate our code, we present the streakline simulation from our computation depicting the well-known von Kármán vortex street for $Re = 140$ with the the experimental results of Taneda [36, 154] in figure 4.4. It is heartening to see the striking similarity between our numerical results (figure 4.4(b)) and the experimental visualization for the entire photograph available in literature (figure 4.4(a)). Note that while we were able to accomplish such a comparison on a grid of size 361×241 over a domain of dimension $30.5l \times 13l$, in [90], it could be achieved on a 1400×700 grid over a domain of size $14l \times 13l$, that too, only for a small length behind the cylinder.

Figure 4.4: Streaklines for the flow past an impulsively started circular cylinder for $Re = 140$: (a) Taneda's experiment [154] and (b) Current simulation.

In table 4.1, we compare our computed results for $Re = 9500$ on three different grid sizes 451×361, 526×361 (with $\Delta t = 10^{-3}$) and 601×481 (with $\Delta t = 10^{-4}$) at different time stations in order to study the influence of grid size on the characteristics of the flow. Here we present the wake length L, which is the distance between rear stagnation point A of the cylinder and the end of the separation at the point B, the separation angle θ_s, which is the angle between the x-axis and the line joining the center of the cylinder and the separation point S on the cylinder and the location of the primary vortex center (x, y) in the upper half of the cylinder (see figure 4.5). The maximum differences in all the values of the parameters are found to below 5% signifying the grid independence of the computed results.

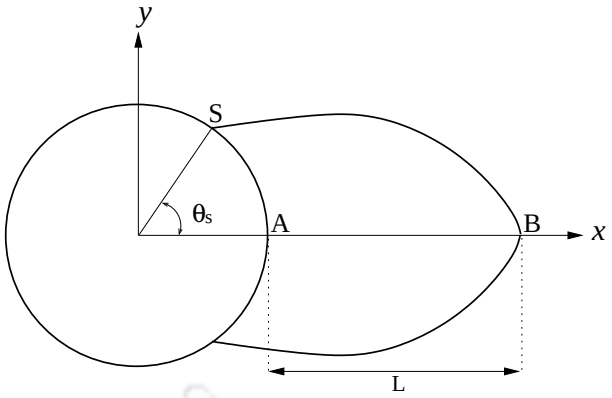

Figure 4.5: Flow parameters corresponding to tables 4.1 and 4.2 for the flow past an impulsively started circular cylinder: A is the rear stagnation point, B, the wake stagnation point, L, the wake length, S, the separation point and θ_s, the angle of separation.

We also endeavored to see how our computation on Cartesian grid fares with the one carried out in polar grid. Quite interestingly, despite drastically different in nature and the polar grid having obvious advantage of grid resolution on the surface of the cylinder, both the grids resulted in simulations which are visually impossible to differentiate. This can be seen from the streamlines for $Re = 5000$ at time $t = 2.5$ in figure 4.6, where the polar grid computation is from [77].

Table 4.1: Grid Independence of the computed results on three different grid of size 451×361, 526×361 and 601×481 for $Re = 9500$

Mesh		M1	M2	M3
Grid Size		451×361	526×361	601×481
$t = 0.5$	θ_s	65	64.28	64.81
	L_s	0.031	0.028	0.030
	(x, y)	$(0.4307, 0.2831)$	$(0.4307, 0.2831)$	$(0.4307, 0.2831)$
$t = 0.75$	θ_s	74	72.85	73.695
	L_s	0.0596	0.0554	0.0587
	(x, y)	$(0.4145, 0.3345)$	$(0.4172, 0.3289)$	$(0.4176, 0.3301)$
$t = 1$	θ_s	80	79.714	80.007
	L_s	0.0889	0.0872	0.0865
	(x, y)	$(0.4373, 0.3473)$	$(0.4367, 0.3455)$	$(0.4380, 0.3468)$
$t = 1.25$	θ_s	84	83.14	83.29
	L_s	0.1389	0.1317	0.1357
	(x, y)	$(0.5339, 0.3078)$	$(0.5197, 0.3175)$	$(0.5245, 0.3185)$
$t = 1.5$	θ_s	89	87.428	88.71
	L_s	0.2333	0.222	0.228
	(x, y)	$(0.5713, 0.2575)$	$(0.5545, 0.2754)$	$(0.5672, 0.2683)$

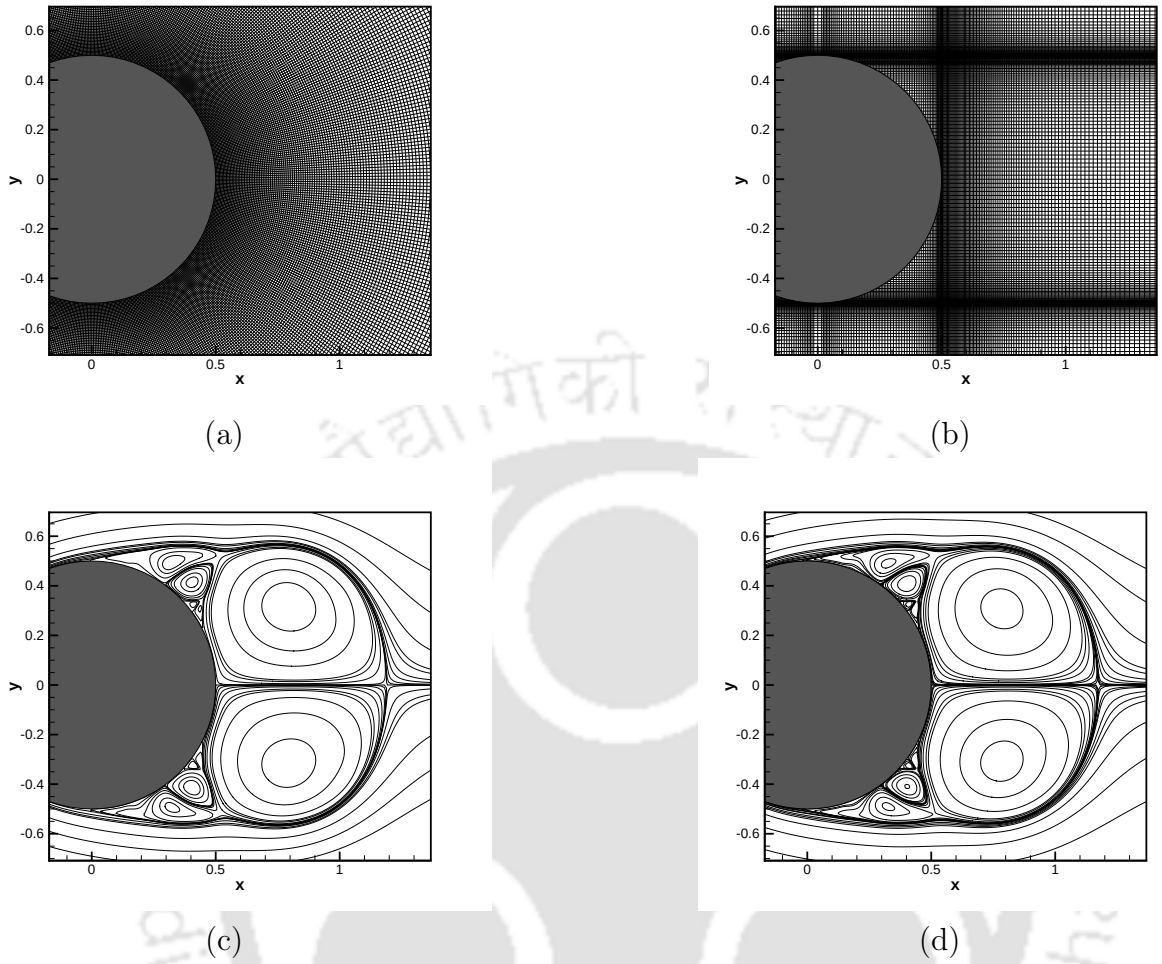

Figure 4.6: Comparison of Cartesian and polar grid computations: (a) grid used in [77], (b) grid used in the present computation, (c) streamlines for $Re = 5000$ at time $t = 2.5$ from from [77] and (d) streamlines for $Re = 5000$ at time $t = 2.5$ from the current computation.

4.4 Results and Discussions

It is a well-known fact for an unsteady laminar flow around a circular cylinder, the flow is irrotational everywhere instantly after the fluid is set into the motion. Momentarily after the fluid movement, the boundary layer starts to grow on the cylinder's surface, leading to separation. Separation is first seen at the rear stagnation point. After a short period, for flows with $Re > 5$, two symmetrical vortices appear behind the cylinder and begin to grow. There is no flow distortion for $Re \leq 5$, and our study confirms it. At $Re \approx 6$, although boundary layer separation takes place on the cylinder surface, the flow remains steady and laminar. Literature confirms that the flow becomes unsteady beyond

some critical Reynolds number(Re_c); numerical studies indicate this Re_c to lie in the range $43 \leq Re_c \leq 50$, where Hopf bifurcations occurs. With increase in Re, the flow becomes more complicated with the appearance of secondary and tertiary vortices. For $Re > Re_c$, the phenomenon of vortex shedding, characterised by von Kármán vortex street starts to appear. Keeping all the above in mind and depending upon the characteristics observed within each range, we have divided the flow regime into the following parts for the Reynolds numbers considered in this study, viz., $5 \leq Re \leq 9500$:

- Flow structures for $5 \leq Re \leq 40$, also known as a steady-state region.
- Flow structures for $100 \leq Re \leq 300$. In this region wake behind the circular cylinder becomes unstable. Oscillations in the wake grow in amplitude and finally leading to vortex shedding with the formation of array of vortices, also known as the von Kármán vortex street.

For $Re > 300$, We focus only on the early stage of the flow, i.e., in the laminar regime.

- Flow structures for $300 \leq Re \leq 1000$: In this regime, secondary vortices form at the initial stage but do not split up further. The secondary flow structure is characterized by the appearance of: (i) bulge phenomenon and (ii) isolated secondary eddy.
- Flow structures for $3000 \leq Re \leq 9500$: Here the most complicated flow properties are associated with the secondary phenomena α, β and tertiary phenomena sub-α and sub-β .

4.4.1 Flows for $5 \leq Re \leq 40$

This is one of the most studied region for the flow past a stationary circular cylinder. As mentioned above, two symmetrical vortices appear behind the cylinder for $5 \leq Re < Re_c$, and with time, They grow in size until it reaches a stead-state.

In figure 4.7, we show the steady-state streamlines for Re = 10, 20, and 40, where one can see that as Re increases, the size of wake also increases. We further present our computed L, θ_s (see Figure:4.5), and C_D in table 4.2 in which is calculated by utilizing the momentum balance along the horizontal direction. We then compared our results with

established numerical as well as the experimental results of Coutanceau and Bouard [27]. We also compare the post-processed surface vorticity for Res mentioned above in figure 4.8. In all the cases, our results are found to be extremely close to the available numerical and experimental results, both qualitative and quantitatively.

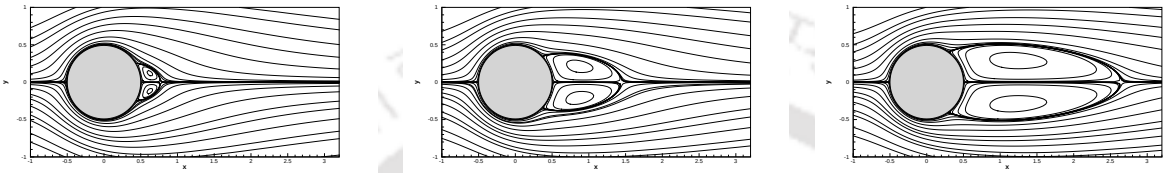

(a) (b) (c)

Figure 4.7: Steady-state streamlines behind the circular cylinder for (a) $Re = 10$, (b) $Re = 20$ and (c) $Re = 40$.

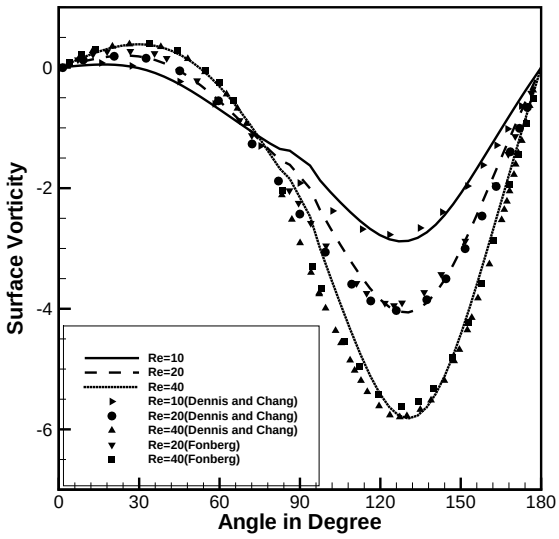

Figure 4.8: Surface vorticity distribution in the steady-state range.

Table 4.2: Comaprison of wake lengths, separation angles and drag coefficients for different Reynolds numbers for circular cylinder.

	Re	[27] (exp)	[137]	[152]	[101]	[87]	[66]	[93]	Present
	10	—	0.504	—	—	—	—	0.533	0.531
L	20	1.86	1.851	1.860	1.940	1.860	1.825	1.830	1.874
	40	4.38	4.625	4.560	4.660	4.620	4.420	4.250	4.278
	10	—	2.699	—	—	—	—	2.629	2.690
C_D	20	—	1.949	2.16	2.07	2.100	2.052	2.172	2.160
	40	—	1.439	1.61	1.55	1.580	1.534	1.590	1.576
	10	—	29.732	—	—	—	—	30	29.69
θ_s	20	44.4	43.141	43.9	44.1	44.40	43.50	45	42.66
	40	53.4	53.226	53.4	54.1	54.1	53.54	54	53.08

4.4.2 Flows for $100 \leq Re \leq 300$

Beyond $Re \geq Re_c$, the flow past an impulsively started circular cylinder becomes periodic sooner or later in the flow evolution process and is known to develop vortex shedding represented by the von Kármán vortex street. The range of Reynolds numbers chosen in this section typically exhibits this phenomenon. The fundamental difference between the present Re range with the previous one is that the wake behind the cylinder develops quickly because of the rapid development of velocity with time, and there is a development of secondary vortex in this region. As time progresses, the wake grows in size and strength. The flow undergoes different phases throughout the evolution till the development of periodic vortex shedding. These phases are portrayed in figures 4.9(a)-(l), which show the evolution of streamlines corresponding to different stages of flow for $Re = 200$. This Re may be considered as the representative of all the three Res presented in this section, although the duration of the stages will vary for different Re. The last three figures 4.9(j)-(l) represent a typical vortex shedding cycle, where one can see two eddies being shed behind the cylinder and washed away into the wake region within each cycle. These three figures are half a vortex shedding cycle apart and figure 4.9(k) is a mirror image of figures 4.9(j) and 4.9(l).

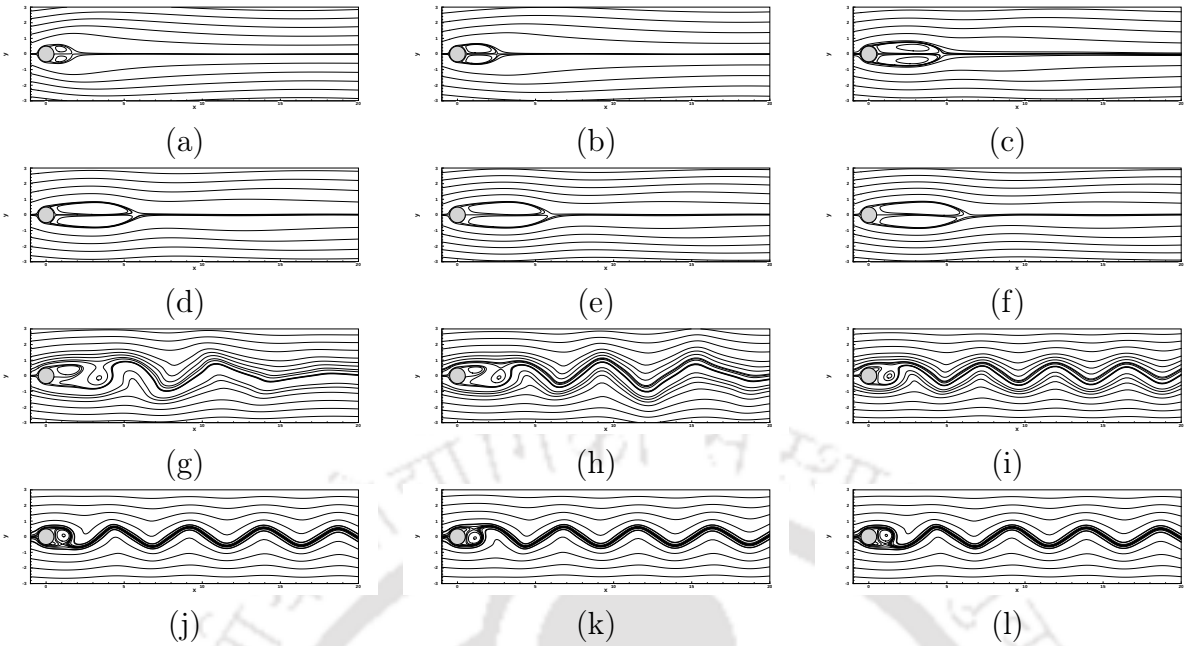

Figure 4.9: Evolution of streamlines for Re = 200 for flow past a circular cylinder at: (a) $t = 2$, (b) $t = 4$ (c) $t = 10$, (d) $t = 55$, (e) $t = 56$, (f) $t = 58$, (g) $t = 75$, (h) $t = 80$, (i) $t = 110$, (j) $t = 281$, (k) $t = 283.5$ and (l) $t = 286$.

Table 4.3: Comparison of the of maximum width l_{max} and the abscissa of this maximum x_{lmax} of the wake with experimental result of [18] for $Re = 200$, 550 and 3000 at different time stations (the experimental data within parenthesis).

t		1.0	1.5	2.0	2.5	3.0
$Re = 200$	x_{lmax}/D	0.39 (0.35)	0.42 (0.51)	0.62 (0.65)	0.73 (0.76)	0.85 (0.86)
	l_{max}/D	0.86 (0.94)	0.92 (0.97)	0.98 (1.02)	1.02 (1.07)	1.06 (1.10)
$Re = 550$	x_{lmax}/D	0.31 (0.30)	0.42 (0.50)	0.68 (0.66)	0.78 (0.76)	0.85 (0.85)
	l_{max}/D	0.93 (0.94)	0.98 (0.98)	1.02 (1.03)	1.08 91.10)	1.14 (1.16)
$Re = 3000$	x_{lmax}/D	0.19 (0.19)	0.28 (0.26)	0.41 (0.40)	0.69 (0.73)	0.83 (0.84)
	l_{max}/D	0.97 (0.93)	1.01 (0.98)	1.08 (1.04)	1.13 (1.11)	1.19 (1.20)

We have tabulated the evolution of maximum width l_{max} and the abscissa of this maximum x_{lmax} of the wake for $Re = 200$, 550 and 3000 in table 4.3 and compared them with the experimental results of Bouard and Coutanceau [18]; one can see a very close match between all of them. Figure 4.10 shows the evolution of drag and lift coefficients for

$Re = 100$, 200 and 300 from the start of the flow to the establishment of vortex shedding. For the range of Reynold number considered here, a pair of symmetric vortices develop behind the cylinder shortly after the flow has started (see figures 4.10(a)-(c)). We can see from figure 4.10(a) that after the impulsive start of the flow, the drag coefficient rises to a very high value. But as time progresses, the value of the drag coefficient begins to fall, and the eddies start to grow in size (see figures 4.9(a)-(f)). As soon as the flow subsides, a quasi-steady state develops with no lift force. The duration of this state decreases with the increase in Re. From figure 4.9(f), we can see that a small fluctuation setting in at the eddy trail, leading to the break in symmetry. With the onset of asymmetry, the lift force becomes nonzero around $t = 60$ for $Re = 200$ as in figure 4.10(b) (also refer figure 4.9(d)). A few moments later, the vortices behind the cylinder start oscillating gradually (see figures 4.9(g)-(j)), and vortex shedding starts leading to the development of the so-called von Kármán vortex street. Note that throughout the computation of all the Reynolds numbers considered in this study, no artificially induced perturbation was introduced to break the symmetry; asymmetry sets in spontaneously for all $Re \geq Re_c$.

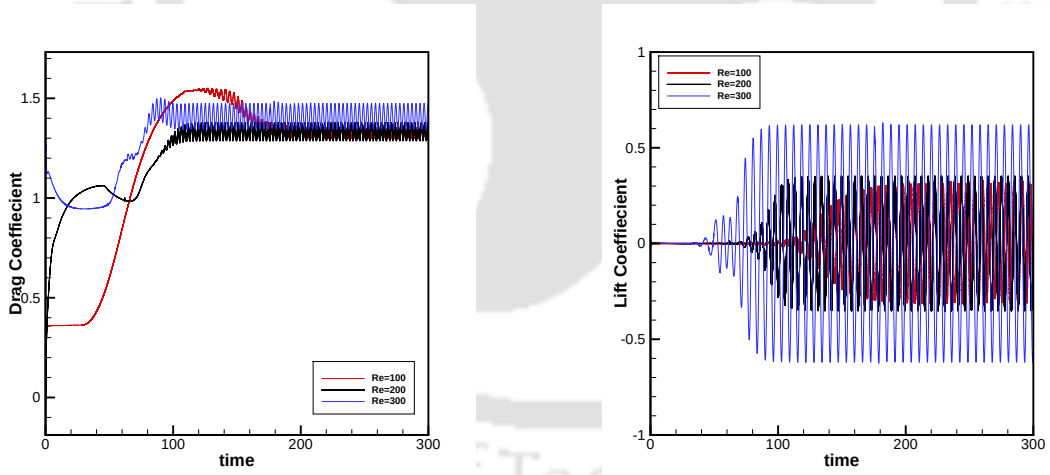

(a) (b)

Figure 4.10: Evolution of (a) Drag coefficient and (b) Lift coefficient for $Re = 100$, 200 and 300.

One of the objectives of the present work is to analyze the properties of the streamline and streakline patterns behind a circular cylinder during vortex shedding. Keeping that in mind, we present the streamlines, post-processed vorticity contours and streaklines for $Re = 100,\ 200,$ and 300 in the left, middle and right panels of figure 4.11 respectively.

These figures correspond to the instants when the lift coefficients reach their peak values during their own vortex shedding cycles. In incompressible flow, vorticity is generated only at solid boundaries, which, for this problem is the surface of the cylinder, and this vorticity dwells within the fluid. Thus the streaklines portrayed in figures 4.11(c1)-(c3) provide a clear view of dominant places in the flow field where the vorticity is inherent. Our computed streakline patterns for the range of Re in these figures are in conjunction with those depicted in [2, 4]. Note that the relationship between instantaneous streamlines and streaklines is exceptionally complex and visualization of both is necessary for a proper understanding of flow field character. In the initial stages, the wake behind the cylinder is in a closed-loop for the streamline patterns (see figures 4.11(a1)-(a3)). But once the vortex-shedding process begins, this closed wake becomes open, and fluid starts to flow in from the surrounding. Our computed streaklines, despite thinning down, remain continuous without breakage. Streaklines now stand for a flexible barrier which a fluid can never cross, and is quite apparent from the figures 4.11(c1)-(c3). The fluid entering the wake moves in and jumps towards the cylinder surface sequentially from both sides and is eventually forced out of the wake and roll-up. The two sets of vortex sheets braid with each other in the far wake, and we are able to capture them entirely. Once shedding starts, the vortices are shed systematically, alternatively from the two sides of the cylinder. It is also apparent from the crests and troughs of the sinuous waves in the streamlines shown in figures 4.11(a1)-(a3), which reflect the alternatively positive and negative vorticities of the eddies presented in figures 4.11(b1)-(b3). Shedding frequency increases over time until a limiting condition is reached. With the onset of vortex shedding, the drag coefficient starts decreasing again, and eventually, both the drag and lift coefficients becomes periodic as the flow becomes fully developed (see figure 4.10).

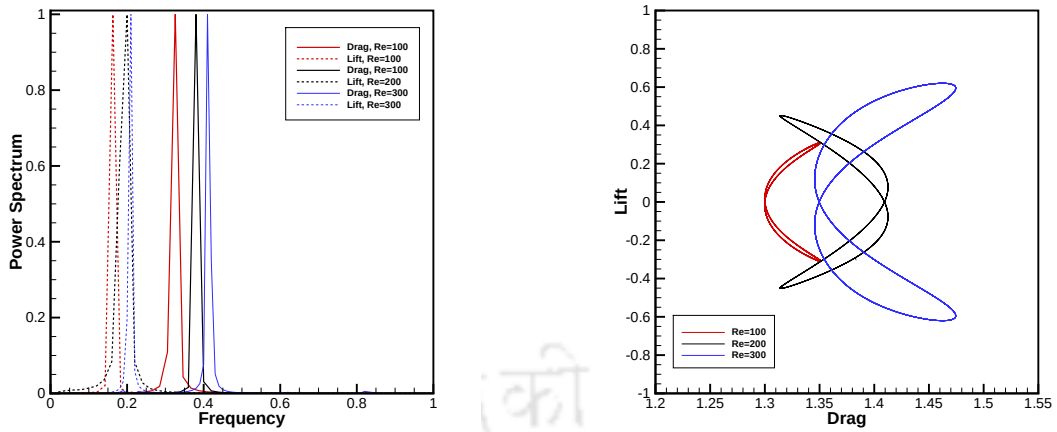

(a) (b)

Figure 4.12: (a) Power spectrum of drag and lift coefficients, and (b) Phase diagram of drag and lift coefficients for $Re = 100$, $Re = 200$, and $Re = 300$.

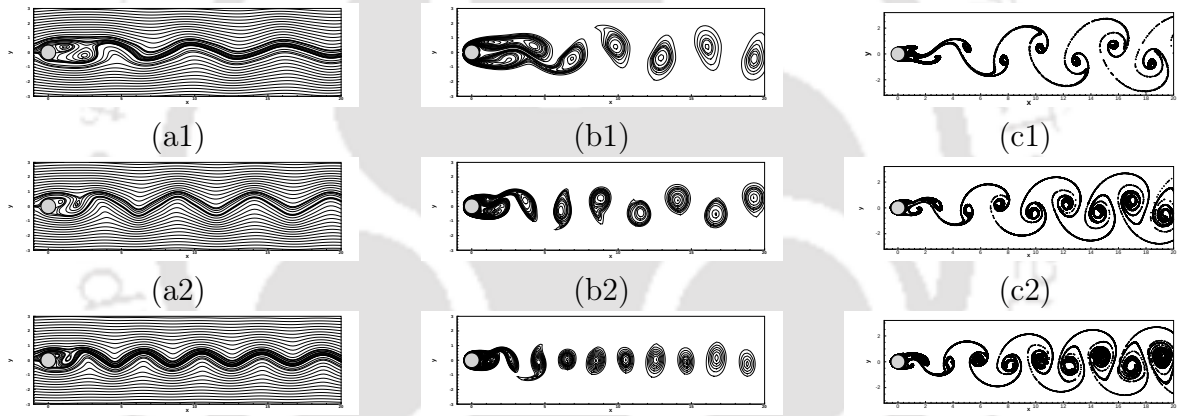

(a1) (b1) (c1)

(a2) (b2) (c2)

(a3) (b3) (c3)

Figure 4.11: Vortex shedding behind the circular cylinder: Streamlines ((a1)-(a3)), vorticity contours ((b1)-(b3)) and streaklines ((c1)-(c3)) for $Re = 100$ (top), $Re = 200$ (middle) and $Re = 300$ (bottom) .

The dominant frequency of the drag and lift variations, can be computed by a spectral analysis of time samples of these coefficients. The power density spectra of this analysis normalized by the maximum value for $Re = 100$, 200 and 300 is shown in figure 4.12(a); figure 4.12(b) displays the phase plane of the drag and lift coefficients for the same time sample for $Re = 100$, 200 and 300; it clearly establishes that the frequency of drag coefficients is twice that of the lift coefficients which is also exemplified by figure 4.10. In table 4.4, we compare our computed Strouhal numbers, drag and lift coefficients for these Re with established experimental and numerical results; for all the Re, we obtain

very close comparisons. As can be seen from the table, the frequency of vortex shedding increases with the increase in Re which is also obvious from figure 4.11.

Table 4.4: Comparison of Strouhal number, drag and lift coefficients of the periodic flow for $Re = 100$, 200, 300.

Re	100			200			300		
Reference	St	C_D	C_L	St	C_D	C_L	St	C_D	C_L
Frank *et al. [39]*	-	-	-	0.194	1.31	± 0.65	0.205	1.32	± 0.84
Williamson [166]	0.163	-	-	0.185	-	-	0.203	-	-
Silva [143]	0.160	1.39	-	0.180	-	-	0.200	1.27	-
Le *et al.* [97]	0.160	1.37 ± 0.009	± 0.323	0.187	1.34 ± 0.030	± 0.430	0.200	-	-
Berthelsen and Faltinsen [15]	0.169	1.38 ± 0.010	± 0.340	0.200	1.37 ± 0.046	± 0.700	-	-	-
Wang *et al.* [162]	0.170	1.379	± 0.357	0.195	1.262	± 0.708	0.206	1.174	-
S.Sen [134]	0.165	1.394 ± 0.007	± 0.191	0.197	1.375 ± 0.038	± 0.453	0.209	1.401 ± 0.068	± 0.607
Present Study	0.162	1.325 ± 0.026	± 0.306	0.200	1.333 ± 0.046	± 0.351	0.210	1.41 ± 0.0645	± 0.62

Note that for the results shown in this section, computations were performed using a rectangular domain $[-8D, 25D] \times [-8D, 8D]$ (where $D = 1$ is the diameter of the cylinder with center $(0, 0)$) up to non-dimensional time $t = 500$. However, behavior of the flow at a much later time (say around $t = 5000$) for $Re = 300$ is known to be fraught with several modes of vortex shedding far downstream the cylinder, as some recent studies [62] suggest. However, the second mode of vortex shedding appears much away from the downstream length $25D$ considered in the current study.

4.4.3 Flows in the early stages for $300 \leq Re \leq 550$

The significant feature of the this range ($300 \leq Re \leq 800$) is the (i) bulge and (ii) secondary eddy phenomenon which is also corroborated by experimental studies. Initially, there is a deflection in streamlines between the rear stagnation and separation points. Some instants later, streamlines close to the cylinder's wall deviate from the cylinder causing a bulge pattern known as the bulging phenomenon. For $Re = 300$, it appears at dimensionless time $t = 2.5$ (see figure 4.13) and for $Re = 550$, at time $t = 1.5$ approximately (see figure 4.14(b)). For $Re > 300$, with time, this bulge triggers a second separation of flow leading to the formation of a small secondary vortex known as the secondary eddy phenomenon. This phenomenon can be seen at $t = 2.5$ for $Re = 550$ (see figure 4.14(b)). The strength of this secondary eddy increases (see figure 4.14(c)) as time progresses and has a rotation opposite to the primary eddy. The comparison of our computed data of early flow evolution for $Re = 550$ with experimental results [18] can also

be found in table 4.3 presented in section 4.4.2. One can also find the existence of these eddies from the distribution of vorticities on the cylinder surface in figure 4.15, where two successive change of signs indicates the presence of a vortex. For example in figure 4.15(b), one can clearly see the proof of the existence of the secondary eddy phenomena at time $t = 2.5$ for $Re = 550$ at around $\theta = 42.6^{\circ}$, which was clealy absent in figure 4.15(a) for $Re = 300$. In figures 4.13(b) and 4.14(d), we also compare the computed streamlines with the experimental visualization of [18] for $Re = 300$ and 550 respectively at time $t = 2.5$. These figures exemplify the extreme closeness of our numerical results with the experimental ones, thus demonstrating the efficiency of our scheme. We have also presented a quantitative comparison of velocity along the flow axis behind the cylinder in figure for $Re = 550$ (see figure 4.4.3).

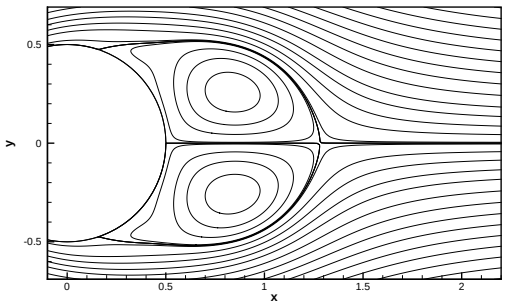

(a)

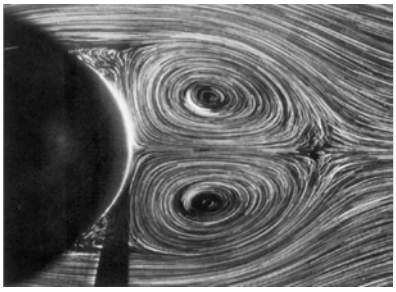

(b)

Figure 4.13: Streamlines for $Re = 300$ at $t = 2.5$, (a) Numerical (b) Experimental [18].

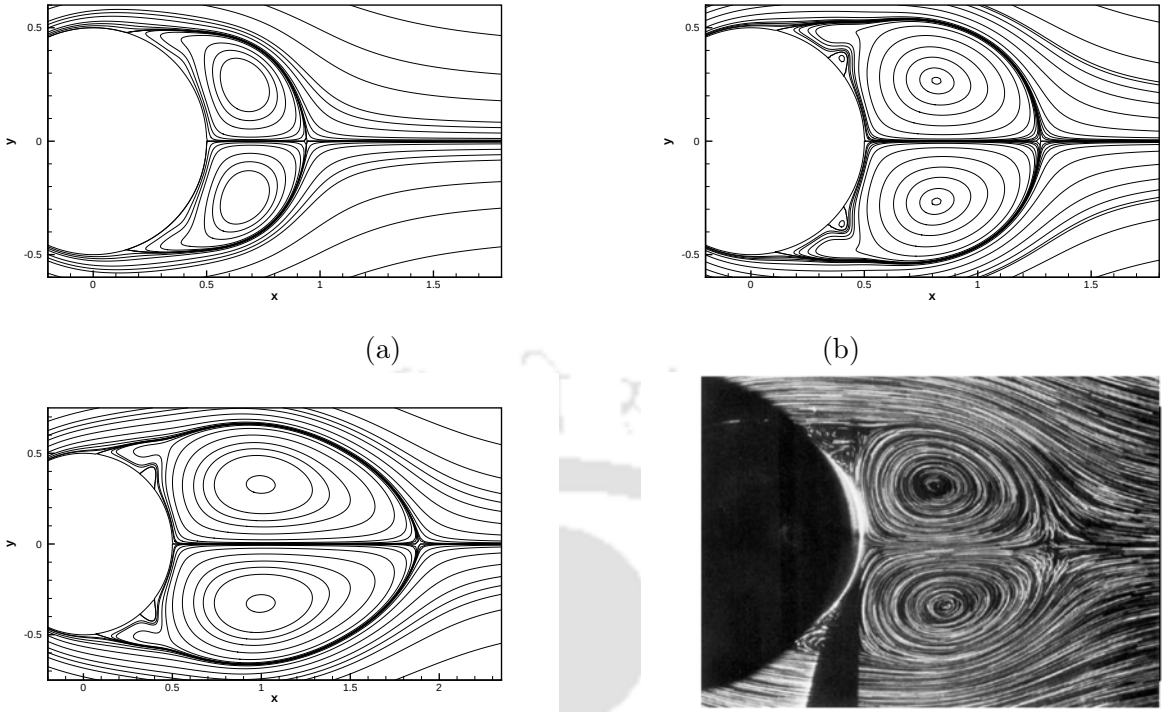

Figure 4.14: Streamlines for $Re = 550$ at (a) $t = 1.5$, (b) $t = 2.5$, (c) $t = 5.0$ and (d) $t = 2.5$ (Experimental) [18].

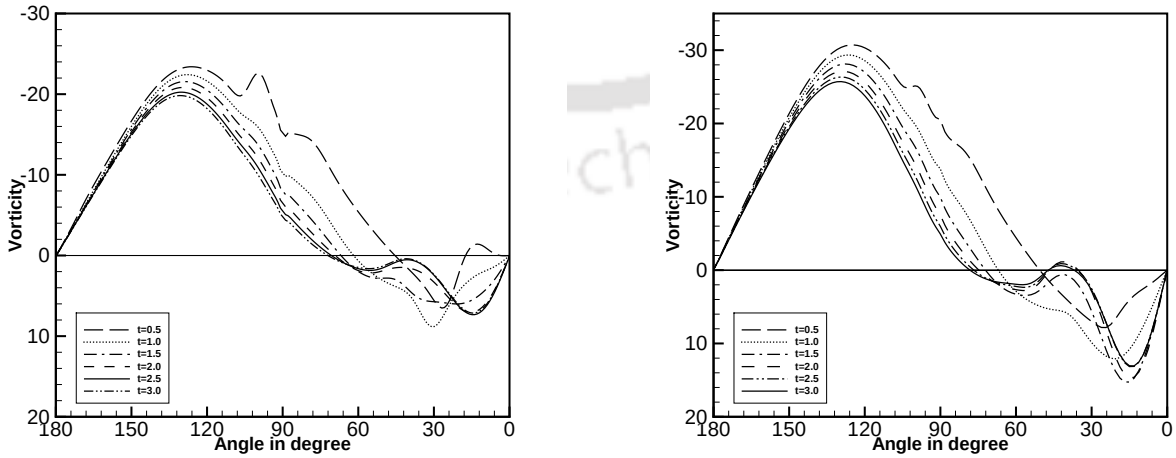

Figure 4.15: Surface vorticity at different time stations for (a) $Re = 300$ and (b) $Re = 550$.

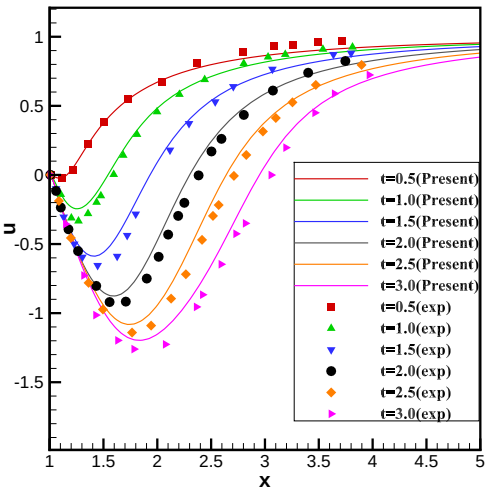

Figure 4.16: Comparison between experimental [18] and numerical results for the velocity distribution on flow axis for $Re = 550$.

4.4.4 Flows beyond $Re = 550$

Flow around a cylinder eventually becomes three dimensional and turbulent at these Res. However, during the early stages, the flow is still laminar as suggested by laboratory experiments and hence we limit our discussion only to the very early stages for this range of Reynolds numbers. This range is characterized by the intriguing interplay between secondary and tertiary vortices leading to very interesting flow phenomena such as α, β, sub-α and sub-β. Before embarking into flow description for this range of Res, we briefly explain these phenomena; the readers may refer to figures 4.17 and 4.18. In these and subsequent figures, only the upper part behind the cylinder is depicted as the flow is still symmetric in the early stages of the flow.

4.4.5 α, β, sub-α and sub-β phenomena

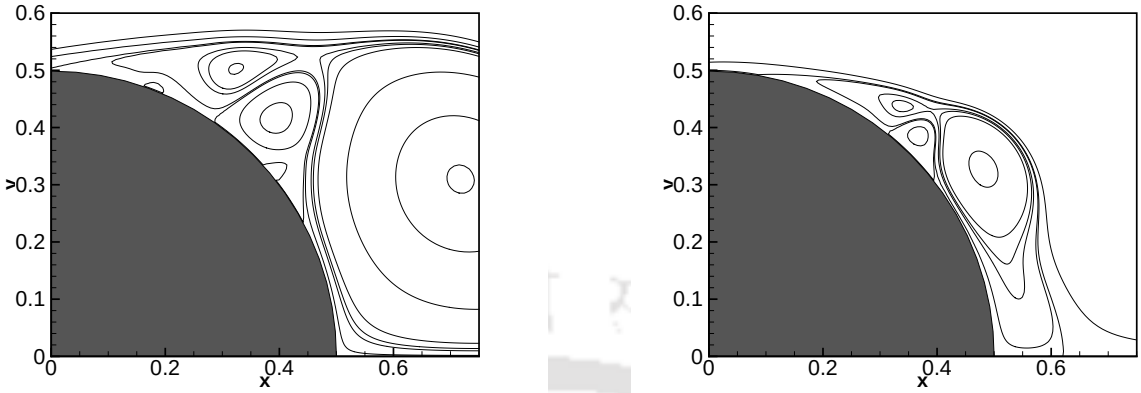

Figure 4.17: Secondary vortex phenomena for $Re = 5000$: (a) α-phenomenon at $t = 2.25$ and (b) β-phenomenon at $t = 1.1$.

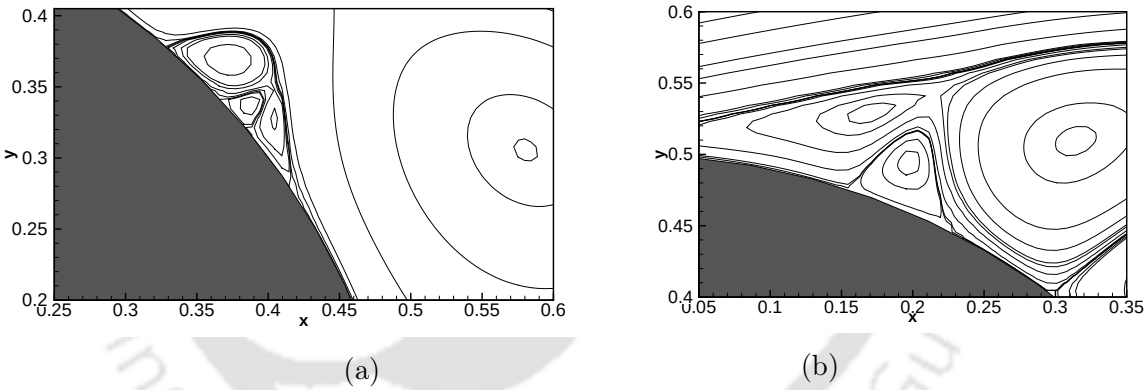

Figure 4.18: Tertiary vortex phenomena for $Re = 5000$: (a) sub-α phenomenon at $t = 1.45$ and (b) sub-β phenomenon at $t = 3.15$.

The terms α and β phenomena were coined by Bouard and Coutanceau in their pathbreaking experimental study [18] in 1980. For some Reynolds numbers in the regime, when the primary vortex P is still growing behind the cylinder and stable, as time progresses, the streamlines close to the cylinder initially deviate from the surface causing a bulge pattern eventually giving rise to a secondary eddy. This eddy grows in size to such an extent that it touches the boundary of the main eddy, thereby splitting the main one into two parts and isolating the region of the wake next to the separation point where another secondary eddy becomes visible. When these two secondary eddies become equivalent in size and

strength, the phenomenon is known as the α-phenomenon (see figure 4.17(a)). On the other hand, for certain Res, just after the start of the flow, a very thin recirculating wake is formed; but soon afterwards, the core of this recirculating zone rotates in one piece with a speed which is much faster than the other part of the separated zone, forming a vortex which gains strength and size with time. After a while, this vortex separates the initial wake into two parts where the one situated near the point of separation is occupied by a pair of secondary eddies, which is known as the β-phenomenon (see figure 4.17(b)). When the α and β phenomena are replicated at the tertiary vortex level, it is termed as sub-α and sub-β phenomena respectively (see figure 4.18(a)-(b)), which was coined by Kalita and Sen [77].

We now provide a comprehensive description of the flow for $Re = 7500$ in the early laminar stage up to $t = 5.0$. This description is more or less representative of the flow structures during the early stages for all the Reynolds numbers considered in this section as would be seen in section 4.4.6. For the benefit of the readers, we have provided a schematic of the primary, secondary and tertiary vortices appearing on the surface of the cylinder in the upper half in figure 4.19.

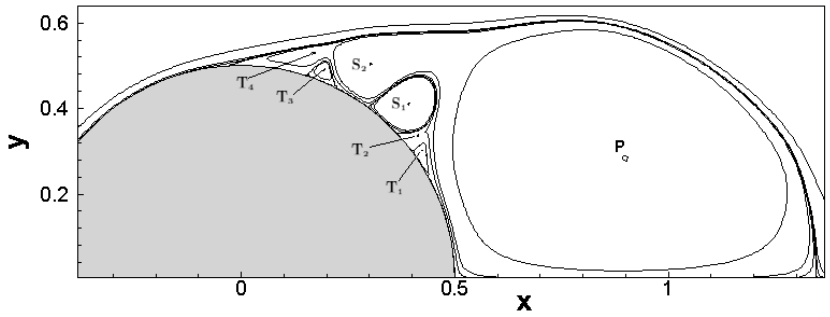

Figure 4.19: Schematic diagram for α, β, sub-α and sub-β phenomena. The letters P, S and T stand for primary, secondary and tertiary vortices respectively.

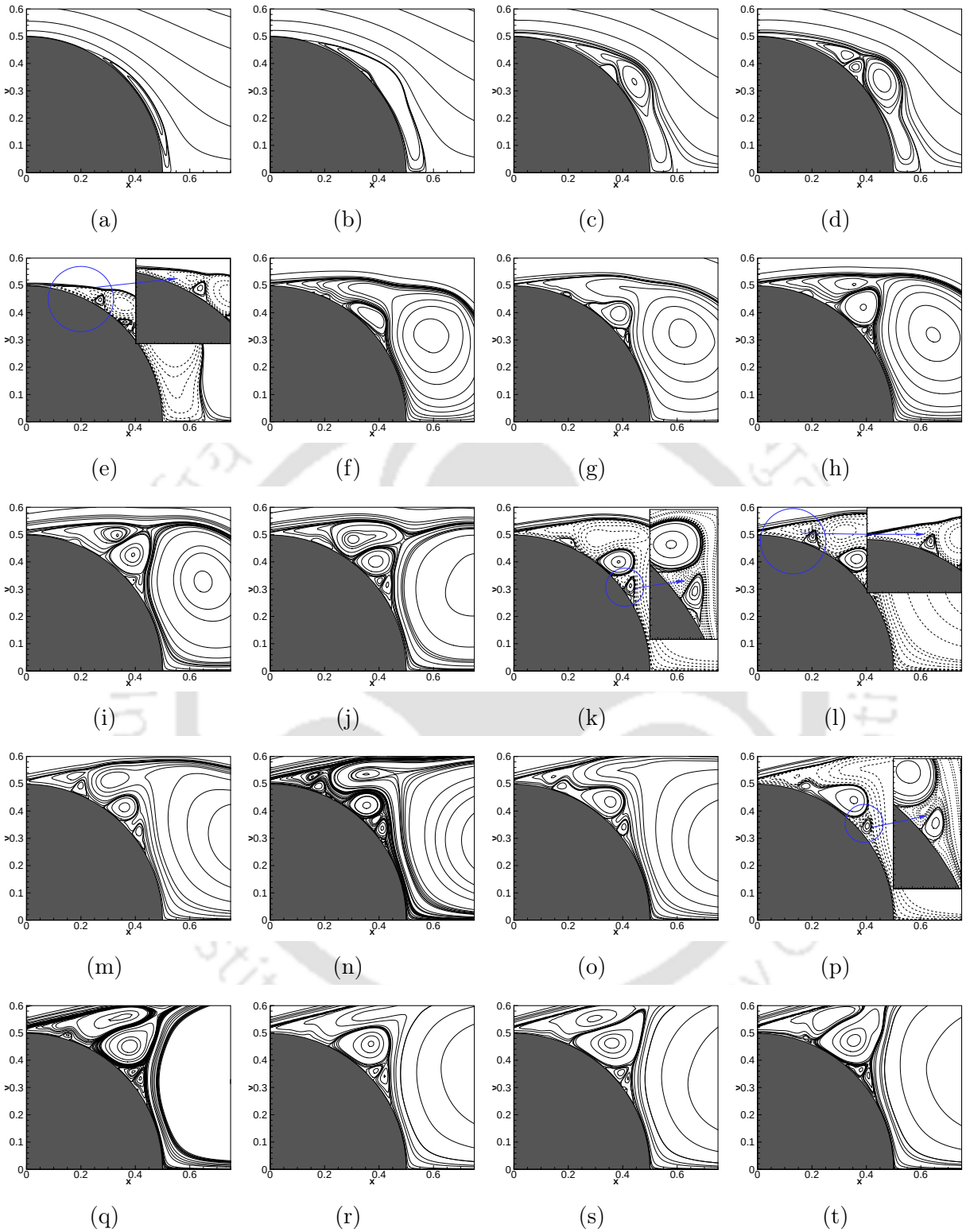

Figure 4.20: Evolution of streamlines for Re = 7500 for flow past a circular cylinder at: (a) $t = 0.5$, (b) $t = 0.85$ (c) $t = 0.95$, (d) $t = 1.05$, (e) $t = 1.3$, (f) $t = 1.75$, (g) $t = 1.75$, (h) $t = 2.0$, (i) $t = 2.05$, (j) $t = 2.3$, (k) $t = 2.4$, (l) $t = 2.6$, (m) $t = 2.65$, (n) $t = 2.95$, (o) $t = 3.10$, (p) $t = 3.15$, (q) $t = 3.75$, (r) $t = 4.00$, (s) $t = 4.25$, and (t) $t = 5.00$.

In figure 4.20, we portray the evolution of primary, secondary and tertiary vortices for $Re = 7500$, which in the process is characterised by the occurrence of α- , β-, sub-α , and sub-β phenomena. At time approximately $t = 0.25$, a pair of symmetric vortices are formed owing to typical boundary layer separation, which can be seen more clearly behind the cylinder at $t = 0.50$ (figure 4.20(a)). As time progresses, the pair of Primary vortices (denoted by 'P' in figure 4.19) grow symmetrically in size and strength. Simultaneously, the core of the Primary vortex moves downstream in the upward direction. At around $t = 0.85$ (figure 4.20(b)), there is a secondary separation on the cylinder's surface leading to the formation of a secondary vortex (S_1 in figure 4.19). This vortex grows in size and strength with time and becomes prominent at around $t = 0.95$ (figure 4.20(c)) and divides the primary vortex into two parts, one of which is the core. We can also see this phenomenon from three alternating rotating zones of surface vorticity of the cylinder (see figure 4.20 (b)-(d)).

However, the weaker part (S_2 in figure 4.19) maintains some communication with its core. With time, both the core and the secondary vortex gain size and strength which triggers the narrowing of the communication between the two parts of the core (see figure 4.20(e)). But as time progresses, the primary vortex becomes more prominent in size again. Both its parts (namely P and S_2) start getting more robust and starts sandwiching the secondary vortex S_1 from left and right, resulting in the reduction of its strength and size at time $t \approxeq 1.05$ (figure 4.20(e)). This is the onset of β-phenomenon.

Momentarily the size and strength of the arm S_2 of the primary vortex gets reduced and reconnects with P. Following that, the secondary vortex S_1 regains strength, grows in size and divides P again to recreate the arm S_2. It grows in size and intensity along with the other secondary vortex S_1 (figure 4.20(f)-(h), and at time $t = 2.05$, they become almost equal in size and strength (figure 4.20(i)), and as such, constitute the α-phenomenon. Both the secondary vortices S_1 and S_2 continue to grow in size and strength (figure 4.20(h), (i)).

Next, we lay down the details of the tertiary vortex dynamics for $Re = 7500$, which first appears on the cylinder's surface at $t \approxeq 1.15$, with the secondary vortex S_2 providing a cushion to it. A closer look at figure 4.20(e) reveals that this vortex appears at $\theta \approxeq 58^{\circ}$; note that during this time, the center of secondary vortex S_1 moves down to the position

$\theta = 45^{\circ}$ on the cylinder's surface. While slowly evolving in size and intensity, this new tertiary vortex divides the primary vortex's arm, S_2, into two parts viz. T_3 and T_4 (figures 4.19 and 4.20(e)). This is nothing but the sub-β phenomenon [77]. This sub-β phenomenon lingers till $t = 1.35$, when the secondary vortex S_2 and its arm reconnects again to form one single vortex pushing the tertiary vortex T_3 downwards reducing its size and strength. After some times, T_3 grows in size and strength (see figure 4.20(i) at $t = 2.05$) which leads to another sub-β phenomenon at $t = 2.60$ (figure 4.20(l)) persisting up to $t = 3.10$ (figure 4.20(o)). The tertiary vortex T_3 is visible till $t = 4.00$ and dissipates afterwards.

In the meantime, similar to the $\alpha-$phenomenon, another interesting event takes place at secondary and tertiary level as early as $t \approxeq 2.00$. A close look at the tertiary vortex T_2 (figures 4.19 and 4.20(h)) at the location $\theta = 42^{\circ}$ reveals that at the instant $t \approxeq 1.85$ (figure 4.20(g)) of the formation of T_2, the streamfunction value of the secondary vortex S_1 cushioning it reaches a local maxima at its center, leading to an adverse pressure gradient. A few moments later, at around $t = 2.4$ this tertiary vortex gains size and strength, and divides the secondary vortex S_1 into two parts T_1 and T_2 (figures 4.19 and 4.20(k)) giving rise to the sub-α phenomenon [77]. At time $t = 2.5$, this tertiary vortex T_2 merges with the secondary one and the split part T_1 of the secondary vortex S_1 gets re-attached. Eventually, the parts of this secondary vortices reconnect to form one single vortex. It resurfaces again at $t = 2.70$, leading to another sub-α phenomenon at $t = 3.15$ (figure 4.20(p)) persisting till $t = 3.45$ after which S_2 and its arm once again coalesce back to form one single vortex. The above occurrences represent the moments when the strengths of these tertiary vortices forming the sub-α phenomenon are almost equal in magnitude (see table 4.5).

Note that in all the cases, the tertiary vortices T_1 , T_2 , T_3 and T_4 are much smaller in size and weaker in strength than their secondary counterparts S_1 and S_2.

Table 4.5: Streamfunction ψ values at the centers of the tertiary vortices constituting the sub-α phenomenon for $Re = 7,500$.

Vortex Center	$t = 2.4$	$t = 3.15$
T_1	0.00281117	0.00149773
T_2	−0.00287632	−0.00146887

4.4.6 Summary on the Reynolds numbers exhibiting secondary and tertiary vortex phenomena

In this section, firstly we summarize the existence of secondary and tertiary vortex phenomena for the Reynolds number in the range of $700 \leq Re \leq 9500$ and provide a brief qualitative and quantitative description of the early evolution of flow for $Re = 3000$, 5000 and 9500

In table 4.6, we summarize the secondary and tertiary vortex characteristics for the early stage of the flow till $t = 5.0$ for all the Reynolds numbers for which we have computed the flow. One should refer to figure 4.19 for the description of the primary vortex P, secondary vortices S_1 and S_2, and tertiary vortices T_1, T_2, T_3 and T_4. Here the first column represents the Reynolds number Re, the second column the instant of time at which the secondary vortices $\mathbf{S}_1$ and $\mathbf{S}_2$ become equivalent in size and strength for the first time, thus auguring the α phenomenon; the entries $(\beta_1, \beta_2, \beta_3)$ in the third column respectively represent the instants at which $\mathbf{S}_1$ is clearly visible, when the pair $(\mathbf{S}_1, \mathbf{S}_2)$ is clearly visible subsequently and the instant at which $\mathbf{S}_2$ gets reattached with $\mathbf{P}$ again, the fourth column represents the times at which sub-α phenomenon occur, the entries (β_1, β_2) in the fifth column respectively represent the instants when $\mathbf{T}_3$ is formed and the pair $(\mathbf{T}_3, \mathbf{T}_4)$ is clearly visible, the entries (β, α) in the sixth column respectively represent the instant at which $\mathbf{T}_3$ emerges to eventually form the sub-β phenomenon and the instant at which the tertiary vortices $\mathbf{T}_3$ and $\mathbf{T}_4$ become equivalent in strength giving rise to the sub-α phenomenon and finally we offer some remarks in the last column.

Re	α	β	sub-α	sub-β	sub-α preceded by sub-β	Remarks
500	...	...	...	...	...	The secondary vortex $\mathbf{S}_1$ appears at around $t = 1.6$ and grows in size creating the arm of the primary vortex $\mathbf{P}$, but never splits into two separate vortices.
750	...	...	...	...	...	$\mathbf{S}_1$ appears at around $t = 1.25$ and eventually splits $\mathbf{P}$ into two parts; however, the secondary vortices $\mathbf{S}_1$ and $\mathbf{S}_2$ are never equivalent in size and strength. $\mathbf{S}_1$ does not reattach with $\mathbf{P}$ again.
800	...	...	...	...	...	$\mathbf{S}_1$ appears at around $t = 1.225$; rest is similar to $Re = 750$.
1,000	...	...	...	...	...	$\mathbf{S}_1$ appears at around $t = 1.15$, splits $\mathbf{P}$ into two parts; $\mathbf{S}_1$ and $\mathbf{S}_2$ are equivalent in size from $t = 4.5$ onwards; however, their strengths are never close to each other. $\mathbf{S}_1$ does not reattach with $\mathbf{P}$ again.
2,000	...	...	...	...	...	$\mathbf{S}_1$ appears at around $t = 1.05$, splits $\mathbf{P}$ into two parts; $\mathbf{S}_1$ and $\mathbf{S}_2$ are equivalent in size from $t = 2.25$ onwards; like $Re = 1,000$ their strengths are never close to each other. In fact, strength of $\mathbf{S}_2$ is almost twice the strength of $\mathbf{S}_1$. $\mathbf{T}_1$ and $\mathbf{T}_2$ make appearance between $t = 2.55$ to 3.0; however, no sub-α phenomenon is observed. $\mathbf{S}_1$ does not reattach with $\mathbf{P}$ again.
3,000			$t = 3.05$.			$\mathbf{S}_1$ appears at around $t = 1.05$, splits $\mathbf{P}$ into two parts; $\mathbf{S}_1$ and $\mathbf{S}_2$ are equivalent in size from $t = 2.1$ onwards; strengths are never close to each other during this period. $\mathbf{S}_1$ does not reattach with $\mathbf{P}$ again.
4,000	$t = 2.65$.	(1.2, 2.2)	$t = 2.75$.	(1.5, 1.85) and (3.25, 3.6).		Once α phenomenon starts, it is persistent throughout the period.
4,500	$t = 2.55$.	(1.1, 2.15)	$t = 2.6$.	(1.4, 1.5) and (3.0, 3.2).		α phenomenon is persistent from inception.
5,000	$t = 2.5$.	(1.1, 2.1)	$t = 1.45$ and 2.545.	(1.3, 1.45) and (2.75, 3.15).		α phenomenon is persistent from inception.
6,000	$t = 2.4$.	(1.1, 2.05)	$t = 1.35$, 2.5 and 3.65.	(1.25, 1.4) and (2.5, 2.7).		After inception, α phenomenon breaks down at around $t = 3.55$; regroups again at 4.5. The sub-β phenomenon at $t = 2.7$ almost leads to a sub-α phenomenon, but not yet.
7,500	$t = 2.3$, 3.9 and 4.35.	(1.1, 2.0)	$t = 2.4$ and 3.15.	1.3 and 2.6.		After inception, α phenomenon breaks down at around $t = 2.6$; regroups again at 3.75. The sub-β phenomenon at $t = 1.3$ almost leads to a sub-α phenomenon, but not yet. At $t = 1.85$, $\mathbf{T}_1$ splits $\mathbf{S}_1$ into two parts creating $\mathbf{T}_2$; at $t = 2.4$, $\mathbf{T}_1$, $\mathbf{T}_2$ and $\mathbf{S}_1$ are almost of the same size unlike what happens in sub-α phenomenon. After the occurrence of sub-α phenomenon at $t = 3.15$, $\mathbf{T}_1$ and $\mathbf{T}_2$ persists throughout.
8,000	$t = 2.2$.	(1.0, 1.5)	2.15, 2.85 and 4.8.	(1.15, 1.275).	(2.0, 2.355)	At $t = 1.2$, $\mathbf{T}_1$, $\mathbf{T}_2$ and $\mathbf{S}_1$ are almost of the same size like $Re = 7,500$ at $t = 1.3$. The sub-α phenomenon at $t = 2.355$ which is preceded by the sub-β phenomenon with the formation of $\mathbf{T}_3$ at $t = 2.0$, the tertiaries $\mathbf{T}_3$, $\mathbf{T}_4$ are persistent till $t = 4.65$. In the meantime their strengths keeps on reducing and increasing alternatively with $\mathbf{T}_4$ showing a tendency of reattaching with $\mathbf{S}_2$. However, $\mathbf{T}_4$ could ultimately reattach with $\mathbf{S}_2$ only at $t = 4.9$. After inception, α phenomenon breaks down at around $t = 2.8$; regroups again at 4.35.
9,500		(1.0, 1.45)	1.85, 3.0, 3.45, 4.2 and 4.65.	(1.1, 1.2).	(2.0, 2.2)	From $t = 1.9$ onwards, $\mathbf{S}_1$ and $\mathbf{S}_2$ are equivalent in size; however, their equivalence breaks down at $t = 2.35$ which regroups again at 2.4 to break down again at 3.1 after which no equivalence in size is seen. $\mathbf{S}_1$ and $\mathbf{S}_2$ are never close to each other in strength. The sub-α phenomenon at $t = 2.2$ which is preceded by the sub-β phenomenon with the formation of $\mathbf{T}_3$ at $t = 2.0$, the tertiaries $\mathbf{T}_3$, $\mathbf{T}_4$ are persistent throughout. As in $Re = 8,000$, after the ups and downs in their strengths, the reattachment of $\mathbf{T}_4$ with $\mathbf{S}_2$ finally takes place at $t = 2.95$. Although α-phenomenon is absent, sub-α phenomenon is very much existent as can be seen from table 4.7. Several tertiary recirculation zones are observed on the surface of the cylinder intermittently (see figure 4.23(b)-(d)). The overall observation for $Re = 10,000$ is similar to $Re = 9,500$.

Table 4.6: Characteristics of the secondary and tertiary vortices for different Reynolds numbers for $0 < t \leq 5.0$.

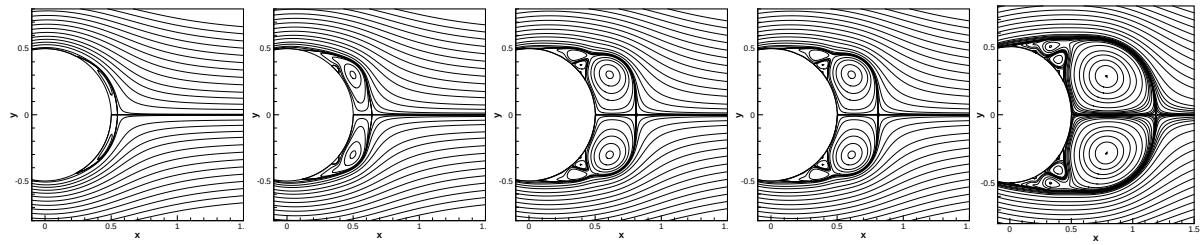

(a) (b) (c) (d) (e)

Figure 4.21: Streamlines for $Re = 3000$ at (a) $t = 0.5$, (b) $t = 1.0$, (c) $t = 1.5$, (d) $t = 2.0$,and (e) $t = 2.5$.

In figures 4.21, 4.22 and 4.23 we show the evolution of streamlines for $Re = 3000$, 5000 and 9500 along with their comparison with some available experimental results. Once again, our computed solutions are extremely close to the experimental ones. The secondary and tertiary vortex phenomena exhibited by these flows are described in table 4.6. The existence of these phenomena is also obvious from the distribution of vorticities on the cylinder surface in figure 4.24 for $Re = 3000$, 5000, 7500 and 9500. The comparison between experimental and numerical results for the velocity distribution on flow axis for these three Reynolds number can be seen in figure 4.25, which is again evident from the proximity of our numerical results with the experimental ones. In table 4.7, we present the strengths of the tertiary vortices T_1 and T_2, which validates the presence of sub-α phenomenon as tabulated in the summary table 4.6.

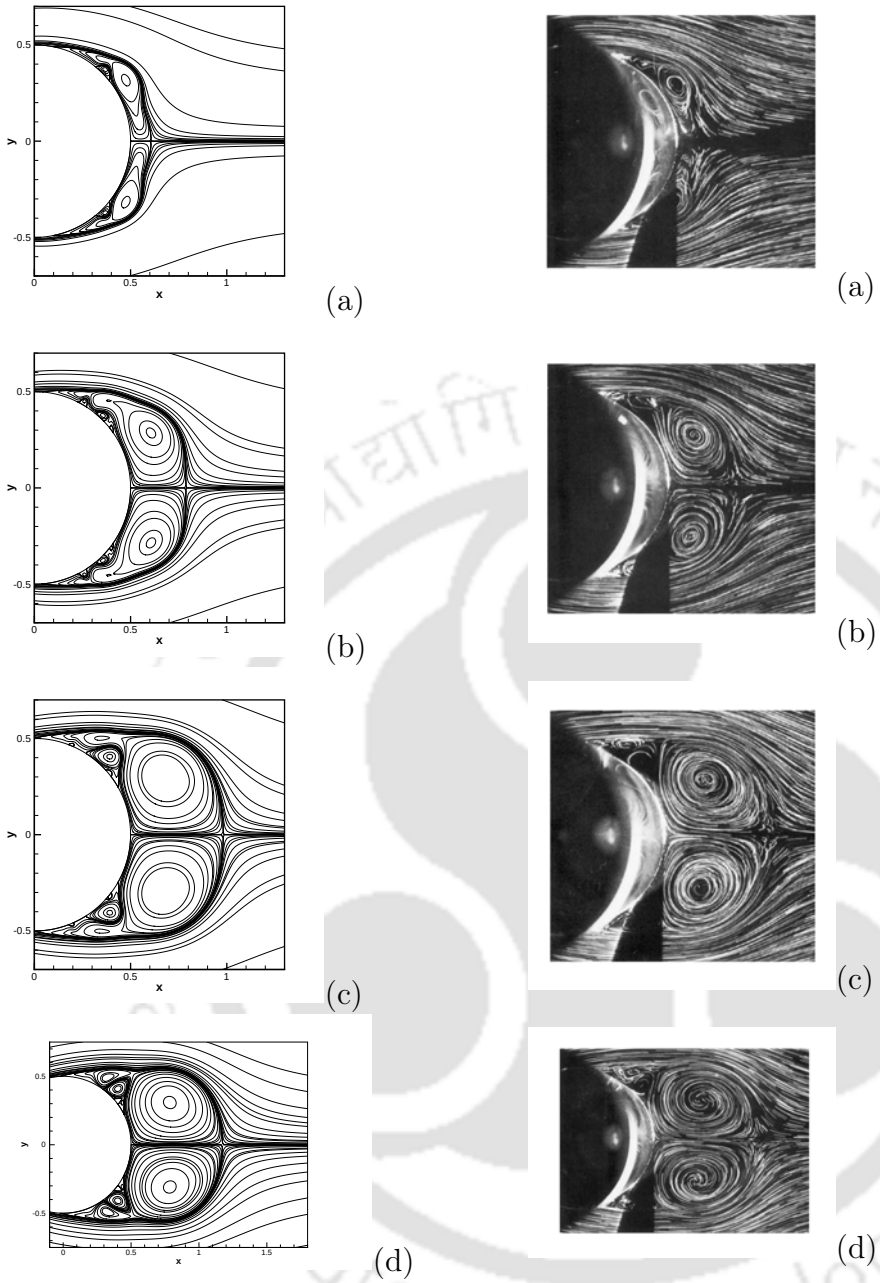

Figure 4.22: Streamlines for $Re = 5000$ at (a) $t = 1.0$, (b) $t = 1.5$, (c) $t = 2.0$ and (d) $t = 2.5$ (left column, numerical and right, experimental [18]).

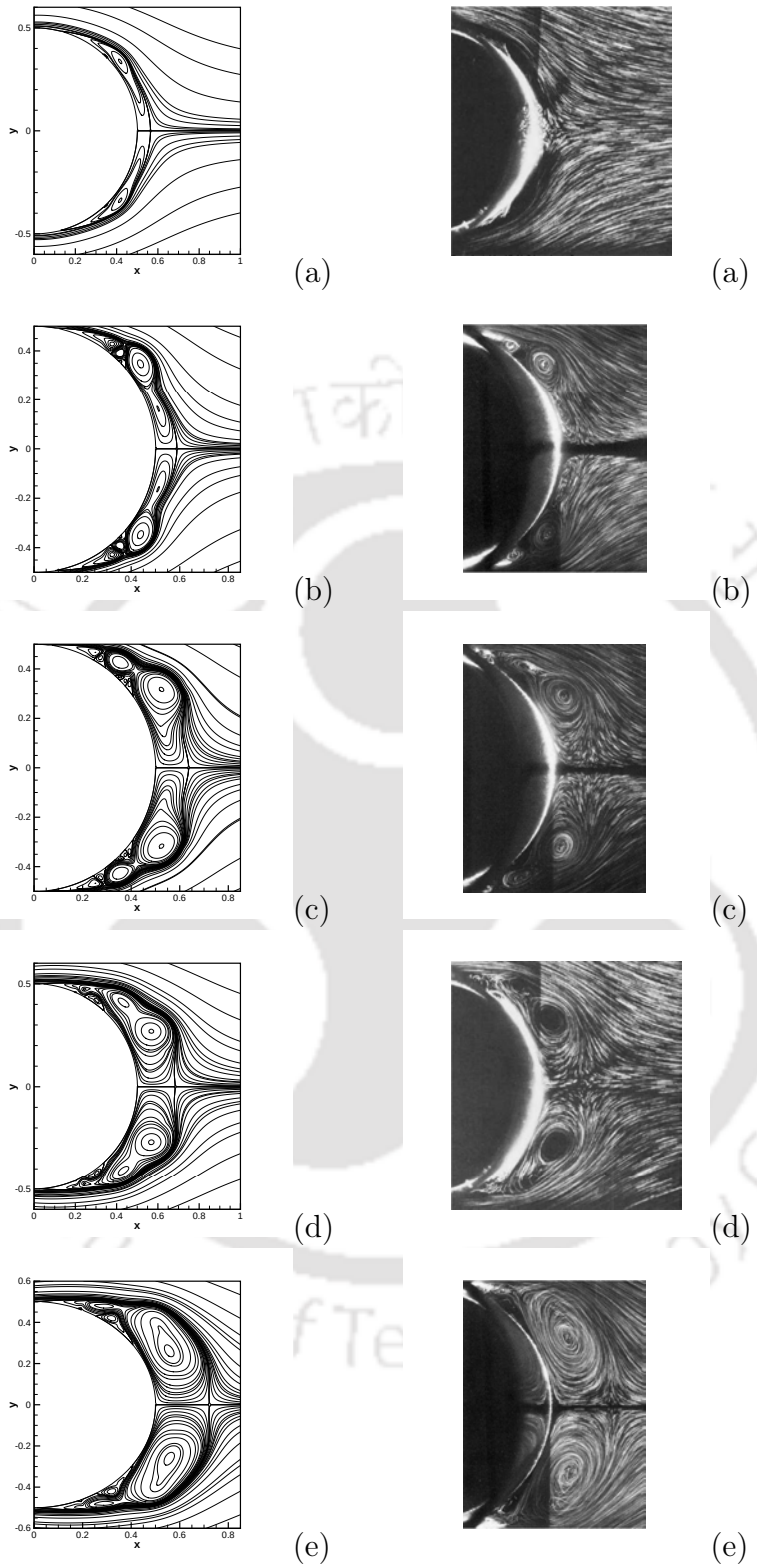

Figure 4.23: Streamlines for $Re = 9500$ at (a) $t = 0.80$, (b) $t = 1.0$, (c) $t = 1.25$, (d) $t = 1.4$ and (e) $t = 1.5$ (left column, numerical and right, experimental [18]).

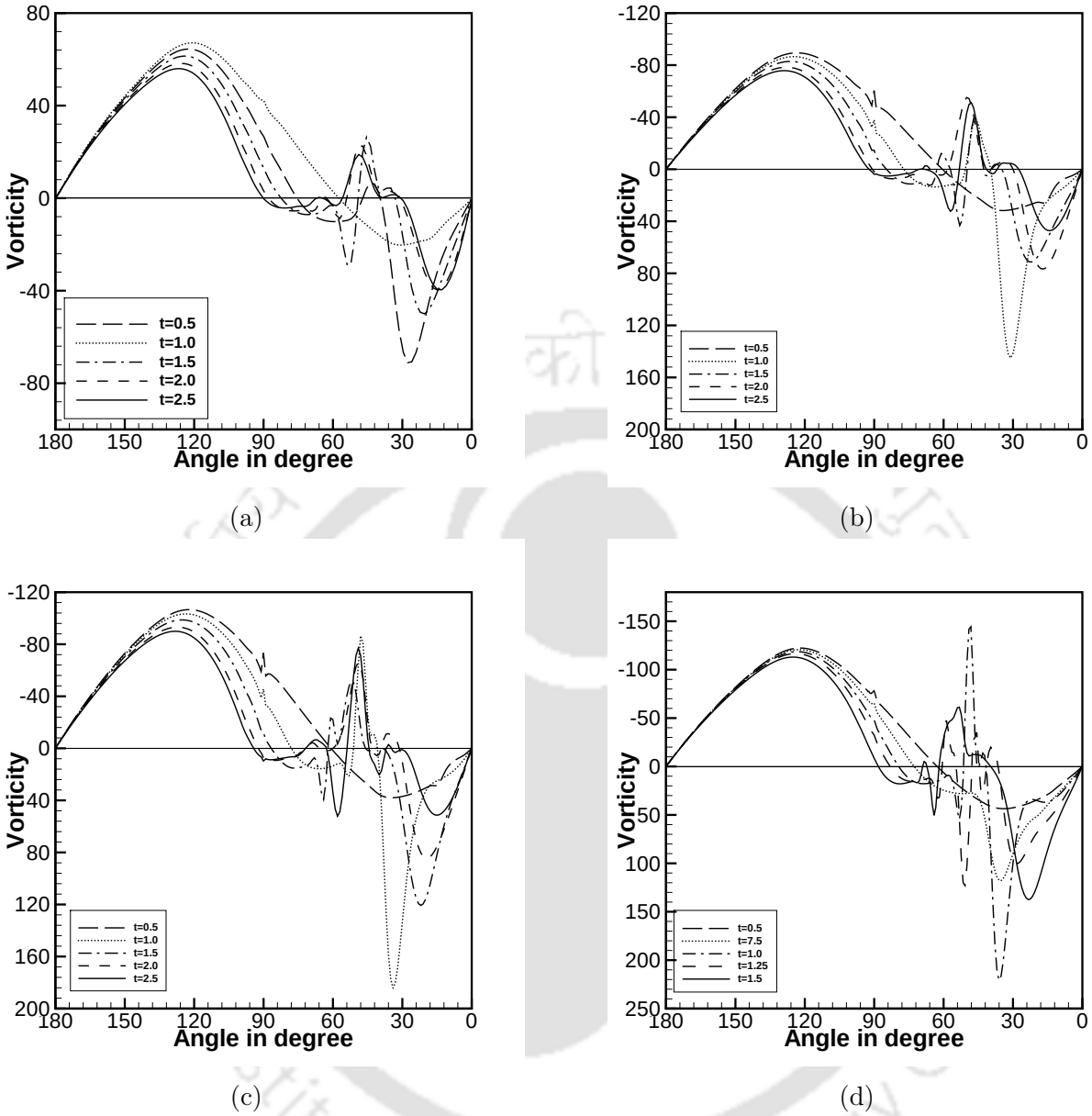

Figure 4.24: Time evolution of surface vorticity for (a) $Re = 3000$, (b) $Re = 5000$, (c) $Re = 7500$ and (d) $Re = 9500$.

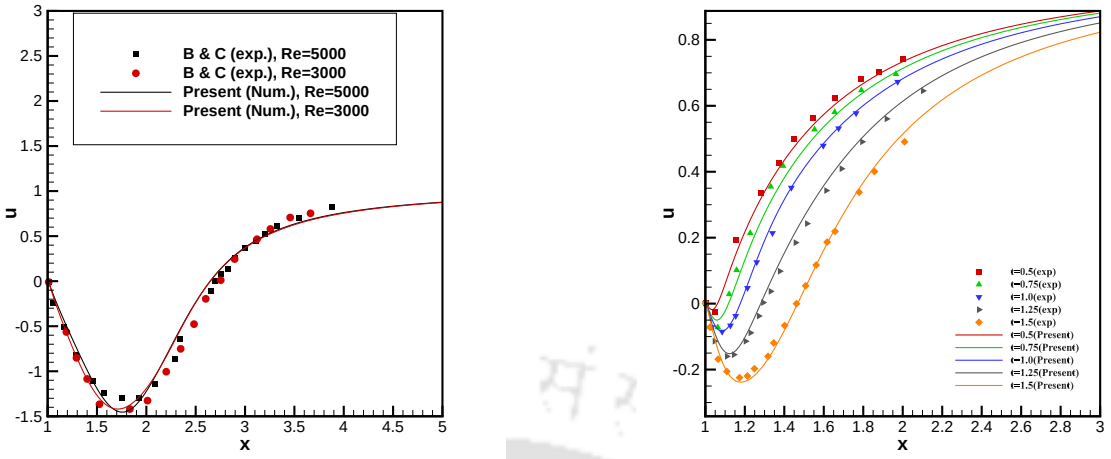

(a) (b)

Figure 4.25: Comparison between experimental and numerical results for the velocity distribution on flow axis for (a) $Re = 3000$, 5000 and (b) 9500.

Time	T_1	T_2
$t = 1.85$	0.00294625	−0.0030587
$t = 3.0$	0.00257713	−0.0027393
$t = 3.45$	0.0174083	−0.0126901
$t = 4.2$	0.0047674	−0.0043727
$t = 4.65$	0.00286996	−0.0030745

Table 4.7: Streamfunction ψ values at the centers of the tertiary vortices constituting the sub-α phenomenon for $Re = 9,500$.

4.5 Conclusion

Finite difference simulation of the flow past an impulsively started circular cylinder is well represented in the existing literature. However, majority of them are performed on polar grids. Most of the simulations for this problem on Cartesian grid utilizes the immersed interface approach, that too, up to Reynolds number regime exhibiting the vortex shedding phenomena only. In the current study, we carry out a comprehensive simulation of the flow past an impulsively started circular cylinder through the finite difference scheme developed in Chapter 3. We provide a detailed account of the generation of the grid in such a way that the cylinder boundary passes through the grid points, thus doing away with the need to use the immersed interface approach. Along with grid independence study, we have also

established the efficiency of the simulation on Cartesian vis a vis polar grid. Results are presented for a wide range of Reynolds numbers (Re) ranging from $5 \leq Re \leq 10000$ in the laminar regime. This includes the periodic regime which is characterized by the presence of von Kármán vortex street highlighting the robustness of the numerical scheme being used. They are validated through comparison with experimental and well established numerical results and the accuracy of the solutions is exemplified by their close proximity to them. Not only the α, β, sub-α and sub-β phenomena, which are the trademark of the secondary and tertiary vortex dynamics associated with such flows, are studied in detail, but for the first time, they have also been documented compactly in a tabular form for $Re \geq 700$.

CHAPTER 5

FLOW PAST SHARP EDGES

5.1 Introduction

Research on flow past a sharp edge of bluff bodies has garnered considerable attention over the years, owing to the fundamental and complex nature of the flow phenomenon, particularly the separation of flows. The boundary layer gets convected around the edge, where it intensifies and forms a vortex. With time the vortex gains strength and grows in size, causing the boundary layer to separate and form a coherent spiral shear-layer, which is a roll-up characteristic of vortex development. Such flows serve as a means of studying the free shear layer and vortex behavior. In the current study, we endeavour to undertake studies on two classic examples of flow past sharp edges: the flow past (a) a flat plate and (b) a wedge.

The flow past a thin plate normal to the free stream is a classic example of bluff body flow. The flow past a normal flat plate is similar to flow past any other bluff bodies. However, fundamental parameters, viz., the drag coefficient and the Strouhal number differ significantly for geometries with sharp edges. Considerable research, both numerical and experimental, has been done for the limiting case of a flat plate, which corresponds to wedges with zero angle of incidence.

Prandtl [119] was the pioneer in such studies, who experimented with the flow past a normal flat plate in 1904 in the first study of this kind. Later, Anton [4](in 1939) and Wedemeyer [163] (in 1956) presented their experimental studies for the same. Pierce [117]

(in 1961) used the spark shadowgraph technique to show photographic evidence of separation at sharp angles. Taneda and Honji [155](in 1971) employed the aluminum dust method to visualize the flow past impulsively started and uniformly accelerated flat plates. Liam and Huang [100](in 1989) used the hydrogen bubble technique to visualize the flow past accelerating plates. Coutanceau and Launay (In Dennis et al. 1993) [32] did an experimental investigation for the impulsively started flat plate at moderate Reynolds numbers. In a similar fashion, Pullin and Perry [121] (in 1980) used dye in water to study the development of the separating shear layer past thin and thick wedges. They presented the trajectory of the vortex center through detailed analysis for different acceleration parameters m and wedge angles. They also compared their observations via inviscid similarity theory [64, 120]. Recent experiments are seen to focus their attention on studying the leading-edge flow past a plate and three-dimensional tip vortex effects (Kriegseis, Kinzel and Rival [92]; Ringuette, Milano, and Gharib [124]) associated with it. Another study worth mentioning in this direction is that of Koumoutsakos and Shiels [88], who numerically simulated the flow past an impulsively started ($m = 0$) and uniformly accelerated ($m = 1$) flat plates.

Unlike other bluff body flows, the separation points for the flat plate or wedge are identified with sharp edges. Even though it looks simple, but their numerical simulations are complicated due to edge singularity. By proper assessment of the development of the circulation at the tips of the plate and away from it, many researchers have presented analytical results for this type of flow (Villat in 1930 [160]; Wedemeyer in 1961 [163]; Pullin in 1978 [120]; Krasny in 1991 [91]) assuming inviscid evolution of the vorticity field.

Also, because of the singularities at the tips, numerical simulation of this type of flows is not straight forward. As such, initially most of the numerical schemes that had been developed to study this flow was confined to steady-state flow for low and moderate Reynolds numbers. Smith (in 1979) was the first to develop a numerical scheme that avoids the plate-tip singularity and presented steady-state results for low Reynolds numbers. Later, Ingham, Tang & Morton (in 1991) [59]; Choi & Kim (in 1995) [58] also developed schemes to handle the singularities at the plate edges. However, as in the earlier studies, theirs were also limited only to the steady-state region. Later on, Nijjar

& Vanka (in 1995) [110] used a High-order finite difference method to solve the Navier-Stokes equations for a wide range of Reynolds numbers in the unsteady regime. They used a very fine grid near the plate's surface to avoid the singularity at the tips of the plate. They further discussed the effect of three-dimensionality in such flows.

The study of two-dimensional flow past a flat plate is analogous to the flow past a square cylinder, which undergoes a Hopf bifurcation (steady to unsteady) at a relatively low Reynolds number ≈ 45. A second transition, also known as a spatial transition (two-dimensional to three-dimensional), occurs at around Re=175 [128]. The other subsequent transitions are related to the appearance of different modes (structures) just after the flow becomes three-dimensional [125,128]. Further increase in Reynolds number takes the flow towards the turbulent state through a route to chaos [130, 131].

However, the flow past a 2D normal flat plate becomes unsteady somewhere in the range $28 \leq Re \leq 30$. This two-dimensionality breaks into a three-dimensional flow around Reynolds number 200. It is conventional to use a 3D model for the flat plate [108, 109] or any bluff bodies [106] to capture the correct drag coefficient and Strouhal number. Most of the studies on flow past bluff bodies are limited to the near-wake, that too in uniform flow. It has been observed that for bluff bodies, particularly elliptic and circular cylinders, [25,63] the far-wake ($x \geq 20$) behavior is distinctly different from the near-wake. One of the experiments of [25] shows the qualitative evidence of large-scale shedding in the far downstream (approximately at an axial location of ($x \geq 150$) of a circular cylinder at $100 \geq Re \geq 160$. Dakin and Falconer [29] (in 1995) numerically studied the interactions of coastal currents with topographic indentations that mimics the flow past a sharp wedge.

Recently, Xu and Nitsche [168] numerically studied viscous flow past a flat plate in accelerating flow. Their results were in good agreement with the experimental study of Pullin and Perry [121] for thin wedges with an angle of 5°. Xu then [167] (in 2016) numerically studied vortex formation in the impulsively started viscous flow past an infinite wedge for wedge angles ranging from 60° to 150° in uniform flow, where potential flow theory was employed to solve this problem. All the previous research, both experimental and numerical [23, 85, 86, 116, 153], including those by Pullin [121] and Xu [167, 168] on the flat plate or wedge, were conducted only for the early part in the near wake region.

The present study aims at extending the earlier studies and deals with the simulation

of flow in the following three problems

1. The transition of the far-wake in uniform flow for flow past a flat plate,

2. Accelerated flow past a flat plate in the near-wake region and

3. Accelerated flow past a wedge mounted on a wall till transition from laminar state.

5.2 Test cases

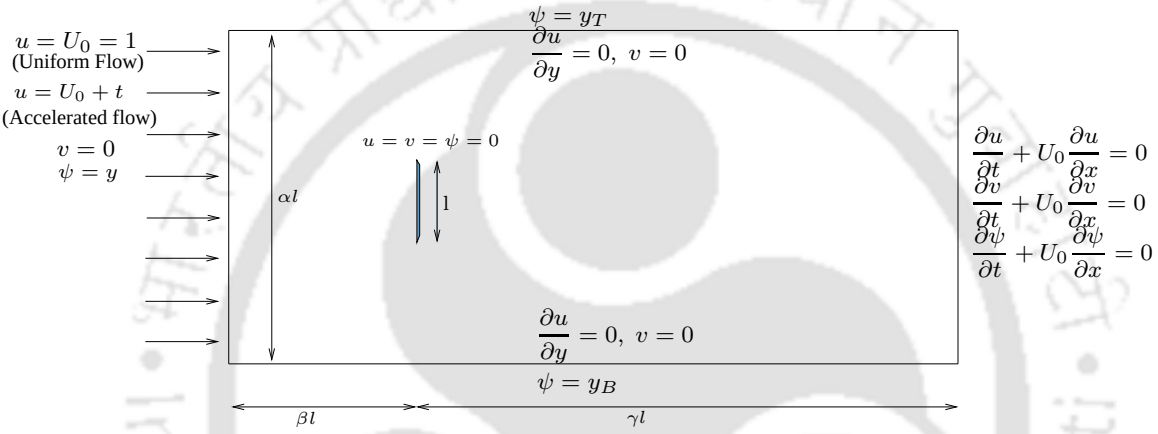

Figure 5.1: Configuration of the flow past a flat plate in uniform and accelerated flow.

5.2.1 uniform flow past a flat plate

As a first case, we consider uniform laminar flow past a flat plate to understand the far wake flow characteristics. The flow configuration for this problem is the one presented in figure 5.1 corresponding to uniform flow at the inlet, where the boundary conditions are also shown. We have chosen $\alpha = 8$, $\beta = 7.5$ and $\gamma = 70$ in figure 5.1 such that the corresponding dimensions of the computational domain are $-7.5 \leq x \leq 70$ and $-4 \leq y \leq 4$; as such $y_T = 4$ and $y_B = -4$. The plate is kept normal to the flow and stationed at $(0, 0)$. Boundary conditions on the surface of the plate $\phi = 0$ is considered (where ϕ represents either u, v or ψ). At the inlet, a uniform velocity $u = U_0 = 1$ is prescribed while at the oulet, a convective boundary condition $\frac{\partial \phi}{\partial t} + U_0 \frac{\partial \phi}{\partial x} = 0$ is imposed. At the other two boundaries, $\frac{\partial u}{\partial y} = 0 = v$ with $\psi = y_T$ and $\psi = y_B$ at the top

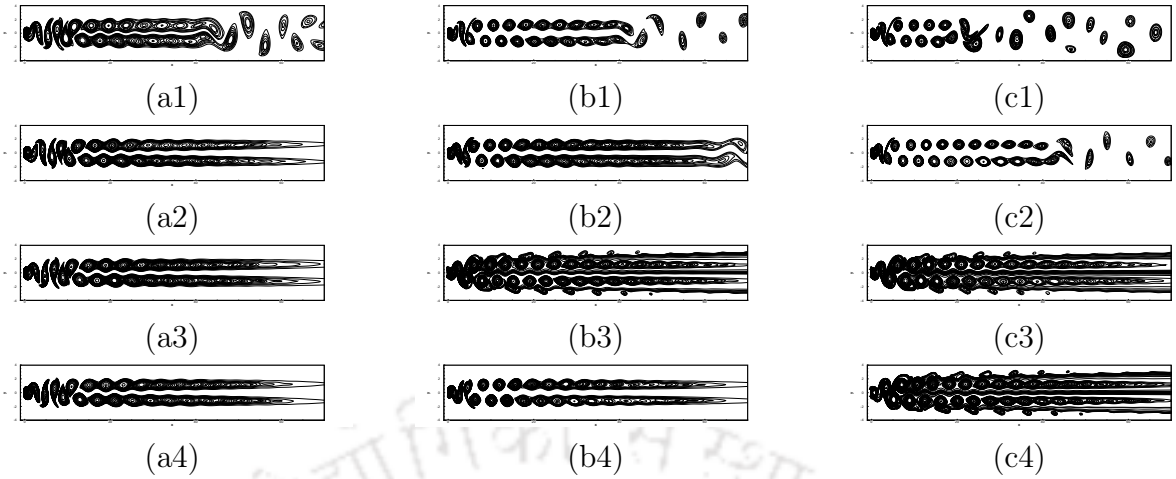

Figure 5.2: Vorticity contours for (a) $Re = 100$, (b) $Re = 140$ and (c) $Re = 175$ at $t = 200$ (first row), $t = 400$ (second row), $t = 750$ (third row), and $t = 1000$ (fourth row).

and bottom boundaries respectively, where y_T and y_B are the y coordinates thereat. The details of the governing equations along with solution method are given in Chapter 3.

Numerical simulations have carried out for $Re = 100$, 140 (with $\Delta t = 10^{-2}$), and 175 (with $\Delta t = 5 \times 10^{-3}$) on grid size 601×201. To generate the grid, we use the same stretching function as in section 3.4.3 in Chapter 3 in both directions. Existing literature [108, 109, 129] suggests that the flow becomes three-dimensional at $Re \approx 200$. Therefore, computations are performed only for these three Re's so that they belong to that range.

We record the time-varying signals of both the velocity components at eight different locations $x = 2,\ 10,\ 20,\ 30,\ 40,\ 50,\ 60$ and 65 along $y = 0$ downstream of the plate up to a non-dimensional time $t = 1000$. These are sufficient to capture enough cycles of the lowest frequency present in the flow field. It is quintessential for the temporal transition of flow past bluff bodies to correspond to a Hopf bifurcation, due to which the steady flow becomes unsteady. For the laminar flow past a flat plate, this critical Reynolds number is found at around $Re = 28$ [60]. As mentioned in the earlier chapters, for Reynolds numbers greater than the critical value, shedding of vortices takes place leading to the formation of von Kármán vortex street.

In figure 5.2, we present vorticity contours for Reynolds numbers $Re = 100$ (on left) $Re = 140$ (middle) and (c) $Re = 175$ (right) at four time stations starting at $t = 200$ and ending at $t = 1000$. It is clear from these figures that the peak vorticity is decaying in

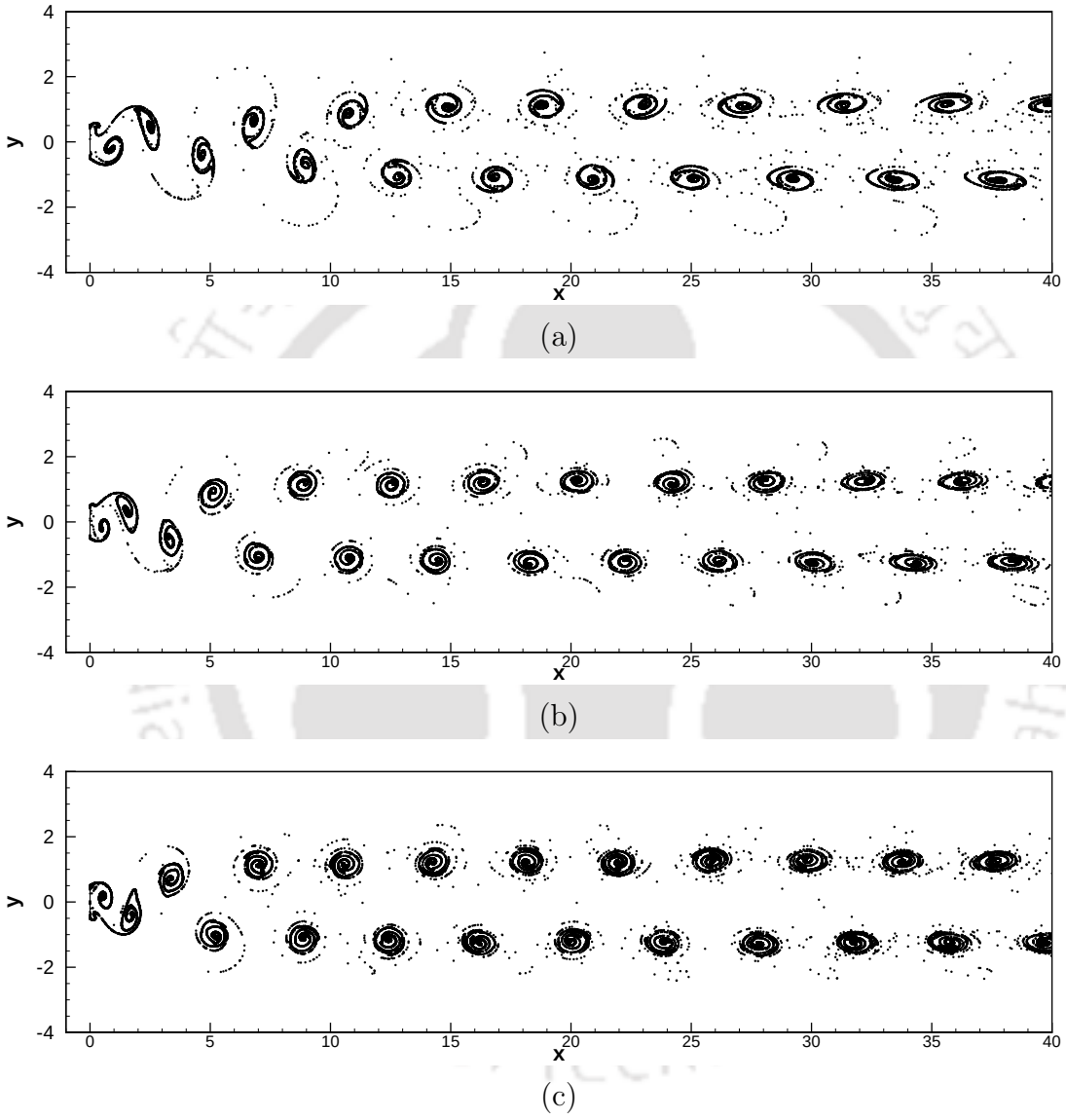

Figure 5.3: Streaklines of flow past a flat plate for (a) $Re = 100$, (b) $Re = 140$, and (c) $Re = 175$ at time $t = 1000$.

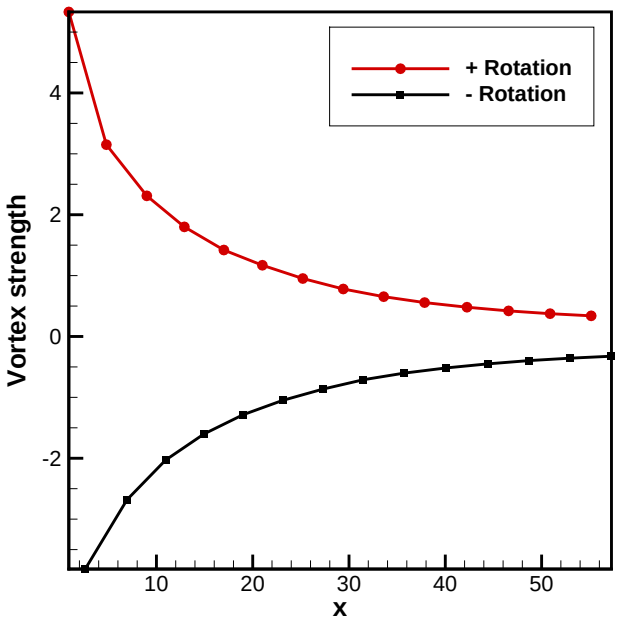

Figure 5.4: Strength of vortices at the core centers for $Re = 100$.

the downstream direction as time progresses. The decay is associated with high viscous diffusion and higher entrapment for a low Reynolds number. Two rows of positive and negative contours with equispaced centers of the vortices can be seen in figures 5.2(a1)-(a4) in the near-wake for Re=100, which is also called $2S$ (two single vortices) pattern of vortices. In far-wake, alternately positive and negative contours are also seen in the early stage of the flow 5.2(a1), also called S (single vortices) pattern of vortices, and which get diffused in the later instants of time. It shows that the flow is unsteady in the near wake and steady in the far-wake. These alternate vortices are convected in the downstream direction in two rows parallel to the $y = 0$ line, with vortices in each row having opposite rotations. The decaying in the strengths of vortices can be seen from figure 5.4, where the strength of the vortices as one moves downstream, is shown. In table 5.1, we compare the near wake flow properties from our computation with those of Saha [129], and Najjar and Venka [109], and a very close comparison is obtained.

The vorticity contours for $Re = 140$ are presented in figures 5.2(b1)-(b4), and it clearly shows the transition from high-frequency vortex shedding structures in the near-wake to low-frequency large scale structures at around $x \approx 40.0$. This suggests that the vortex

Table 5.1: Comparison of vortex strengths and distances between two core centers

		Najjaar & vanka [109]	Saha [129]	Present
Vortex Strength (ω value at core)		5.1 at $x = 1$	4.6 at $x = 1.15$	5.3 at $x = 0.9$
		0.9 at $x = 24$	0.7 at $x = 25$	0.95 at $x = 25.2$
Gap between two core centers ($\times$ plate height)	Identical rotation in the near-wake	≈ 4	≈ 4	≈ 4
	opposite rotation in cross stream	≈ 3	≈ 3	≈ 3

street at $Re = 140$ also experiences a two-dimensional transition similar to $Re = 100$; however, this transition occurs earlier than the one for $Re = 140$. This is probably owing to the far-wake time-averaged streamwise velocity profiles at various Reynolds numbers becoming unstable, the instability increasing with increasing Reynolds number. At a low Reynolds number, the higher viscous force is able to counter this instability. However, the instability growing within the far-wake amplifies at a slightly higher Reynolds number, and the larger vortices of opposite signs start forming downstream. At a later instant in time, the flow structures changes from $2S$ pattern to $2P + 2S$ (two single and two pairs of vortices) pattern as can be seen in figure 5.2(b3). However, they eventually settle into two parallel rows of vortices of opposite rotations as can be seen from figure 5.2(b4).

At a slightly higher Reynolds number $Re = 175$, additional instabilities are observed at time $t = 200$ beyond $x = 20$ towards far wake as can be seen from figure 5.2(c1). Although they become stable just behind $x = 20$ at a later instant of time (see figure 5.2(c2)), the undulation continues at the far wake. While the small $2S$ flow structure is visible in the near wake, a slightly larger S flow structure is observed in the far wake. Later on, the flow structures change from $2S$ pattern to $2P + 2S$ pattern in the near wake yielding a diffused $2S$ pattern in the far wake (figure 5.2(c3)-(c4)). However, the shedding pattern at the far wake is markedly different from the ones observed for $Re = 100$ and 140, where one can see vortices being shed along four rows parallel to $y = 0$ line. This settled diffused pattern in the far wake was not reported in the study of Saha [129] probably because of the fact that his study had carried out computation only up to non-dimensional final time $t = 675$ against $t = 1000$ used by us.

The streaklines for $Re = 100$, 140 and 175 at time $t = 1000$ are shown in figures 5.3(a)-(c) beyond the near wake extending up to the front of far wake at $x = 40$. From

these figures it is obvious that higher the Reynolds number, closer is the location from the plate where the $2S$ or $2P + 2S$ pattern starts. Also the frequency of vortex shedding increases with the increase in Reynolds number resulting in the reduction in the space between two successive vortices lying in each rows.

In order to analyze the near- and far-wake flow characteristics more closely, we perform a fast Fourier transform (FFTs) of velocity components in the near- and far-wakes and present them in figures 5.5 and 5.6. To perform these FFTs, data from a minimum of 2×10^6 time stations are used. The same eight locations downstream of the plate mentioned earlier have been chosen to perform the FFTs. Although the power spectra of only the v-velocity are shown in the figures, the ones corresponding to the streamwise velocity u reveals exactly similar behaviour.

We depict the FFTs of v-velocity in three locations, viz., near-wake ($x = 10$), front of the far-wake ($x = 40$) and far-wake ($x = 60$) corresponding to Reynolds numbers $Re = 100$, $Re = 140$ and $Re = 175$ in figures 5.5(a)-(c) respectively. The near wake FFTs show a single dominant frequency (designated as primary frequency f_p) as in figures for $x = 10$ (see figure 5.6 corresponding to $x = 2$ as well), which is also corroborated by the periodic vortex shedding patterns of the flows in the region $0 \leq x \leq 10$ in figures 5.2 and 5.3. A single dominant frequency, viz., the primary one with rapidly receding power can be seen for $Re = 100$ as one moves further downstream culminating at the far wake for $Re = 100$. The density of this dominant frequency in the near wake region at $x = 10$ reduces from around 14000 to an almost negligible value 20 in the far wake region at $x = 60$ suggesting that the flow becomes steady at the far wake region. It also explains the consistent $2S$ pattern and gradual reduction in the strength of the vortices as shown in figures 5.4, 5.2(a1)-(a4) and 5.3(a).

For $Re = 140$, the same trend is observed for the primary frequency. Besides, one can see the appearance of a secondary frequency f_s at the far wake with a density higher than f_p, however negligible (compared to the the density of f_p at near wake). This is indicative of some traces of the $2P$ pattern observed earlier at $t = 750$ in figure 5.2(b3) still being present at the far wake for this Reynolds number.

In figure 5.6, we depict FFTs of the v-velocity at six locations $x = 2.0$, 10.0, 20.0, 30.0, 50.0 and 65.0 for $Re = 175$. FFTs at $x = 2.0$ and 10 show a single dominant

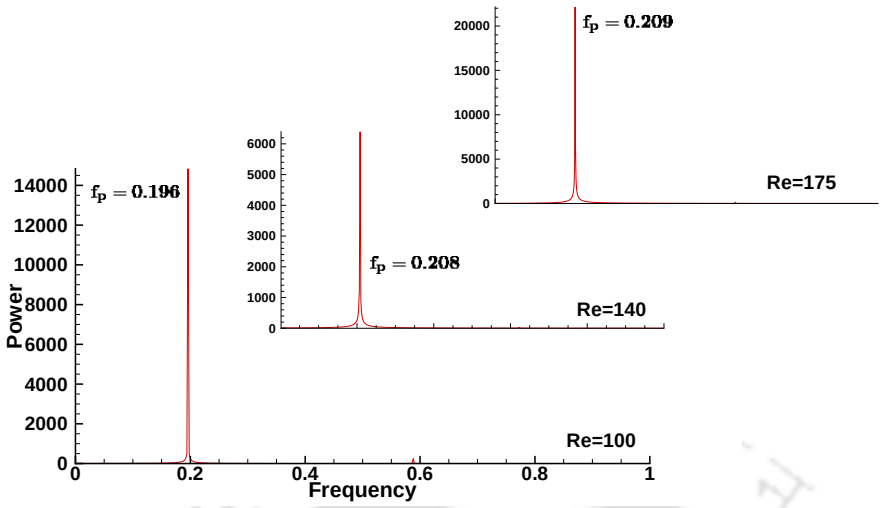

(a)

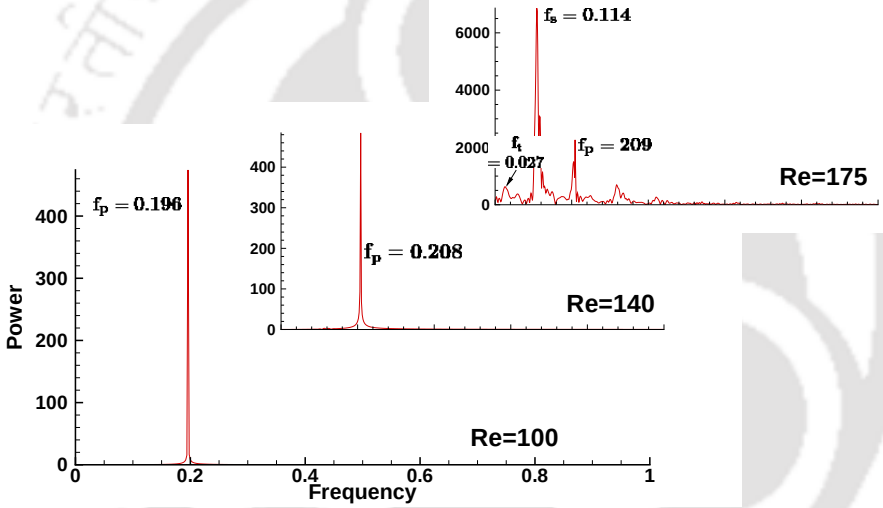

(b)

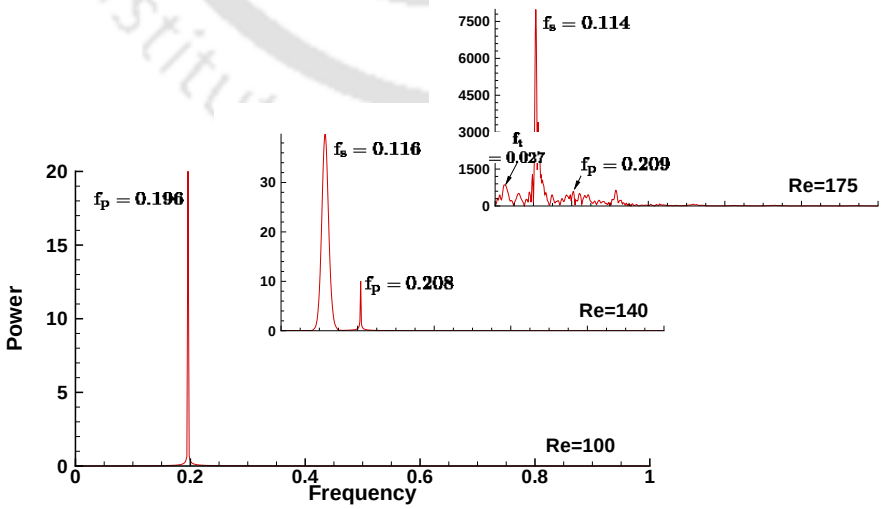

(c)

Figure 5.5: Fourier Transformation of transverse component of velocity for $Re = 100$, 140 and 175 at (a) $x = 10$, (b) $x = 40$ and (c) $x = 60$.

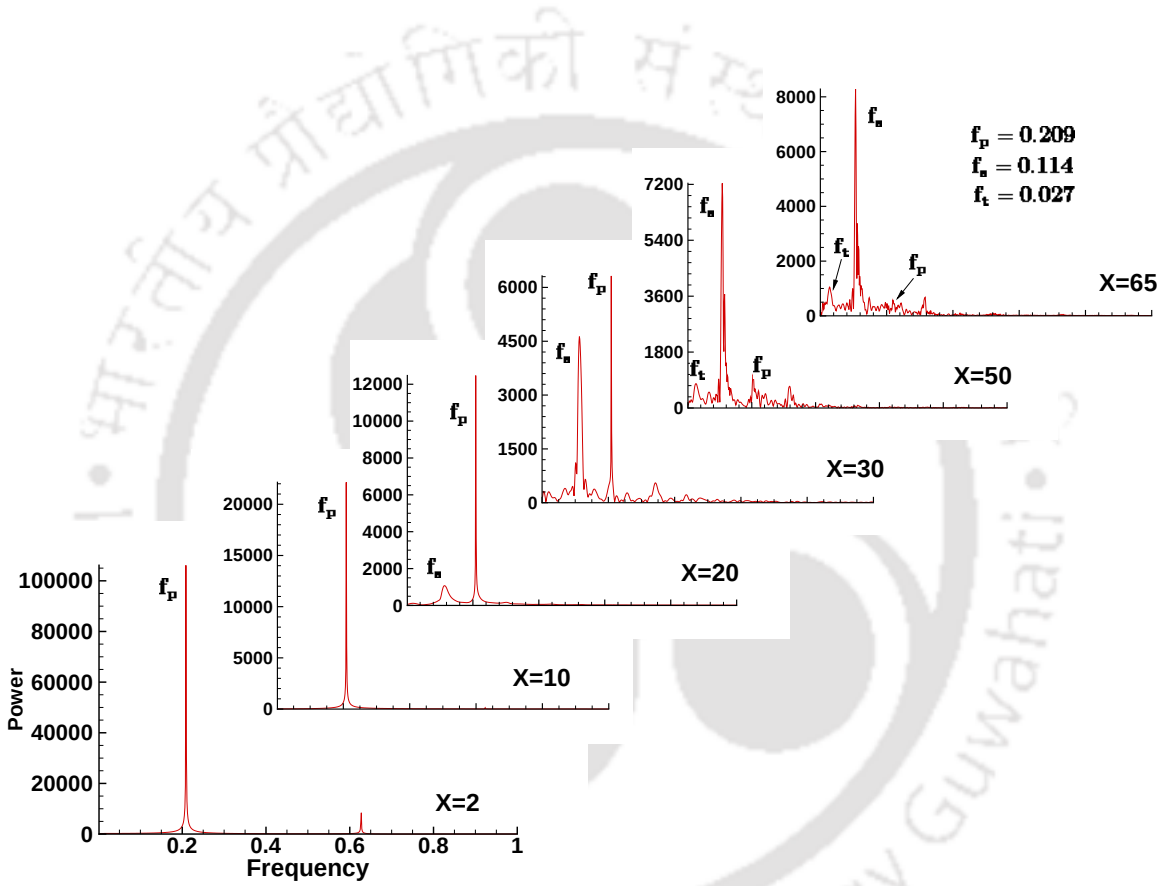

Figure 5.6: Fourier Transformation of transverse component of velocity at various axial locations for $Re = 175$.

frequency $f_p = 0.209$ corresponding to the regular periodic von Kármán vortex street in the near-wake and the large scale vortex structures seen in the far wake respectively. On the other hand, FFT at $x = 20$ reveals the appearance of an additional secondary frequency $f_s = 0.114$ which is related to the low-frequency small scale vortex structures seen in the near wake ($2P + 2S$ pattern). This low frequency secondary structures gain in strength at $x = 30$ as can be seen from their high energy content. Meanwhile, one can see the addition of many more frequencies at the same juncture. A close look at the same reveals that another low frequency, called the tertiary frequency $f_t = 0.027$ is also present gradually acquiring more energy (see figure 5.5(b) for $Re = 175$ also) further downstream at $x = 50.0$ and 65.0. FFT at $x = 50$ shows multiple frequencies corresponding to different shedding patterns, generated due to complex interaction among different vortices. However, in the far wake, the secondary frequency is seen to dominate the whole procedure with the primary f_p losing its ground. This probably explains the four parallel rows in the far wake in figures 5.2(c3)-(c4). Here the inner rows correspond to $2S$ pattern with frequency f_p containing vortices with a much reduced strength. On the other hand, the outer rows are linked to the $2P$ pattern, with each pair containing a vortex corresponding to the dominant secondary frequency f_s and another vortex corresponding to the weaker tertiary frequency f_t. Interestingly, the high energy content of the vortices at the far wake is still evident for this Reynolds number opposed to the other two as can be seen from figures 5.5(c) and 5.6.

5.2.2 flow past bluff bodies in accelerated flow

The next case considered here is the flow past a flat plate in uniformly accelerated flow. Since the flow is accelerated, it becomes turbulent after a very short period of time and as such, we have computed the flow only for the early stages of evolution in the laminar regime.

Start-up vortex for the flat plate flow

We consider the flow past a flat plate in accelerated flow where the plate is kept normal to the flow. Such flows are innately associated with the existence of start-up vortex. The computational set-up for this flow is similar to the one shown in figure 5.1 along with the

boundary conditions, with the inlet velocity now assuming the value for an accelerated flow. For this flow set-up, Reynolds number is defined as $Re = \frac{l^2}{\nu T}$, where l is the plate height, ν is the kinematic viscosity of the fluid and T is a characteristic time-scale defined by $T = \left(\frac{l}{a}\right)^{\frac{1}{2}}$ for some constant a [168]. In all our computations l and a were set as 1.0. We have chosen $\alpha = 5$, $\beta = 7.5$ and $\gamma = 22.5$ in figure 5.1 such that the corresponding dimensions of the computational domain are $-7.5 \leq x \leq 22.5$ and $-2.5 \leq y \leq 2.5$; as such $y_T = 2.5$ and $y_B = -2.5$. The plate was placed at $(x, y) = (0, 0)$ and fluid is flowing from left to right. The boundary conditions at the inlet is taken as $u = u_0 + t,\ v = 0$. By integrating u and v we can calculate stream function at inlet as $\psi = y$. By the definition of stream function, ψ is constant along the streamline. Therefore at the top and bottom wall $\psi_{top} = 2.5$ and $\psi_{bottom} = -2.5$; also $\frac{\partial u}{\partial y} = 0,\ v = 0$ thereat. At the outlet, the boundary conditions are $\frac{\partial \psi}{\partial t} + U_0 \frac{\partial \psi}{\partial x} = \frac{\partial u}{\partial t} + U_0 \frac{\partial u}{\partial x} = \frac{\partial v}{\partial t} + U_0 \frac{\partial v}{\partial x} = 0$. Note that while Xu and Nitsche [168] had employed potential boundary conditions at the boundaries of the computational domain using a complex potential function, we have used exact physical conditions thereat.

A note on non-dimensionalization: If u, t, u_0, and a represent the dimensional horizontal velocity, time, velocity at the inlet at time $t = 0$ and acceleration respectively, then $u = u_0 + at$. With characteristic time-scale T and non-dimensional variables with asterisks, we have

$$t^* = \frac{t}{T}, \quad x^* = \frac{x}{l}, \quad \text{and} \quad u^* = \frac{uT}{l},$$

which yields $u^* = u_0^* + t^*$ and as such the non-dimensional velocity at the inlet is taken as $u = u_0 + t$.

We carry out numerical simulations for the Reynolds number 500 on a grid of size 601×401 with $\Delta t = 10^{-3}$. The grid is generated as in the uniform flow case in section 3.4.3 in chapter 3. In figure 5.7, we present the evolution of the flow in terms of streamlines, velocity vector and vorticity. The accelerated nature of the flow is clearly evident from the velocity field where one can see the length of the vectors increasing rapidly with passage of time. The flow being accelerated from rest, a start-up spiral vortex stems out from each of the sharp edges of the plate, the evolution of which can be divided into four main stages:

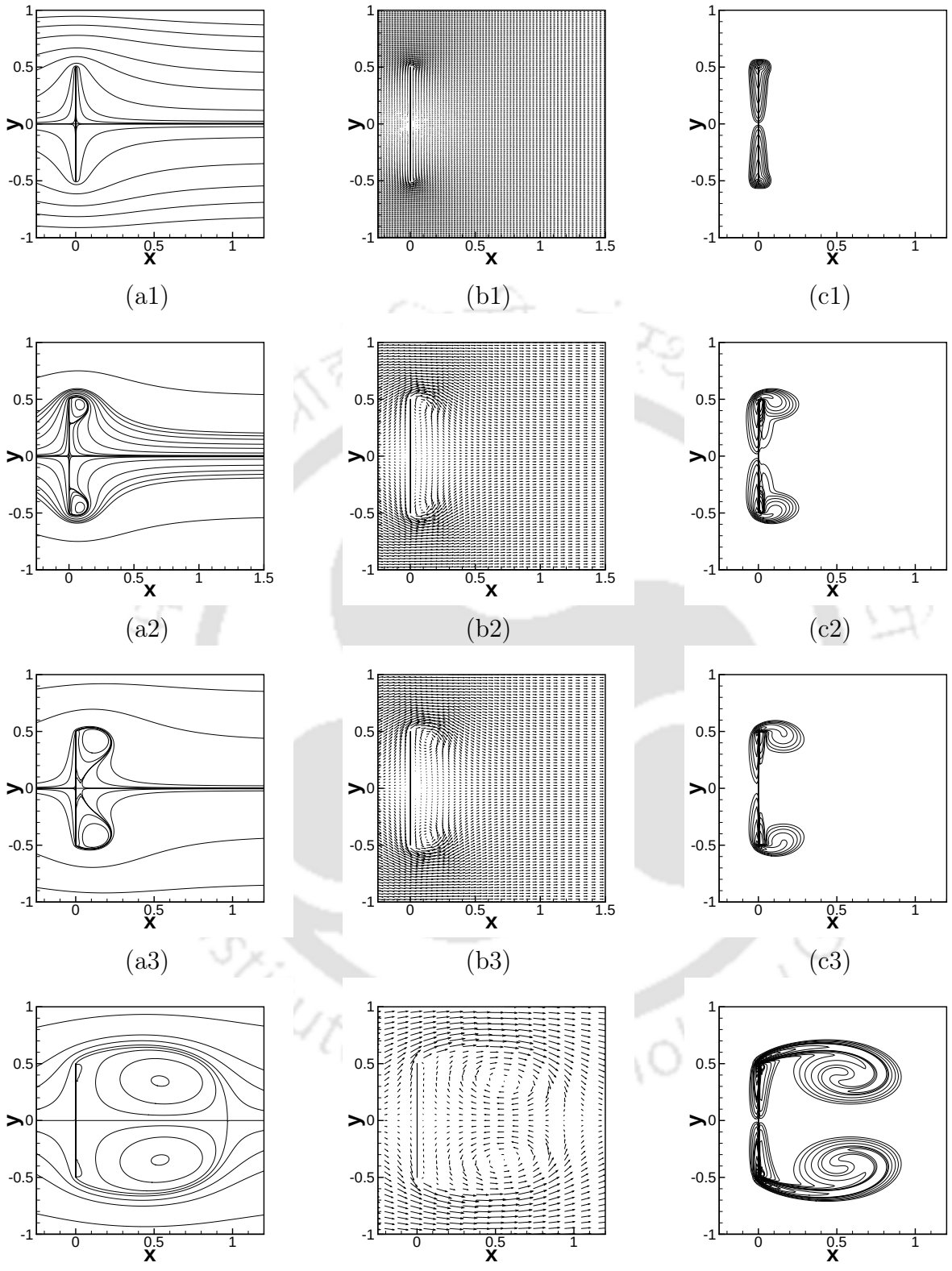

Figure 5.7: Evolution of flow patterns for accelerated flat plate for $Re = 500$: The rows from the top to bottom corresponds to time $t = 0.2$, 0.8, 1.0 and 2.0 and the columns represent (a) Streamfunction, (b) velocity vector field and (c) vorticity.

- Rayleigh stage: in the flow, there is a viscous boundary layer around the plate and it's tips (figure. 5.7 (a1, b1, c1), $t = 0.2$).

- Viscous stage: the convective terms of the Navier-Stokes equations become comparable with the viscous terms and thus vortex structures begin to appear (figure. 5.7 (a2, b2, c2), $t = 0.8$).

- Self-similar inviscid stage: convective terms become dominant, but the vortex is still small enough to be independent of the geometry except for the local edges (figure. 5.7 (a3, b3, c3), $t = 1.0$).

- Vortex expulsion: the initial recirculation bubble opens up and the vortex starts lagging behind the body (figure. 5.7 (a4, b4, c4), $t = 2.0$).

All our observations are consistent with the ones made by Xu and Nitsche [168]. However, we also observed the formation of secondary vortex structures emanating from the edges as well, seen in figures 5.7 (a3-a4, c3-c4), which was not reported in their study.

Starting flow past a wedge mounted on a wall

The next problem considered here is the accelerated flow past a wedge mounted on a wall, which was experimentally carried out by Pullin and Perry [121]. Note that flow past a flat plate is a limiting example of flow past a wedge of zero angle and because of its sharp edge singularity, flow computation is complicated and difficult to perform. This sharp edge fixes the point of separation which leads to generation of spiral shear layer and vortex formation.

For this flow, the viscous fluid is assumed to obey $\hat{u} = \hat{u}_0 + a\hat{t}^m$ enabling its acceleration, with $\hat{u}$, $\hat{u}_0$ and $\hat{t}$ denoting the dimensional horizontal velocity, initial inlet velocity and time respectively. As such, the non-dimensionalization is carried out by assuming the characteristic time scale to be $T = \left(\frac{l}{a}\right)^{\frac{1}{m+1}}$, where l stands for the channel width here; this allows incorporation of acceleration other than a uniform one. For example, $m = 0$ renders a uniform velocity at the inlet indicating an impulsive start, while $m = 1$ and 2 stand for uniform and linear acceleration respectively [168]. For the other variables,

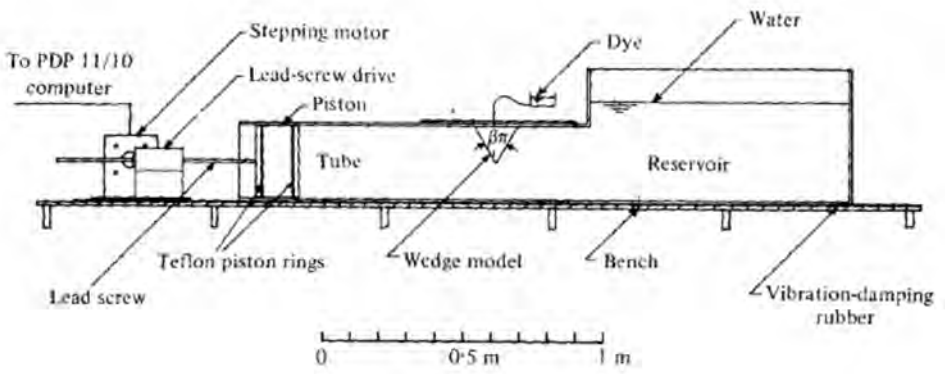

Figure 5.8: Experimental set-up for starting vortex flow visualization by Pullin and Perry ([121]).

the same scaling is used as in the accelerated flat plate case. This leads to the the non-dimensional velocity at the inlet at non-dimensional time t as $u = U_0 + t^m$ where U_0 is the inlet velocity at $t = 0$. The definition of Reynolds number is the same as in the accelerated flat plate case.

The experimental set-up of the starting vortex flow visualization by Pullin and Perry [121] is shown in figure 5.8. The wedge of height h is kept normal to the accelerated flow in a channel of width H and is fixed to the wall with an angle 60° (Pullin and Perry [121] defined the wedge angle as $\theta = \beta\pi$ so that the case undertaken here corresponds to $\beta = \frac{1}{3}$). Note that the flow was driven by the rectangular piston as shown in the figure. Following Pullin and Perry [121], we have set the ratio of the channel width H and wedge-height h at $2 : 1$ as well.

The schematic of the flow along with boundary conditions is shown in figure 5.9. The dimensions of the computational domain was set as $-6.0 \leq x \leq 6.0$ and $-0.5 \leq y \leq 0.5$ such that $H = 1$. As per computational set-up, fluid is flowing from left to right. The boundary conditions at the inlet is taken as $u = U_0 + t^m$, $v = 0$ and $\psi = u(y - h)$, where t is the non dimensional time. ψ is scaled this way in order to attain a value zero on the top wall, i.e., $\psi_{top} = 0$ and consequently boundary condition for ψ at the bottom wall is $\psi_{bottom} = -(U_0 + t^m)\, H$; also $u = 0$, $v = 0$ thereat. At the outlet, we have used the zero gradient boundary condition $\dfrac{\partial \psi}{\partial x} = \dfrac{\partial u}{\partial x} = \dfrac{\partial v}{\partial x} = 0$.

For our simulations, we have selected $m = 0$, 0.45 and 0.88 which corresponds to the Reynolds number 1560, 6621 and 6873 respectively. Computations are performed on a

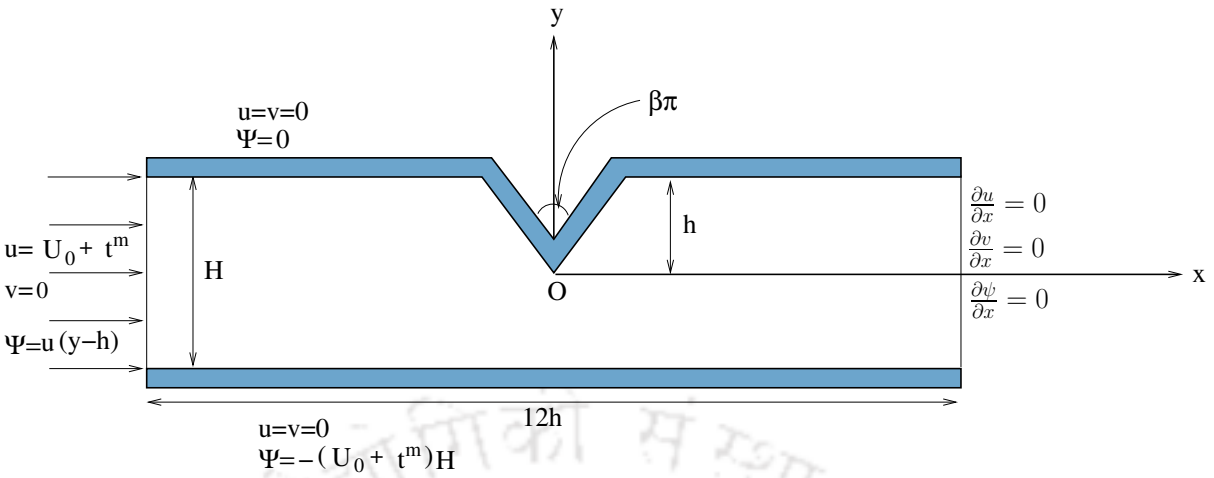

Figure 5.9: Problem statement of flow past a wedge in accelerated flow.

grid of sizes 401×101, 641×161 and 801×201 which are generated in such a way that the wedge geometry passes through grid points. In order to generate the grid following the wedge angle, we followed the procedure described in section 2.4.5 of chapter 2 for the flow past an inclined flat plate. The grid and it's close-up view are shown in figures 5.10 and 5.11 respectively.

Next, we carry out a grid-convergence study of our computed results. For this, we present the horizontal and vertical velocities (u and v) along the vertical line at $x = 0.3$ on the three different grids used in computation, viz., 401×101, 641×161 and 801×201 with $\Delta t = 10^{-5}$ for $Re = 6621$ at three different instants of non-dimensional time $t = 0.3$, 0.6 and 0.75 in figure 5.12. These figures clearly demonstrates the grid-independence of our computed solutions presented in figure 5.14. Note that for all the numerical results that follow, a grid of size 801×201 with $\Delta t = 10^{-5}$ has been used.

As in the last test case, in this problem also, we focus only on the starting flow development. Evolution of starting vortex starts with the boundary layer development on leeward direction which thickens with time. The vorticity accumulates near the tip on leeward direction leading to formation of starting vortex. Initially, all vorticity values are positive with the maximum occurring at the wedge tip. After some time, a negative vorticity region develops within the starting vortex at the wedge wall. The negative vorticity boundary layer thickens with time leading to separation of starting vortex from the wedge.

One of the major objectives of our computational endeavour is to replicate the flow

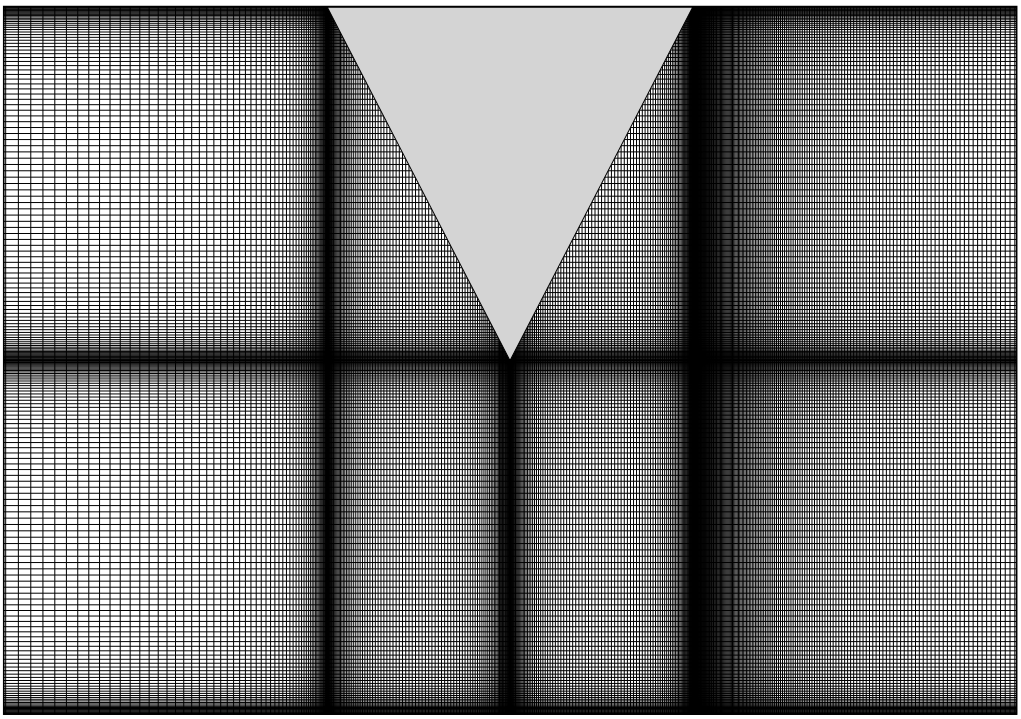

Figure 5.10: The grid used for accelerated flow past an wedge mounted on wall.

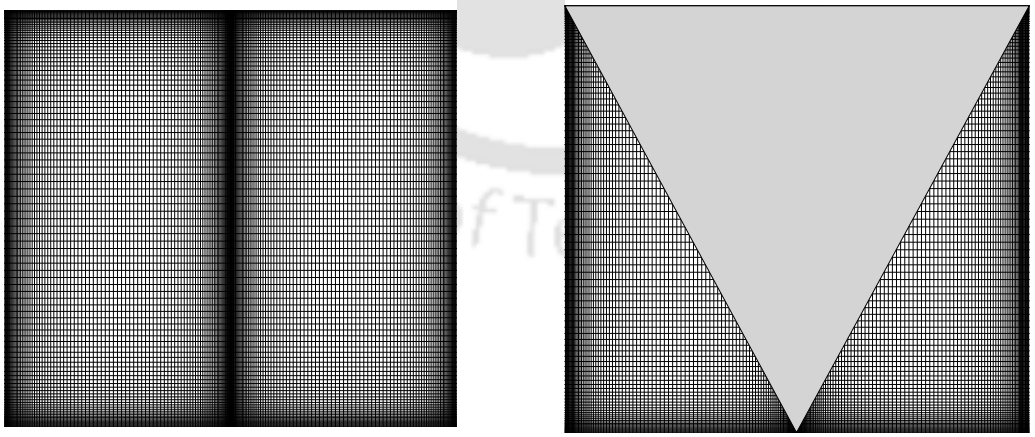

(a) (b)

Figure 5.11: *The close-up view of the grid and wedge used for accelerated flow past an wedge mounted on wall.*

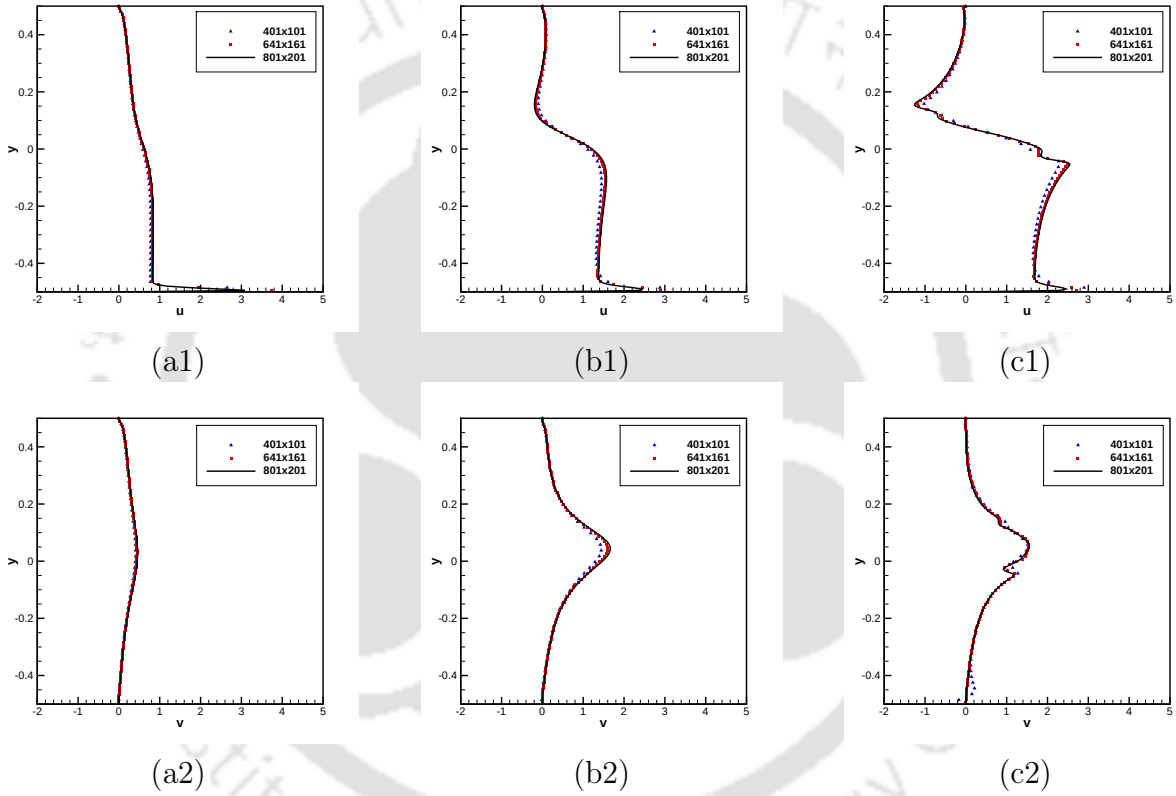

Figure 5.12: Grid independence of the computed solutions for three different grids at three different time step (a1,a2) $t = 0.3$, (b1,b2) $t = 0.6$ and (c1,c2) $t = 0.75$.

features of obtained by Pullin and Perry [121] in their lab experiment of start and stop type. Note that in their experiments, the flow was stopped at actual time $t = 12.52s$ for $Re = 1560$, $t = 5.96s$ for $Re = 6621$, and $t = 7.08s$ for $Re = 6873$ and as such we are comparing our simulations up to the same corresponding dimensional times; they correspond to non-dimensional times 0.62, 0.93 and 1.09 respectively [121]. In the next figures 5.13-5.15, we plot the streaklines resulting from our numerical simulation at different time stations with the experimental visualization of [121] side by side corresponding to these Reynolds numbers. One can see all the four stages of start-up vortex evolution observed in the accelerated flat plate here also; however, such evolution is much more rapid than the flat plate case. It is heartening to see that our computed results are extremely close to the experimental results of [121]. Apart from the computational accuracy of the data, this example also aptly demonstrates the capacity of the scheme developed in Chapter 3 in handling both Dirichlet and Neumann boundary conditions with equal ease. A close look at the boundary conditions mentioned above would reveal that while Dirichlet boundary conditions have been used for ψ at the top and bottom walls, inlet and on the surface of the wedge, Neumann boundary condition has been employed at the outlet.

In figures 5.16 and 5.17, we show the effect of m on the flow. In figure 5.16, we show the streamlines at time $t = 0.8$ for different values of m. One observes that with increase in m, the size of primary vortex is reducing. However, the role of m could be better understood by looking at the flow for a fixed displacement d of the piston as detailed in figure 5.8 for varying m's. Such a strategy was also used by Xu and Nitchz [168] in their study of the flow past a flat plate, where for a fixed frame at infinity, the plate was assumed to move from right to left with a velocity t^m in a fluid at rest. Likewise, in the present case, the piston being moved from rest in the horizontal direction with a driving velocity obeying $u = t^m$, it will traverse a distance $d = \dfrac{t^{m+1}}{m+1}$ [121]. The solution at a fixed time depends on m, as the piston would have traversed significantly different distances for different values of m as the formula for d suggests.

In figure 5.17, we compare the vortcity contours, streaklines and the streamlines for a fixed displacement $d = 1$ of the piston for $m = 0$, 0.45 and 0.88. The corresponding vector field in the vicinity of the tip of the wedge is shown in figure 5.18. One can see from figures 5.17(a1)-(a3) that as m increases, the vortex size decreases gradually. The

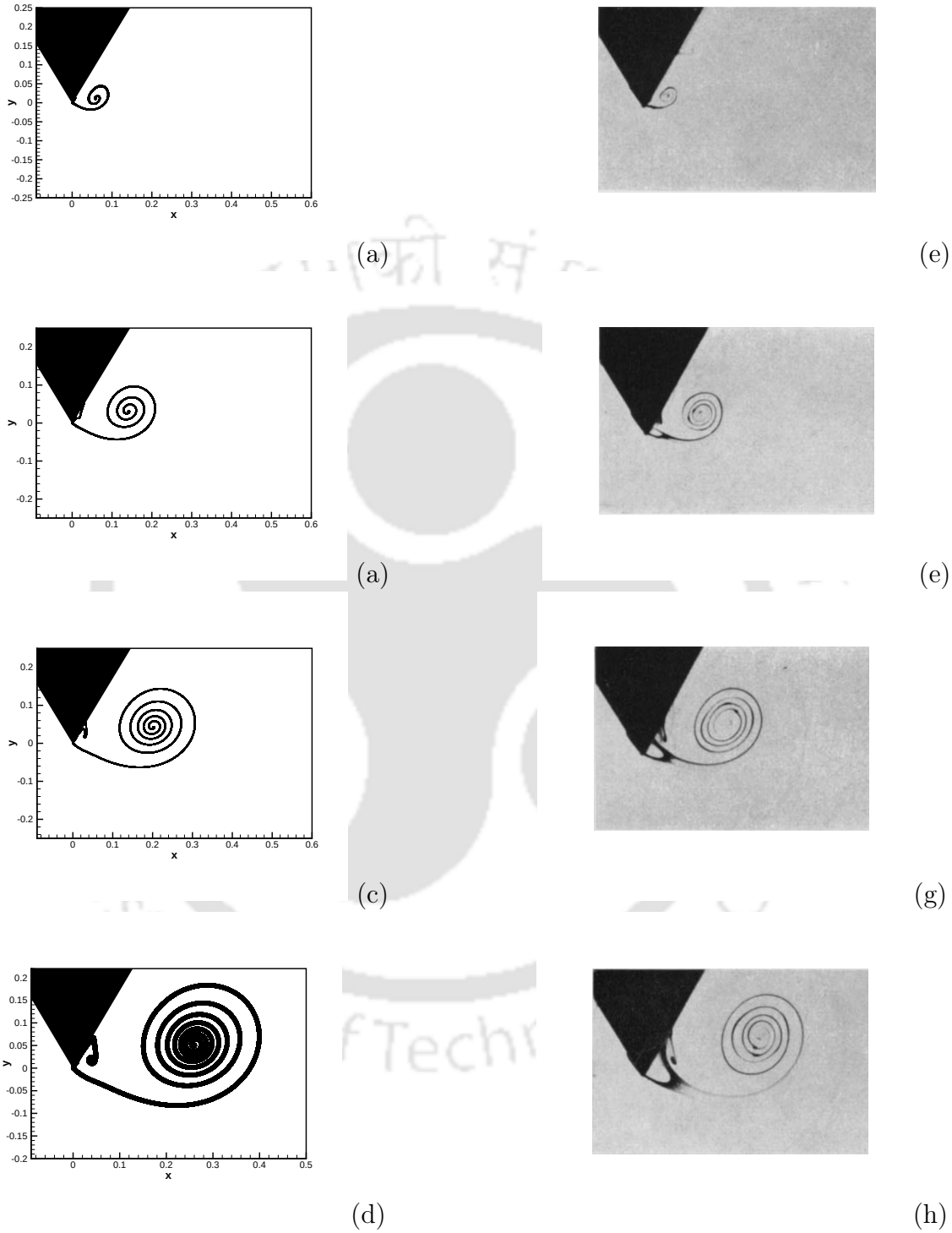

Figure 5.13: *Streaklines for flow past a wedge at different instants (a) $t = 1s$, (b) $t = 3s$,(c) $t = 5s$, (d) $t = 7s$, (e) $t = 1s$ (exp.), (f) $t = 3s$ (exp.),(g) $t = 5s$ (exp.), and (h) $t = 7s$ (exp.) for $Re = 1560$ and $m = 0$.*

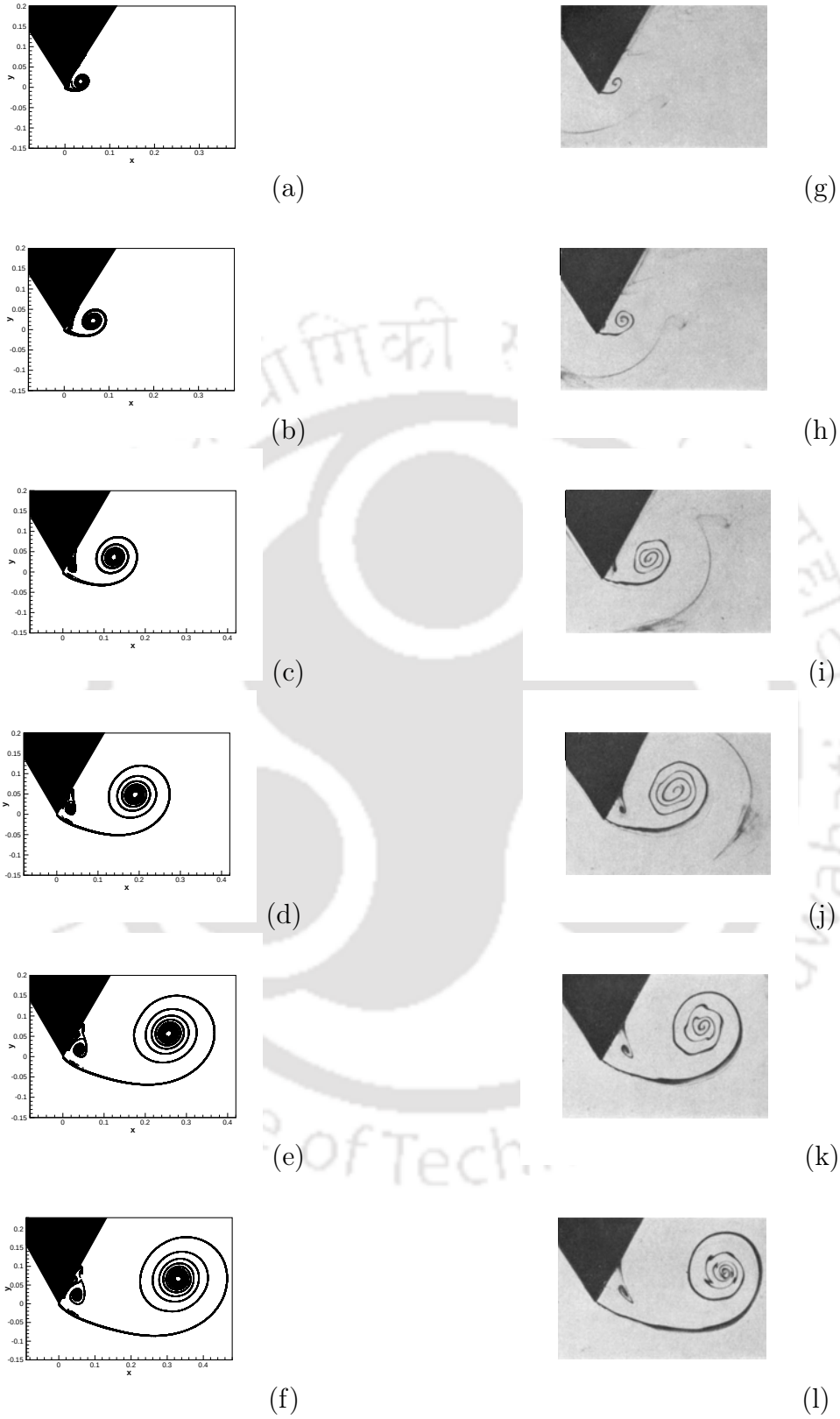

Figure 5.14: *Streaklines for flow past a wedge at different instants (a) $t = 1s$, (b) $t = 1.6s$,(c) $t = 2.8s$, (d) $t = 4s$, (e) $t = 5s$, (f) $t = 5.6s$, (g) $t = 1s$ (exp.), (h) $t = 1.6s$ (exp.),(i) $t = 2.8s$ (exp.), (j) $t = 4s$ (exp.) (k) $t = 5s$ (exp.), (l) $t = 5.6s$ (exp.) for $Re = 6621$ and $m = 0.45$.*

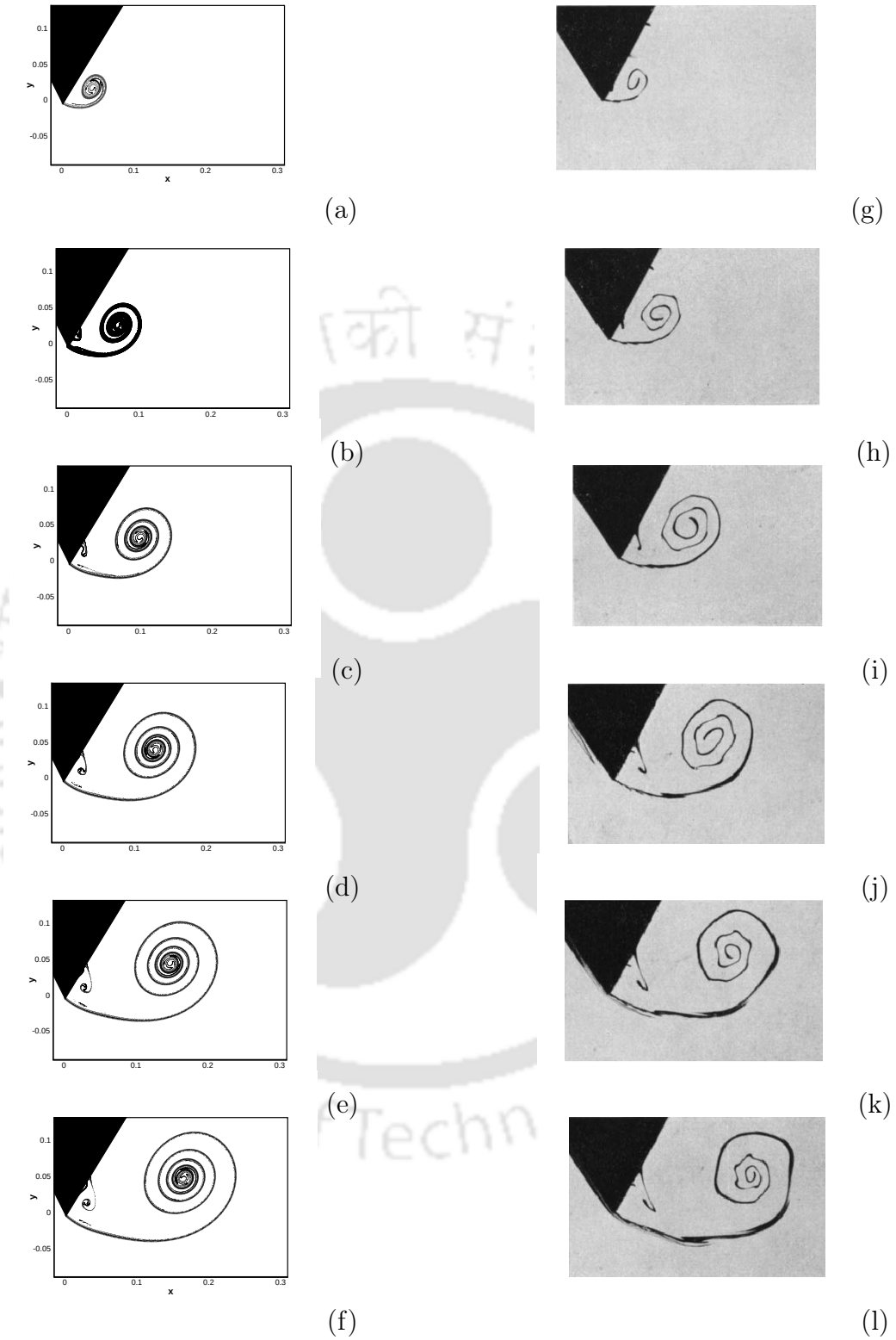

Figure 5.15: *Streaklines for flow past a wedge at different instants (a) $t = 2.8s$, (b) $t = 4s$,(c) $t = 5s$, (d) $t = 6s$, (e) $t = 6.6s$, (f) $t = 7s$, (g) $t = 2.8s$ (exp.), (h) $t = 4s$ (exp.),(i) $t = 5s$ (exp.), (j) $t = 6s$ (exp.) (k) $t = 6.6s$ (exp.), and (l) $t = 7s$ (exp.) for $Re = 6873$ and $m = 0.88$.*

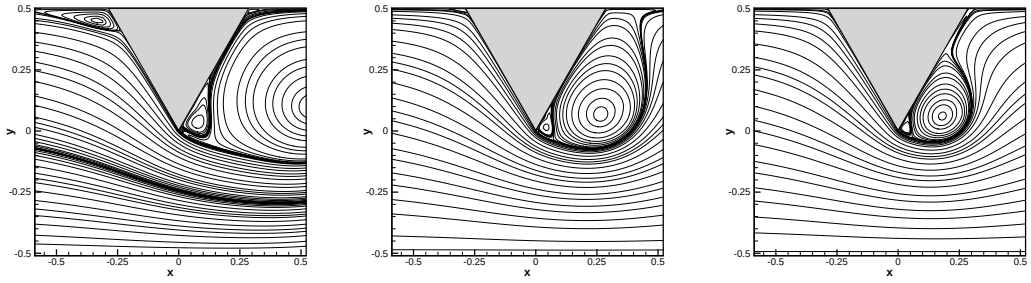

Figure 5.16: Streamlines for accelerated flow past a 60^o wedge at time $t = 0.8$ for $Re = 1560$ (left, m=0), $Re = 6621$ (middle, m=0.45) and $Re = 6873$ (right, m=0.88).

development of shear layer is more prominent as m increases, which is also obvious from the velocity vector plots in figures 5.18(a)-(c). The density of the streamlines below the bounding streamline of the core vortex clearly indicates a stronger velocity field with increase in m, which is also reflected by the length of the vectors. The streaklines and vortcity contours in figures 5.17(b2)-(b3) and 5.17(c2)-(c3) clearly demonstrate that for the accelerated flow, shear layer instability has set in, which is indicated by the waviness of the outermost vortex layer of the starting vortex (see figure 5.18(b)-(c) also). This will be discussed in more details in the next section. Lastly, in figure 5.19, we show the vorticity profile as a function of a zero and non-zero values of m which corresponds to the wedge experiencing a uniform and accelerated flow respectively. Here we plot the vorticity values corresponding to $m = 0$ and 0.88, and $d = 1$ along the horizontal line passing through the core vortex center. One can clearly see larger maximal vorticity occurring for smaller value of x for non-zero m, reflecting the smaller shape of the vortices for the accelerated flow. The shear layer instability for the accelerated case is clearly indicated by the highly oscillating nature of the graph against a much well-behaved one for the uniform flow case.

5.2.3 Existence of Coherent Structures

A coherent structure is a structure that stays in the flow for a relatively long period of time, and it is not just a transient phenomenon. For example, let us consider a two-dimensional turbulent flow; there are many structures that look like vortices and stay in the flow but only for a brief time. They will have a rotational velocity and has a

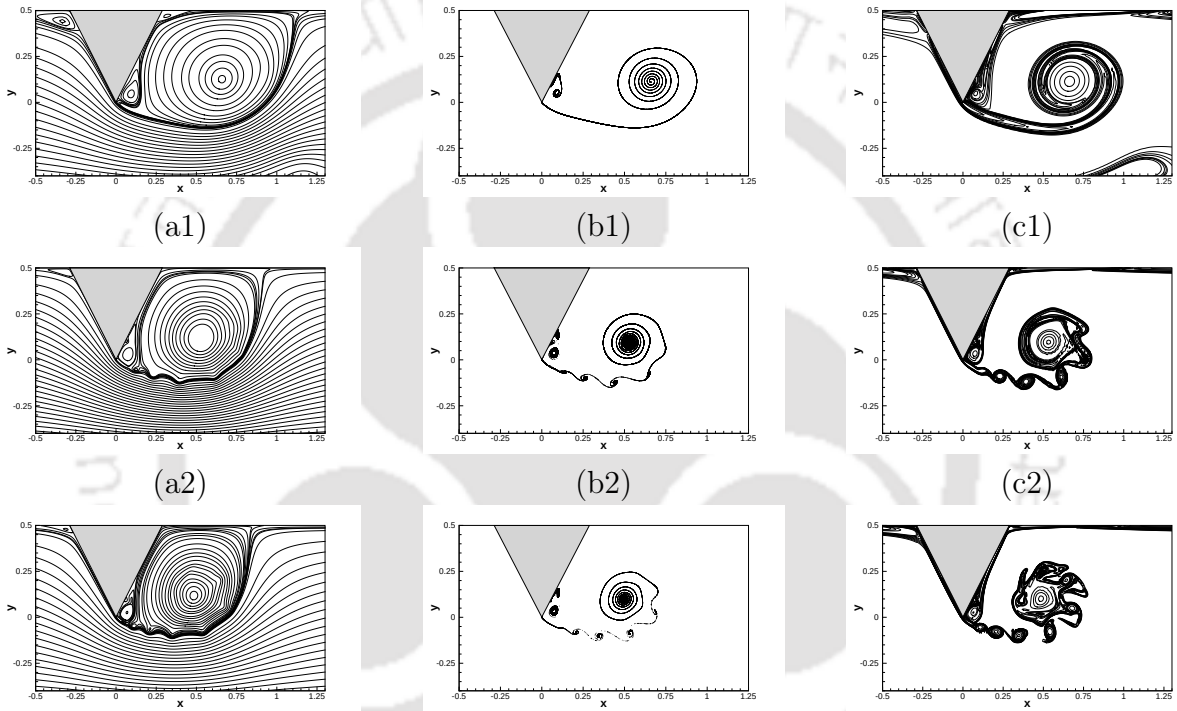

Figure 5.17: Effect of m on the flow field for a fixed displacement $d = 1$: The rows from the top to bottom corresponds to $m = 0$, 0.45 and 0.88 and the columns represent (a) Streamlines, (b) streaklines and (c) vorticity contours.

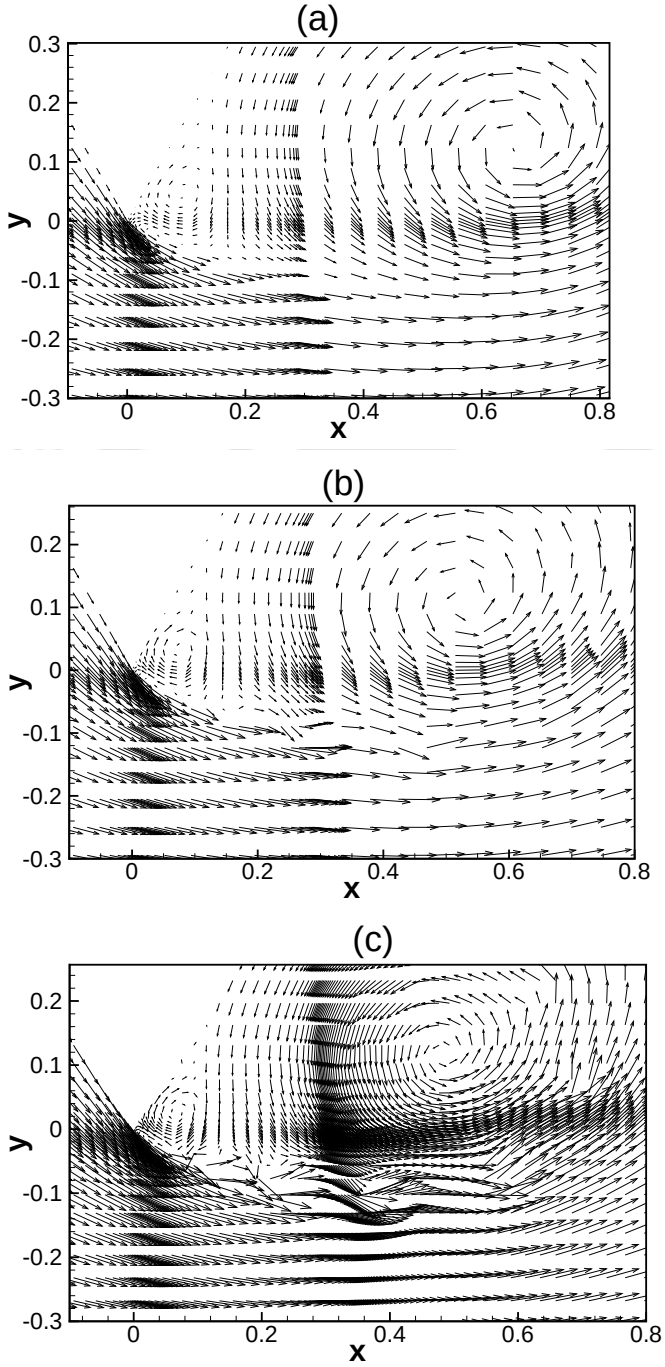

Figure 5.18: The velocity vector field close to the wedge tip for $d = 1$ and (a) $Re = 1560$, (b) $Re = 6621$ and (c) $Re = 6873$.

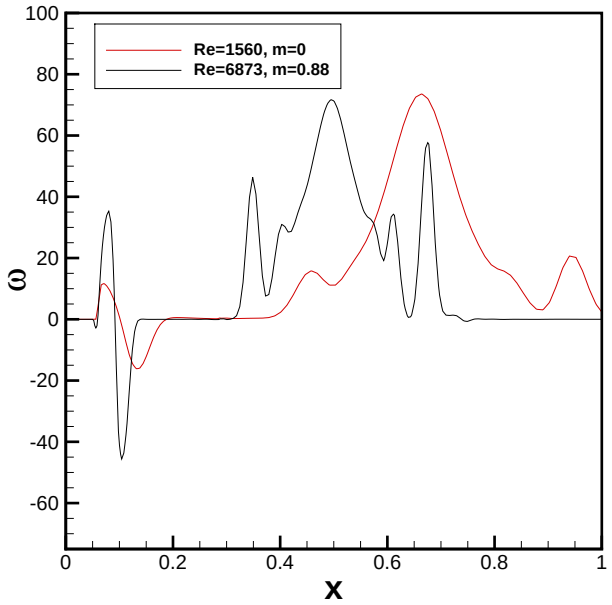

Figure 5.19: Vorticity distribution across the horizontal line through the core vortex center for $d = 1$: (a) $Re = 1560$ and (b) $Re = 6873$.

shape resembling a circle, and if they do not last more than a few dynamical times, they are transient, non-coherent, and defined just as Eddies. However, if we have an 'Eddy' that stays there for quite a while and does not seem to disappear, it is already a vortex rather than an Eddy, and it is not transient any more. These structures can last a viscous time scale and more, depending on the conditions, and these are coherent structures. Turbulent flows are characterized by multi-scale vorticity fluctuations. There are several methods to identify vortical coherent structures. For example, closed-loop streamlines and pathlines, minimum pressure regions, and absolute magnitude of vorticity, but these methods do not actually identify vortex cores as they unify rotational motion and shear. Nevertheless, Jeong and Hussain [61] demonstrated that the second invariant of the rate of strain-tensor and the negative part of the second largest eigenvalue of the same tensor are reliable indicators of coherent structures in various flow situations. The second invariant in terms of streamfunction is given by the **Q criterion** [14]. A quick backdrop of this criterion could be given as follows:

The eigenvalue analysis of the perturbed velocity field mentioned above, the eigenval-

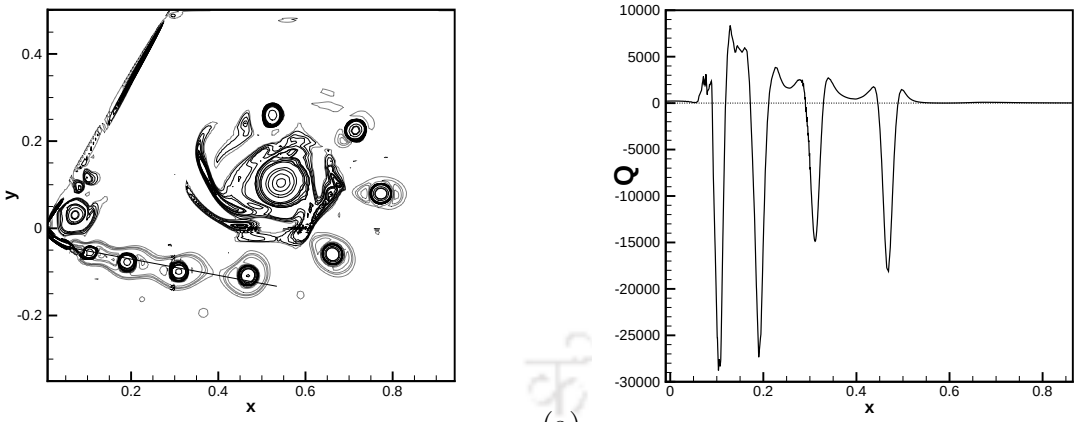

(a)
(b)

Figure 5.20: (a) Contour maps of Q at $t = 14.08$ (b) Distribution of Q along the line shown in (a) for $Re = 6873$.

ues are given by the formula $\lambda = \pm\sqrt{Q}$, where

$$Q = \left(\frac{\partial^2\psi}{\partial x \partial y}\right)^2 - \frac{\partial^2\psi}{\partial x^2}\frac{\partial^2\psi}{\partial y^2}.$$

It follows that in the regions of the fluid where $Q < 0$, the distance between two particles embedded in the original velocity field will not diverge as a function of time. In figure 5.20(a), we plot the Q contours for the flow past a mounted wedge discussed in the previous section for $Re = 6873$ at non-dimensional time $t = 14.08$. Here, the solid curves represent negative values of Q which corresponds to stable eigenvalues while dotted curves represent positive values corresponding to unstable ones. As such the vortical shapes bounded by closed solid curves are coherent structures. One can see that these structures are always surrounded by dense negative contours indicating that large instabilities occur only at the edge of the vortices. This phenomenon can be understood more clearly by drawing a straight line through the centres of the vortices (see figure 5.20(a)) emanating from the wedge, and plotting the Q distribution along it as shown in figure 5.20(b). Here the segments of the graph below the zero-line represent the coherent structures. One can always see some oscillations on the edge of these structures just above the zero-line indicating the instabilities surrounding them.

5.2.4 The Structure of Vortex shedding

In this section, we provide a detailed description of different stages of evolution for the flow past a mounted wall subjected to accelerated flow for $Re = 6873$ until transition to turbulence. Note that in their study [121], Pullin and Perry continued their laboratory experiment only up to a non-dimensional time $t = 1.09$, while we carried out our numerical experiment for the same up to $t = 3.10$. In the absence of any experimental visualization beyond $t = 1.09$ for this flow configuration, in order to compare our computed results, we looked up to the experimental visualization of the study by Lian and Huang [100], who carried out a series of experiments for the accelerated flow past a flat plates with sharp edges in the range $2000 \leq Re \leq 15000$. They used hydrogen bubble technique to visualize the flow and reported three stages of evolution of the starting vortices culminating in a three-fold structure leading to the onset of transition to turbulence. Our investigation also revealed that all these three stages are very much evident during the course of the flow. Note that since Lian and Huang [100] provided pictures only for the upper edge of the plate, in some of the figures that follow next, the computational frame has been tilted upside down to compare our results with them.

Initial Stage

The structure of the starting vortex has a spiral vortex sheet as shown in the figure 5.21 where Lian and Huang's [100] experimental visualization on the top has been compared with the streaklines resulting from our computation on the bottom. The vortex shedding from the edge has rolled up into spiral shape with a core closely wound-up layer (see figures 5.15(c)-(f) also) [120]. For real fluids like the ones considered in these experiments, the viscous effect makes the closely spaced shear layers merge quickly into a rigid core, where the concentrated vorticity in the vortex sheet diffuses into uniformly distributed vorticity as can be seen in figure 5.21(a) and the velocity vectors and vorticity contours (solid red lines) presented in figure 5.22.

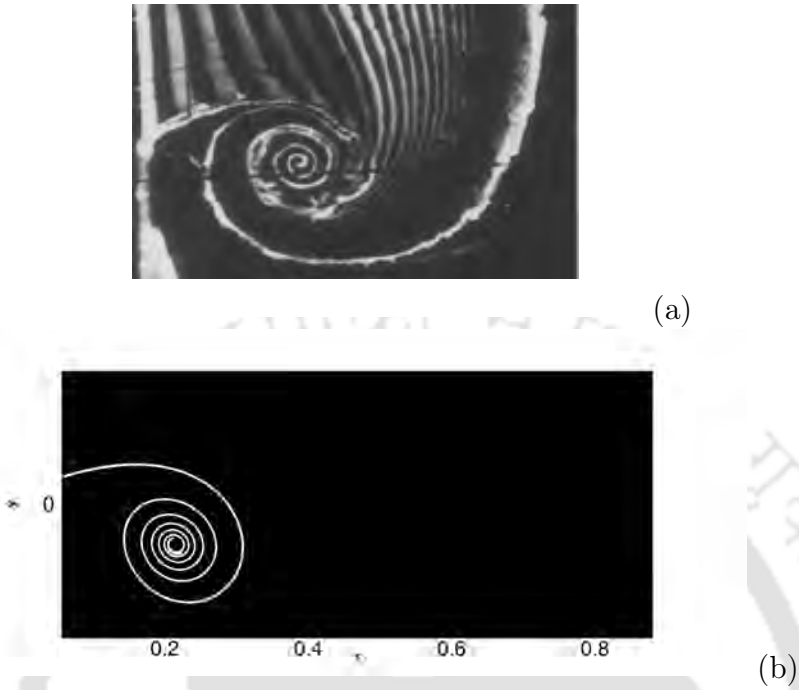

Figure 5.21: The initial stage: Comparison of streaklines between (a) the experimental result of Lian and Huan [100] ($t = 1.44$) and (b) the present numerical simulation ($t = 1.0$).

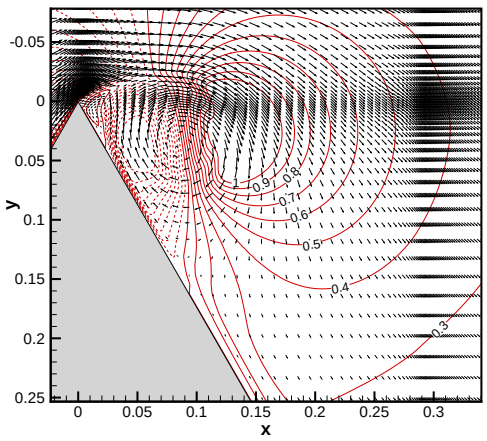

Figure 5.22: The initial stage: Velocity vectors and vorticity contours from the present computation for $Re = 6873$ at time $t = 0.5$.

Second Stage

The outermost vortex layer of the starting vortex becomes wavy due to instability of the shear layers as shown in figure 5.23 where we have compared our computed streaklines on bottom with the experimental visualization of Lian and Huang [100] on the top. Afterwards, a part of the outermost vortex sheet breaks and rolls up into small vortices as shown in these figures. That stating vortex breaking into wavy structure is the announcement of shear layer instability can be seen more clearly from figure 5.24, where we have shown the streaklines more closer to the wedge tip at $t = 2.0$ in figure 5.24(a). These small vortices have a double-branched spiral roll structure as shown in figure 5.24(b), which is typical of shear layer instability [158]. Similar small vortex structures were also observed by Pierce (1961), and Pullin and Perry (1980). One can clearly see from figures 5.23(a)-(b) that these small vortices are spaced almost uniformly, with their centers lying across the spiral curve of the the large starting vortex. This confirms that they are nothing but parts of the large starting vortex only. Each small vortex has also rolled up in spiral shape as can be seen from figures 5.24(a)-(b) with an apparently very thin shear layer that can be seen from the mean subtracted velocity vector plots in 5.24(c).

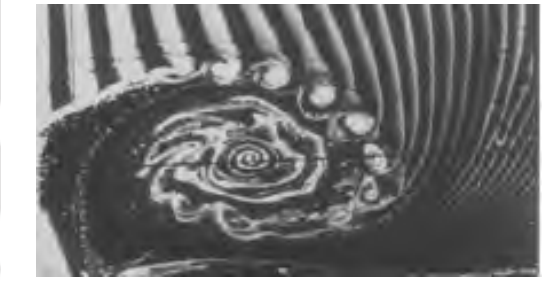

(a)

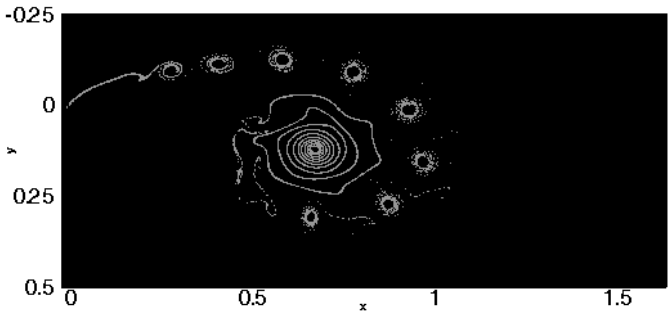

(b)

Figure 5.23: The second stage: Comparison of streaklines between (a) the experimental result of Lian and Huan [100] ($t = 2.09$) and (b) the present numerical simulation ($t = 2.0$).

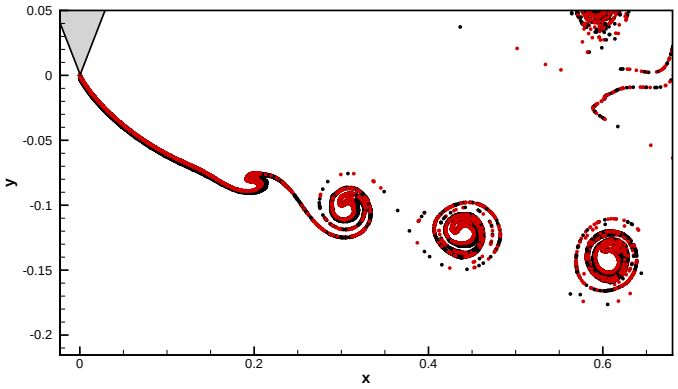

(a)

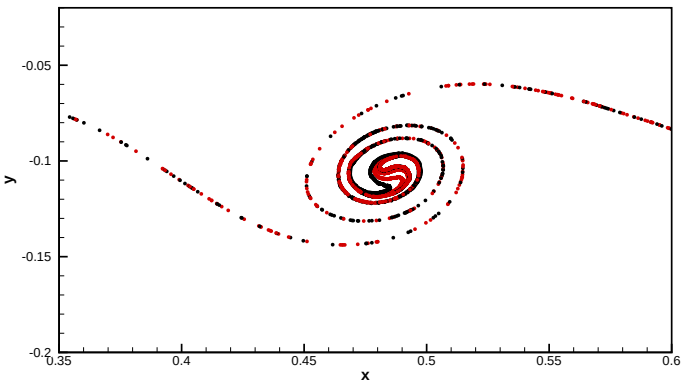

(b)

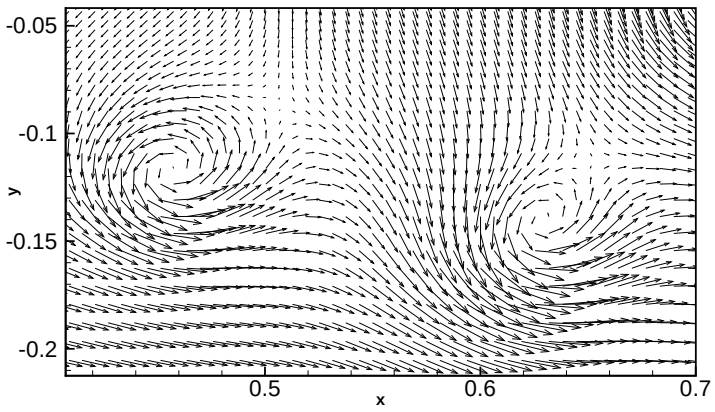

(c)

Figure 5.24: Close up view of the shear layer instability for $Re = 6873$ at time $t = 2.0$: (a) the small vortices nearby the edge, (b) the double-branching structure of the individual vortex and (c) mean subtracted velocity vector plots.

Third Stage: Three fold structure

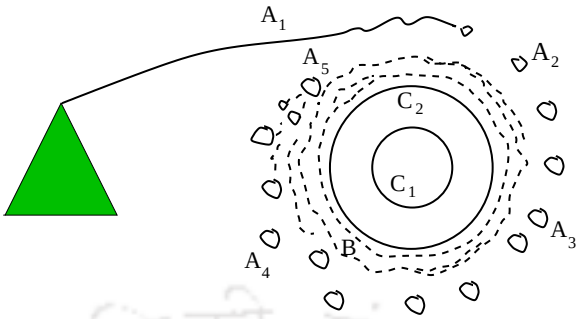

Figure 5.25: Schematic of the three-fold structure.

The schematic of the typical shape of the starting vortex behind the wedge at this stage is shown in figure 5.25. It can be further divided into three parts as shown in this sketch: the outer most vortex layer, the core and the annular region. The outermost layer may be divided into several segments:

- A1: The shear layer just shedded from edge, it is smooth in the initial part and becomes wavy in the downstream.
- A2: This is the segment where the shear layer breaks into small vortices; these are uniformly spread over a smooth curve.
- A3: This is the region where these small vortices lose their uniform spacing as a result of interaction between the shedded small vortices. The instability of the interaction may cause the location of these vortices to become chaotic.
- A4: The small vortices are spaced even more randomly in this segment.
- A5: It is at the end of the outermost layer. The flow is apparently very turbulent here.

The core can be divided into two parts: The Central core 'C_1' and the outer core 'C_2'.

- C_1: Laminar diffusion is the main reason behind the formation of this core. The concentrated vorticity of the initial spiral shear layer was diffused by viscous shear stress. Since it is not accompanied by any mass transfer, the shape of the spiral line

remains undisturbed as shown in the the central part of the starting vortex in figure 5.26. However, the flow pattern surrounding this part appears very turbulent. This part is a rigid core.

- C_2: It is the region around the undisturbed core and the streak lines appear very chaotic. However a close look at figure 5.23 would reveal that some instants earlier, in the same region 'C_2' the streak line used to be smooth, that implies there is no shear layer and no turbulent flow. Through a series of visualization, Lian and Huang [100] had established that but some time before the event of figure 5.23(a), it was in fact turbulent, the turbulence appearance in the region C_2 of figure 5.26 had germinated at that time. Thus the fluid in the outer core C_2 has passed three stages; in the initial stage there were spiral shear layer, which then broke into turbulent flow, and later, the turbulence has dissipated and the flow has again become laminar with distributed vorticity. This is the reason C_2 is sometimes termed as a "relaminarized" region.

The region marked as B is the annular region which is turbulent in nature, a thin one and sometimes one can see this layer itself breaking into small vortices as in figure 5.23(a).

Thus it is clear from the above discussion that our simulation has very aptly captured all three stages of the evolution of the starting vortex leading to the three-fold structure which is exemplified the comparison of our computed results with those of Lian and Huang [100] in figure 5.23. This further re-establishes the robustness of the scheme developed in Chapter 3, which despite being primarily developed for laminar flows, has remarkably resolved the early stage of turbulent flows as well.

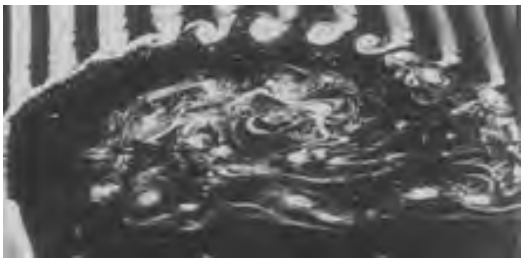

(a)

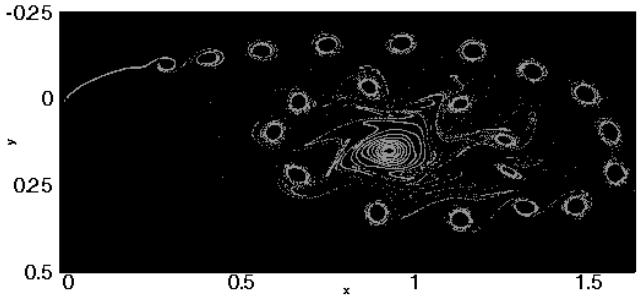

(b)

Figure 5.26: The third stage: Comparison of streaklines between (a) the experimental result of Lian and Huan [100] ($t = 2.885$) and (b) the present numerical simulation ($t = 2.6$).

5.3 Conclusion

In this chapter, we have employed the finite difference scheme developed in Chapter 3 to some complex fluid flow problems involving flow past sharp edges in uniform and accelerated flow. In the first problem, we have investigated the far wake characteristics of the flow past a normal flat plate subjected to uniform cross flow. Several modes of vortex shedding pertaining to three different Reynolds numbers are detailed and these modes are explained through an FFT study of the transverse velocity at eight different locations of the flow field. For $Re = 100$, the flow with unsteady near and far wakes at the beginning is seen to settle down to an unsteady near wake and steady far wake. For $Re = 140$, the flow in the far wake is seen to undergo a transition and undulate with a very low frequency vortex street. Although these low frequency vortex has insignificant energy content, at a higher Reynolds number 175, it acquires more energy to become the dominant one in the far wake along with a tertiary vortex pattern having even a much lower frequency.

In the next problems for bluff bodies subjected to accelerated cross flow, we firstly study the start-up vortex of the flow past a normal flat plate for $Re = 500$. All the four main stages of early evolution of the flow: (a) Rayleigh, (b) Viscous, (c) Self-similar inviscid and (d) Vortex expulsion, have been aptly captured by our simulation. Then we move to the problem of the flow past a wedge mounted on a wall for $Re = 1560$, 6621 and 6873. Our numerical simulation was able to replicate all the flow features of the famous 1980 laboratory experiment of Pullin and Perry [121] very accurately. We also investigated the effect of the parameter m that determines the intensity of acceleration. Our study found that a higher value of m enables a stronger flow field despite a reduction in the size of the starting vortices. For $m \neq 0$, shear layer instability sets in very early in the flow. However, the most significant achievement of the current study is the simulation of the flow for a time range much beyond Pullin and Perry's experimental endeavour. In the process, we have been able to resolve flow features at the instants of transition to turbulence. The accuracy of our simulation has been validated not only by the existence of coherent structures in the flow, but also by the remarkable closeness of our simulation to the high Reynolds number experimental results of Lian and Huang [100] for the accelerated flow past a normal flat plate. All the three stages of vortex shedding, including the extremely complicated three-fold structure were resolved very efficiently.

CHAPTER 6

CONCLUSION

6.1 Observations and Remarks

This dissertation is concerned with the development of compact finite difference schemes for incompressible viscous flows governed by the Navier-Stokes (N-S) equations. Two compact schemes were developed for the biharmonic form of the N-S equations on nonuniform grids without transformations for simulating fluid flow problems, firstly for steady-state and then for the transient one. The schemes are first tested against analytical problems to understand its working mechanism. Both schemes were then applied to different complex physical problems with or without heat transfer to examine their efficiency, accuracy, and robustness. A comprehensive study is carried out by comparing results obtained through the schemes with existing analytical, numerical, and experimental results. Hereinafter, the work carried out in this thesis is described briefly so that some insightful comments can be made at the end.

Highlights of the thesis:

- A second order compact finite difference scheme for the steady-state N-S equations is developed. This approach adopted here enables us to simulate flow problems having curved boundaries or those involving bluff bodies. It is applied to one problem having an analytical solution and numerous fluid flow and heat transfer problems having different complexities. We have also established the numerical convergence rate of

the scheme. The scheme's robustness was demonstrated by its remarkable ability to handle extreme clustering that enable us to capture the smaller scale vortices in the lid-driven cavity and backward-facing flows. One of the rarest examples, "flow past an inclined flat plate mounted on a wall," was computed in a finite-difference setup where the grid lines are not aligned the immersed body. The steady flow past a circular cylinder, which represents a bluff body having a curved boundary is another example of a body immersed in fluid flow. We were able to simulate this flow very elegantly resolving all typical features of it. The scheme was also applied to heat transfer problems, viz., natural convection around a heated solid body in a square cavity and conjugate heat transfer in a suddenly expanding channel. All the test cases were simulated for a wide range of flow parameters, and the results were extremely close to well-established results, including experimental ones.

- Next, we have developed a compact, implicit and stable finite difference scheme for the biharmonic form of the transient N-S equations on nonuniform Cartesian grids, which is uniformly second order accurate both in time and space. To the best of our knowledge, this is probably the first finite difference scheme to compute transient flows past bluff bodies on nonuniform Cartesian grids without transformation or roping in the immersed interface approach. The scheme was applied to seven different problems of varying physical complexities to investigate its efficiency and robustness. The scheme's robustness is highlighted by the accurate resolution of a host of complex flows past bluff bodies with different configurations and boundary conditions viz., a flat plate, a circular cylinder, and an inclined square cylinder. All the details of the shedded vortex structures under different circumstances have been captured very elegantly. Grid-independence of computed solutions was established not only for the problem of having an analytical solution but also for flow past bluff bodies in uniform flows. In addition to the stationary cylinder, the scheme has also been able to capture flows past an oscillatory and a rotating cylinder very accurately demonstrating its ability to tackle moving boundaries as well. The advantage of the proposed scheme over the ones with grid transformations in terms of the flexibility of placing suitable Cartesian grids away from bluff bodies with curved boundaries has also been demonstrated. Again the test cases are simulated for a

wide range of parameters. Results were extremely close to the available numerical and experimental results in all the cases, both qualitative and quantitatively.

- Next, we have applied the transient scheme mentioned above to investigate comprehensively the flow past an impulsively started circular cylinder. The scheme was able to capture all the typical flow features associated with this flow for a wide range of Reynolds numbers $10^0 \leq Re \leq 10^4$. The robustness of the scheme is highlighted not only by the fact that it captures very accurately the periodic nature of the flow for $50 \leq Re \leq 300$ characterized by von Karman vortex street but also the secondary phenomena for moderate Re ($300 \leq Re \leq 1000$), α and β-phenomena for higher ones ($3000 \leq Re \leq 9500$), and finally sub-α and sub-β-phenomena for $Re = 5000$ and 7500. In the process, the secondary and tertiary vortex dynamics for $Re = 7500$ have also been documented in detail. Analysis of the vortex shedding process has been carried out further through the study of the streaklines and time history of drag and lift coefficients. We extensively compare our results with experimental and numerical results available in literature both qualitatively and quantitatively. Along with the grid independence study, we have also established the efficiency of the simulation through a comparison on Cartesian vis a vis polar grid.

- Lastly, we applied the scheme to study the flows past sharp edged bluff bodies in uniform and accelerated flows; flat plate and wedge were considered as a bluff body. First, we have performed simulations for uniform flow past a flat plate to understand the far wake characteristics. Several vortex shedding modes are thoroughly analyzed via an FFT of the transverse velocity at different flow field locations. Next, we studied the start-up vortex of the accelerated cross flow past a normal flat plate for $Re = 500$. All four main stages of the early evolution of the flow: (a) Rayleigh, (b) Viscous, (c) Self-similar inviscid, and (d) Vortex expulsion, have been aptly captured by our simulation. Next, we have simulated flow past wedge hinged on a wall. We accurately replicated the flow visualization from Pullin and Perry's famous experiment of 1980 through our simulation. In all the cases, our results are found to be extremely close to the experimental results. In Pullin and Perry's experiment, the flow was stopped after some instant, but we have continued our simulation

numerically. We have shown that the flow is the onset of turbulence using Q-criterion. We have also shown and described the threefold stages and two cores of the spiral shear layer. We have also studied effect of accelerating parameter m on shear layer instability. The validation of this comes from the immense proximity of our simulations to the experimental visualizations, specifically in the case of the spiral vortex for the accelerated flow past the wedge.

The above discussions clearly establish that all the objectives set out at the beginning have been accomplished by the work carried out in the thesis. It has also opened up a host of other interesting research possibilities which can be listed in a nutshell as follows:

6.2 Scope for Future Work

- So far the schemes developed in the thesis have been used only to simulate bluff bodies which was symmetric about either x or y-axis. Simulation of fluid flow problems associated with asymmetric bluff bodies viz. inclined elliptic cylinder, airfoil with different angle of attack could be another intriguing area of research.

- Although the transient scheme in this work have been mainly developed for incompressible laminar fluid flow problems, its potential was also evident in aptly capturing transition to turbulence in the mounted wedge problem. It would be interesting to see how the scheme extends to problems involving compressible and turbulent flows.

- Comprehensive study on shear layer stability and flow instability for different bluff bodies in transition flow through the proposed transient scheme is another area worth exploring.

- Since compact schemes are already available for the 3D biharmonic equation in uniform grids, it would be interesting to see whether one could fit it in simulating fluid flows in 3D on nonuniform grid.

APPENDIX A

DETAILS OF FINITE DIFFERENCE OPERATORS

The following is concerned with section 3.2 related to the development of the numerical scheme. The mixed derivatives here can be calculated as:

$$\frac{\partial^4\psi}{\partial x^2\partial y^2} = \delta_x^2\delta_y^2\psi - \left(\frac{x_f - x_b}{3}\right)\frac{\partial^5\psi}{\partial x^3\partial y^2} - \left(\frac{y_f - y_b}{3}\right)\frac{\partial^5\psi}{\partial x^2\partial y^3} + O\left((x_f - x_b)(y_f - y_b)\right) \quad \text{(A.1)}$$

Differentiating (A.1) with respect to 'x'

$$\frac{\partial^5\psi}{\partial x^3\partial y^2} = -\delta_x^2\delta_y^2 v - \left(\frac{x_f - x_b}{3}\right)\frac{\partial^6\psi}{\partial x^4\partial y^2} - \left(\frac{y_f - y_b}{3}\right)\frac{\partial^6\psi}{\partial x^3\partial y^3} + O\left((x_f - x_b)(y_f - y_b)\right) \quad \text{(A.2)}$$

likewise, differentiating (A.1) with respect to 'y' yields

$$\frac{\partial^5\psi}{\partial x^2\partial y^3} = \delta_x^2\delta_y^2 u - \left(\frac{x_f - x_b}{3}\right)\frac{\partial^6\psi}{\partial x^3\partial y^3} - \left(\frac{y_f - y_b}{3}\right)\frac{\partial^6\psi}{\partial x^2\partial y^4} + O\left((x_f - x_b)(y_f - y_b)\right) \quad \text{(A.3)}$$

Making use of (A.2)-(A.3), (A.1) becomes,

$$\frac{\partial^4\psi}{\partial x^2\partial y^2} = \delta_x^2\delta_y^2\psi + \left(\frac{x_f - x_b}{3}\right)\delta_x^2\delta_y^2 v - \left(\frac{y_f - y_b}{3}\right)\delta_x^2\delta_y^2 u + O\left((x_f - x_b)(y_f - y_b)\right) \quad \text{(A.4)}$$

Also, the third order partial derivatives of ψ can be approximated as follows

$$\begin{aligned}\frac{\partial^3\psi}{\partial x^2\partial y} &= \frac{\partial^2 u}{\partial x^2}\\ &= \delta_x^2 u - \frac{(x_f - x_b)}{3}\frac{\partial^3 u}{\partial x^3} + O\left(x_f^2 + x_b^2 - x_f x_b\right)\\ &= \delta_x^2 u - \frac{(x_f - x_b)}{3}\frac{\partial^4 \psi}{\partial x^3\partial y} + O\left(x_f^2 + x_b^2 - x_f x_b\right)\\ &= \delta_x^2 u + \frac{(x_f - x_b)}{3}\frac{\partial^3 v}{\partial x^2\partial y} + O\left(x_f^2 + x_b^2 - x_f x_b\right)\\ &= \delta_x^2 u + \frac{(x_f - x_b)}{3}\delta_x^2\delta_y v + O\left(x_f^2 + x_b^2 - x_f x_b\right)\end{aligned} \tag{A.5}$$

$$\begin{aligned}\frac{\partial^3\psi}{\partial x\partial y^2} &= -\frac{\partial^2 v}{\partial y^2}\\ &= -\delta_y^2 v + \frac{(y_f - y_b)}{3}\frac{\partial^3 v}{\partial y^3} + O\left(y_f^2 + y_b^2 - y_f y_b\right)\\ &= -\delta_y^2 v - \frac{(y_f - y_b)}{3}\frac{\partial^4 \psi}{\partial x\partial y^3} + O\left(y_f^2 + y_b^2 - y_f y_b\right)\\ &= -\delta_y^2 v - \frac{(y_f - y_b)}{3}\frac{\partial^3 u}{\partial x\partial y^2} + O\left(y_f^2 + y_b^2 - y_f y_b\right)\\ &= -\delta_y^2 v - \frac{(y_f - y_b)}{3}\delta_x\delta_y^2 u + O\left(y_f^2 + y_b^2 - y_f y_b\right)\end{aligned} \tag{A.6}$$

$$\begin{aligned}\frac{\partial^3\psi}{\partial x^3} &= -\frac{\partial^2 v}{\partial x^2}\\ &= -\delta_x^2 v + \frac{(x_f - x_b)}{3}\frac{\partial^3 v}{\partial x^3} + O\left(x_f^2 + x_b^2 - x_f x_b\right)\\ &= -\delta_x^2 v - \frac{(x_f - x_b)}{3}\frac{\partial^4 \psi}{\partial x^4} + O\left(x_f^2 + x_b^2 - x_f x_b\right).\end{aligned} \tag{A.7}$$

Likewise in $y-$direction,

$$\begin{aligned}\frac{\partial^3\psi}{\partial y^3} &= \frac{\partial^2 u}{\partial y^2}\\ &= \delta_y^2 u - \frac{(y_f - y_b)}{3}\frac{\partial^3 u}{\partial y^3} + O\left(y_f^2 + y_b^2 - y_f y_b\right)\\ &= \delta_y^2 u - \frac{(y_f - y_b)}{3}\frac{\partial^4 \psi}{\partial y^4} + O\left(y_f^2 + y_b^2 - y_f y_b\right),\end{aligned} \tag{A.8}$$

Here δ_t^+, δ_x, δ_y,δ_x^2 and δ_y^2 are defined as follows:

$$\delta_t^+\psi = \frac{\psi_{i,j}^{n+1} - \psi_{i,j}^n}{\Delta t},$$

$$\delta_x\psi = \frac{\psi_{i+1,j} - \psi_{i-1,j}}{x_f + x_b} \text{ and } \delta_x^2\psi = \frac{2}{(x_f + x_b)}\left[\frac{\psi_{i+1,j}}{x_f} - \left(\frac{1}{x_f} + \frac{1}{x_b}\right)\psi_{i,j} + \frac{\psi_{i-1,j}}{x_b}\right],$$

Likewise in the $y-$direction

$$\delta_y\psi = \frac{\psi_{i,j+1} - \psi_{i,j-1}}{y_f + y_b} \text{ and } \delta_y^2\psi = \frac{2}{(y_f + y_b)}\left[\frac{\psi_{i,j+1}}{y_f} - \left(\frac{1}{y_f} + \frac{1}{y_b}\right)\psi_{i,j} + \frac{\psi_{i,j-1}}{y_b}\right].$$

and the mixed derivative operator can written as ([70])

$$\delta_x\delta_y^2\psi = \frac{1}{2hk}\left\{\frac{1}{y_f}\left(\psi_{i+1,j+1} - \psi_{i-1,j+1}\right) - \left(\frac{1}{y_f} + \frac{1}{y_b}\right)\left(\psi_{i+1,j} - \psi_{i-1,j}\right) + \frac{1}{y_b}\left(\psi_{i+1,j-1} - \psi_{i-1,j-1}\right)\right\}$$

$$\delta_x^2\delta_y\psi = \frac{1}{2hk}\left\{\frac{1}{x_f}\left(\psi_{i+1,j+1} - \psi_{i+1,j-1}\right) - \left(\frac{1}{x_f} + \frac{1}{x_b}\right)\left(\psi_{i,j+1} - \psi_{i,j-1}\right) + \frac{1}{x_b}\left(\psi_{i-1,j+1} - \psi_{i-1,j-1}\right)\right\}$$

$$\begin{aligned}\delta_x^2\delta_y^2\psi = \frac{1}{hk}[&\frac{\psi_{i+1,j+1}}{x_f y_f} + \frac{\psi_{i-1,j+1}}{x_b y_f} - \left(\frac{1}{x_f y_f} + \frac{1}{x_b y_f}\right)\psi_{i,j+1} - \left(\frac{1}{x_f y_f} + \frac{1}{x_f y_b}\right)\psi_{i+1,j}\\ &+ \left(\frac{1}{x_f y_f} + \frac{1}{x_f y_b} + \frac{1}{x_b y_f} + \frac{1}{x_b y_b}\right)\psi_{i,j}\\ &- \left(\frac{1}{x_f y_b} + \frac{1}{x_b y_b}\right)\psi_{i,j-1} - \left(\frac{1}{x_b y_f} + \frac{1}{x_b y_b}\right)\psi_{i-1,j} + \frac{\psi_{i+1,j-1}}{x_f y_b} + \frac{\psi_{i-1,j-1}}{x_b y_b}],\end{aligned}$$

with $h = 0.5(x_f + x_b)$ and $k = 0.5(y_f + y_b)$.

In equation (3.17), the coefficients that appear are as follows

$$A = \frac{2}{hkx_f y_f}$$

$$B = \left[-\frac{36qy_f^2 y_b^2}{k(2y_f^2 + 2y_b^2 - y_f y_b)} \frac{1}{y_f^5} - \frac{2}{hk}\left(\frac{1}{x_f y_f} + \frac{1}{x_b y_f}\right)\right]$$

$$C = \frac{2}{hkx_b y_f}$$

$$D = \left[-\frac{36px_f^2 x_b^2}{h(2x_f^2 + 2x_b^2 - x_f x_b)} \frac{1}{x_f^5} - \frac{2}{hk}\left(\frac{1}{x_f y_f} + \frac{1}{x_f y_b}\right)\right]$$

$$E = \left[\frac{36px_f^2 x_b^2}{h(2x_f^2 + 2x_b^2 - x_f x_b)} \left(\frac{1}{x_f^5} + \frac{1}{x_b^5}\right) + \frac{36qy_f^2 y_b^2}{k(2y_f^2 + 2y_b^2 - y_f y_b)} \left(\frac{1}{y_f^5} + \frac{1}{y_b^5}\right) + \frac{2}{hk}\left(\frac{1}{x_f y_f} + \frac{1}{x_f y_b} + \frac{1}{x_b y_f} + \frac{1}{x_b y_b}\right)\right]$$

$$F = \left[-\frac{36px_f^2 x_b^2}{h(2x_f^2 + 2x_b^2 - x_f x_b)} \frac{1}{x_b^5} - \frac{2}{hk}\left(\frac{1}{x_b y_f} + \frac{1}{x_b y_b}\right)\right]$$

$$G = \frac{2}{hkx_f y_b}$$

$$H = \left[-\frac{36qy_f^2 y_b^2}{k(2y_f^2 + 2y_b^2 - y_f y_b)} \frac{1}{y_b^5} - \frac{2}{hk}\left(\frac{1}{x_f y_b} + \frac{1}{x_b y_b}\right)\right]$$

$$I = \frac{2}{hkx_b y_b}$$

and

$$\phi_{i,j} = \Bigg[\frac{36p(x_f^2 + x_b^2 - x_f x_b)}{2h(2x_f^2 + 2x_b^2 - x_f x_b)} \left(\frac{v_{i+1,j} - v_{i-1,j}}{x_f x_b} \right) - \frac{36q(y_f^2 + y_b^2 - y_f y_b)}{2k(2y_f^2 + 2y_b^2 - y_f y_b)} \left(\frac{u_{i,j+1} - u_{i,j-1}}{y_f y_b} \right)$$
$$- \frac{1}{h} \left(\frac{6p(3x_f^2 + 3x_b^2 - x_f x_b)(x_f - x_b)}{x_f x_b (2x_f^2 + 2x_b^2 - x_f x_b)} + Re.u_{i,j} \right) \left\{ \frac{v_{i+1,j}}{x_f} + \frac{v_{i-1,j}}{x_b} - \left(\frac{1}{x_f} + \frac{1}{x_b} \right) v_{i,j} \right\}$$
$$- \frac{Re.u_{i,j}}{k} \left\{ \frac{v_{i,j+1}}{y_f} + \frac{v_{i,j-1}}{y_b} - \left(\frac{1}{y_f} + \frac{1}{y_b} \right) v_{i,j} \right\} - \frac{72p(x_f^2 + x_b^2)(x_f - x_b)}{x_f^2 x_b^2 (2x_f^2 + 2x_b^2 - x_f x_b)} v_{i,j}$$
$$+ \frac{1}{k} \left(\frac{6q(3y_f^2 + 3y_b^2 - y_f y_b)(y_f - y_b)}{y_f y_b (2y_f^2 + 2y_b^2 - y_f x_b)} + Re.v_{i,j} \right) \left\{ \frac{u_{i,j+1}}{y_f} + \frac{u_{i,j-1}}{y_b} - \left(\frac{1}{y_f} + \frac{1}{y_b} \right) u_{i,j} \right\}$$
$$+ \frac{Re.v_{i,j}}{h} \left\{ \frac{u_{i+1,j}}{x_f} + \frac{u_{i-1,j}}{x_b} - \left(\frac{1}{x_f} + \frac{1}{x_b} \right) u_{i,j} \right\} + \frac{72q(y_f^2 + y_b^2)(y_f - y_b)}{y_f^2 y_b^2 (2y_f^2 + 2y_b^2 - y_f y_b)} u_{i,j}$$
$$- Re.u \frac{(y_f - y_b)}{6hk} \left\{ \frac{1}{y_f} (u_{i+1,j+1} - u_{i-1,j+1}) - \left(\frac{1}{y_f} + \frac{1}{y_b} \right) (u_{i+1,j} - u_{i-1,j}) + \frac{1}{y_b} (u_{i+1,j-1} - u_{i-1,j-1}) \right\}$$
$$+ Re.v \frac{(x_f - x_b)}{6hk} \left\{ \frac{1}{x_f} (v_{i+1,j+1} - v_{i+1,j-1}) - \left(\frac{1}{x_f} + \frac{1}{x_b} \right) (v_{i,j+1} - v_{i,j-1}) + \frac{1}{x_b} (v_{i-1,j+1} - v_{i-1,j-1}) \right\}$$
$$- \frac{2(x_f - x_b)}{3hk} \Bigg\{ \frac{v_{i+1,j+1}}{x_f y_f} + \frac{v_{i-1,j+1}}{x_b y_f} - \left(\frac{1}{x_f y_f} + \frac{1}{x_b y_f} \right) v_{i,j+1} - \left(\frac{1}{x_f y_f} + \frac{1}{x_f y_b} \right) v_{i+1,j}$$
$$+ \left(\frac{1}{x_f y_f} + \frac{1}{x_f y_b} + \frac{1}{x_b y_f} + \frac{1}{x_b y_b} \right) v_{i,j} - \left(\frac{1}{x_f y_b} + \frac{1}{x_b y_b} \right) v_{i,j-1} - \left(\frac{1}{x_b y_f} + \frac{1}{x_b y_b} \right) v_{i-1,j}$$
$$+ \frac{v_{i+1,j-1}}{x_f y_b} + \frac{v_{i-1,j-1}}{x_b y_b} \Bigg\}$$
$$+ \frac{2(y_f - y_b)}{3hk} \Bigg\{ \frac{u_{i+1,j+1}}{x_f y_f} + \frac{u_{i-1,j+1}}{x_b y_f} - \left(\frac{1}{x_f y_f} + \frac{1}{x_b y_f} \right) u_{i,j+1} - \left(\frac{1}{x_f y_f} + \frac{1}{x_f y_b} \right) u_{i+1,j}$$
$$+ \left(\frac{1}{x_f y_f} + \frac{1}{x_f y_b} + \frac{1}{x_b y_f} + \frac{1}{x_b y_b} \right) u_{i,j} - \left(\frac{1}{x_f y_b} + \frac{1}{x_b y_b} \right) u_{i,j-1} - \left(\frac{1}{x_b y_f} + \frac{1}{x_b y_b} \right) u_{i-1,j}$$
$$+ \frac{u_{i+1,j-1}}{x_f y_b} + \frac{u_{i-1,j-1}}{x_b y_b} \Bigg\} \Bigg]$$

BIBLIOGRAPHY

[1] I. Altas, J. Dym, M. M. Gupta, and R. P. Manohar. Multigrid solution of automatically generated high-order discretizations for the biharmonic equation. *SIAM Journal on Scientific Computing*, 19(5):1575–1585, 1998.

[2] D. Anderson and S. Davis. Two-fluid viscous flow in a corner. *Journal of Fluid Mechanics*, 257:1–31, 1993.

[3] J. D. Anderson and J. Wendt. *Computational fluid dynamics*, volume 206. Springer, 1995.

[4] L. Anton. Formation of a vortex at the edge of a plate. Technical report, NATIONAL AERONAUTICS AND SPACE ADMINISTRATION WASHINGTON DC, 1956.

[5] B. F. Armaly, F. Durst, J. Pereira, and B. Schönung. Experimental and theoretical investigation of backward-facing step flow. *Journal of fluid Mechanics*, 127:473–496, 1983.

[6] H. Badr, M. Coutanceau, S. Dennis, and C. Menard. Unsteady flow past a rotating circular cylinder at reynolds numbers 10 3 and 10 4. *Journal of Fluid Mechanics*, 220:459–484, 1990.

[7] E. Barragy and G. Carey. Stream function-vorticity driven cavity solution using p finite elements. *Computers & Fluids*, 26(5):453–468, 1997.

[8] I. Barton. A numerical study of flow over a confined backward-facing step. *International Journal for Numerical Methods in Fluids*, 21(8):653–665, 1995.

[9] C. K. Batchelor and G. Batchelor. *An introduction to fluid dynamics*. Cambridge university press, 2000.

[10] M. Ben-Artzi, I. Chorev, J.-P. Croisille, and D. Fishelov. A compact difference scheme for the biharmonic equation in planar irregular domains. *SIAM Journal on Numerical Analysis*, 47(4):3087–3108, 2009.

[11] M. Ben-Artzi, J.-P. Croisille, and D. Fishelov. Convergence of a compact scheme for the pure streamfunction formulation of the unsteady navier–stokes system. *SIAM journal on numerical analysis*, 44(5):1997–2024, 2006.

[12] M. Ben-Artzi, J.-P. Croisille, and D. Fishelov. A high order compact scheme for the pure-streamfunction formulation of the Navier-Stokes equations. *Journal of Scientific Computing*, 42(2):216–250, 2010.

[13] M. Ben-Artzi, J.-P. Croisille, D. Fishelov, and S. Trachtenberg. A pure-compact scheme for the streamfunction formulation of navier–stokes equations. *Journal of Computational Physics*, 205(2):640–664, 2005.

[14] R. Benzi, S. Patarnello, and P. Santangelo. On the statistical properties of two-dimensional decaying turbulence. *EPL (Europhysics Letters)*, 3(7):811, 1987.

[15] P. A. Berthelsen and O. M. Faltinsen. A local directional ghost cell approach for incompressible viscous flow problems with irregular boundaries. *Journal of Computational Physics*, 227(9):4354–4397, 2008.

[16] G. Biswas, M. Breuer, and F. Durst. Backward-facing step flows for various expansion ratios at low and moderate reynolds numbers. *J. Fluids Eng.*, 126(3):362–374, 2004.

[17] S. Biswas and J. C. Kalita. Moffatt eddies in the driven cavity: A quantification study by an HOC approach. *Computers & Mathematics with Applications*, 76(3):471–487, 2018.

[18] R. Bouard and M. Coutanceau. The early stage of development of the wake behind an impulsively started cylinder for $40 < Re < 10^4$. *Journal of Fluid Mechanics*, 101(3):583–607, 1980.

[19] A. Brüger, B. Gustafsson, P. Lötstedt, and J. Nilsson. High order accurate solution of the incompressible navier–stokes equations. *Journal of Computational Physics*, 203(1):49–71, 2005.

[20] C.-H. Bruneau and C. Jouron. An efficient scheme for solving steady incompressible Navier-Stokes equations. *Journal of Computational Physics*, 89(2):389–413, 1990.

[21] C.-H. Bruneau and M. Saad. The 2D lid-driven cavity problem revisited. *Computers & Fluids*, 35(3):326–348, 2006.

[22] D. Calhoun. A cartesian grid method for solving the two-dimensional streamfunction-vorticity equations in irregular regions. *Journal of Computational Physics*, 176(2):231–275, 2002.

[23] R. Chein and J. Chung. Discrete-vortex simulation of flow over inclined and normal plates. *Computers & fluids*, 16(4):405–427, 1988.

[24] T. Chung. *Computational fluid dynamics*. Cambridge university press, 2010.

[25] J. M. Cimbala, H. M. Nagib, and A. Roshko. Large structure in the far wakes of two-dimensional bluff bodies. *Journal of Fluid Mechanics*, 190:265–298, 1988.

[26] N. R. Council. *Twenty-First Symposium on Naval Hydrodynamics*. The National Academies Press, Washington, DC, 1997.

[27] M. Coutanceau and R. Bouard. Experimental determination of the main features of the viscous flow in the wake of a circular cylinder in uniform translation. Part 2. Unsteady flow. *Journal of Fluid Mechanics*, 79(2):257–272, 1977.

[28] M. Coutanceau and J.-R. Defaye. Circular Cylinder Wake Configurations: A Flow Visualization Survey. *Applied Mechanics Reviews*, 44(6):255–305, 06 1991.

[29] P. A. Davies, J. M. Dakin, and R. A. Falconer. Eddy formation behind a coastal headland. *Journal of Coastal Research*, pages 154–167, 1995.

[30] A. K. De and A. Dalal. A numerical study of natural convection around a square, horizontal, heated cylinder placed in an enclosure. *International journal of heat and mass transfer*, 49(23-24):4608–4623, 2006.

[31] G. de Vahl Davis. Natural convection of air in a square cavity: a bench mark numerical solution. *International Journal for numerical methods in fluids*, 3(3):249–264, 1983.

[32] S. Dennis, W. Qiang, M. Coutanceau, and J.-L. Launay. Viscous flow normal to a flat plate at moderate reynolds numbers. *Journal of Fluid Mechanics*, 248:605–635, 1993.

[33] M. Deshpande and S. G. Milton. Kolmogorov scales in a driven cavity flow. *Fluid dynamics research*, 22(6):359, 1998.

[34] S. Dutta, P. Kumar, and J. C. Kalita. Streamfunction-velocity computation of natural convection around heated bodies placed in a square enclosure. *International Journal of Heat and Mass Transfer*, 152:119550, 2020.

[35] S. Dutta, P. Kumar, and J. C. Kalita. Steady state conjugate heat transfer in backward facing step: A streamfunction-velocity approach. *Heat Transfer*, 2021.

[36] M. V. Dyke, editor. *An Album of Fluid Motion*. The Parabolic Press, Stanford, 1982.

[37] E. Erturk, T. C. Corke, and C. Gökçöl. Numerical solutions of 2-D steady incompressible driven cavity flow at high Reynolds numbers. *International Journal for Numerical Methods in Fluids*, 48(7):747–774, 2005.

[38] B. Fornberg. A numerical study of steady viscous flow past a circular cylinder. *Journal of Fluid Mechanics*, 98(4):819–855, 1980.

[39] R. Franke, W. Rodi, and B. Schönung. Numerical calculation of laminar vortex-shedding flow past cylinders. *Journal of Wind Engineering and Industrial Aerodynamics*, 35:237–257, 1990.

[40] D. K. Gartling. A test problem for outflow boundary conditions—flow over a backward-facing step. *International Journal for Numerical Methods in Fluids*, 11(7):953–967, 1990.

[41] U. Ghia, K. N. Ghia, and C. Shin. High-Re solutions for incompressible flow using the Navier-Stokes equations and a multigrid method. *Journal of Computational Physics*, 48(3):387–411, 1982.

[42] J. W. Goodrich and W. Sox. Time-dependent viscous incompressible navier-stokes equations: the finite difference galerkin formulation and streamfunction algorithms. *Journal of Computational Physics*, 84(1):207–241, 1989.

[43] J. P. Guerrero and R. Cotta. Benchmark integral transform results for flow over a backward-facing step. *Computers & fluids*, 25(5):527–540, 1996.

[44] M. M. Gupta. High accuracy solutions of incompressible navier-stokes equations. *Journal of Computational Physics*, 93(2):343–359, 1991.

[45] M. M. Gupta. High-accuracy compact difference schemes for differential equations in mathematical sciences. *Annals of Mathematical Sciences and Applications*, 5(1):101–138, 2020.

[46] M. M. Gupta and J. C. Kalita. A new paradigm for solving navier–stokes equations: streamfunction–velocity formulation. *Journal of Computational Physics*, 207(1):52–68, 2005.

[47] M. M. Gupta and J. C. Kalita. New paradigm continued: Further computations with streamfunction-velocity formulations for solving Navier-Stokes equations. *Communications in Applied Analysis*, 10(4):461–490, 2006.

[48] M. M. Gupta and R. P. Manohar. Direct solution of the biharmonic equation using noncoupled approach. *Journal of Computational Physics*, 33(2):236–248, 1979.

[49] M. M. Gupta, R. P. Manohar, and J. W. Stephenson. A single cell high order scheme for the convection-diffusion equation with variable coefficients. *International Journal for Numerical Methods in Fluids*, 4(7):641–651, 1984.

[50] X. He and G. Doolen. Lattice Boltzmann method on curvilinear coordinates system: flow around a circular cylinder. *Journal of Computational Physics*, 134(2):306–315, 1997.

[51] X. He and G. D. Doolen. Lattice Boltzmann method on a curvilinear coordinate system: Vortex shedding behind a circular cylinder. *Physical Review E*, 56(1):434, 1997.

[52] W. D. Henshaw. A fourth-order accurate method for the incompressible navier-stokes equations on overlapping grids. *Journal of computational physics*, 113(1):13–25, 1994.

[53] W. D. Henshaw, H.-O. Kreiss, and L. G. Reyna. A fourth-order-accurate difference approximation for the incompressible navier-stokes equations. *Computers & fluids*, 23(4):575–593, 1994.

[54] J. D. Hoffman and S. Frankel. *Numerical methods for engineers and scientists*. CRC press, 2018.

[55] F. Homann. Einfluß großer zähigkeit bei strömung um zylinder. *Forschung auf dem Gebiet des Ingenieurwesens A*, 7(1):1–10, 1936.

[56] T.-L. Horng, P.-W. Hsieh, S.-Y. Yang, and C.-S. You. A simple direct-forcing immersed boundary projection method with prediction-correction for fluid-solid interaction problems. *Computers & Fluids*, 176:135–152, 2018.

[57] S. Hou, Q. Zou, S. Chen, G. Doolen, and A. C. Cogley. Simulation of cavity flow by the Lattice Boltzmann method. *Journal of Computational Physics*, 118(2):329–347, 1995.

[58] K. In, D. H. Choi, and M. Kim. Two-dimensional viscous flow past a flat plate. *Fluid Dynamics Research*, 15(1):13, 1995.

[59] D. Ingham, T. Tang, and B. Morton. Steady two-dimensional flow past a normal flat plate. *Zeitschrift für angewandte Mathematik und Physik ZAMP*, 42(4):584–604, 1991.

[60] C. Jackson. A finite-element study of the onset of vortex shedding in flow past variously shaped bodies. *Journal of fluid Mechanics*, 182:23–45, 1987.

[61] J. Jeong and F. Hussain. On the identification of a vortex. *Journal of fluid mechanics*, 285:69–94, 1995.

[62] H. Jiang and L. Cheng. Transition to the secondary vortex street in the wake of a circular cylinder. *Journal of Fluid Mechanics*, 867:691–722, 2019.

[63] S. A. Johnson, M. C. Thompson, and K. Hourigan. Predicted low frequency structures in the wake of elliptical cylinders. *European Journal of Mechanics-B/Fluids*, 23(1):229–239, 2004.

[64] H. Kaden. Aufwicklung einer unstabilen unstetigkeitsfläche. *Ingenieur-Archiv*, 2(2):140–168, 1931.

[65] J. C. Kalita. Effects of clustering on the simulation of incompressible viscous flows. *Engineering Applications of Computational Fluid Mechanics*, 1(1):36–48, 2007.

[66] J. C. Kalita. Effect of boundary location on the steady flow past an impulsively started circular cylinder. *International Journal of Computing Science and Mathematics*, 5(3):252–279, 2014.

[67] J. C. Kalita, S. Biswas, and S. Panda. Finiteness of corner vortices. *Zeitschrift für angewandte Mathematik und Physik*, 69(2):37, 2018.

[68] J. C. Kalita, D. Dalal, and A. K. Dass. Fully compact higher-order computation of steady-state natural convection in a square cavity. *Physical Review E*, 64(6):066703, 2001.

[69] J. C. Kalita, D. Dalal, and A. K. Dass. A class of higher order compact schemes for the unsteady two-dimensional convection–diffusion equation with variable convection coefficients. *International Journal for Numerical Methods in Fluids*, 38(12):1111–1131, 2002.

[70] J. C. Kalita, A. K. Dass, and D. Dalal. A transformation-free HOC scheme for steady convection–diffusion on non-uniform grids. *International journal for numerical methods in fluids*, 44(1):33–53, 2004.

[71] J. C. Kalita, A. K. Dass, and N. Nidhi. An efficient transient Navier–Stokes solver on compact nonuniform space grids. *Journal of Computational and Applied mathematics*, 214(1):148–162, 2008.

[72] J. C. Kalita and B. B. Gogoi. A biharmonic approach for the global stability analysis of 2D incompressible viscous flows. *Applied Mathematical Modelling*, 40(15-16):6831–6849, 2016.

[73] J. C. Kalita and M. M. Gupta. A streamfunction–velocity approach for 2D transient incompressible viscous flows. *International journal for numerical methods in fluids*, 62(3):237–266, 2010.

[74] J. C. Kalita and R. K. Ray. A transformation-free HOC scheme for incompressible viscous flows past an impulsively started circular cylinder. *Journal of Computational Physics*, 228(14):5207–5236, 2009.

[75] J. C. Kalita and S. Sen. The (9, 5) HOC formulation for the transient Navier–Stokes equations in primitive variable. *International journal for numerical methods in fluids*, 55(4):387–406, 2007.

[76] J. C. Kalita and S. Sen. The biharmonic approach for unsteady flow past an impulsively started circular cylinder. *Communications in Computational Physics*, 12(4):1163–1182, 2012.

[77] J. C. Kalita and S. Sen. Unsteady separation leading to secondary and tertiary vortex dynamics: the sub-α and sub-β-phenomena. *Journal of Fluid Mechanics*, 730:19–51, 2013.

[78] S. Karaa. A high-order compact ADI method for solving three-dimensional unsteady convection-diffusion problems. *Numerical Methods for Partial Differential Equations: An International Journal*, 22(4):983–993, 2006.

[79] S. Karaa and J. Zhang. High order ADI method for solving unsteady convection–diffusion problems. *Journal of Computational Physics*, 198(1):1–9, 2004.

[80] S. Karabelas. Conformal cartesian grids for symmetric bodies: a novel boundary fitted grid method. *Appl. Comput. Math.*, 4(4):1–15, 2015.

[81] B. Kim, D. Lee, M. Ha, and H. Yoon. A numerical study of natural convection in a square enclosure with a circular cylinder at different vertical locations. *International journal of heat and mass transfer*, 51(7-8):1888–1906, 2008.

[82] D. Kim and H. Choi. A second-order time-accurate finite volume method for unsteady incompressible flow on hybrid unstructured grids. *Journal of Computational Physics*, 162(2):411–428, 2000.

[83] J. Kim and P. Moin. Application of a fractional-step method to incompressible navier-stokes equations. *Journal of computational physics*, 59(2):308–323, 1985.

[84] W. Kim and H. Choi. Immersed boundary methods for fluid-structure interaction: A review. *International Journal of Heat and Fluid Flow*, 75:301–309, 2019.

[85] M. KIYA and M. ARIE. Discrete-vortex simulation of unsteady separated flow behind a nearly normal plate. *Bulletin of JSME*, 23(183):1451–1458, 1980.

[86] M. Kiya and M. Matsumura. Incoherent turbulence structure in the near wake of a normal plate. *Journal of Fluid Mechanics*, 190:343–356, 1988.

[87] E. M. Kolahdouz, A. P. S. Bhalla, B. A. Craven, and B. E. Griffith. An immersed interface method for discrete surfaces. *Journal of Computational Physics*, 400:108854, 2020.

[88] P. Koumoutsakos and D. Shiels. Simulations of the viscous flow normal to an impulsively started and uniformly accelerated flat plate. *Journal of Fluid Mechanics*, 328:177–227, 1996.

[89] L. Kovasznay. Hot-wire investigation of the wake behind cylinders at low Reynolds numbers. *Proceedings of the Royal Society of London. Series A. Mathematical and Physical Sciences*, 198(1053):174–190, 1949.

[90] I. M. Kozlov, K. V. Dobrego, and N. N. Gnesdilov. Application of RES methods for computation of hydrodynamic flows by an example of a 2D flow past a circular cylinder for Re= 5–200. *International Journal of Heat and Mass Transfer*, 54(4):887–893, 2011.

[91] R. Krasny. Vortex sheet computations: roll-up, wakes, separation. *Lectures in Applied Mathematics*, 28(1):385–401, 1991.

[92] J. Kriegseis, M. Kinzel, and D. E. Rival. On the persistence of memory: do initial conditions impact vortex formation? *Journal of Fluid Mechanics*, 736:91–106, 2013.

[93] P. Kumar and J. C. Kalita. A transformation-free ψ-v formulation of the Navier-Stokes equations on compact nonuniform grids. *Journal of Computational and Applied Mathematics*, 353:292 – 317, 2019.

[94] P. Kumar and J. C. Kalita. An efficient $\psi - v$ scheme for two-dimensional laminar flow past bluff bodies on compact nonuniform grids. *International Journal for Numerical Methods in Fluids*, 92(12):1723–1752, 2020.

[95] P. Kumar and J. C. Kalita. A comprehensive study of secondary and tertiary vortex phenomena of flow past a circular cylinder: A cartesian grid approach. *Physics of Fluids*, 33(5), 2021.

[96] R. Kupferman. A central-difference scheme for a pure stream function formulation of incompressible viscous flow. *SIAM Journal on Scientific Computing*, 23(1):1–18, 2001.

[97] D.-V. Le, B. C. Khoo, and J. Peraire. An immersed interface method for viscous incompressible flows involving rigid and flexible boundaries. *Journal of Computational Physics*, 220(1):109–138, 2006.

[98] P. Le Quéré. Accurate solutions to the square thermally driven cavity at high rayleigh number. *Computers & Fluids*, 20(1):29–41, 1991.

[99] Y. Li, R. Shock, R. Zhang, and H. Chen. Numerical study of flow past an impulsively started cylinder by the Lattice-Boltzmann method. *Journal of Fluid Mechanics*, 519:273, 2004.

[100] Q.-X. Lian and Z. Huang. Starting flow and structures of the starting vortex behind bluff bodies with sharp edges. *Experiments in Fluids*, 8(1-2):95–103, 1989.

[101] M. N. Linnick and H. F. Fasel. A high-order immersed interface method for simulating unsteady incompressible flows on irregular domains. *Journal of Computational Physics*, 204(1):157–192, 2005.

[102] Y. Liu, W. Zhang, Y. Jiang, and Z. Ye. A high-order finite volume method on unstructured grids using RBF reconstruction. *Computers & Mathematics with Applications*, 72(4):1096–1117, 2016.

[103] S. Luo, Y. Chew, and Y. Ng. Characteristics of square cylinder wake transition flows. *Physics of Fluids*, 15:2549–2559, 2003.

[104] J. P. Magalhães, D. M. Albuquerque, J. M. Pereira, and J. C. Pereira. Adaptive mesh finite-volume calculation of 2D lid-cavity corner vortices. *Journal of Computational Physics*, 243:365–381, 2013.

[105] H. Mittal, J. C. Kalita, and R. K. Ray. A class of finite difference schemes for interface problems with an HOC approach. *International Journal for Numerical Methods in Fluids*, 82(9):567–606, 2016.

[106] R. Mittal and S. Balachandar. Effect of three-dimensionality on the lift and drag of nominally two-dimensional cylinders. *Physics of Fluids*, 7(8):1841–1865, 1995.

[107] R. Mittal and P. Moin. Suitability of upwind-biased finite difference schemes for large-eddy simulation of turbulent flows. *AIAA journal*, 35(8):1415–1417, 1997.

[108] F. Najjar and S. Balachandar. Low-frequency unsteadiness in the wake of a normal flat plate. *Journal of Fluid Mechanics*, 370:101–147, 1998.

[109] F. Najjar and S. P. Vanka. Effects of intrinsic three-dimensionality on the drag characteristics of a normal flat plate. *Physics of fluids*, 7(10):2516–2518, 1995.

[110] F. M. Najjar and S. Vanka. Simulations of the unsteady separated flow past a normal flat plate. *International Journal for Numerical Methods in Fluids*, 21(7):525–547, 1995.

[111] A. Nishida, A. Fujii, and Y. Oyanagi. Lis: Library of iterative solvers for linear systems. *URL: http://www. phy. duke. edu/˜ rgb/General/rand_ rate. php (online.*

[112] X. Niu, Y. Chew, and C. Shu. Simulation of flows around an impulsively started circular cylinder by Taylor series expansion-and least squares-based Lattice Boltzmann method. *Journal of Computational Physics*, 188(1):176–193, 2003.

[113] S. K. Pandit. On the Use of Compact Stream Function-Velocity Formulation of Steady Navier-Stokes Equations on Geometries beyond Rectangular. *Journal of Scientific Computing*, 36:219–242, 2008.

[114] S. K. Pandit, J. C. Kalita, and D. Dalal. A transient higher order compact scheme for incompressible viscous flows on geometries beyond rectangular. *Journal of Computational Physics*, 225(1):1100–1124, 2007.

[115] S. K. Pandit, J. C. Kalita, and D. Dalal. A fourth-order accurate compact scheme for the solution of steady Navier–Stokes equations on non-uniform grids. *Computers & fluids*, 37(2):121–134, 2008.

[116] A. Perry and T. Steiner. Large-scale vortex structures in turbulent wakes behind bluff bodies. Part 1. Vortex formation processes. *Journal of Fluid Mechanics*, 174:233–270, 1987.

[117] D. Pierce. Photographic evidence of the formation and growth of vorticity behind plates accelerated from rest in still air. *Journal of Fluid Mechanics*, 11(3):460–464, 1961.

[118] R. H. Pletcher, J. C. Tannehill, and D. Anderson. *Computational fluid mechanics and heat transfer*. CRC press, 2012.

[119] L. Prandtl. Über flussigkeitsbewegung bei sehr kleiner reibung. *Verhandl. III, Internat. Math.-Kong., Heidelberg, Teubner, Leipzig, 1904*, pages 484–491, 1904.

[120] D. Pullin. The large-scale structure of unsteady self-similar rolled-up vortex sheets. *Journal of Fluid Mechanics*, 88(3):401–430, 1978.

[121] D. Pullin and A. Perry. Some flow visualization experiments on the starting vortex. *Journal of Fluid Mechanics*, 97(2):239–255, 1980.

[122] B. Rajani, A. Kandasamy, and S. Majumdar. Numerical simulation of laminar flow past a circular cylinder. *Applied Mathematical Modelling*, 33(3):1228–1247, 2009.

[123] M. Ramšak. Conjugate heat transfer of backward-facing step flow: A benchmark problem revisited. *International Journal of Heat and Mass Transfer*, 84:791–799, 2015.

[124] M. J. Ringuette, M. Milano, and M. Gharib. Role of the tip vortex in the force generation of low-aspect-ratio normal flat plates. *Journal of Fluid Mechanics*, 581:453–468, 2007.

[125] J. Robichaux, S. Balachandar, and S. P. Vanka. Three-dimensional floquet instability of the wake of square cylinder. *Physics of Fluids*, 11(3):560–578, 1999.

[126] A. Roshko. Perspectives on bluff body aerodynamics. *Journal of Wind Engineering and Industrial Aerodynamics*, 49(1-3):79–100, 1993.

[127] D. Russell and Z. J. Wang. A cartesian grid method for modeling multiple moving objects in 2D incompressible viscous flow. *Journal of Computational Physics*, 191(1):177–205, 2003.

[128] A. Saha, G. Biswas, and K. Muralidhar. Three-dimensional study of flow past a square cylinder at low reynolds numbers. *International Journal of Heat and Fluid Flow*, 24(1):54–66, 2003.

[129] A. K. Saha. Far-wake characteristics of two-dimensional flow past a normal flat plate. *Physics of Fluids*, 19(12):128110, 2007.

[130] A. K. Saha, K. Muralidhar, and G. Biswas. Transition and chaos in two-dimensional flow past a square cylinder. *Journal of engineering mechanics*, 126(5):523–532, 2000.

[131] A. K. Saha, K. Muralidhar, and G. Biswas. Vortex structures and kinetic energy budget in two-dimensional flow past a square cylinder. *Computers & fluids*, 29(6):669–694, 2000.

[132] H. Schlichting and K. Gersten. *Boundary layer theory*. Springer, 2016.

[133] R. Schreiber and H. B. Keller. Driven cavity flows by efficient numerical techniques. *Journal of Computational Physics*, 49(2):310–333, 1983.

[134] S. Sen. *Compact Biharmonic Computation of the Navier-Stokes Equations: Extension to Complex Flows*. PhD thesis, Indian Institute of Technology Guwahati, Guwahati 781039, Assam, 2012.

[135] S. Sen. A new family of (5, 5) CC-4OC schemes applicable for unsteady Navier-Stokes equations. *Journal of Computational Physics*, 251:251–271, 2013.

[136] S. Sen. Fourth order compact schemes for variable coefficient parabolic problems with mixed derivatives. *Computers & Fluids*, 134:81–89, 2016.

[137] S. Sen and J. C. Kalita. A 4OEC scheme for the biharmonic steady Navier-Stokes equations in non-rectangular domains. *Computer Physics Communications*, 196:113–133, 2015.

[138] S. Sen, J. C. Kalita, and M. M. Gupta. A robust implicit compact scheme for two-dimensional unsteady flows with a biharmonic stream function formulation. *Computers & Fluids*, 84:141–163, 2013.

[139] S. Sen, S. Mittal, and G. Biswas. Steady separated flow past a circular cylinder at low Reynolds numbers. *Journal of Fluid Mechanics*, 620:89, 2009.

[140] P. Shankar. The eddy structure in Stokes flow in a cavity. *Journal of Fluid Mechanics*, 250:371–383, 1993.

[141] P. Shankar. Moffatt eddies in the cone. *Journal of Fluid Mechanics*, 539:113, 2005.

[142] P. Shankar and M. Deshpande. Fluid mechanics in the driven cavity. *Annual Review of Fluid Mechanics*, 32(1):93–136, 2000.

[143] A. L. E. Silva, A. Silveira-Neto, and J. Damasceno. Numerical simulation of two-dimensional flows over a circular cylinder using the immersed boundary method. *Journal of Computational Physics*, 189(2):351–370, 2003.

[144] G. Sleijpen and H. van der Vorst. Hybrid bi-conjugate gradient methods for CFD problems. In M. Hafez and K. Oshima, editors, *Computational Fluid Dynamics Review*, pages 457 – 476. Wiley–Blackwell, 1995.

[145] J. Sohn. Evaluation of fidap on some classical laminar and turbulent benchmarks. *International Journal for Numerical Methods in Fluids*, 8(12):1469–1490, 1988.

[146] W. Spotz. Formulation and experiments with high-order compact schemes for nonuniform grids. *International Journal of Numerical Methods for Heat & Fluid Flow*, 1998.

[147] W. Spotz and G. Carey. High-order compact scheme for the steady stream-function vorticity equations. *International Journal for Numerical Methods in Engineering*, 38(20):3497–3512, 1995.

[148] W. Spotz and G. Carey. Extension of high-order compact schemes to time-dependent problems. *Numerical Methods for Partial Differential Equations: An International Journal*, 17(6):657–672, 2001.

[149] K. Srinivasan and S. G. Rubin. Segmented multigrid domain decomposition procedure for incompressible viscous flows. *International journal for numerical methods in fluids*, 15(11):1333–1355, 1992.

[150] J. Stephenson. Single cell discretizations of order two and four for biharmonic problems. *Journal of Computational Physics*, 55(1):65–80, 1984.

[151] J. C. Strikwerda. High-order-accurate schemes for incompressible viscous flow. *International Journal for Numerical Methods in Fluids*, 24(7):715–734, 1997.

[152] K. Taira and T. Colonius. The immersed boundary method: a projection approach. *Journal of Computational Physics*, 225(2):2118–2137, 2007.

[153] H. Tamaddon-Jahromi, P. Townsend, and M. Webster. Unsteady viscous flow past a flat plate orthogonal to the flow. *Computers & fluids*, 23(2):433–446, 1994.

[154] S. Taneda. Visualization of separating stokes flows. *Journal of the Physical Society of Japan*, 46(6):1935–1942, 1979.

[155] S. Taneda and H. Honji. Unsteady flow past a flat plate normal to the direction of motion. *Journal of the Physical Society of Japan*, 30(1):262–272, 1971.

[156] J. F. Thompson, Z. U. Warsi, and C. W. Mastin. *Numerical grid generation: foundations and applications*, volume 45. North-holland Amsterdam, 1985.

[157] D. Triton. Experiments on the flow past a circular cylinder at low Reynolds number. *Journal of Fluid Mechanics*, 6:547, 1959.

[158] W.-T. Tsai and D. K. P. Yue. Interaction between a free surface and a vortex sheet shed in the wake of a surface piercing plate. *Journal of fluid mechanics*, 257:691–721, 1993.

[159] S. P. Vanka. Block-implicit multigrid solution of Navier-Stokes equations in primitive variables. *Journal of Computational Physics*, 65(1):138–158, 1986.

[160] H. Villat. *Leçons sur la théorie des tourbillons, par Henri Villat...* Gauthier-Villars et cie, 1930.

[161] M. Vynnycky and S. Kimura. An investigation of recirculating flow in a driven cavity. *Physics of Fluids*, 6(11):3610–3620, 1994.

[162] Z. Wang, J. Fan, and K. Cen. Immersed boundary method for the simulation of 2D viscous flow based on vorticity–velocity formulations. *Journal of Computational Physics*, 228(5):1504–1520, 2009.

[163] E. Wedemeyer. Ausbildung eines wirbelpaares an den kanten einer platte. *Ingenieur-Archiv*, 30(3):187–200, 1961.

[164] E. Weinan and J.-G. Liu. Essentially compact schemes for unsteady viscous incompressible flows. *Journal of Computational Physics*, 126(1):122–138, 1996.

[165] C. Williamson and A. Roshko. Vortex formation in the wake of an oscillating cylinder. *Journal of Fluids and Structures*, 2(4):355 – 381, 1988.

[166] C. H. Williamson. Vortex dynamics in the cylinder wake. *Annual review of fluid mechanics*, 28(1):477–539, 1996.

[167] L. Xu. Numerical study of viscous starting flow past wedges. *Journal of Fluid Mechanics*, 801:150–165, 2016.

[168] L. Xu and M. Nitsche. Start-up vortex flow past an accelerated flat plate. *Physics of Fluids*, 27(3):033602, 2015.

[169] P. Yu and Z. F. Tian. A compact streamfunction–velocity scheme on nonuniform grids for the 2D steady incompressible Navier–Stokes equations. *Computers & Mathematics with Applications*, 66(7):1192–1212, 2013.